Probing Cytochrome P450 with Sensitizer-linked Substrates

Thesis by

Ivan J. Dmochowski

In Partial Fulfillment of the Requirements
For the Degree of
Doctor of Philosophy

California Institute of Technology
Pasadena, California

Submitted May 12, 2000

ACKNOWLEDGEMENT

In those first few years when it felt as if my research were conducted underwater, Harry and Jay Winkler were invaluable in providing THE MOTIVATION. Their vision and guidance fortified me for the search, and the dives gradually became deeper and more fruitful. I thank Harry for the incredible generosity he has shown me with his ideas, time, and resources. Thanks to him, I improved my writing, interacted with many remarkable people, ate well, and tried to think about big scientific problems during the past 4 1/2 years. My years in BILRC were very formative as well, and Jay instilled a sorely needed rigor to my experiments and data analysis. Between Harry, Jay, Caltech, and the Internet, I cannot imagine a better education.

When the six of us from '95 – Akif, Liz, Mike, Cindy, Lila, and I - joined the group it was a heady time. I shall never forget our first Christmas skit as the "Gray Group Bunch." My ignorance was not blissful for long, however, and I greatly appreciated the tutorials in inorganic synthetic chemistry, photochemistry, lasers, and protein purification from the experienced hands of Angelo, Don, T.P., and Johann.

I feel lucky to have interacted with so many talented researchers on various aspects of my work. I thank John Dawson for introducing me to many of the controversies in heme enzymes. From Jon Wilker I learned two important lessons, including a more methodical approach to my work. I thank Mike Green for challenging my thinking on numerous chalkboards and looking more deeply at P450 than the rest of us. Brian Crane's passion for and approach to science continue to inspire me on a regular basis. From him I was privileged to learn a smattering of protein crystallography, and I thank Alex Bilwes for sharing her knowledge of molecular biology and protein purification. I gratefully acknowledge Changmoon and Vaidehi for their introduction to simulations and calculations in the Goddard group. And, finally, I feel fortunate to be leaving sensitizer-linked substrates in the exceptional hands of Alex Dunn.

In the end, I have many people to thank for constantly renewing my happiness, energy, and creativity during graduate school. The Gray group is and has been a wonderful group of people to get to know. My years with Akif, Derek, and Kevin living together in San Gabriel are full of good memories. Adrian single-handedly brightened the B.I. sub-basement with his personality, and I couldn't ask for a better person with whom to have shared so many birthdays. Jim was always there when I needed him to go pound the streets and have good, long talks. Marathoning in San Francisco, playing soccer, skiing before work under the beautiful California sun, mountain biking, championship softball seasons, eating sushi in Tokyo, hiking in the Brazilian rain forest and craters of Maui, helicoptering to Catalina--So many wonderful times.

Finally, I want to thank all of my family for their moral support. Most importantly, I thank my wife, Jane, for all of her encouragement and understanding. I credit her for opening up my life to many new possibilities and adventures. With her I have lived life to its fullest.

Table of Contents

ABSTRACT

The covalent attachment of the photosensitizer $[Ru(bpy)_3]^{2+}$ to a substrate constitutes a powerful new method for probing the steric and electronic properties of buried enzyme active sites. Particularly important targets are oxygenases (cytochromes P450) involved in drug metabolism and many disease states. The crystal structure of a P450:Ru-adamantyl complex reveals that the substrate moiety gains access to the active center via a deep channel and rests above the heme much like the natural substrate camphor. This structure also identifies significant P450 conformational changes associated with substrate binding for the first time: the channel opens via a 6-Å loop movement. Turnover studies show that activity is not significantly diminished in the P450:Ru-adamantyl complex. Preliminary *light-activated* substrate turnover experiments also show promise.

The binding of Ru-substrates to P450 was measured by time-resolved luminescence and UV-vis assays. These molecules specifically recognize submicromolar cytochrome $P450_{cam}$ in the presence of other heme proteins. In the P450:Ru-substrate conjugates, energy transfer to the heme dramatically accelerates the Ru-luminescence decay. Quantifying the fraction of quenched Ru^{2+*} provides an accurate method for determining dissociation constants. In addition, for the P450:Ru-adamantyl complex, Förster analysis of the energy-transfer kinetics yields a Ru-Fe distance (21 Å) virtually the same as that measured in the crystal structure. Similar analysis for other Ru-substrates of varying length shows a narrow range of Ru-Fe distances, indicating favorable association of the $\{Ru(bpy)_3\}^{2+}$ moiety with the protein. The binding of the Λ and Δ enantiomers of Ru-C_9-Ad to P450 was measured, and the results, $K_D(\Delta/\Lambda) \sim 2$, suggest that the bipyridyl ligands interact with aromatic residues at the mouth of the substrate channel. Thus, enantiospecific interactions may be exploited in the design of enzyme-metallosubstrate conjugates.

Oxidative and reductive quenching of P450:$[Ru\text{-}(CH_2)_n\text{-substrate}]^{2+*}$ conjugates in solution triggers the injection of holes and electrons from ruthenium to the heme on sub-millisecond time scales. In order to accelerate electron transfer, conjugated (perfluorobiphenyl-bridged) Ru-probes were synthesized which bind P450 strongly ($K_D <$ 1 μM). Photoexcitation of conjugated Ru-imidazole-P450 complexes reduces the heme on submicrosecond time scales, opening new avenues for the study of short-lived enzyme intermediates.

Chapter 1

Introduction

Nature relies on metalloenzymes for myriad functions. These workhorse proteins employ transition metal ions to catalyze numerous complex transformations, including nitrogen fixation, water splitting (photosynthesis), dioxygen reduction (respiration) and dioxygen activation. Many enzymatic reactions are tightly regulated by long-range (> 10 Å) electron-transfer (ET) steps mediated by cofactors such as NADH, pterins, flavins, iron-sulfur clusters, or hemes. Strategies for characterizing reactive intermediates involve slowing their consumption (e.g., with cryogenic conditions, slow substrates, or mutagenesis) or, most pertinent to this thesis, accelerating the rate-limiting ET processes.

One particularly ubiquitous yet difficult target is cytochrome P450, a superfamily of heme monooxygenases responsible for xenobiotic metabolism and steroidogenesis (1,2). It is estimated that 1% of the plant genome and 0.1% of the human genome codes for these enzymes. Attempts to elucidate P450's mechanism of oxygen activation and unique reactivity towards hydrocarbons have been thwarted by sluggish electron transfer to the heme by physiologic redox partners. Very recently, researchers have exploited the versatility of the laser-triggered photoredox chemistry of $[Ru(bpy)_3]^{2+}$ (Figure 1.1) for the rapid modulation of enzyme oxidation states (3-6). Relative to conventional stopped-flow methods, this photochemical approach effects oxidation and reduction on a wide range of time scales (nanosecond-millisecond) and with varying thermodynamic

Figure 1.1. Latimer diagram for $[Ru(bpy)_3]^{2+}$. Excited-state Ru^{2+*} acts as both a good oxidant and reductant with a lifetime of roughly 600 ns in deaerated, aqueous solution. The ground states $[Ru(bpy)_3]^{3+}$ and $[Ru(bpy)_2(bpy^{\bullet-})]^{+}$ are much longer-lived and provide larger driving forces for oxidation and reduction, respectively.

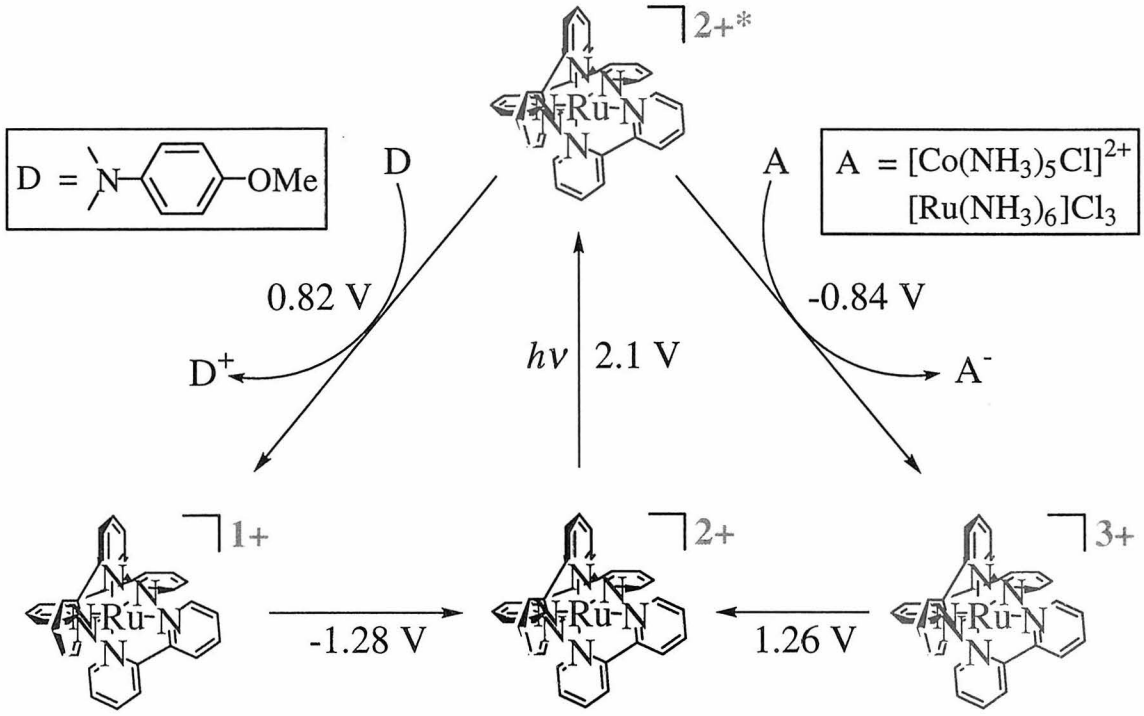
2+*
D = N OMe
D
A
A = [Co(NH3)5Cl]2+
[Ru(NH3)6]Cl3
0.82 V
-0.84 V
D+
hν 2.1 V
A-
1+
2+
3+
-1.28 V
1.26 V

driving forces. Horseradish peroxidase (HRP) (5) and microperoxidase-8 (MP-8) (6) were shown to undergo facile photooxidation by $[Ru(bpy)_3]^{3+}$. In contrast to HRP, P450 possesses a buried heme (Figure 1.2) that, like many metalloenzyme active sites, is poorly accessible to transiently generated photoredox agents. The development of active-site-directed strategies would expand the utility of these powerful photochemical methods.

Based on the affinity of P450 for a wide variety of organic molecules, new photochemical probes of enzyme structure and function have been created by the attachment of a Ru photosensitizer to a substrate. With these Ru-compounds, sub-microsecond oxidation and reduction of the P450 heme is now possible (Chapter 6), and energy-transfer measurements provide a practical method for quickly measuring enzyme dimensions, detecting specific enzymes in solution, and screening substrates (Chapter 2). This chapter will briefly examine the most compelling controversies in P450 catalysis, and provide a framework for the development of new *sensitizer-linked substrates* for studies of P450 and many other metalloproteins.

Figure 1.2. Top: Crystal structure of horseradish peroxidase at 2.0 Å resolution. This surface rendering (van der Waals) shows that the heme edge is accessible to organic substrates and photooxidants in solution. Below: Crystal structure of $P450_{cam}$ at 1.7 Å resolution. This surface rendering shows the buried heme from its most visible perspective, barely solvent accessible on the proximal face.

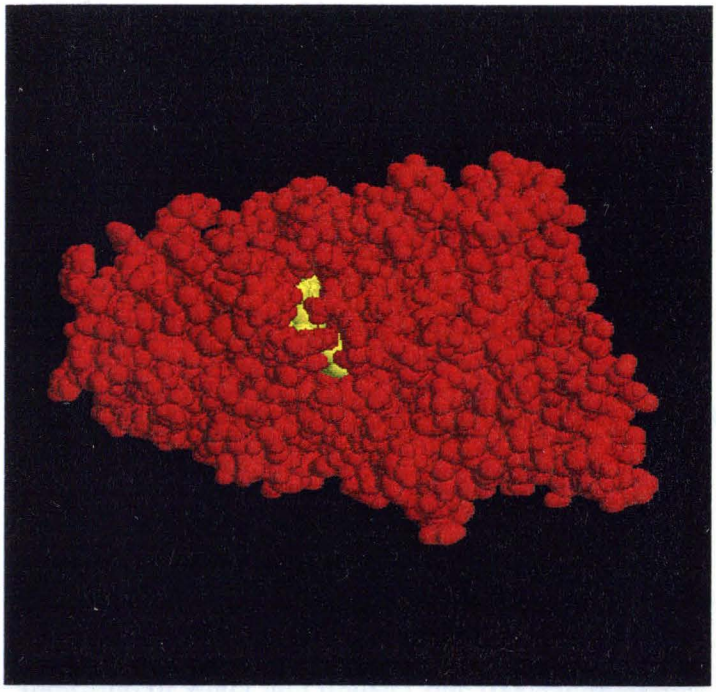

HRP

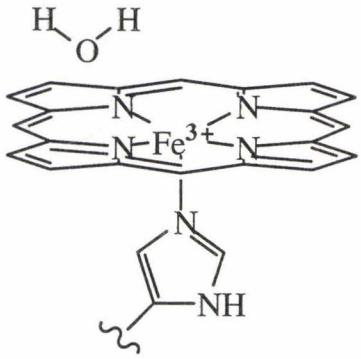

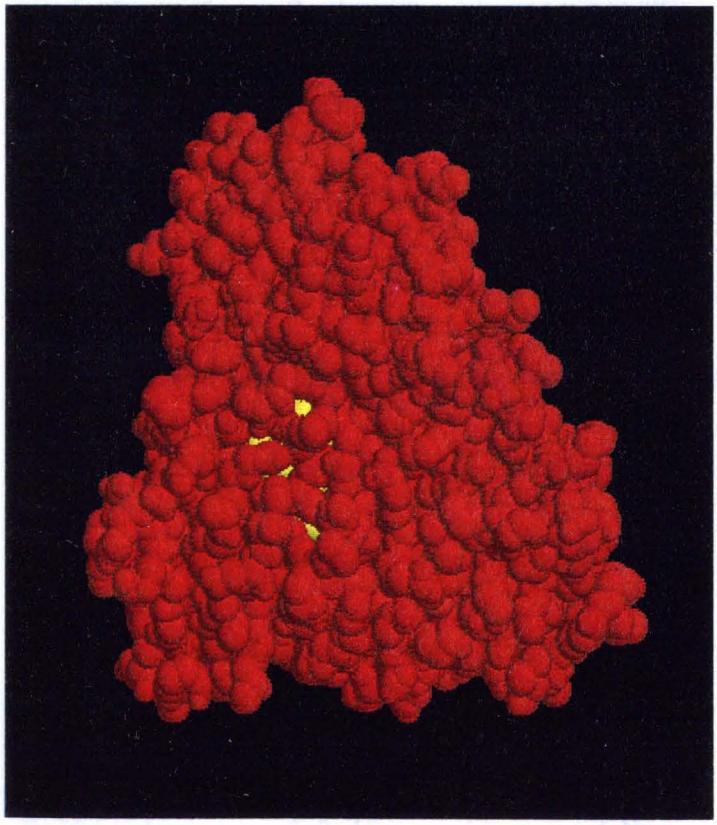

P450$_{cam}$

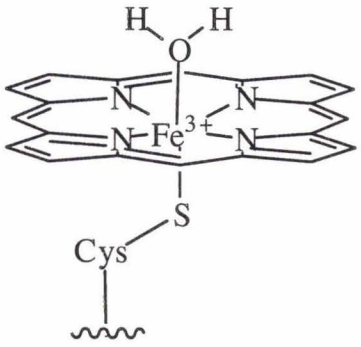

Three Puzzles of Cytochrome P450

Since the discovery of a CO-binding pigment in liver microsomes in 1958 (7,8), P450 has been perhaps the most intensely studied of all enzymes. Due to its early discovery and ease of growth and purification, much research, including the work in this thesis, has focused on the bacterial, camphor-metabolizing $P450_{cam}$. At their catalytic sites, all P450s possess a Cys-ligated, low potential, buried heme (iron protoporphyrin IX). As monooxygenases, P450s split dioxygen by a 2-electron process to make one molecule of water and transfer one oxygen atom to a substrate. $P450_{cam}$ accepts reducing equivalents from β-nicotinamide adenine dinucleotide dihydride (NADH) via putidredoxin reductase (PdR, an FAD-containing flavoprotein) and putidaredoxin (Pd, an Fe_2S_2 protein) to reduce bound molecular oxygen (Figure 1.3). These cytochromes catalyze over 20 different reactions, including hydrocarbon hydroxylation, alkene and arene epoxidation, alkyne oxygenation, N, S, and O-dealkylations, oxidative and reductive dehalogenations, N and S-oxidations, NO reduction, and C-C bond cleavage.

Despite considerable investigation, however, the details of the P450 catalytic cycle (represented schematically in Figure 1.4) remain highly controversial. Three key questions (listed in the order in which they appear in the catalytic cycle) are 1) How does P450 bind substrates? 2) How are electrons delivered to the heme? 3) What is (are) the

Figure 1.3. Top: The tightly controlled delivery of electrons to cytochrome $P450_{cam}$. Two reducing equivalents are passed from NADH to PdR, to Pd which binds P450 tightly (K_D ~ 1 μM) and supplies two 1-electron equivalents to the heme for each catalytic cycle.

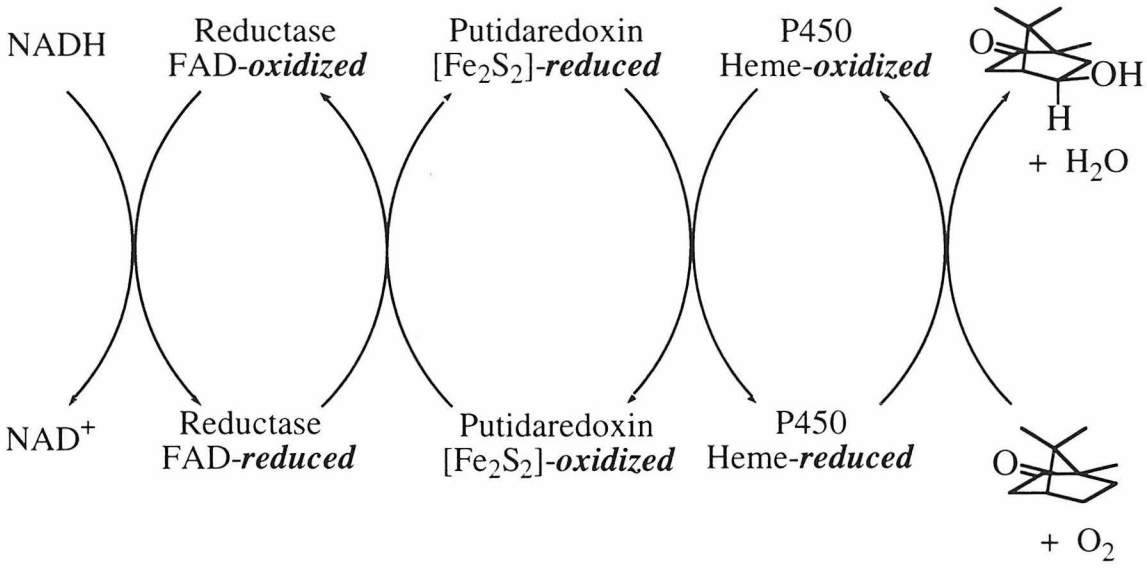
NADH
Reductase
FAD-oxidized
Putidaredoxin
[Fe2S2]-reduced
P450
Heme-oxidized
O
OH
H
+ H2O
NAD+
Reductase
FAD-reduced
Putidaredoxin
[Fe2S2]-oxidized
P450
Heme-reduced
O
+ O2

Figure 1.4. Catalytic cycle of cytochrome $P450_{cam}$. RH represents the substrate and ROH the product. Species 1-6a have been well characterized by numerous physical methods, including X-ray crystallography. Structures 6b and 7 are putative intermediates, each with several possible resonance structures. The oxidizing equivalent on the putative compound I species (7) has been assigned alternatively to the oxygen, the sulfur, the iron, and the porphyrin. The peroxide shunt (and uncoupling) pathways are shown (2-6b), as well as oxidase (and O-atom transfer) chemistry (2-7). The second electron transfer is rate limiting under physiological conditions.

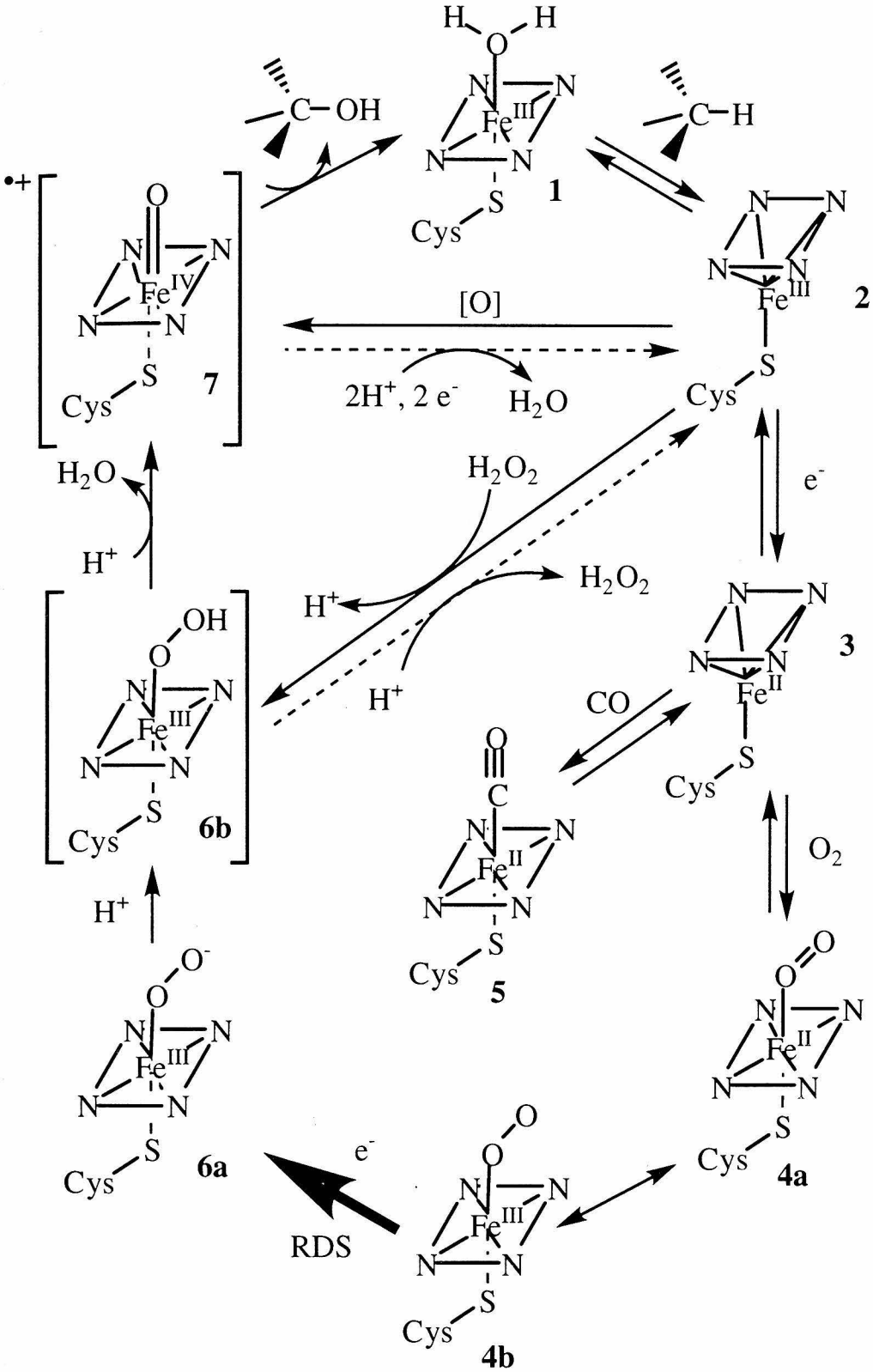
C–OH
C–H
[O]
2H+, 2 e-
H2O
H2O2
H+
e-
CO
O2
RDS
Cys
1
2
3
4a
4b
5
6a
6b
7

reactive intermediate(s)? This final quest(ion) has been called the Holy Grail of P450 research. In Camelot, after the conventional approaches have been tried, one is left with the quixotic.

In the resting state with a ferric, water-bound, low-spin (S = 5/2) heme iron, P450 binds substrate. Several structures of P450s cocrystallized with organic molecules have been solved which identify a large cavity on the distal side of the heme; however, only subtle differences exist between substrate-free and substrate-bound forms. $P450_{cam}$ sequesters substrates from bulk solvent particularly well, and no path from the surface to the active site is readily identified (9). Indeed, the enzyme dynamics and substrate trajectories during binding remain intriguing problems.

Mutagenesis experiments have tried unsuccessfully to identify the residue motions responsible for channel opening (10), as the enzyme has shown itself to be relatively insensitive to point mutations. Photoacoustic calorimetry experiments measured significant changes in enzyme enthalpy (-15.9 kcal mol^{-1}) and volume (10.3 mL mol^{-1}) during camphor ejection (driven by CO photolysis) with a lifetime of 130 ns (11). These data, taken in conjunction with time-resolved Raman spectra (12), suggest that camphor leaves the pocket concomitant with CO photolysis and induces considerable conformational change in the protein. Although important protein dynamical questions persist, a recent crystal structure of $P450_{cam}$ in an open conformation (Chapters 2, 4)

solidifies a wealth of experimental work which had previously identified the F-G loop and aromatic residues Phe 87, Phe 193, Tyr 96, and Tyr 23 as important in substrate binding (1,13). Molecular dynamics simulations continue to challenge assumptions that substrates bind singly and enter and exit by only one route (14).

Substrate binding initiates the catalytic cycle by facilitating electron transfer to P450. Ferric $P450_{cam}$ complexation of camphor displaces five or six water molecules from the pocket and produces a (low-to-high) spin shift of the heme (S = 1/2). By a mechanism common to most P450s, this change in structure raises the reduction potential ($E^0_{ls} = -300$ mV $\rightarrow$ $E^0_{hs} = -170$ mV vs. NHE) to within the thermodynamic range of the Fe_2S_2 redox partner, Pd ($E^0 = -196$ mV). Diffraction quality crystals of Pd, either alone or complexed to P450, have not yet been grown. Thus, characterization of the P450-Pd electron-transfer pair has relied largely on mutagenesis/turnover studies (15-18) and modeling based on the NMR structure of Pd (19). Various mutants of Pd and P450 have been generated which identify residues important for favorable binding as well as those providing ET pathways (15,17,18).

P450 is an acidic protein (pI ~ 5.5) but possesses a patch of four basic residues on the proximal face which promote strong binding interactions (K_D ~ 1 μM) with negatively charged redox partners. Substantial efforts have been made to circumvent these Fe_2S_2 enzymes, due to the slow rates of electron transfer (~ 50 s^{-1}) and the relative expense of

these reducing agents; in addition, the frequent discovery of new P450s often necessitates finding new redox partners that effect turnover. Electrochemically driven catalysis has been achieved with modest success, and it appears that electrostatic interactions at the proximal face promote association with the electrode (20). The possibilities for light-driven P450 catalysis motivate the design of Ru-probes.

Pd plays an important, but incompletely defined role in the $P450_{cam}$ catalytic cycle. One mechanism postulates that steric or electrostatic interactions on the proximal face contribute to the unique reactivity of P450 by modulating the Fe-S bond strength. Supporting this hypothesis are resonance Raman studies showing a 3 cm^{-1} upshift in the Fe-S stretching mode of ferric P450 upon Pd binding (21). Surrogate electron donors include rubredoxin and adrenodoxin. Interestingly, dithionite is a stronger reductant than either of these redox partners, and yet can only supply the first electron in the catalytic cycle and fails to effect substrate turnover. Although this may point to a unique role of the Fe_2S_2 proteins, in truth dithionite is ill-suited for the second ET step because it generates superoxide. Beratan et al. have proposed two competing paths from Pd to the heme, the most strongly coupled via Cys357 to the heme iron, and, alternatively, a hydrogen-bonded path involving one of the heme propionates (18). In considering the design of new ET pathways into P450, it is important to recognize that these enzymes

have evolved specific and favorable protein-protein interactions to drive both ET reactions necessary for catalysis.

Following reduction, Fe^{2+} P450 binds dioxygen to make a species best formulated as ferric-superoxide (4b, Figure 1.4). First characterized in 1971 (22), this intermediate lasts only 5 minutes at room temperature, decaying to the aquo-bound resting state (23). Autoxidation is not a significant uncoupling pathway under normal catalytic conditions, however, since ET from reduced Pd occurs more rapidly. Oxy P450 is greatly stabilized at reduced temperatures ($\tau_{1/2}$ = 90 minutes at –30 °C) rendering it amenable to numerous physical studies, including UV-vis (22), MCD, EPR, ENDOR, Raman (24), and, most recently, X-ray crystallography (25). As the last stable and well-characterized species, oxy P450 has served as the base camp for most attempts to visualize high-valent species. It is into this form of the enzyme that photo-triggered electron injection is most likely to generate the elusive intermediate(s).

After the second electron injection into P450, there is little consensus about the subsequent events leading to substrate hydroxylation. Numerous indirect studies of both dioxygen and peroxide driven catalysis have provided insight into the chemical nature of intermediates involved in P450 oxygen activation (22,26-28). Recent EPR and ENDOR studies of the reduced oxy intermediate (6a, Figure 1.4) in WT and D251N P450 (29), and UV-vis characterization of this species in D251N (30), fill an important gap in the

catalytic pathway. In probably the most sustained effort at spectroscopically characterizing the high-valent species, several sequential crystal structures were determined of ferrous-oxy, and reduced ferrous-oxy, which forms electron density not inconsistent with an iron-oxo and finally hydroxylates camphor. Turnover was induced at cryogenic temperatures by irradiation with long-wavelength X-rays that presumably generate photoelectrons (25).

The oxy P450 structure's striking similarity to that of P450:Ru-C_9-Ad is discussed in Chapter 4. Both structures show Asp 251 and Thr 252 conformational changes stabilizing two water molecules at the active site that likely play important roles in proton transfer to dioxygen. Less satisfying, however, are the conclusions drawn from the P450 "ferryl" structure. There are two molecules in the asymmetric unit; in the first, there is little electron density above the heme, which could indicate partial occupancy of either an O-atom or water. In the second molecule, residual electron density from the dioxygen could be assigned to a hydroperoxo-iron species. In fact, a recent accumulation of data suggests that, similarly to nitric oxide synthase (NOS), P450 hydroxylates by both O-atom and OH^+ insertion (31). More sophisticated probes of the heme active site are needed to discriminate between these two oxidants. Also, new methods for rapid electron injection would facilitate characterization of both the putative ferric hydroperoxo and ferryl intermediates.

Figure 1.5. Competing mechanisms of substrate activation and oxygen insertion. The (Groves) oxygen rebound mechanism best describes many kinetic isotope studies, excluding those with radical clocks, such as those designed by Newcomb et al.

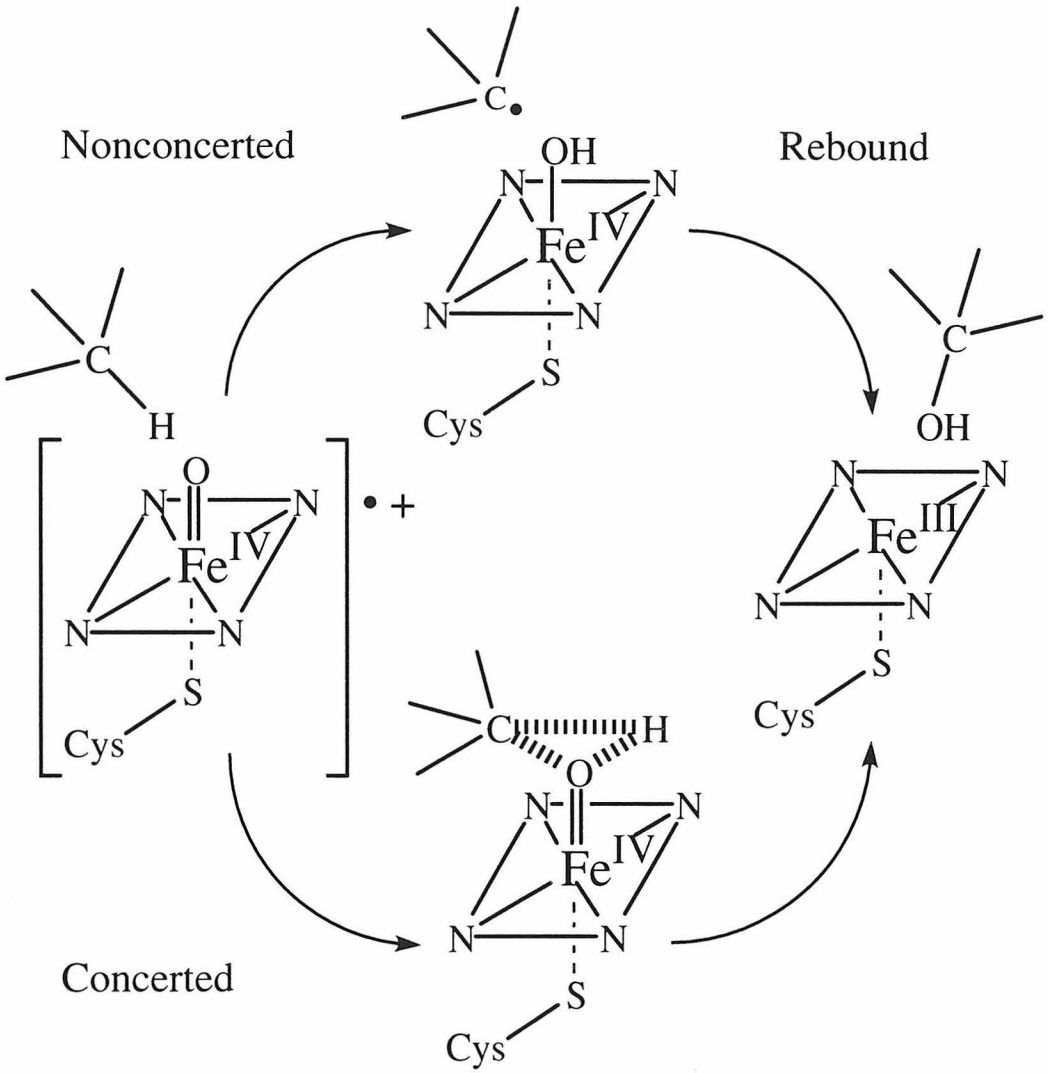
Nonconcerted
Rebound
Concerted
OH
Fe IV
Fe III
Cys
S
N
O
H
C
• +

From studies applying a variety of catalytic, kinetic, and spectroscopic techniques to P450 enzymes and model complexes, it has become clear that P450 operates as an electrophilic oxidant. Mechanisms of oxygen insertion from a ferryl species have been hotly contested (Figure 1.5). Whether the reaction is two "concerted, nonsynchronous" steps occurring in 80-200 fs (32), or involves H-abstraction followed by "oxygen rebound" (33,34), is still unresolved. The position of the two oxidizing equivalents (on the iron, sulfur, heme, or oxygen), and the electron-donating ability of the thiolate in the active intermediate(s) have been studied by numerous computational (35-38) and experimental approaches (39-41). The lack of agreement between these data stems, in part, from the subtleties of H-bonding to the cysteine, the general instability of porphyrin Fe-S model compounds, and differing theoretical (HF/DFT) methods for these complex systems.

In conclusion, considerable progress has been made in the elucidation of the P450 mechanism in the last five years. These advances have been driven by the study of new protein mutants, refinement of spectroscopic techniques, development of better theoretical methods and faster computers, and the synthesis of novel small molecule probes. Sensitizer-linked substrates have identified conformational changes associated with substrate binding, and hold promise as conduits for rapid ET for studies of short-lived intermediates in P450 and other metalloenzymes.

Designing Probes for Efficient Electron Transfer

Studies of ET proteins at Caltech have focused on protein surface modification with Ru photosensitizers (42,43). The general stability of ET proteins such as azurin and cytochrome *c*, and the development of methodologies for site-directed mutagenesis, surface histidine labeling, and protein purification have rendered this approach quite versatile. In several proteins with different ET pathways (distances, through-bond, through-space, mediated by aromatic residues, through alpha helical or β-sheet proteins), and activation energies (by varying the driving force, as well as temperature), rates of ET were measured. Interpreting these data based on the semiclassical expression (44) for weakly coupled donor and acceptor molecules (Eqs. 1.1 & 1.2)

$$\mathbf{k_{ET}} = \left(\frac{4\pi^3}{h^2\lambda k_B T}\right)^{1/2} \mathbf{H_{AB}^2}\ \mathbf{exp}\left[\frac{-(\Delta G^\circ + \lambda)^2}{4\lambda k_B T}\right] \qquad \text{Eq. 1.1}$$

$$k_{max} \propto H_{AB}^2 \exp[-\beta(R-R_o)] \qquad \text{Eq. 1.2}$$

yields a predictive model for long-range ET in proteins (42,43). Figure 1.6 shows that for a Ru-metal distance of 20 Å (typical of a buried active site), it should be possible to transfer an electron in ten microseconds, provided that the reaction is activationless ($-\Delta G^0 = \lambda$).

Theoretical and experimental work suggests, however, that the electronic-coupling matrix element, H_{AB}, does not always correlate with the direct donor-acceptor

Figure 1.6. Rates of electron transfer, $\log k_{ET}$, extrapolated to $-\Delta G^0 = \lambda$ versus Ru-metal distance in several different metalloproteins. The slope of the best-fit line gives the exponential decay factor, β, a value of 1.0 $Å^{-1}$. Also shown is a much shallower distance dependence corresponding to $\beta = 0.4$ $Å^{-1}$, as is found experimentally for donors and acceptors separated by a polyphenylene bridge.

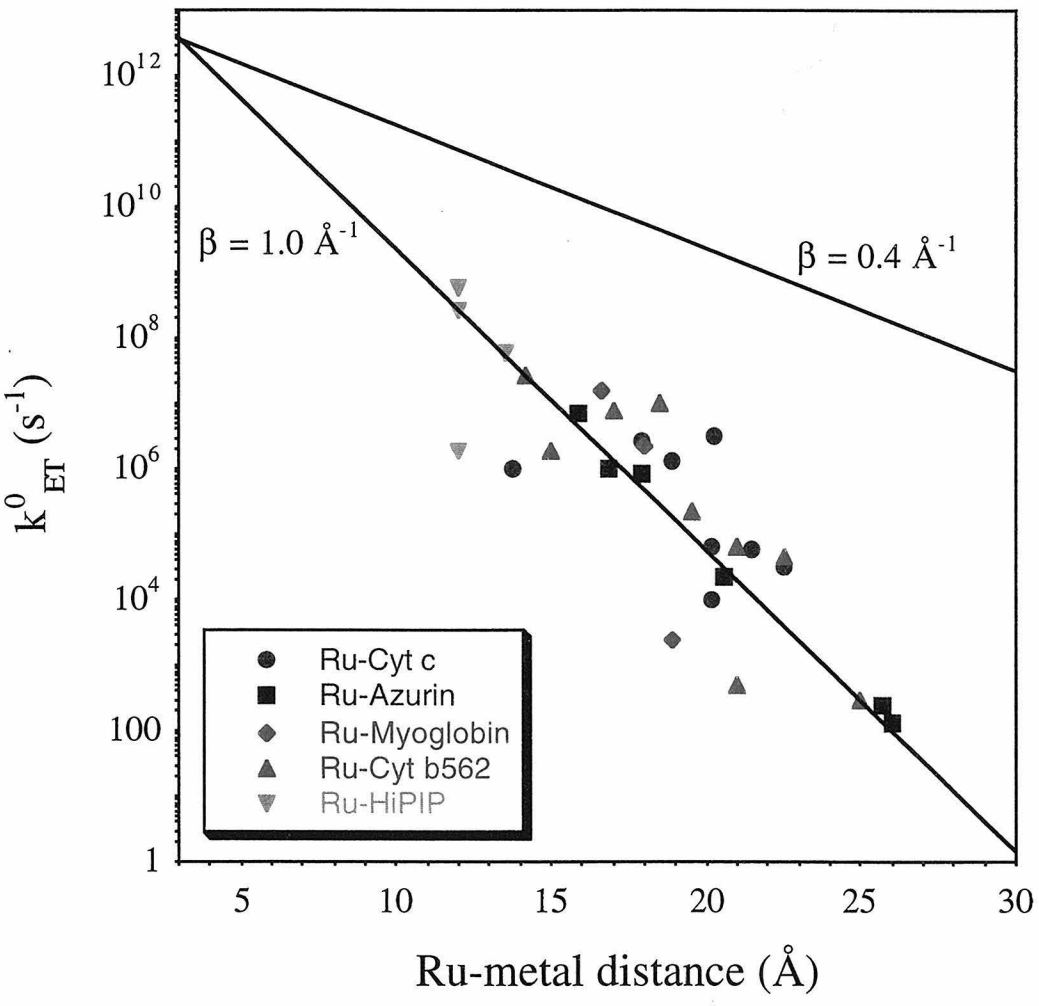
10^{12}
10^{10}
10^{8}
10^{6}
10^{4}
100
1
k^0_{ET} (s^{-1})
β = 1.0 Å^{-1}
β = 0.4 Å^{-1}
Ru-Cyt c
Ru-Azurin
Ru-Myoglobin
Ru-Cyt b562
Ru-HiPIP
5
10
15
20
25
30
Ru-metal distance (Å)

separation (45-49). Coupling depends on the intervening medium, namely the number and types of bonds, separating the donor and acceptor. This behavior is generalized by a superexchange model in which D-A coupling is the repeated product of bridge-unit (e.g., methylene, phenylene) couplings (48,50). Inherent in this simple model is the prediction that the coupling should depend exponentially upon the number of atoms in the bridge (50). As shown by work in model D-A systems with bridging organic molecules, conjugation brings marked rate enhancements (51-54). With an oligophenylene bridge, the exponential decay constant, β, is only 0.4 $Å^{-1}$ (55), which increases the theoretical maximum rate of a 20-Å ET to over 1 x 10^9 s^{-1} (Figure 1.6). For studies of short-lived intermediates, conjugated Ru-probes offer distinct advantages over ET reactions mediated by a protein matrix or saturated hydrocarbon bridge.

One could envision injecting electrons more rapidly into P450 by three routes: a) covalent modification of P450 with a Ru complex, b) labeling a natural cofactor (such as Pd or the heme) with a photosensitizer, or c) creating an unnatural (and more reducing) cofactor. In practice, however, P450 is difficult to modify on the proximal face since the residues on the ET path are highly conserved and surrounding residues are not very solvent accessible. In addition, attachment of the photosensitizer $[Ru(bpy)_3]^{2+}$ at these positions has been found to destabilize the enzyme (unpublished work). Farmer et al. (work in press) succeeded in labeling surface cysteines of cytochrome BM-3 with

$[Ru(bpy)_3]^{2+}$, but due to the inefficient ET pathways, reduction of the buried heme by $[Ru(bpy)_3]^{1+}$ was slower than the competing reaction with exogenous dioxygen. Without a crystal structure of the P450-Pd pair, it is difficult to design effective site-directed mutants to exploit this natural ET conduit. Efforts to complex P450 with negatively charged photosensitizers and inject electrons rapidly have not been successful, highlighting the complexity of the surface binding interactions. Reduction of P450 with $[Ru(bpy)_3]^{2+}$ in the presence of a sacrificial donor (EDTA) has also been shown to be inefficient (56) and efforts to reconstitute P450 with a Ru-tethered heme (as was done previously for myoglobin (3)) thus far have failed.

Alternatively, one may consider the only unobstructed path to the heme: via the substrate channel. Extremely relevant to the design of large, active-site-directed probes were previous binding studies and X-ray structures that illustrated the malleability of the active site channel in $P450_{cam}$. Poulos et al. (57) crystallized P450 with a large imidazole-terminated inhibitor (Figure 1.7). Their original goal—to trap P450 in its open conformation—was unsuccessful due to the short length and small steric bulk of the alkyl chain. However, the structure highlighted that Tyr 96, Phe 87, and Phe 193 may adopt alternate conformations in the channel to allow large substrates access to the heme.

In a different study, Wade et al. (58) showed that the affinity of borneol (a reduced camphor derivative) increased upon alkylation of the alcohol (Figure 1.7);

Figure 1.7. Top: An imidazole terminated inhibitor and a borneol ether that binds better than the natural substrate camphor. In both cases, the alkyl tether appeared to improve binding. Below: Cutaway view of the substrate channel and active site of cytochrome $P450_{cam}$. The channel is blocked by Phe 193, a hydrophobic "gate keeper." Camphor sits in close proximity to the distal face of the heme and displaces water from the active site; water molecules are evident at the top of the channel.

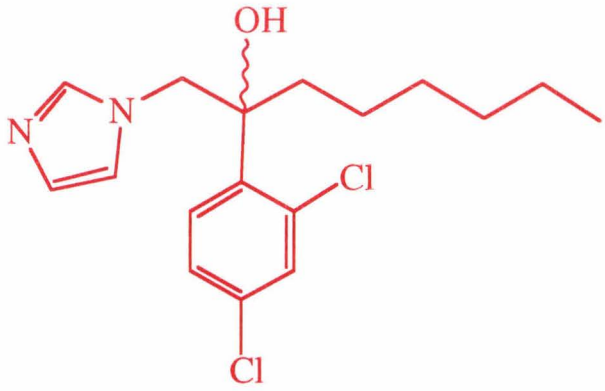
OH
N
N
Cl
Cl

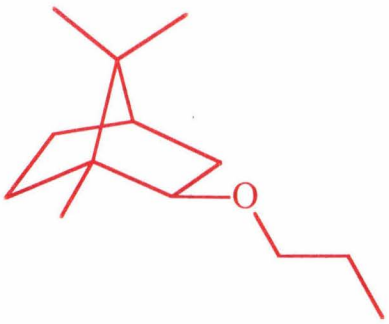
O

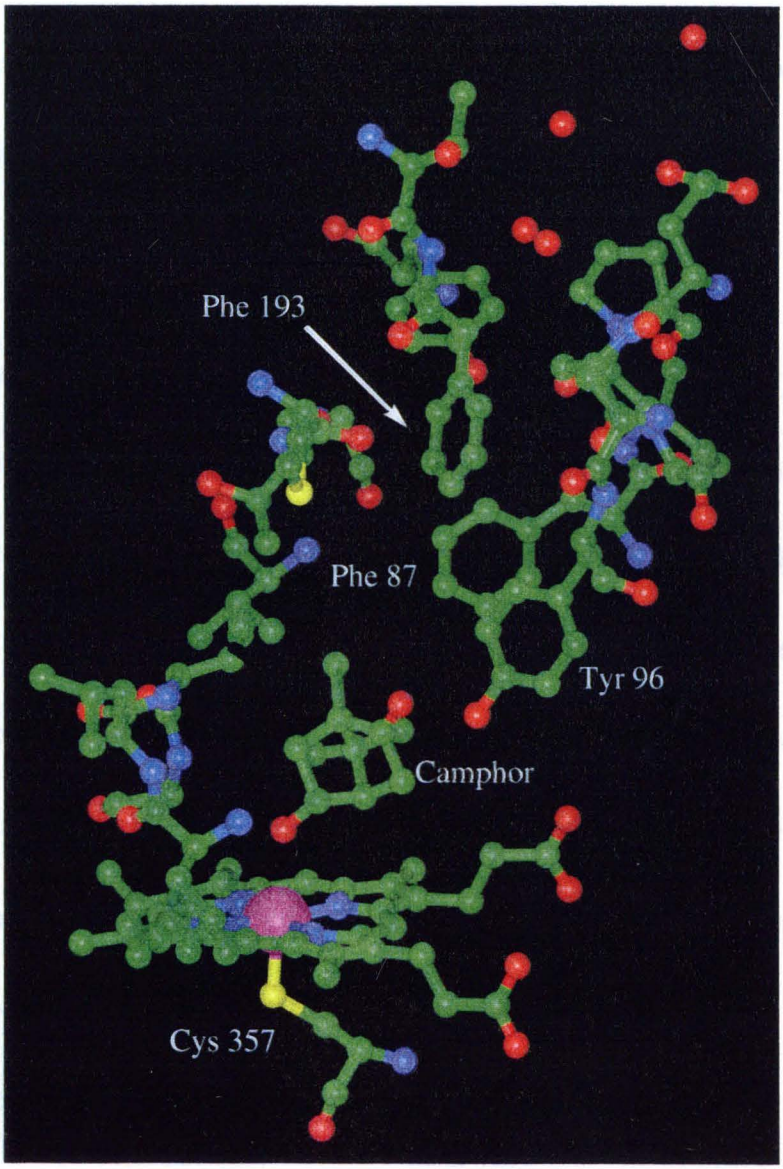
Phe 193
Phe 87
Tyr 96
Camphor
Cys 357

modeling suggested that a propyl chain filled empty space in the pocket and pointed towards the mouth of the channel. Indeed, there are numerous P450 isozymes with open channels that bind large molecules such as fatty acids (i.e., cytochrome BM-3) and cholesterol (i.e., P450scc) (2). However, it seemed likely that long molecules terminating in a bulky photosensitizer would not bind the poorly defined $P450_{cam}$ channel. It was eventually via the substrate channel that electrons were delivered to P450. Computer modeling of Ru-substrates into P450 (Figure 1.7) focused on three parts: the sensitizer, linker, and substrate.

Synthesizing Ru-Probes

The rich literature on the varied synthesis and photophysics of Ru complexes greatly aided the design of these molecules (59). The Ru^{2+*} excited-state lifetime and reduction potential, as well as the size, charge, and attachment point may be easily varied with the proper choice of ligands. Energy transfer from Ru^{2+*} to the heme proved to be a useful tool for quickly screening compounds for binding, and the emission spectrum of the photosensitizer may be red-shifted or blue-shifted, depending on whether energy transfer is a desired property of the final compound. The synthetic flexibility of 2,2'-bipyridine recommended this ligand, but phenanthroline and terpyridine ligands each have advantages, depending on the application. The choice of linkers was narrowed by

requirements for considerable length (> 15 Å), hydrophobicity, and conformational flexibility. Once binding was established with a "floppy" alkyl tether, more conjugated, bulky, and rigid linkers were tested. Numerous metal catalyzed coupling schemes make the synthesis of conjugated linkers of varying length and size quite feasible (60).

The choice of substrate or ligand greatly depends on the requirements of the active site. $P450_{cam}$ proved to be surprisingly indiscriminate towards hydrophobic organic substrates. Covalent attachment of the substrate/ligand to the Ru-tether was accomplished via an amide, ether, C-C, or C-N linkage. The ease of varying the terminal moiety permits a combinatorial approach towards the design of Ru-probes. These same design principles may be applied to many other metalloenzymes, including NOS and a variety of oxygenases. Finally, the development of new strategies in chemical biology for engineering specific binding interactions at enzyme (i.e., kinase) active sites will amplify the range of targets and problems that may be addressed with sensitizer-linked substrates.

REFERENCES AND NOTES

1. E. J. Mueller, P. J. Loida, S. G. Sligar, in *Cytochrome P450: Structure, Mechanism, and Biochemistry, 2nd edn* P. R. Ortiz de Montellano, Ed. (Plenum Press, New York, 1995) pp. 83-124.

2. P. R. Ortiz de Montellano, M. A. Correia, in *Cytochrome P450: Structure, Mechanism, and Biochemistry, 2nd edn* P. R. Ortiz de Montellano, Ed. (Plenum Press, New York, 1995) pp. 305-364.

3. I. Hamachi, S. Tanaka, S. Tsukiji, S. Shinkai, S. Oishi, *Inorg. Chem.* **37**, 4380-4388 (1998).

4. I. Hamachi, et al., *Chem. Commun.* , 1735-1736 (1997).

5. J. Berglund, T. Pascher, J. R. Winkler, H. B. Gray, *J. Am. Chem. Soc.* **119**, 2464-2469 (1997).

6. D. W. Low, J. R. Winkler, H. B. Gray, *J. Am. Chem. Soc.* **118**, 117-120 (1996).

7. Klingenberg, *Arch. Biochem. Biophys.* **75**, 376 (1958).

8. D. Garfinkel, *Arch. Biochem. Biophys.* **77**, 493 (1958).

9. T. L. Poulos, B. C. Finzel, A. J. Howard, *J. Mol. Biol.* **195**, 687-700 (1987).

10. N. C. Gerber, University of Illinois (1993).

11. C. DiPrimo, G. H. B. Hoa, E. Deprez, P. Douzou, S. G. Sligar, *Biochemistry* **32**, 3671-3676 (1993).

12. A. V. Wells, L. Pusheng, P. M. Champion, S. A. Martinis, S. G. Sligar, *Biochemistry* **31**, 4384-4393 (1992).

13. T. L. Poulos, J. R. Cupp-Vickery, H. Li, in *Cytochrome P450: Structure, Mechanism, and Biochemistry, 2nd edn* P. R. Ortiz de Montellano, Ed. (Plenum Press, New York, 1995) pp. 125-150.

14. S. K. Ludemann, O. Carugo, R. C. Wade, *J. Mol. Modeling* **3**, 369-374 (1997).

15. M. Holden, M. Mayhew, D. Bunk, A. Roitberg, V. Vilker, *J. Biol. Chem.* **272**, 21720-21725 (1997).

16. M. J. Hintz, D. M. Mock, L. L. Peterson, K. Tuttle, J. A. Peterson, *J. Biol. Chem.* **257**, 14324-14332 (1982).

17. M. Unno, H. Shimada, Y. Toba, R. Makino, Y. Ishimura, *J. Biol. Chem.* **271**, 17869-17874 (1996).

18. A. E. Roitberg, et al., *J. Am. Chem. Soc.* **120**, 8927-8932 (1998).

19. T. C. Pochapsky, N. U. Jain, M. Kuti, T. A. Lyons, J. Heymont, *Biochemistry* **38**, 4681-4690 (1999).

20. K. K. Lo, L.-L. Wong, H. A. O. Hill, *FEBS Lett.* **451**, 342-346 (1999).

21. M. Unno, et al., *J. Am. Chem. Soc.* **119**, 6614-6620 (1997).

22. Y. Ishimura, V. Ulrich, J. A. Peterson, *Biochem. Biophys. Res. Comm.* **42**, 140-146 (1971).

23. J. D. Lipscomb, S. G. Sligar, M. J. Namtvedt, I. C. Gunsalus, *J. Biol. Chem.* **251**, 1116-1124 (1975).

24. I. D. G. Macdonald, S. G. Sligar, J. F. Christian, M. Unno, P. M. Champion, *J. Am. Chem. Soc.* **121**, 376-380 (1999).

25. I. Schlichting, et al., *Science* **287**, 1615-1622 (2000).

26. F. P. Guengerich, D. P. Ballou, M. J. Coon, *Biochem. Biophys. Res. Comm.* **70**, 951-956 (1976).

27. K. Kobayashi, M. Amano, Y. Kambara, K. Hayashi, *J. Biol. Chem.* **262**, 5445-5447 (1986).

28. R. E. White, S. G. Sligar, M. J. Coon, *J. Biol. Chem.* **255**, 11108-11111 (1980).

29. R. Davydov, I. D. G. Macdonald, T. M. Makris, S. G. Sligar, B. M. Hoffman, *J. Am. Chem. Soc.* **121**, 10654-10655 (1999).

30. D. E. Benson, K. S. Suslick, S. G. Sligar, *Biochemistry* **36**, 5104-5107 (1997).

31. M. Newcomb, et al., *J. Am. Chem. Soc.* **122**, 2677-2686 (2000).

32. M. Newcomb, M.-H. LeTadic-Biadatti, D. L. Chestney, E. S. Roberts, P. F. Hollenberg, *J. Am. Chem. Soc.* **117**, 12085-12091 (1995).

33. P. R. Ortiz de Montellano, R. A. Stearns, *J. Am. Chem. Soc.* **109**, 3415-3420 (1987).

34. J. T. Groves, D. V. Subramanian, *J. Am. Chem. Soc.* **106**, 2177-2181 (1984).

35. G. H. Loew, D. L. Harris, *Chem. Rev.* **100**, 407-419 (2000).

36. D. L. Harris, G. Loew, L. Waskell, *J. Am. Chem. Soc.* **120**, 4308-4318 (1998).

37. M. T. Green, *J. Am. Chem. Soc.* **121**, 7939-7940 (1999).

38. M. Filatov, N. Harris, S. Shaik, *Angew. Chem. Int. Ed.* **38**, 3510-3512 (1999).

39. N. Ueyama, et al., *Inorg. Chem.* **37**, 2415-2421 (1998).

40. X. Yi, M. Mroczko, K. M. Manoj, X. Wang, L. P. Hager, *Proc. Natl. Acad. Sci. USA* **96**, 12412-12417 (1999).

41. H. A. Wagenknecht, C. Claude, W. D. Woggon, *Helv. Chim. Acta* **81**, 1506-1520 (1998).

42. H. B. Gray, J. R. Winkler, *Annu. Rev. Biochem.* **65**, 537-561 (1996).

43. M. J. Bjerrum, et al., *J. Bioenerget. Biomembr.* **27**, 295-302 (1995).

44. R. A. Marcus, N. Sutin, *Biochim. Biophys. Acta* **811**, 265-322 (1985).

45. D. N. Beratan, J. N. Betts, J. N. Onuchic, *Science* **252**, 1285-1288 (1991).

46. J.-M. Lopez-Castillo, A. Filali-Mouhim, E. N. V. Binh-Otten, J.-P. Jay-Gerin, *J. Am. Chem. Soc.* **119**, 1978-1980 (1997).

47. P. F. Barbara, T. J. Meyer, M. A. Ratner, *J. Phys. Chem.* **100**, 13148-13168 (1996).

48. C. Liang, M. D. Newton, *J. Phys. Chem.* **97**, 3199-3211 (1993).

49. K. D. Jordan, M. N. Paddon-Row, *Chem. Rev.* **92**, 395-410 (1992).

50. H. M. McConnell, *J. Chem. Phys.* **35**, 508-515 (1961).

51. G. Jones, D. X. Yan, D. J. Gosztola, S. R. Greenfield, M. R. Wasielewski, *J. Am. Chem. Soc.* **121**, 11016-11017 (1999).

52. W. B. Davis, W. A. Svec, M. A. Ratner, M. R. Wasielewski, *Nature* **396**, 60-63 (1998).

53. S. Creager, et al., *J. Am. Chem. Soc.* **121**, 1059-1064 (1999).

54. R. S. Farid, I.-J. Chang, J. R. Winkler, H. B. Gray, *J. Phys. Chem.* **98**, 5176-5179 (1994).

55. A. Helms, D. Heiler, G. McLendon, *J. Am. Chem. Soc.* **114**, 6227-6238 (1992).

56. J. Contzen, C. Jung, *Biochemistry* **38**, 16253-16260 (1999).

57. R. Raag, H. Li, B. C. Jones, T. L. Poulos, *Biochemistry* **32**, 4571-4578 (1993).

58. V. Helms, et al., *Biochemistry* **35**, 1485-1499 (1996).

59. K. Kalyanasundaram, *Photochemistry of Polypyridine and Porphyrin Complexes* (Academic Press, Lmtd., London, 1992).

60. S. L. Huang, J. M. Tour, *J. Am. Chem. Soc.* **121**, 4908-4909 (1999).

Chapter 2

Optical Detection of Cytochrome P450 by Sensitizer-linked Substrates[‡]

[‡]Adapted from I. J. Dmochowski, B. R. Crane, J. J. Wilker, J. R. Winkler, H. B. Gray, *Proc. Natl. Acad. Sci.* **96**, 12987-12990 (1999).

Acknowledgements:

This work would not have been possible without the data collection facilities at SSRL, Brian Crane for significant help involving P450 crystallization and structure determination, Alex Bilwes for assistance with protein expression and crystallization, Mike Machczynski for computational assistance, Prof. Doug Rees for use of facilities, and Prof. Stephen Sligar for providing a $P450_{cam}$ vector.

INTRODUCTION

New methods for detecting mammalian P450s and characterizing their structures (1) would facilitate rational drug design (2) and the engineering of new catalysts (3, 4). Although more than 100 mammalian microsomal P450 isozymes have been identified, direct information about their structures and physiological function is lacking. Crystal structures are available for only four P450 oxygenases (5), all of which are water-soluble bacterial enzymes; the best characterized of these, cytochrome $P450_{cam}$ (P450), was targeted in our studies. Here we report that substrates linked to $\{Ru(bpy)_3\}^{2+}$ (bpy is 2,2'-bipyridine, Figure 2.1) (6) can selectively probe the enzyme in complex media.

The attachment of a sensitizer to substrate-, nucleotide-, or flavin-analogs should improve the ability of such small-molecule probes (7-10) to resolve enzyme active centers while minimizing the need for intensive synthesis, metabolite characterization and enzyme mutagenesis. Our modular, active-site-directed approach to detection is superior to enzyme- and antibody-based assays: sensitizer-linked substrates assess ligand specificity and enzyme structure and are amenable to combinatorial chemistry. Furthermore, because Ru-substrates interact with their targets reversibly, they differ from current probes of heme proteins that rely on covalent modification and chemical analysis (1, 11).

Figure 2.1. The structures of sensitizer-linked substrates (ethyl benzene, adamantane) and ligands (imidazole). Six methylene units, or roughly 7 angstroms in the all trans conformation, differentiate the shortest from the longest Ru-EB compound.

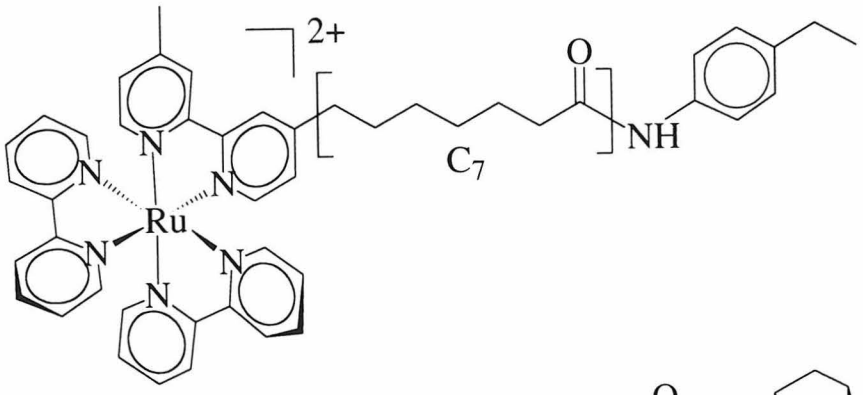

Ru-C_n-EB

n = 7, 9-13

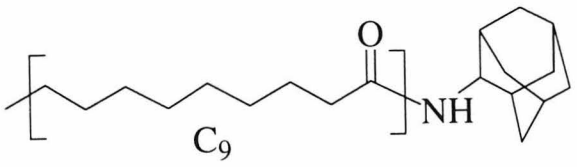

Ru-C_n-Ad

n = 9, 11

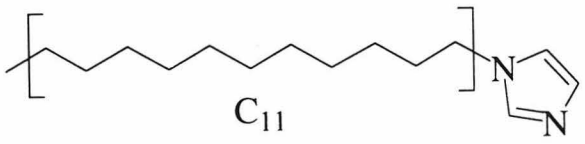

Ru-C_n-Im

n = 11, 13

Sensitizer-linked substrates also show great promise as a rapid screening tool for P450 substrates. P450s are important pharmaceutical targets, due to their role in xenobiotic metabolism. Current protocols for determining substrate binding involve absorbance measurements, which require fairly high protein concentrations and homogeneous samples. Both steady-state and time-resolved fluorescence measurements offer enhanced sensitivity over conventional optical methods and offer exciting possibilities for studying membrane-bound enzymes.

MATERIALS AND METHODS

General

All reagents were used as received, unless specified otherwise, and were of the highest available quality. Absorption spectra were recorded on an HP-8452A spectrophotometer. Fluorescence measurements were made on an ISS K2 fluorometer (courtesy of the Barton group) exciting at 470 nm and scanning from 500-800 nm. Distilled water was further purified by a Barnstead Nano-Pure system. *P. putida* cytochrome $P450_{cam}$ (residues 1-414) containing the mutation Cys334Ala (Quickchange mutagenesis, Stratagene) was overexpressed in *E. coli* TBY cells from plasmid pUS200

(12) and purified in the presence of camphor with slight modification to procedures previously described (13). See Appendix A for full details.

Highly purified (OD 392 nm/OD 280 nm > 1.4), decamphored P450 was stored at –70 °C and thawed just before use. Yeast cytochrome *c* peroxidase (CcP) was a gift from Dr. David Gooden (via Dr. Judy Hirst), both of the Scripps Research Institute. Chloroperoxidase (CPO) was a gift from Prof. John Dawson of the University of South Carolina (via Prof. Lowell Hager of the University of Illinois). Horse skeletal muscle myoglobin, bovine liver catalase, horseradish peroxidase (Type VI-A, RZ (A_{403}/A_{275}) ~ 3.0), and yeast cytochrome *c* were obtained from Sigma and used as received. Bovine lipase cytochrome *b5* was inherited from the cold room and purified by gel filtration chromatography (Sephadex G-25).

Synthesis of Ru-substrates

Variable length $(CH_2)_{7\text{-}13}$ bromoalkanoic acids were converted to their respective bromo-acid chlorides and reacted with 2-adamantanamine. Deprotonation of 4,4'-dimethyl-2,2'-bipyridine promoted nucleophilic attack on the bromoamide. Ruthenation of the functionalized bpy (2,2'-bipyridine) with $[Ru(bpy)_2Cl_2]$ afforded the desired Ru-substrate in good yield. Full synthetic details are provided in Appendix B.

$P450_{cam}$ Expression/Crystallization Conditions

P450:Ru-C_9-Ad seed crystals of space group $P2_12_12_1$ (cell dimensions 65.4 x 74.5 x 91.7 $Å^3$, one molecule/asymmetric unit, Matthews coefficient (V_M) = 2.4, solvent content = 49%) nucleated overnight (4 °C, vapor diffusion) from protein separated from camphor and complexed with stoichiometric Ru-C_9-Ad. Hanging drops contained an equal volume mixture of reservoir and 430 μM P450:Ru-C_9-Ad in 20 mM HEPES pH 7.5, 100 mM KCl, and 1 mM dithiothreitol. The reservoir contained 100 mM NaOAc pH 4.9, 200 mM NH_4OAc pH 7.0, and 9-11% polyethylene glycol (PEG) MW 8000 (W/V) (final pH ~6.0). Diffraction quality crystals (0.15 x 0.15 x 0.5 mm^3) were grown over 24-48 hours by moving seed crystals into sitting drops of reduced PEG concentrations (5-7%).

Structure Determination

An initial molecular replacement solution (correlation coefficient = 0.53 and R_{cryst} = Σ $||F_{obs}|-|F_{calc}||/\Sigma$ $|F_{obs}|$ = 43.4%, for 15.0 to 3.5 Å resolution data) was found by AMoRe (14) with a probe derived from the structure of camphor-bound $P450_{cam}$, PDB code: 2cpp (15), using diffraction data collected from P450:Ru-C_9-Ad crystals (1.55 Å resolution, overall R_{sym} = $\Sigma\Sigma_j$ I_j - $<I>|/\Sigma\Sigma_j I_j$ = 4.8%, overall signal-to-noise ratio = $I/\sigma I$ = 37.4, redundancy = 6.5, 99.2% complete). Diffraction data were collected at 100 K on Beam-line 7-1 (1.08 Å) of the Stanford Synchrotron Research Laboratory (SSRL) and processed

with DENZO (16). Substantial changes in the regions of P450 distal to the heme were modeled to omit electron density maps with XFIT (17). Ru-C_9-Ad was positioned into the remaining difference density. The structure was refined by torsion-angle molecular dynamics and positional refinement with CNS (18) amidst model rebuilding, water molecule placement, and resolution extension to 1.55 Å. Following an overall anisotropic thermal factor correction, bulk-solvent correction, and individual thermal factor refinement, grouped occupancy refinement of Ru-C_9-Ad and those residues in multiple conformations produced the final model (4019 scatterers, 1 Ru-C_9-Ad as a superposition of the two (Δ and Λ) $\{Ru(bpy)_3\}^{2+}$ enantiomers, 23 residues in multiple conformations, 427 water molecules, and 5 acetate molecules; R_{cryst} = 21.6%, R_{free} = 22.6% for 8% of the reflections removed at random, no σ cutoff).

The adamantyl moiety of Ru-C_9-Ad is well ordered, but static and/or dynamic disorder increases up the methylene chain toward the sensitizer, where only one of the three bpy ligands is well resolved. The ruthenium atom position was confirmed by the largest peak in the initial F_{obs}-F_{calc} electron density map (4σ) and also by a peak in the Bijvoet difference Fourier map (calculated with coefficients $|F^+| - |F^-|$ and phases $\phi_{model} - \pi/2$), which identified all sulfur and metal atoms in the model. The final model has excellent stereochemistry (root mean square deviation from ideal bond lengths < 0.009 Å and ideal bond angles < 1.3°) with 90.3% of all residues in the most favored regions of ϕ/φ

Figure 2.2. Crystal structure of the $P450_{cam}$:Ru-C_9-Ad complex. The Ru-substrate is shown to highlight docking of $\{Ru(bpy)_3\}^{2+}$ at the surface of the protein as predicted by computer modeling and energy-transfer experiments. The methylene linker occupies a large channel from the enzyme surface to the heme. A hydrogen bond connects the Ru-substrate amide carbonyl to Tyr 96. The adamantyl moiety (center) resides at the P450 active site above the heme in the same position as adamantane, shown in superposition from the 4cpp crystal structure (25). Although both Δ and Λ $\{Ru(bpy)_3\}^{2+}$ enantiomers are present in the complex, only Λ is shown.

space, as defined by PROCHECK(19). No residues fall in disallowed regions. Larger refined thermal factors for Ru-C_9-Ad (<B> = 48.2 Å^2) compared to the overall model (<B> = 28.0 Å^2, $<B>_{mainchain}$ = 19.4 Å^2, $<B>_{sidechain}$ = 20.4 Å^2) reflect the mobility and conformational heterogeneity of the bound $\{Ru(bpy)_3\}^{2+}$. The ribbon representation (Figure 2.2) was generated using Molscript (20) and Raster3D (21).

Energy Transfer Measurements

Solution experiments were performed in sealed cuvettes with P450 and Ru-substrate in 100 mM KCl and 20 mM KPhos buffer, pH 7.4. Samples were fitted with a magnetic stir bar and deoxygenated by repeated evacuations followed by backfilling with purified argon (3 x 10 cycles). Single crystal experiments were conducted aerobically. All samples were excited with XeCl excimer-pumped dye laser pulses (25 ns, 480 nm, 1-2 mJ/pulse). Dye laser output was attenuated as needed by passage through crossed polarizers. Laser shots with energies differing by more than 10% from the mean value (laser pulses detected by a photodiode and selected by a discriminator, Phillips Scientific Model 6930) were rejected. Emission was collected 180° to the incident excitation with reflective optics (f/10), sent through a long-pass filter (λ > 600 nm), and focused onto the entrance slit of an ISA double 0.1 meter monochromator. Luminescence was detected by a Hamamatsu photomultiplier tube (R928); the output signal passed through a high-speed

(100 MHz) current to voltage amplifier, digitized (Sony/Tektronix digitizer, Model RTD710A), and recorded on a PC. Instrument response was ~20 ns (FWHM). Emission kinetics data are averages of at least 250 laser shots.

The emission decay traces were generally fit to a biexponential function, $y = c_0 + c_1e^{-(ken + k0)t} + c_2e^{-k0t}$, using the least-squares fitting program *Kinfit* written by Dr. Jay Winkler (PC version) and Dr. T.P. Pascher (Macintosh version). The ratio $c_1:(c_1 + c_2)$ was used to calculate dissociation constants. The rate of energy transfer, k_{en}, was calculated for each compound by subtracting the intrinsic rate constant, k_0, from the faster rate constant ($k_0 + k_{en}$). Donor-acceptor spectral overlap gives a Förster distance (Ru-Fe distance at which half the emission is quenched by energy transfer) (22) of R_0 = 26.2 Å for the ferriheme enzyme and R_0 = 27.6 Å for the carbonmonoxy species. Ru-Fe distances, r, were calculated using the equation, $k_{en} = k_0(R_0/r)^6$. The details of the Förster calculations are provided in Appendix C.

Steady-State Emission Measurements

Experiments were conducted aerobically, at room temperature, with 10 μM P450 and Ru-C_9-EB (in 100 mM KCl and 20 mM KPhos buffer, pH 7.4). The Ru emission spectrum was measured both with and without P450. To the sample containing P450, camphor was titrated from water/ethanol stock solutions (0.5 μL aliquots, final

concentration = 395 μM). Camphor binding was quantified concomitantly by monitoring absorbance changes at 416 and 392 nm.

RESULTS AND DISCUSSION

Ru-substrates (Figure 2.1) were modeled into the substrate-free P450 crystal structure (23) to position ethyl benzene (EB) and adamantane (Ad) at the active site and $\{Ru(bpy)_3\}^{2+}$ at the protein surface. Ru-C_n-EB and Ru-C_n-Ad were constructed by the covalent attachment of EB and Ad to variable length methylene chains $[(CH_2)_{7\text{-}13}]$ terminating in the photosensitizer (6). See Appendix B for full details. An amide functionality was incorporated into the Ru-substrates to permit hydrogen bonding, as occurs between Tyr96 and camphor (15). To generate Ru-ligands that could bind the heme iron (24), imidazole was linked to alkyl-tethered $\{Ru(bpy)_3\}^{2+}$ (Ru-C_n-Im). One of these complexes, P450:Ru-C_9-Ad, we have crystallized and structurally characterized to 1.55 Å (Figure 2.2). The Ru-substrate binds as predicted, with the Ad moiety mimicking substrate (25), a hydrogen bond between Tyr 96 and the amide functionality, and $\{Ru(bpy)_3\}^{2+}$ at the mouth of a large channel that has opened to accommodate the sensitizer.

Figure 2.3. UV-vis measurements indicate small changes in the heme ligation and spin state upon binding of Ru-Ad/Im/EB. To a lesser degree than adamantane, Ru-Ad compounds also displace water from the heme pocket, inducing a small (~ 30%) low to high spin conversion (shoulder at 392 nm). Ru-Ad binding diminishes the intensity of the Q bands (535 and 570 nm). Ru-EB also binds strongly, but fails to displace water from the heme pocket and produces only subtle spectroscopic changes in the Soret region and Q bands. Whereas direct ligation of imidazole to the iron would blue-shift the Soret by 7 nm (417→424 nm), Ru-C_{13}-Im appears to incompletely displace water from the heme (417→420 nm). Binding is also evident in the Q bands, as the peaks are red-shifted (538, 575 nm) and attenuated.

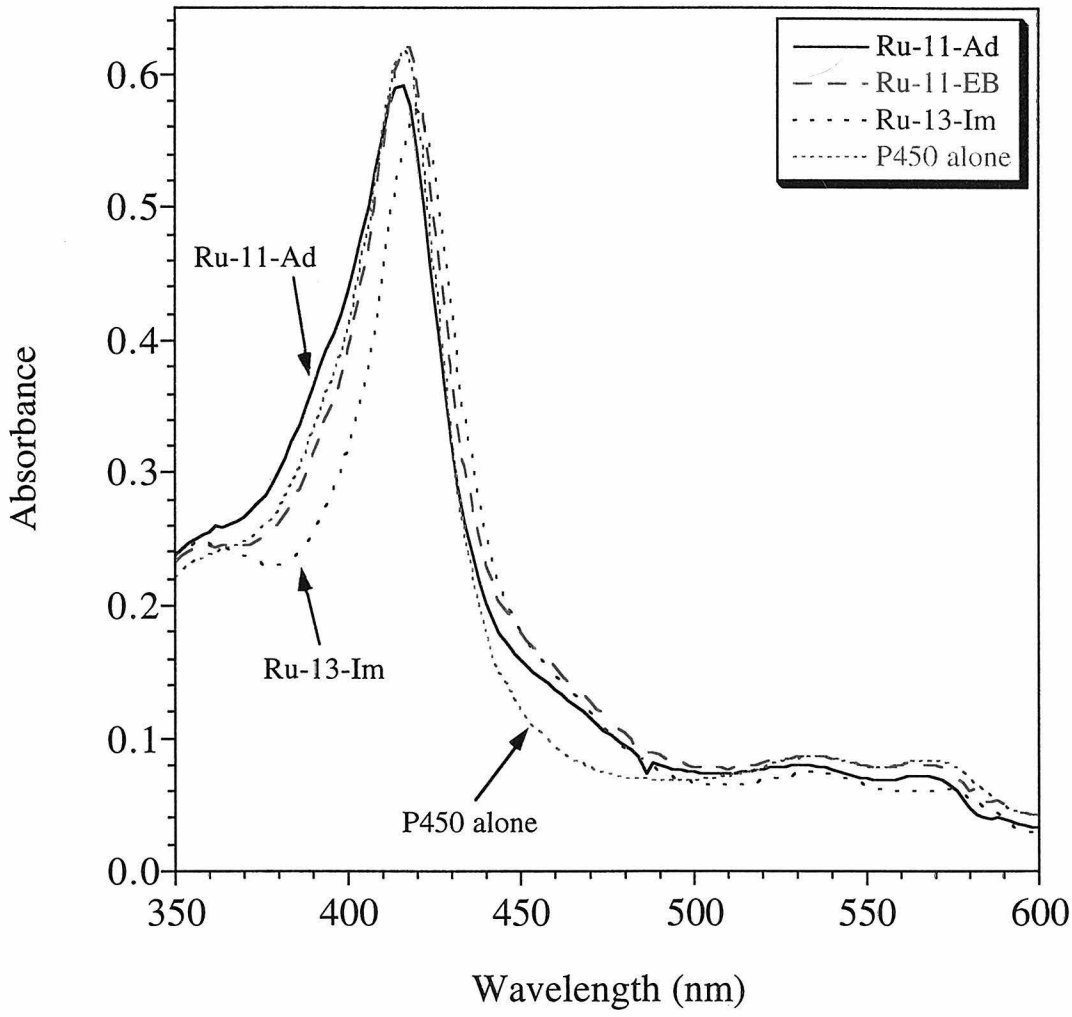
Ru-11-Ad
Ru-11-EB
Ru-13-Im
P450 alone
Ru-11-Ad
Ru-13-Im
P450 alone
Absorbance
Wavelength (nm)
0.0
0.1
0.2
0.3
0.4
0.5
0.6
350
400
450
500
550
600

Ru-EB/Ad compounds, as well as Ru-Im, bind at the P450 active site, as shown by both UV-vis (Figure 2.3) and emission lifetime measurements (6). Binding of the Ru-C_n-EB/Ad/Im compounds to the P450 target was detected by decreases in Ru^{2+} excited-state (Ru^{2+*}) lifetimes (6). [Ru-substrate]$^{2+*}$ emission decay is normally monophasic (k_0 = 2.1 x 10^6 s^{-1}), but becomes biphasic with a dominant fast component (k_{en} = 0.5-1.4 x 10^7 s^{-1}; k_0 = 2.1 x 10^6 s^{-1}) in the presence of P450 (Figure 2.4). Thus, upon addition of enzyme, the Ru-substrate or Ru-ligand partitions between a "bound" state, in which Ru^{2+*} is quenched, and a "free" state, in which it is not.

Photoexcitation of a P450:Ru-C_9-Ad single crystal yields a predominantly monophasic luminescence decay (Figure 2.4) that is strongly quenched by the protein (k_{en} = 1.1 x 10^7 s^{-1}), thereby confirming that the fast decay component, k_{en}, is attributable to P450:Ru- substrate complex formation. Competitive binding between Ru-substrates and camphor at the active site is indicated by the ability of the natural substrate (K_D ~ 1 μM) to diminish the fraction of bound [Ru-substrate]$^{2+*}$ decaying at the faster rate, k_{en}. At the titration end-point, camphor completely displaces the Ru-substrate from P450, as shown by monophasic Ru^{2+*} emission decay kinetics (k_0 = 2.1 x 10^6 s^{-1}).

Analysis of Ru-C_{11}-Ad emission quenching by P450 yields a dissociation constant (K_D = 0.6 μM) in good agreement with Ru-C_{11}-Ad/camphor competitive binding assays monitored by UV/Vis spectroscopy (K_D = 0.7 μM). This competition may be also be

Figure 2.4. Kinetics traces of $[Ru\text{-}C_9\text{-}Ad]^{2+*}$ emission decay at room temperature in solution and in a single crystal of $P450_{cam}$:Ru-C_9-Ad. $[Ru\text{-}C_9\text{-}Ad]^{2+*}$ (10 μM) exhibits monophasic decay. Emission decay of $[Ru\text{-}C_9\text{-}Ad]^{2+*}$ equimolar with P450 (10 μM) is biphasic. In a P450:Ru-C_9-Ad crystal, $\{Ru(bpy)_3\}^{2+*}$ quenching is predominantly monophasic. A secondary (< 10%) slower phase (k_0 = 4.8 x 10^6 s^{-1}) also was observed, suggesting that a small percentage of the Ru-substrate may remain unbound in the crystal. Faster $\{Ru(bpy)_3\}^{2+*}$ emission decay, k_{en}, in the crystal relative to solution most likely reflects small conformational differences in P450 between the two phases. Faster decay of the intrinsic $\{Ru(bpy)_3\}^{2+*}$ emission, k_0, in the crystal is attributable to quenching by oxygen.

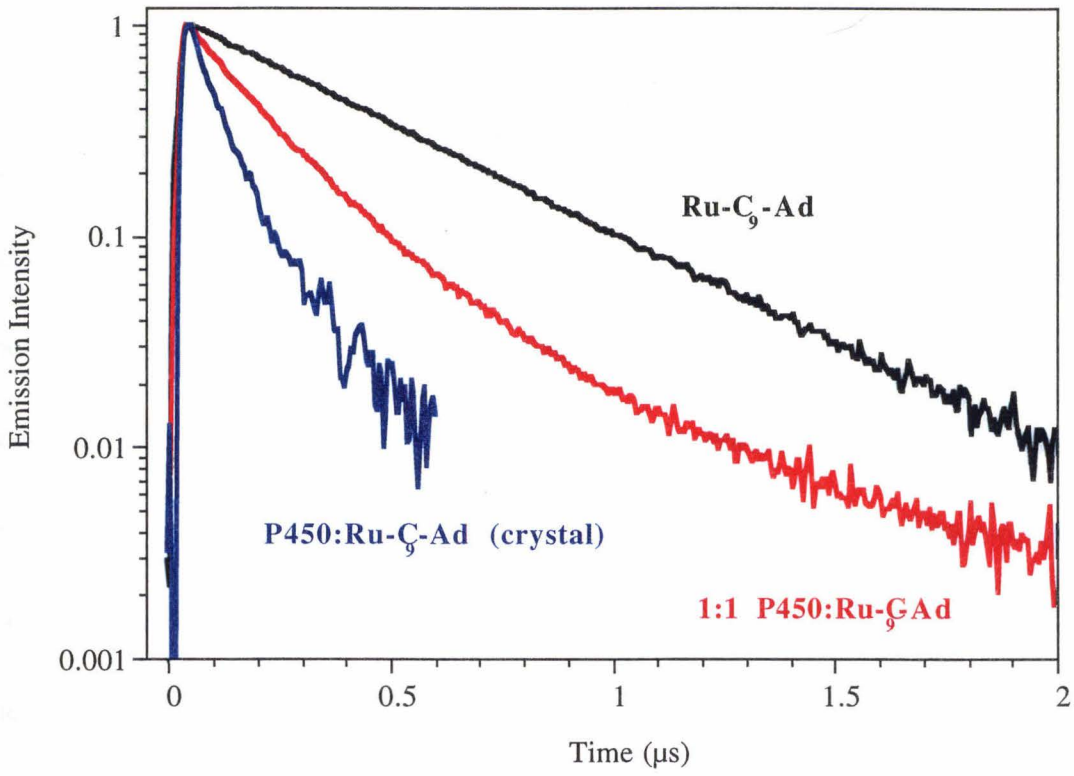
Emission Intensity
1
0.1
0.01
0.001
0
0.5
1
1.5
2
Time (μs)
Ru-C9-Ad
P450:Ru-C9-Ad (crystal)
1:1 P450:Ru-C9Ad

demonstrated by steady-state luminescence experiments. Camphor displacement of Ru-C_9-EB increases the Ru^{2+*} luminescence by roughly a factor of 1.7, while producing a low to high spin conversion (Figure 2.5). Interestingly, Ru binding in the hydrophobic enzyme pocket blue shifts the luminescence by 7 nanometers (617 → 610 nm), as would be predicted for destabilization of the charge-transfer excited state.

Association of Ru-substrates and Ru-ligands with P450 is sufficiently strong to allow detection of the enzyme at submicromolar concentrations (Table 2.1). The emission decay profile of Ru-C_9-Ad (2.5 μM) in 50 mM sodium phosphate buffer, pH 7, was monophasic (k_0 = 2.1 x 10^6 s^{-1}) in the presence of six heme proteins (yeast cytochrome *c*, horse skeletal muscle myoglobin, bovine lipase cytochrome b_5, bovine liver catalase, recombinant yeast CcP, and HRP), each at 5 μM. Our finding that the addition of 500 nM $P450_{cam}$ to this mixture yielded biphasic Ru^{2+*} kinetics (~ 10% k_{en}, ~ 90% k_0) demonstrates the feasibility of detecting specific biomolecules in complex media (Figure 2.6).

Specificity of Ru-substrates for P450 is controlled largely by interactions of the substrate moiety with the active site. Particularly noteworthy is the fact that $\{Ru(bpy)_3\}^{2+}$ is a sensitive reporter of binding even for substrates that do not shift the heme absorption spectrum by displacing ligated water (6). Dissociation constants for Ru-C_n-EB compounds are the first presented for derivatives of ethyl benzene. The chain-length dependence of binding in the Ru-C_n-EB series (K_D = 0.7-6.5 μM for n = 7-13)

Figure 2.5. Top: Dependence of the Ru-C_9-EB steady-state luminescence intensity on camphor concentration. The camphor titration (0-395 μM) displaces Ru-C_9-EB from the P450 pocket into solution, red-shifting the emission by 7 nm. Spectra were collected with an ISS K2 fluorometer. Bottom: Absorbance changes were also monitored during the camphor titration, using a HP-8452A diode array spectrophotometer. UV-vis measurements show a complete low to high spin conversion, consistent with camphor displacing both water and Ru-C_9-EB from the substrate pocket.

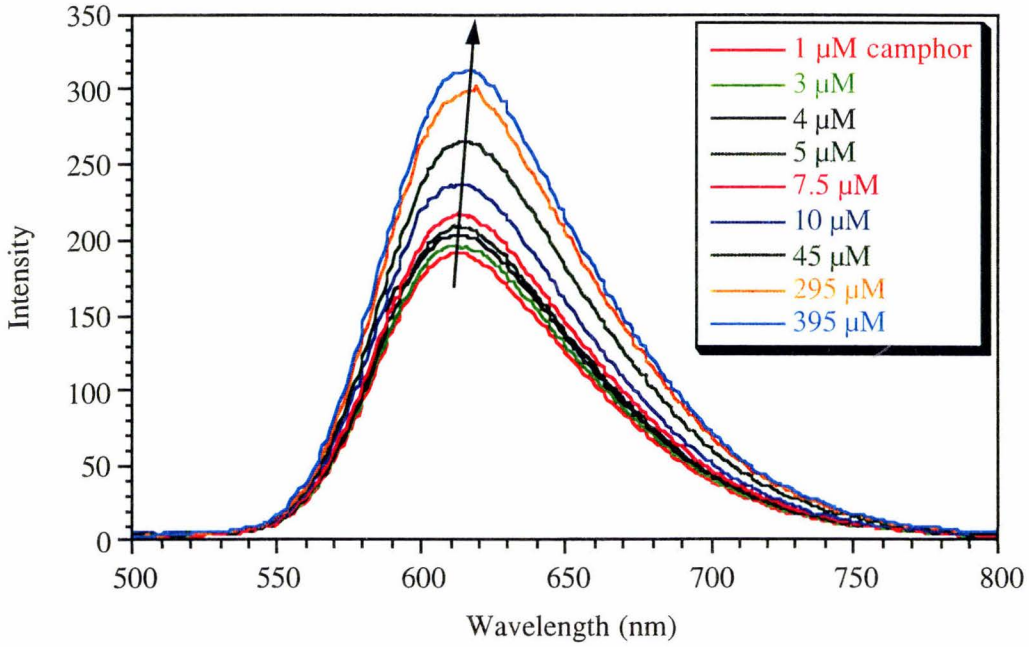
Intensity
Wavelength (nm)
1 μM camphor
3 μM
4 μM
5 μM
7.5 μM
10 μM
45 μM
295 μM
395 μM

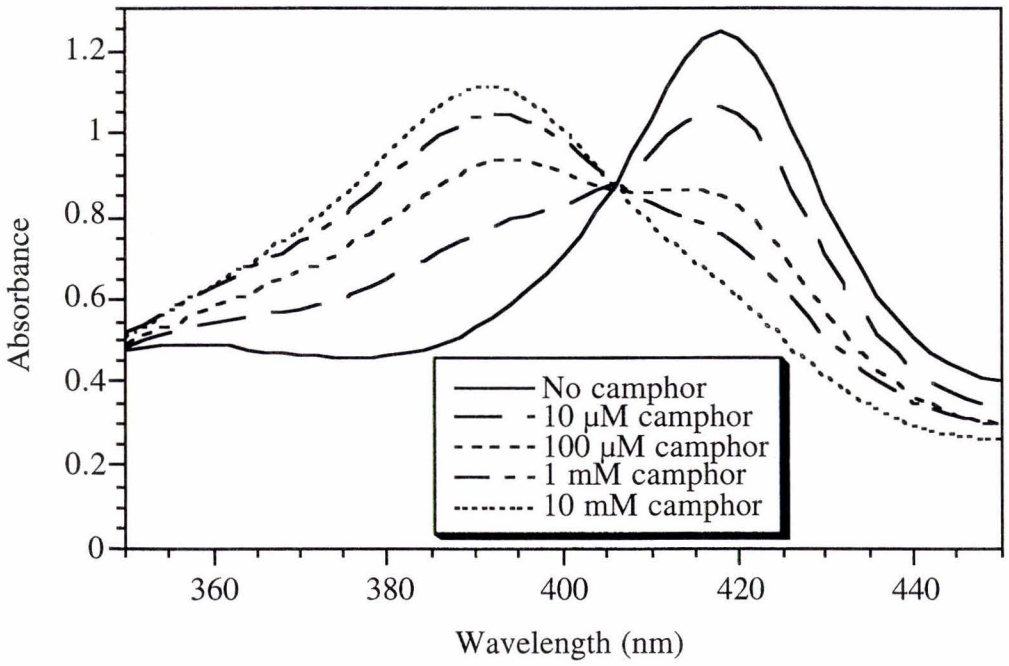
Absorbance
Wavelength (nm)
No camphor
10 μM camphor
100 μM camphor
1 mM camphor
10 mM camphor

Table 2.1. Dissociation constants, Ru^{2+*} excited-state lifetimes, and Ru-Fe distances

Compound	K_D(μM)	k_{en}^{-1}(ns)	Ru-Fe(Å)
$[Ru\text{-}C_{13}\text{-}EB]^{2+*}$	1.7 ± 0.4	107 ± 8	20.6 ± 0.2
$[Ru\text{-}C_{12}\text{-}EB]^{2+*}$	1.5 ± 0.3	103 ± 7	20.5 ± 0.2
$[Ru\text{-}C_{11}\text{-}EB]^{2+*}$	0.9 ± 0.4	94 ± 7	20.1 ± 0.3
$[Ru\text{-}C_{10}\text{-}EB]^{2+*}$	0.9 ± 0.4	88 ± 2	19.9 ± 0.1
$[Ru\text{-}C_{9}\text{-}EB]^{2+*}$	0.7 ± 0.1	75 ± 2	19.4 ± 0.1
$[Ru\text{-}C_{7}\text{-}EB]^{2+*}$	6.5 ± 1.3	77 ± 2	19.5 ± 0.1
$[Ru\text{-}C_{11}\text{-}Ad]^{2+*}$	0.6 ± 0.3	203 ± 16	21.0 ± 0.3
$[Ru\text{-}C_{9}\text{-}Ad]^{2+*}$	0.4 ± 0.2	231 ± 11	21.4 ± 0.2
$[Ru\text{-}C_{13}\text{-}Im]^{2+*}$	4.1 ± 1.1	190 ± 8	21.2 ± 0.1
$[Ru\text{-}C_{11}\text{-}Im]^{2+*}$	----------	488 ± 35	N/A

Uncertainties represent one standard deviation of the data averaged from three to six experiments.

Figure 2.6. Specific detection of cytochrome $P450_{cam}$ by Ru-C_9-Ad (2.5 μM) in the presence of six other heme enzymes (myoglobin, catalase, cytochrome *c*, cytochrome *c* peroxidase, horseradish peroxidase, cytochrome *b5*, each at 5 μM). Monophasic luminescence decays become biphasic upon addition of 500 nM P450. The quenched phase is more pronounced at higher P450 concentrations.

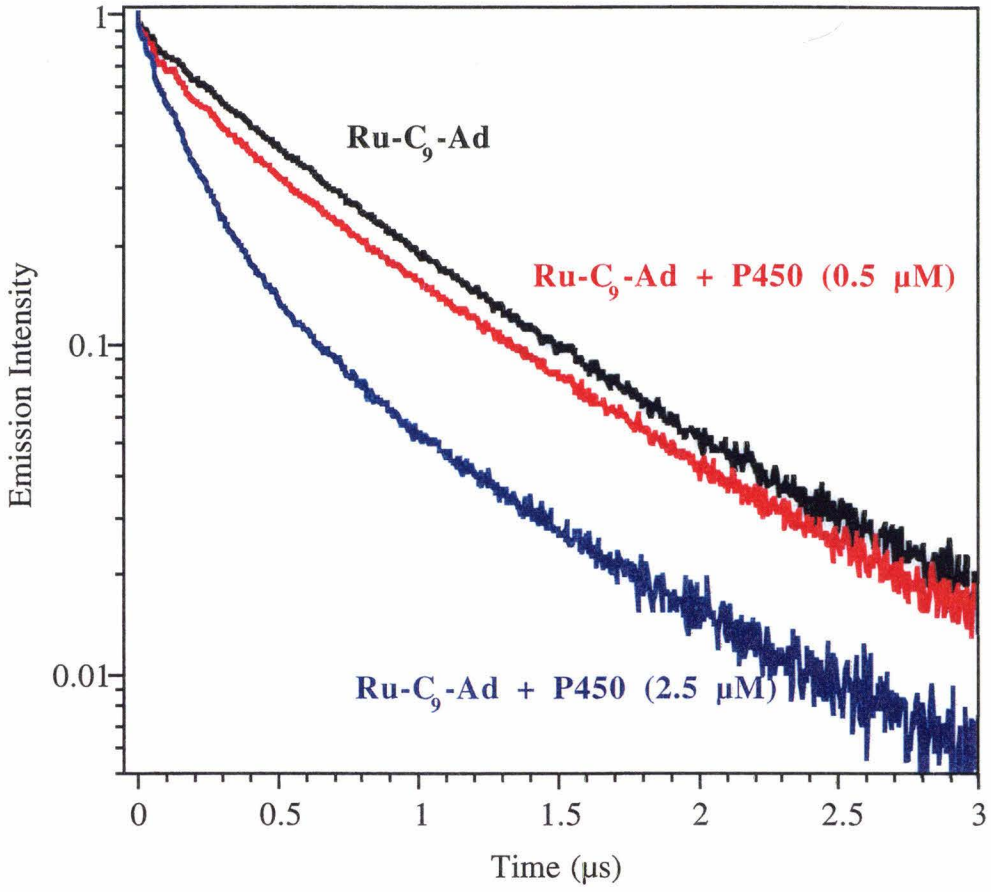
Ru-C9-Ad
Ru-C9-Ad + P450 (0.5 μM)
Ru-C9-Ad + P450 (2.5 μM)
Emission Intensity
1
0.1
0.01
0
0.5
1
1.5
2
2.5
3
Time (μs)

Figure 2.7. Top: Rates of Förster energy transfer, k_{en}, and calculated Fe-Ru distances (19.5-20.6 Å) as a function of the alkyl chain length in the Ru-C_n-EB series (n =7-13). These compounds serve as steric probes of the substrate channel depth, with the shortest compounds providing the minimum length of the channel (19.5 Å). This value is in excellent agreement with the P450:Ru-C_9-Ad crystal structure. All energy transfer rates are the average of at least four time-resolved luminescence measurements. Larger error bars accompany the data for the longer compounds, most likely due to greater conformational flexibility of the $\{Ru(bpy)_3\}^{2+}$ moiety. It is evident that the Ru-Fe distance varies little with chain length, which suggests a favorable interaction between P450 and $\{Ru(bpy)_3\}^{2+}$. Bottom: Dissociation constants of Ru-C_n-EB compounds (n =7-13) versus chain length. With chains of sufficient length (n > 9), the enzyme appears relatively insensitive to linker modification.

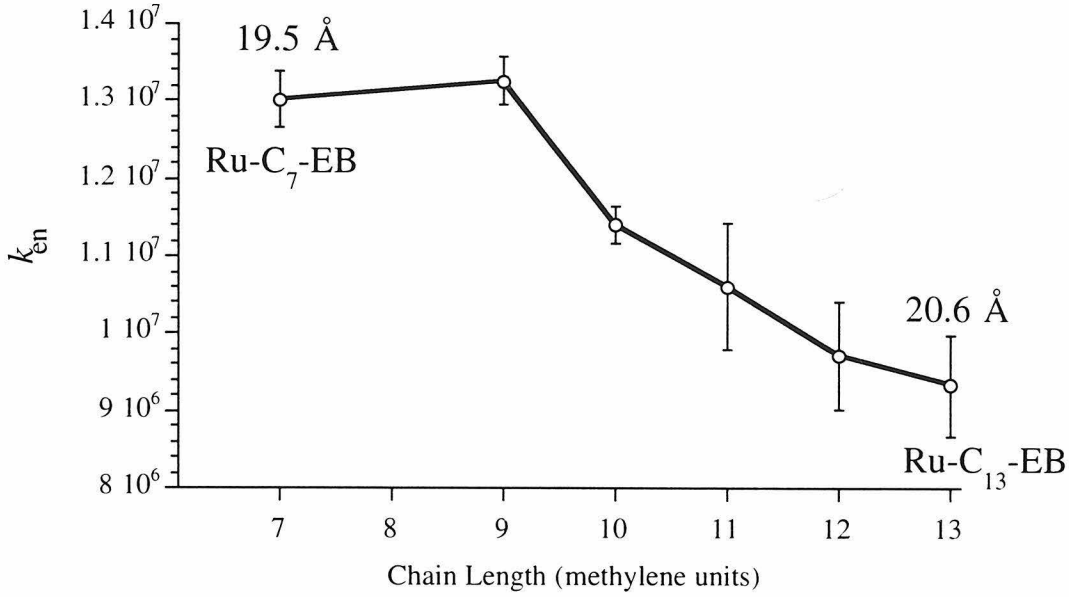
1.4 10^7
1.3 10^7
1.2 10^7
1.1 10^7
1 10^7
9 10^6
8 10^6
k_en
19.5 Å
Ru-C7-EB
20.6 Å
Ru-C13-EB
7
8
9
10
11
12
13
Chain Length (methylene units)

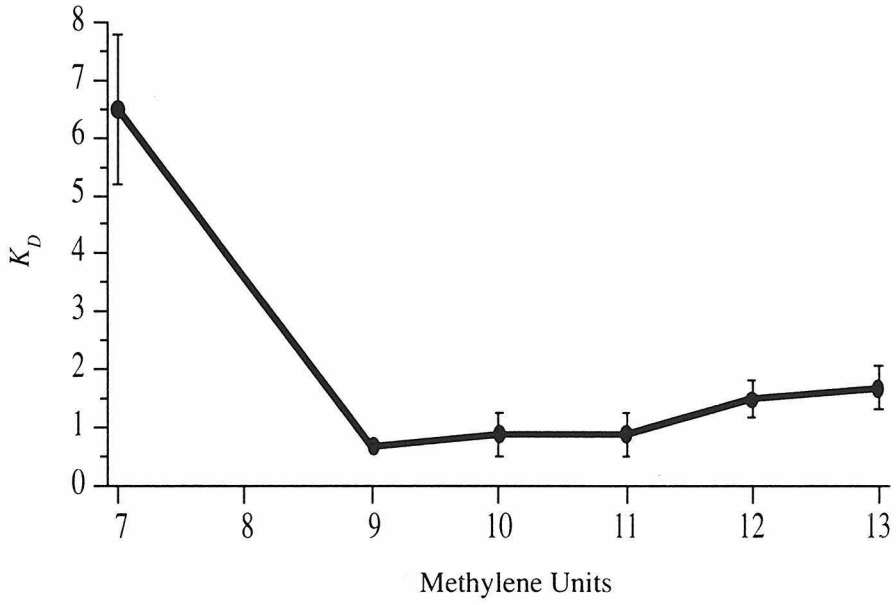
8
7
6
5
4
3
2
1
0
K_D
7
8
9
10
11
12
13
Methylene Units

demonstrates that detection of P450 by Ru-substrates may be fine-tuned by modification of the linker component. The removal of just two methylene units to give Ru-C_7-EB decreases the binding affinity substantially (~ 1.4 kcal/mol), suggesting that the tether is too short to allow the substrate to bind in its ideal conformation (Figure 2.7). This effect is seen more clearly with Im-terminated tethers, where Ru-C_{11}-Im has no measurable affinity for P450, whereas Ru-C_{13}-Im binds the enzyme tightly (Table 2.1). Apparently, the shorter linker does not allow the Im to extend far enough into the protein to ligate the heme iron.

Förster (dipole-dipole) energy transfer (FET) dominates the quenching in P450:Ru-substrate complexes. Evidence that electron transfer does not contribute significantly to this quenching is the finding that ferriheme reduction by $\{Ru(bpy)_3\}^+$ is ~10^3 times slower than k_{en} (6). Spectral overlap of $\{Ru(bpy)_3\}^{2+*}$ emission with the absorption of $Fe(CO)^{2+}$ P450 is greater than with the ferriheme enzyme, suggesting that FET should be more efficient in the carbonyl complex (where both oxidation and reduction of the heme-CO complex are energetically disfavored). Not only is the decay of Ru^{2+*} in P450 $Fe(CO)^{2+}$:Ru-C_{11}-EB 1.5 times faster (k_{en} = 1.6 x 10^7 s^{-1}), the calculated Ru-Fe distances differ by only 0.4 Å for the two heme oxidation states (26, 27).

The Ru-Fe distance found in the P450:Ru-C_9-Ad crystal (21 Å) is in excellent agreement with the Förster analysis of energy-transfer kinetics for this complex in

solution. Similar Ru-Fe distances were calculated for the various Ru-substrates, suggesting a common mode of Ru-substrate binding at the P450 active site. The shallow Ru-Fe distance dependence on chain length in the Ru-C_n-EB series confirms that $\{Ru(bpy)_3\}^{2+}$ always binds at the protein surface (Figure 2.7). The shortest ethyl benzene derivatives, Ru-C_7-EB and Ru-C_9-EB, report the minimum length of the substrate access channel (19.5 Å). These data also indicate that the region occupied by the methylene linker represents the most likely path followed by natural substrates to access the P450 active center. The swath cut by Ru-substrates in P450 is a channel of considerable breadth (3-8 Å) and depth (~ 20 Å).

CONCLUSION

We have developed a novel method of sensing specific biomolecules that involves tethering a photosensitizer to a molecule with high affinity for an active site. Analysis of Ru/heme FET kinetics has revealed the dimensions and conformational flexibility of the access channel, and probed the mechanism of substrate binding. This approach can be broadly expanded through a combinatorial approach to designing substrate moieties that target P450s as well as other enzymes, modifying sensitizers to produce desired signals, and optimizing linkages to fine-tune specificity or probe target conformations.

Replacement of $\{Ru(bpy)_3\}^{2+}$ with osmium polypyridyl complexes (28) would tune the emission further towards the near infrared, thereby improving tissue penetration and optical detection over the background of scattered light from cellular components. Furthermore, substitution of $\{Ru(bpy)_3\}^{2+}$ with a high quantum efficiency, blue-emitting organic fluorophore would greatly enhance Förster quenching by P450 and provide an even more sensitive substrate screening method. Finally, the ability of sensitizer-linked substrates to detect proteins and perform photochemical oxidation and reduction reactions at specific enzyme active sites (6) opens new avenues for intervention in metabolic processes.

REFERENCES AND NOTES

1. R. A. Tschirret-Guth, K. F. Medzihradszky, P. R. Ortiz de Montellano, *J. Am. Chem. Soc.* **121,** 4731-4737 (1999).

2. P. R. Ortiz de Montellano, M. A. Correia (1995) in *Cytochrome P450: Structure, Mechanism, and Biochemistry, 2nd edn*, P. R. Ortiz de Montellano, Ed. (Plenum Press, New York, 1995), pp. 305-364.

3. H. Joo, L. Zhanglin, F. H. Arnold, *Nature* **399,** 670-673 (1999).

4. J.-A. Stevenson, A. C. G. Westlake, C. Whittock, L.-L.Wong, *J. Am. Chem. Soc.* **118,** 12846-12847 (1996).

5. T. L. Poulos, J. R. Cupp-Vickery, H. Li, in *Cytochrome P450: Structure, Mechanism, and Biochemistry, 2nd edn*, P. R. Ortiz de Montellano, Ed. (Plenum Press, New York, 1995), pp. 125-150.

6. J. J. Wilker, I. J. Dmochowski, J. H. Dawson, J. R. Winkler, H. B. Gray, *Angew. Chem. Int. Ed.* **38,** 90-92 (1999).

7. R. N. Atkinson, L. Moore, J. Tobin, S. B. King, *J. Org. Chem.* **64,** 3467-3475 (1999).

8. Y. Kobayashi, X. J. Fang, G. D. Szklarz, J. R. Halpert, *Biochemistry* **37,** 6679-6688 (1998).

9. T. Fukui, K. Tanizawa, *Meth. Enzymol.* **280,** 41-50 (1997).

10. Y. Murthy, V. Massey, *Meth. Enzymol.* **280,** 436-460 (1997).

11. R. A. Tschirret-Guth, K. F. Medzihradszky, P. R. Ortiz de Montellano, *J. Am. Chem. Soc.* **120,** 7404-7410 (1998).

12. B. P. Unger, I. C. Gunsalus, S. G. Sligar, *J. Biol. Chem.* **261,** 1158-1163 (1986).

13. D. Nickerson, L.-L. Wong, Z. H. Rao, *Acta Crystallogr.* **D54,** 470-472 (1998).

14. J. Navaza, *Acta Crystallogr.* **A50,** 157-163 (1994).

15. T. L. Poulos, B. C. Finzel, A. J. Howard, *J. Mol. Biol.* **195,** 687-700 (1987).

16. Z. Otwinowski, W. Minor, *Meth. Enzymol.* **276,** 307-326 (1997).

17. D. E. McRee, *J. Mol. Graphics* **10,** 44 (1992).

18. A. T. Brünger, et al. *Acta Crystallogr.* **D54,** 905-921 (1998).

19. R. A. Laskowski, M. W. Macarthur, D. S. Moss, J. M. Thornton, *J. Appl. Crystallogr.* **26,** 283-291 (1993).

20. P. J. Kraulis, *J. Appl. Cryst.* **24,** 946-950 (1991).

21. E. A. Merritt, D. J. Bacon, *Methods Enzymol.* **277,** 505-524 (1997).

22. T. Förster, in *Modern Quantum Chemistry*, O. Sinanoglu, Ed. (Academic Press, New York, 1965), Vol. 3, pp. 93-137.

23. T. L. Poulos, B. C. Finzel, A. J. Howard, *Biochemistry* **25,** 5314-5322 (1986).

24. J. H. Dawson, L. A. Andersson, M. Sono, *J. Biol. Chem.* **257,** 3606-3617 (1982).

25. R. Raag, T. L. Poulos, *Biochemistry* **30,** 2674-2684 (1991).

26. T. Förster, *Discussions Faraday Soc.* **27,** 7-17 (1959).

27. W. C. Galley, L. Stryer, *Biochemistry* **8,** 1831-1833 (1969).

28. E. M. Kober, J. L. Marshall, W. J. Dressick, B. P. Sullivan, J. V. Caspar, T. J. Meyer, *Inorg. Chem.* **24,** 2755-2763 (1985).

Chapter 3

Enantiomeric Discrimination of Ru-Substrates by Cytochrome $P450_{cam}$[‡]

[‡]Adapted from I. J. Dmochowski, J. R. Winkler, H. B. Gray, *J. Inorg. Biochem.*(2000), in press.

INTRODUCTION

Much attention is being given to the design, synthesis, and employment of molecular probes of enzyme structure and function (1-11), owing in part to the abundance of naturally occurring cavity proteins (12-15) and in part to the power of site-directed mutagenesis to modify existing cavities and create new substrate binding sites (16-20). Especially appealing targets are the cytochromes P450 (an important family of monooxygenases involved in drug metabolism and steroid biosynthesis) because they possess hydrophobic pockets capable of sequestering a wide variety of substrates (21).

We have found that substrates and ligands attached via an alkyl chain to the inorganic photosensitizer $[Ru(bpy)_3]^{2+}$ (where bpy is 2,2'-bipyridine, Figure 3.1) bind P450 reversibly (1) with high affinity ($K_D \sim 1$ μM) and specificity (2). The substrate [Ru-C_9-Ad]Cl_2 was recently crystallized with P450 and the X-ray structure determined to 1.55 Å (PDB code, 1qmq; Figure 3.2) (2). Electron density (data not shown) from the ruthenium and bipyridyl ligands appears in multiple positions near the substrate channel, thereby indicating either considerable mobility of the $\{Ru(bpy)_3\}^{2+}$ moiety or the existence of stable enzyme-Ru conjugates that could correspond to specific interactions of Λ and Δ enantiomers with the protein surface. High thermal factors for the

Figure 3.1. Synthesis of [Ru-C_9-Ad]Cl_2. Steps 1 and 2 give nearly quantitative yields. Steps 3 and 4 each return roughly 30% of the desired product after chromatography, to give an overall yield between 5 and 10% based on the starting bromo-acid.

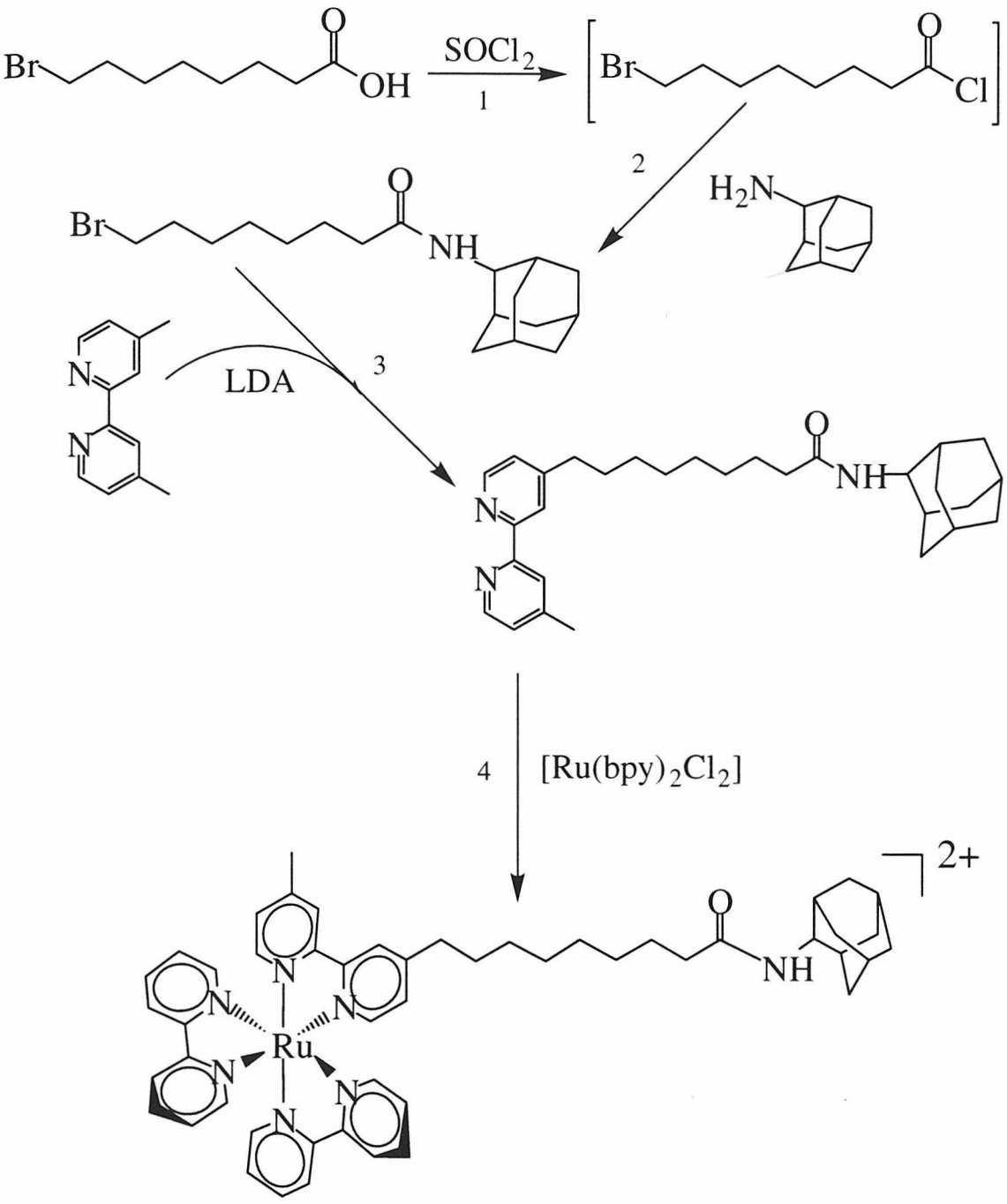
Br
OH
O
SOCl2
1
Br
Cl
2
H2N
Br
NH
LDA
3
N
N
NH
4
[Ru(bpy)2Cl2]
Ru
2+

Figure 3.2. Crystal structure of the $P450_{cam}$:Ru-C_9-Ad conjugate. Although both Λ and Δ isomers are present, only Λ is shown. The substituted bipyridyl ligand sits at the mouth of the cavity in close proximity to several hydrophobic residues, including Phe 193 and Tyr 29 (highlighted). The Ru-substrate amide carbonyl hydrogen bonds to Tyr 96. The adamantyl moiety resides in the heme pocket, much like the substrate adamantane.

$\{Ru(bpy)_3\}^{2+}$ moiety in the crystal structure prevented unambiguous assignment of either isomer. The inherent chirality of both P450 and $\{Ru(bpy)_3\}^{2+}$ raises the possibility that hydrophobic interactions with aromatic residues at the channel entrance favor the binding of one isomer relative to the other. We have probed this potential enantioselectivity by resolving the Λ and Δ [Ru-C_9-Ad]Cl_2 isomers and comparing their affinities for P450.

Chromatographic techniques using SP Sephadex C-25 with chiral eluents have been developed for the separation of many enantiomeric ruthenium polypyridyl complexes (22-25). The Sephadex ion exchange matrix itself is chiral, since it is made of dextran, a three-dimensional network of cross-linked D-glucose units. Interestingly, the ability of dextran to achieve chiral resolutions of d^6 (Re^{I}, Ru^{II}, Os^{II}, Co^{III}, Rh^{III}) polypyridyl compounds is greatly enhanced by the addition of tartrate salts (26). X-ray structures of these metal complexes crystallized with aromatic tartrate counterions (i.e., (+)-O,O'-di-4-toluoyl-D-tartrate) show well-ordered stacking interactions between the ditoluoyl and phenanthroline groups (24). Well-defined structures incorporating a variety of organic salts also have been observed in solution by ^1H NMR (22). Aromatic stacking has been implicated as a major factor in the mechanism of stereoisomer separation with these eluents (24), and provides a mechanism for chiral discrimination by the enzyme. In our work, sodium (−)-O,O'-dibenzoyl-L-tartrate was chosen for the isolation of the (±)-

[Ru-C_9-Ad]Cl_2 isomers because it most efficiently resolves the parent compound, [Ru(bpy)$_2$(Me_2bpy)]Cl_2 (Me_2bpy is 4,4'-dimethyl-2,2'-bipyridine) (27).

Time-resolved luminescence measurements precisely quantify the binding of Ru-substrates to P450 (1,2). Laser excitation of the Ru-protein solutions yields biphasic luminescence kinetics. The faster quenching process (k = 4–14 × 10^6 s^{-1}, depending on substrate and chain length) has been identified as Förster energy transfer from Ru^{2+*} to the heme (2). The slower luminescence decay process (τ ~ 500 ns) is the same as that of Ru^{2+*} in deoxygenated solution. Thus, dissociation constants can be calculated from the quenched fraction of [Ru-substrate]$^{2+*}$ luminescence. Traditional P450 substrate-binding assays rely on monitoring the low-to-high-spin shift (417 → 392 nm) associated with water loss from a ferric-aquo heme. Time-resolved emission profiles much more reliably assess the affinity of substrates (e.g., (±)-[Ru-C_9-Ad]Cl_2) that displace little water from the channel and only slightly perturb the spin state of the heme.

MATERIALS AND METHODS

Protein Preparation

Cytochrome $P450_{cam}$ was overexpressed in *E. coli* TBY cells from plasmid pUS200 (28) and purified in the presence of camphor with slight modification to standard procedures (29). See Appendix A for full details.

Synthesis of [Ru-C_9-Ad]Cl_2

Refer to Figure 3.1. Appendix B provides full synthetic details.

Chiral Resolution of (±)-[Ru-C_9-Ad]Cl_2

Circular dichroism (CD) spectra were measured on samples dissolved in acetonitrile (50-100 μM) using an Aviv Model 62A DS spectropolarimeter. Chiral separation was achieved by cation exchange chromatography (SP Sephadex C-25, Fluka) using 50 mM sodium (−)-O,O'-dibenzoyl-L-tartrate as the eluent. The aqueous tartrate solution was prepared by neutralization of the acid with two equivalents of NaOH, followed by filtration to remove insoluble impurities. Racemic [Ru-C_9-Ad]Cl_2 (4 mg) was loaded onto a column (dimensions 120 x 3.5 cm) covered with aluminum foil to eliminate the possibility of photoracemization. Eluent flow was regulated (~1 mL/min) with a peristaltic pump. The resolution of two bands occurred after traversing an effective column length (ECL) of 2 meters.

Upon separation, the Sephadex was expelled from the column with air, and the first and second bands were collected and soaked in acetonitrile to remove Ru from the dextran. The red solutions were rotary evaporated at room temperature, redissolved in water, and metathesized by ion exchange to their chloride salts. Band 1 (the first eluted fraction) had a negative rotation and was assigned the Δ absolute configuration based on the CD characteristics of similar complexes (24). CD [λ (Δε), CH_3CN]: Δ-(−): 227 nm (+26), 240 (+23), 260 (−10), 278 (+134), 294 (+307), 325 (+18), 365 (+11), 424 (+19), 476 (−15); Λ-(+): 227 (−27), 240 (−23), 260 (+7), 278 (−126), 294 (+281), 325 (−17), 365 (−11), 424 (−19), 476 (+13).

K_I Determination

A Hewlett Packard 8452A spectrophotometer was used to collect UV-vis data. Buffer conditions were 50 mM potassium phosphate, 100 mM potassium chloride, pH 7.4 for all protein solutions (~5 μM P450). UV-vis titrations were performed at 20 °C with stirring (500 rpm) using a Hewlett Packard 89090A stirrer/temperature controller. Λ and Δ-[Ru-C_9-Ad]Cl_2 displace little water from the ferric-aquo heme and binding results in only 25% conversion to the high-spin species, due, presumably, to the abundance of water in the Ru-bound (open) structure. Thus, affinities were determined by the ability of these complexes to inhibit the low- to high-spin transition produced by camphor.

Concentrated ethanolic stock solutions of camphor titrated in small aliquots (0.5–1.0 μL) into the protein solutions gave the desired range of camphor concentrations (250 nM–2 mM). The concentration of ethanol never exceeded 1% of the total volume. Dissociation constants of camphor, K_S, were spectroscopically determined at three concentrations (0–20 μM, 99% bound) of both Ru-C_9-Ad isomers. K_S was calculated by fitting the data to $1/\Delta A$ vs. 1/[S], the slope of which yields $K_S/([E]\Delta\varepsilon)$ from the relationship $1/\Delta A = ((K_S/[S]) + 1)/([E]\Delta\varepsilon)$, where ΔA is the absorbance change from the initial value, [S] is the concentration of camphor, [E] is the concentration of P450, and $\Delta\varepsilon$ is the difference in molar absorptivity between [Ru-C_9-Ad]- and camphor-bound P450. Absorbance changes were recorded at 392 and 416 nm. Values of K_I, the equilibrium constant between Ru-bound and camphor-bound P450, were determined for both isomers by plotting K_S against the Ru-C_9-Ad concentration. The dissociation constants, K_D, of (±)-[Ru-C_9-Ad]Cl_2 were calculated based on a single-substrate binding model (Figure 3.3).

K_D Determination

Emission experiments were conducted under similar conditions (20 °C, buffered solutions, 5 μM in both Ru-substrate and protein). Samples were prepared in a 1-cm-pathlength quartz cuvette with a long neck fitted with a 24/40 joint and a threaded

Figure 3.3. Binding of a single substrate to P450: by definition, $K_D = K_{cam}/K_I$, where K_{cam} is the dissociaton constant of camphor (in the absence of Ru-substrate), and K_I is the equilibrium constant between camphor- and ruthenium-bound P450, spectroscopically determined by measuring the dissociation constant of camphor at multiple Ru concentrations. Luminescence experiments measure K_D directly.

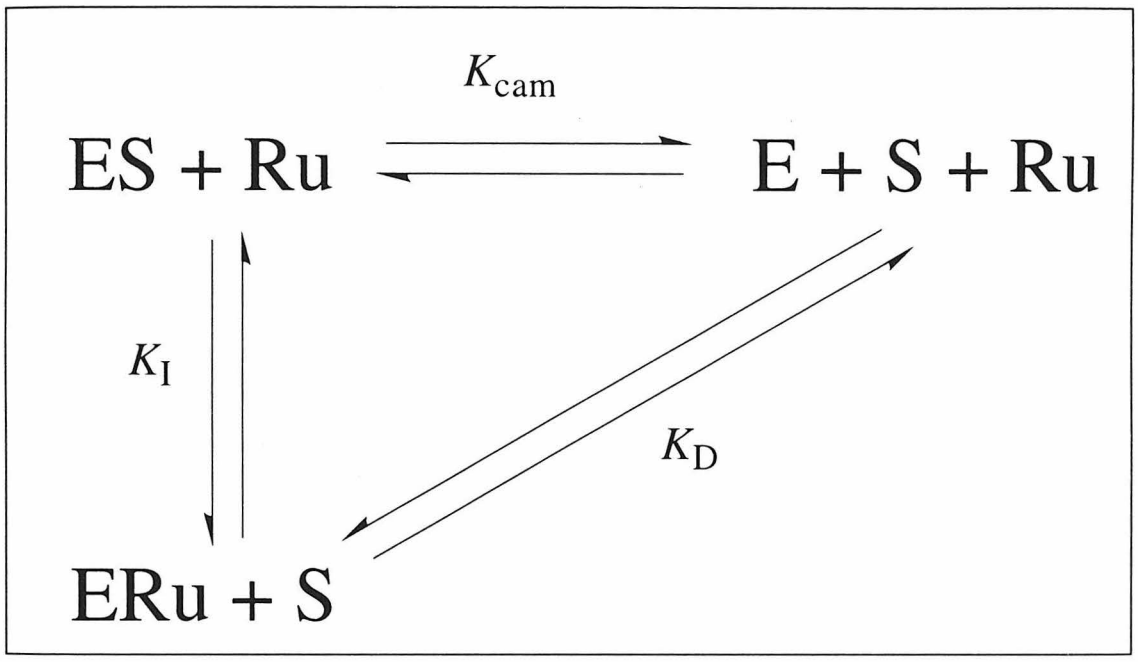
K_{cam}
ES + Ru
E + S + Ru
K_I
K_D
ERu + S

compression seal. The samples (1.5 mL) were deoxygenated by repeated cycles of vacuum followed by argon back-filling. Bubbling of the samples was avoided to minimize protein denaturation. UV-vis spectra were measured routinely before and after each luminescence measurement to verify that the protein samples had not degraded. Nanosecond emission kinetics were fit to the sum of two exponentials ($I(t) = c_0 + c_1\exp(-k_1t) + c_2\exp(-k_2t)$) using an in-house nonlinear least-squares fitting program. Dissociation constants for both isomers were determined using the ratio of the coefficients for the fast and slow phases, $c_1/(c_1+c_2)$.

Time-resolved Emission

The excitation source for all experiments was a tunable (220-2000 nm) optical parametric oscillator (Spectra Physics, MOPO) pumped by a frequency-tripled Q-switched Nd:YAG laser (Spectra Physics, 355 nm, 350 mJ/pulse, 8-ns FWHM). The OPO output power was attenuated by passage through a polarizer. Deoxygenated Ru-protein samples were excited at 470 nm, typically 2 mJ/pulse at the sample. Instrument response was 10 ns (FWHM). Emission kinetics data are averages of at least 250 laser shots.

RESULTS

Resolution of racemic $[Ru\text{-}C_9\text{-}Ad]^{2+}$ was accomplished by cation-exchange chromatography using a chiral eluent, sodium (−)-O,O'-dibenzoyl-L-tartrate. The CD spectra of the Λ-(+) and Δ-(−)-$[Ru\text{-}C_9\text{-}Ad]Cl_2$ isomers are shown in Figure 3.4. In both cases, enantiomeric excess is > 90% based on the similarity of their extinction coefficients at every wavelength (< 10% deviation), as well as their similarity to published values for (±)-$[Ru(bpy)_3]Cl_2$ (24). Initial efforts to purify $[Ru\text{-}C_9\text{-}Ad]Cl_2$ in larger quantities (40 mg) and with more concentrated eluent (150 mM) were unsuccessful.

Figure 3.5 shows a standard low- to high-spin conversion involving the titration of camphor into the P450 active site in the presence of Λ and Δ-[Ru-C_9-Ad] isomers. The dissociation constant for camphor alone (K_{cam}) was found to be 3.0 ± 0.2 μM under the experimental conditions, in good agreement with the literature value (21). The steric bulk of Ru-substrates appears to preclude co-occupation of the active site with camphor, an observation supported by the P450:Ru-C_9-Ad crystal structure in which the adamantyl moiety binds above the heme and hydrogen bonds to Tyr 96 much like camphor (2). UV-vis absorption measurements of Ru-C_9-Ad displacement show a preference for the Λ isomer (K_D (Λ) = 200 ± 50 nM; K_D (Δ) = 300 ± 50 nM). It was found empirically that

Figure 3.4. CD spectra of the enantiomeric forms of $[Ru(bpy)_2(bpy\text{-}C_9\text{-}Ad]^{2+}$: Δ (dotted line); Λ (solid line).

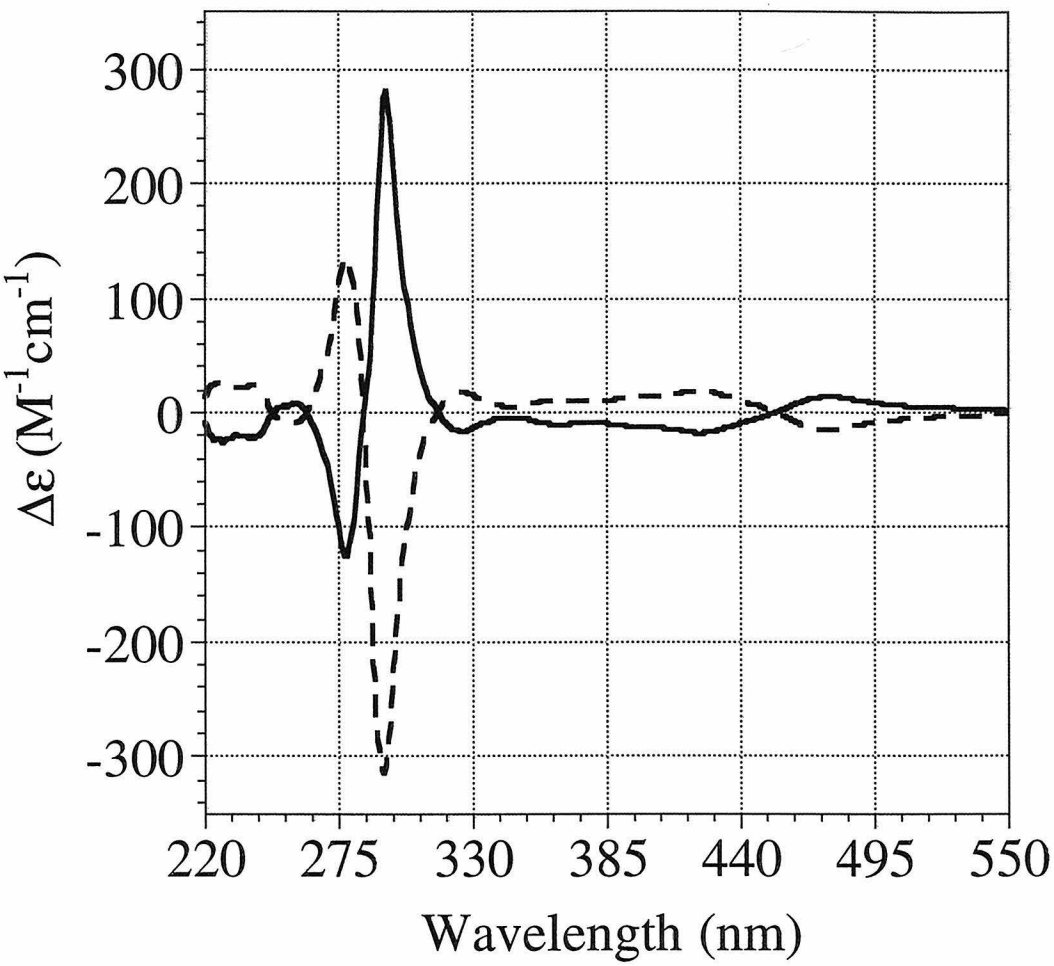
300
200
100
0
-100
-200
-300
Δε (M-1cm-1)
220
275
330
385
440
495
550
Wavelength (nm)

Figure 3.5. Inverse absorbance changes at 392 nm as functions of inverse camphor concentration on titrating camphor into buffered (50 mM potassium phosphate, 100 mM potassium chloride, pH 7.4) solutions of ferric-aquo cytochrome $P450_{cam}$ (~5 μM). The triangles denote the binding of camphor to P450 in the absence of any Ru-substrate (slope = $K_S/([P450]\Delta\varepsilon$; K_S = 3.0 ± 0.2 μM, [P450] = 5.50 μM, $\Delta\varepsilon_{392\ nm}$ = 54,000 $M^{-1}cm^{-1}$). Inhibition of camphor binding by Λ-[Ru-C_9-Ad]Cl_2 (squares, K_S = 74 ± 10, [P450] = 5.15 μM, $\Delta\varepsilon_{392\ nm}$ = 34,000 $M^{-1}cm^{-1}$ (difference between camphor- and [Ru-C_9-Ad]-bound P450), [Ru] = 4.83 μM, K_I = 15 ± 1, K_D = 200 ± 50 nM) and Δ-[Ru-C_9-Ad]Cl_2 (circles, K_S = 53 ± 10, [P450] = 5.29 μM, [Ru] = 4.99 μM, K_I = 10 ± 1, K_D = 300 ± 50 nM) is reflected by steeper slopes. Reported dissociation constants are averages of three titrations.

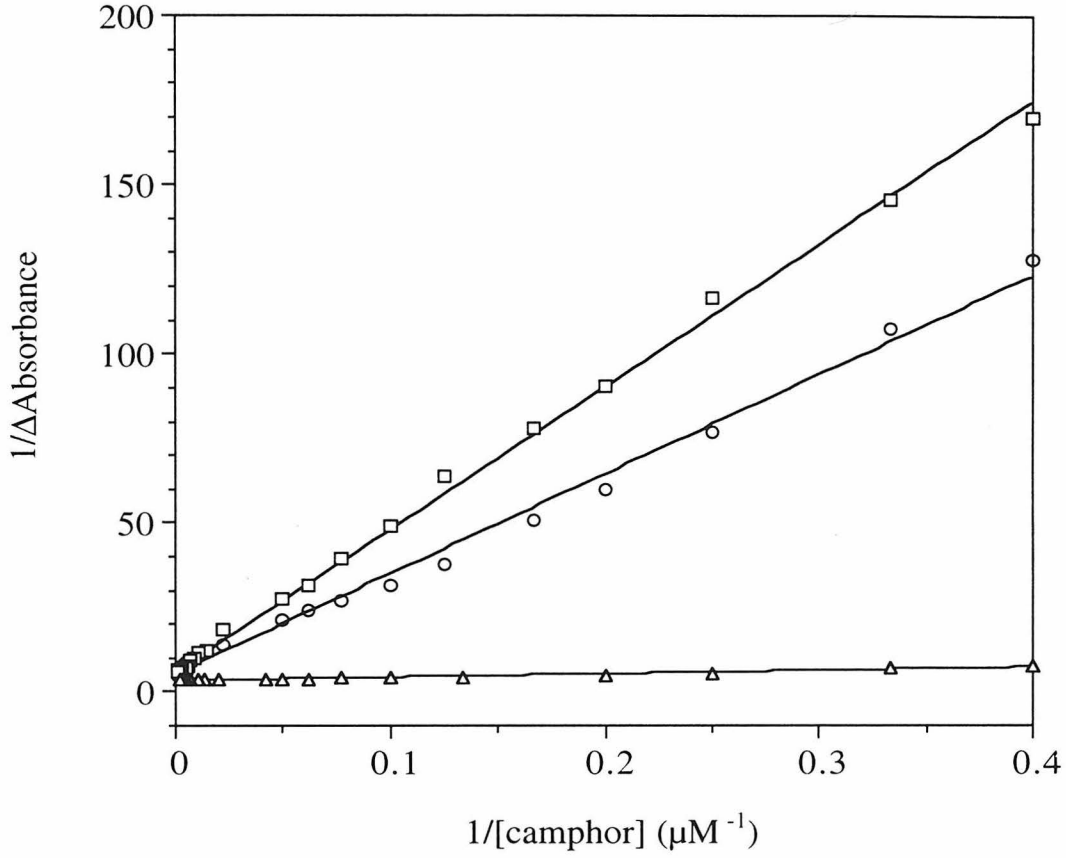
200
150
100
50
0
1/ΔAbsorbance
0
0.1
0.2
0.3
0.4
1/[camphor] (μM -1)

displacement of camphor (100 μM camphor, 4.67 μM P450, 99% bound) by Ru-substrates yields dissociation constants with higher precision. The apparent dissociation constant, K_D = 240 ± 20 nM, of racemic Ru-C_9-Ad determined by this Ru-titration method (Figure 3.6) agrees with the predicted value (K_D = 248 nM). See Appendix D for a full treatment of these calculations.

Time-resolved luminescence measurements also distinguish the binding of Λ and Δ-[Ru-C_9-Ad] isomers to P450 (Figure 3.7). The monophasic emission decay ($k = 2.0 \times 10^6$ s^{-1}) of Ru-C_9-Ad alone in solution is nearly identical with that of the slower phases of the two solutions containing P450. This provides strong evidence that binding can be modeled as a two-state equilibrium, and in the "free" state the Ru-substrates are completely dissociated from the protein. Virtually the same quenching rate constants ($k = 4.5 \times 10^6$ s^{-1}) from the Λ and Δ "bound" states indicate comparable Ru-Fe distances for the two isomers. The proportion of the decay (Λ, 87.5 ± 0.5%; Δ, 82.5 ± 0.5%; 5 μM P450, 5 μM Ru) that is attributable to this faster (quenched) phase is clearly greater for Λ-[Ru-C_9-Ad]. The K_D values for the enantiomers determined by time-resolved emission (Λ, 90 ± 20; Δ, 190 ± 20 nM) are in good agreement with the K_D for racemic Ru-C_9-Ad (150 ± 30 nM).

In order to test whether the single-substrate binding model (Figure 3.3) accurately describes camphor displacement of Ru-C_9-Ad from P450, a series of UV-vis absorption

Figure 3.6. Absorbance (open circles, 392 nm; filled circles, 416 nm) versus Ru-C_9-Ad concentration; UV-vis data monitored the displacement of camphor from P450, and were corrected for Ru absorbance. Data are fit by the function: $A = A_0 + \Delta\varepsilon^*([P450]^*[Ru])/([Ru] + K_S)$, where A_0 is the initial absorbance, $\Delta\varepsilon_{392} = 34{,}000$, $\Delta\varepsilon_{416} = 41{,}000\ M^{-1}cm^{-1}$, [P450] = 4.67 μM; K_S(392 nm) = 13.3, K_S(416 nm) = 11.7. $K_D = K_{cam}/K_S = 240 \pm 20$ nM.

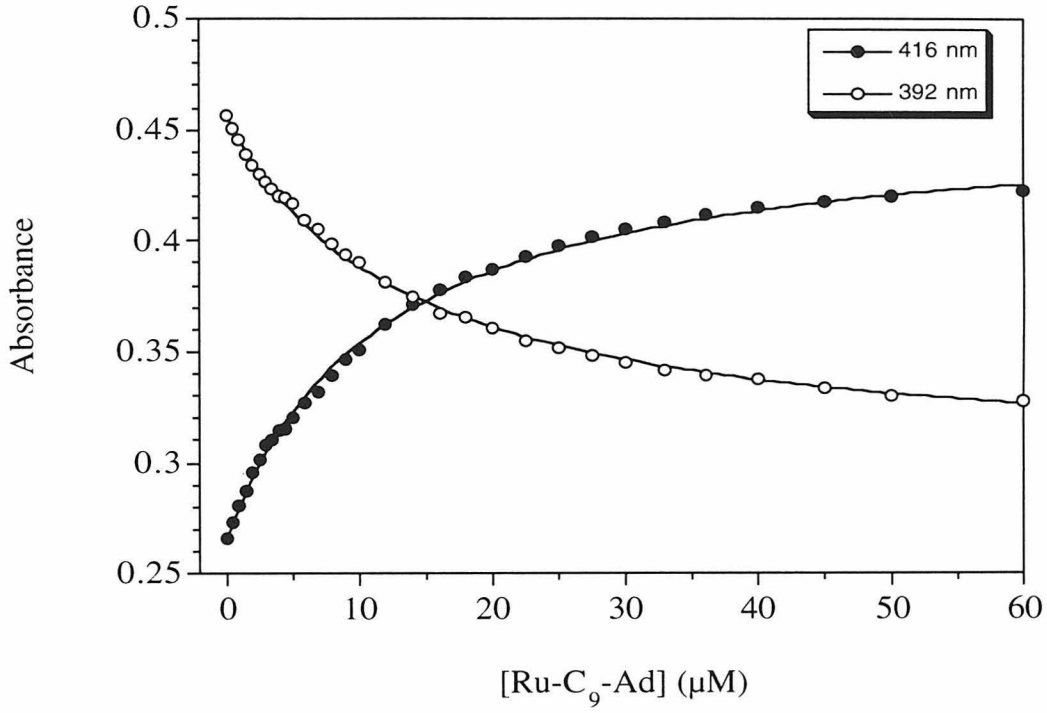
0.5
0.45
0.4
0.35
0.3
0.25
Absorbance
0
10
20
30
40
50
60
[Ru-C9-Ad] (μM)
416 nm
392 nm

Figure 3.7. Kinetics traces of $[Ru\text{-}C_9\text{-}Ad]^{2+*}$ emission decay. A larger fraction of Λ-$[Ru\text{-}C_9\text{-}Ad]Cl_2$ emission (monitored at 620 nm) is quenched by P450.

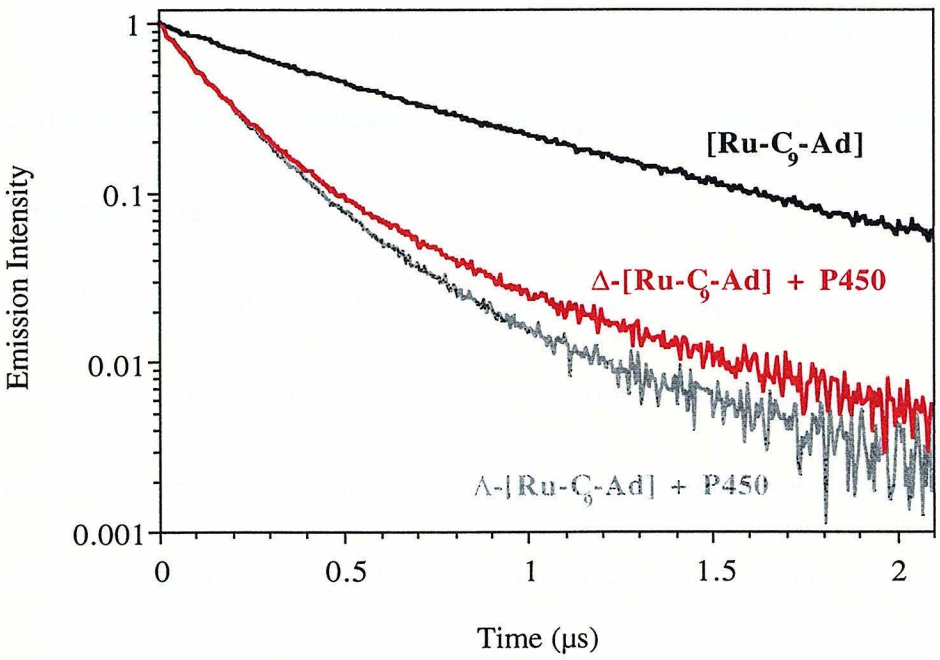
1
0.1
0.01
0.001
Emission Intensity
0
0.5
1
1.5
2
Time (μs)
[Ru-C9-Ad]
Δ-[Ru-C9-Ad] + P450
Λ-[Ru-C9-Ad] + P450

and emission experiments were performed in parallel. Figure 3.8 reveals that the amounts of unbound Ru^{2+*} (by luminescence) and low-spin P450 (by UV-vis) track closely during camphor titration into the 1:1 P450:Ru-C_9-Ad complex. However, persistent quenching of Ru^{2+*} at high camphor concentrations suggests that a small fraction (%quenched-%low spin ~ 5%) of Ru-C_9-Ad binds cooperatively *in the P450 channel*, presumably above the camphor binding site. Energy-transfer kinetics do not change during the titration, indicating that $\{Ru(bpy)_3\}^{2+}$ remains at the surface (~ 20 Å from the heme) in this ternary complex.

Confirmation that Λ-[Ru-C_9-Ad] binds P450 with roughly twice the affinity of the Δ isomer comes from an experiment in which buffered P450 (20 μM) and (±)-[Ru-C_9-Ad]Cl_2 (40 μM) were centrifuged together through a size-selective membrane (Centricon, YM-10). CD measurement showed that the Ru-substrate effluent (23 μM, in good agreement with the dissociation constant) was enantiomerically enriched by 15% with the Δ (more weakly bound) isomer. In the absence of P450, no enantiomeric enhancement was found to occur during filtration. Thus, of the 17 μM Ru-C_9-Ad remaining bound to the enzyme, 10.2 μM corresponded to Λ and 6.8 μM to the Δ isomer. The ratio of the concentrations of bound isomers (Λ/Δ ~ 1.5) is in reasonable agreement with the corresponding K_D ratio (Δ/Λ ~ 2).

Figure 3.8. 1/fraction of quenched Ru^{2+*} luminescence and 1/fraction of low-spin P450 as functions of camphor concentration. Luminescence data (samples at ambient conditions, monitored at 620 nm; kinetics fit to biphasic decay give fraction Ru^{2+*} quenched by P450) were collected subsequent to each UV-vis measurement. The spin state of the heme was calculated from changes in absorbance at 416 nm. Luminescence measurements report persistent Ru^{2+*} binding at high camphor concentrations.

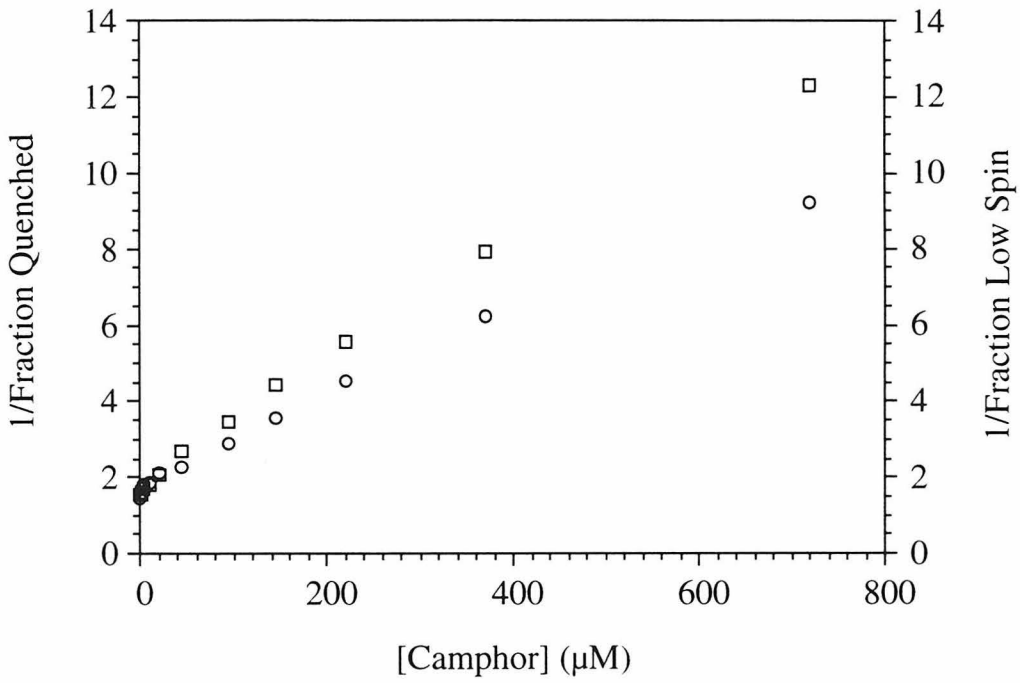
1/Fraction Quenched
1/Fraction Low Spin
[Camphor] (μM)
0
2
4
6
8
10
12
14
0
200
400
600
800

DISCUSSION

Sodium (−)-O,O'-dibenzoyl-L-tartrate proved much less efficient at resolving (±)-[Ru-C_9-Ad]Cl_2 (ECL = 200 cm) than reported for the model compound [$Ru(bpy)_2(Me_2bpy)$]Cl_2 (ECL = 70 cm) (24), presumably due to interference from the long alkyl substituent. Chiral ruthenium polypyridyl compounds have been synthesized directly by starting with one of the enantiomers of $[Ru(bpy)_2(CO)_2]^{2+}$ (24). Addition of the third bipyridyl ligand occurs with stereoretention if the temperature, solvent, and ligand concentration are carefully controlled (23). This method would seem preferable to chiral separations of functionalized $[Ru(bpy)_2(bpy')]Cl_2$ compounds, which in our hands required 2-3 weeks for purification of milligram quantities of material.

That K_D(energy transfer) < K_D(UV-vis) reflects subtle, method-dependent differences in the quantification of Ru-substrate binding. Nonspecific binding of Ru-C_9-Ad to the enzyme will affect the Ru^{2+*} emission decay profile, owing to energy transfer to the heme, but will not perturb the UV-vis spectrum if camphor is in place at the active site. Interestingly, when the Ru-C_9-Ad concentration exceeds that of P450, the luminescence results begin to deviate from predictions based on a single-substrate binding model. Energy-transfer experiments reveal that when [Ru] >> [P450], at least four equivalents of Ru-C_9-Ad associate with the enzyme (5 μM P450, 50 μM Ru; 20 μM

Ru quenched at ~ 20 Å from the heme). In fact, the P450 interior is greatly expanded in this open form (see Figure 3.1) and should permit orientations of Ru-C_9-Ad different from that found in the crystallized complex.

An electrostatic map of the protein surface indicates that the entrance to the substrate channel is neutral, favoring hydrophobic rather than electrostatic interactions in recruiting $\{Ru(bpy)_3\}^{2+}$ to this region, especially at high ionic strengths. Evidence of the dominance of hydrophobic interactions is the finding that bipyridyl-substituted adamantane itself, before ruthenation, strongly binds P450 (data not shown). It also is of interest that hydrophobic interactions appear to play a role in certain stereoselective bimolecular electron-transfer reactions between metalloproteins and inorganic complexes (30-32).

Experiments with other Ru-linked moieties (1,2) indicate that the terminal group moderately influences the overall affinity of the Ru-substrate for P450. (Ru-adamantane compounds bind with 3-fold higher affinity than Ru-(ethyl benzene) analogs, and 9-fold higher affinity than unsubstituted Ru-alkyl chains.) A comparable effect (K_D increases 9-fold) is observed when short linkers connecting the ethyl benzene to the photosensitizer prohibit optimal positioning of the substrate within the active-site pocket (2). Sufficient chain length is especially critical for imidazole-terminated compounds, where the ability to bind the iron appears to be requisite for association. The modest 2-fold discrimination

of Λ and Δ-[Ru-C_9-Ad] provides strong evidence that interactions near the protein surface are of lesser importance than the shape complementarity and hydrophobicity of the Ru-substrate in binding to the enzyme.

Enantiospecific binding indicates that noncovalent interactions over 10 Å from the active site impact substrate selection even when the channel is open, as must occur during entrance and egress of natural substrates. Similar long-range secondary interactions also influence the binding of benzenesulfonamide ligands to carbonic anhydrase (33). Based on the P450:Ru-C_9-Ad crystal structure (2), which confirms the ability of P450 to accommodate large substrates, and identifies hydrophobic interactions of the bipyridyl groups with Phe 193 and Tyr 29 (Figure 3.1), we infer that aromatic stacking plays an important role in chiral discrimination. Aromatic residues at the mouth of the P450 channel have been implicated previously in the recognition of hydrophobic substrates (34).

CONCLUSION

Submicromolar affinities, protein specificity, reversible binding, and synthetic versatility make sensitizer-linked substrates ideal for probing P450 active sites

Employing UV-vis and time-resolved luminescence measurements, we have found a 2-fold preference of P450 for Λ-[Ru-C_9-Ad]Cl_2. Emission experiments, especially with highly luminescent $\{Ru(bpy)_3\}^{2+}$ complexes, are particularly sensitive and convenient for measuring substrate binding. It is well known that the chirality and shape of substrate pockets promote enantio- and regioselective P450 catalysis. We have demonstrated that specific long-range interactions with a pendant metal complex also affect substrate binding at the active site of the enzyme.

REFERENCES AND NOTES

1. J. J. Wilker, I. J. Dmochowski, J. H. Dawson, J. R. Winkler, H. B. Gray, *Angew. Chem. Int. Ed.* **38**, 90-92 (1999).

2. I. J. Dmochowski, B. R. Crane, J. J. Wilker, J. R. Winkler, H. B. Gray, *Proc. Natl. Acad. Sci. USA* **96**, 12987-12990 (1999).

3. R. N. Atkinson, L. Moore, J. Tobin, S. B. King, *J. Org. Chem.* **64**, 3467-3475 (1999).

4. R. A. Tschirret-Guth, K. F. Medzihradszky, P. R. Ortiz de Montellano, *J. Am. Chem. Soc.* **121**, 4731-4737 (1999).

5. K. DiGleria, D. P. Nickerson, H. A. O. Hill, L.-L. Wong, V. Fülöp, *J. Am. Chem. Soc.* **120**, 46-52 (1998).

6. Y. Murthy, V. Massey, *Meth. Enzymol.* **280**, 436-460 (1997).

7. I. Hamachi, S. Tsukiji, S. Shinkai, S. Oishi, *J. Am. Chem. Soc.* **121**, 5500-5506 (1999).

8. M. Newcomb, M. H. Letadic, D. A. Putt, P. F. Hollenberg, *J. Am. Chem. Soc.* **117**, 3312-3313 (1995).

9. J. K. Atkinson, K. U. Ingold, *Biochemistry* **32**, 9209-9214 (1993).

10. K. E. Liu, C. C. Johnson, M. Newcomb, S. J. Lippard, *J. Am. Chem. Soc.* **115**, 939-947 (1993).

11. R. A. Tschirret-Guth, K. F. Medzihradszky, P. R. Ortiz de Montellano, *J. Am. Chem. Soc.* **120**, 7404-7410 (1998).

12. J. A. Tainer, E. D. Getzoff, K. M. Beem, J. S. Richardson, D. C. Richardson, *J. Mol. Biol.* **160**, 181-217 (1982).

13. T. L. Bigler, et al., *Prot. Sci.* **2**, 786-799 (1993).

14. J. Badger, et al., *Proc. Natl. Acad. Sci. USA* **85**, 3304-3308 (1988).

15. T. L. Poulos, B. C. Finzel, A. J. Howard, *Biochemistry* **25**, 5314-5322 (1986).

16. S. K. Wilcox, et al., *Biochemistry* **37**, 16853-16862 (1998).

17. J. O. Goldsmith, B. King, S. G. Boxer, *Biochemistry* **35**, 2421-2428 (1996).

18. G. D. DePillis, S. M. Decatur, D. Barrick, S. G. Boxer, *J. Am. Chem. Soc.* **116**, 6981-6982 (1994).

19. M. M. Fitzgerald, M. J. Churchill, D. E. McRee, D. B. Goodin, *Biochemistry* **33**, 3807-3818 (1994).

20. A. E. Eriksson, W. A. Baase, J. A. Wozniak, B. W. Matthews, *Nature* **355**, 371-373 (1992).

21. E. J. Mueller, P. J. Loida, S. G. Sligar, in *Cytochrome P450: Structure, Mechanism, and Biochemistry, 2nd edn* P. R. Ortiz de Montellano, Ed. (Plenum Press, New York, 1995) pp. 83-124.

22. N. C. Fletcher, F. R. Keene, *J. Chem. Soc., Dalton Trans.* **5**, 683-689 (1999).

23. N. C. Fletcher, P. C. Junk, D. A. Reitsma, F. R. Keene, *J. Chem. Soc. Dalton* **1**, 133-138 (1998).

24. T. J. Rutherford, P. A. Pellegrini, J. Aldrich-Wright, P. C. Junk, F. R. Keene, *Eur. J. Inorg. Chem.* **11**, 1677-1688 (1998).

25. T. J. Rutherford, M. G. Quagliotto, F. R. Keene, *Inorg. Chem.* **34**, 3857-3858 (1995).

26. Y. Yoshikawa, K. Yamasaki, *Coord. Chem. Rev.* **28**, 205-229 (1979).

27. F. R. Keene, personal communication (1999).

28. B. P. Unger, I. C. Gunsalus, S. G. Sligar, *J. Biol. Chem.* **261**, 1158-1163 (1986).

29. D. Nickerson, L.-L. Wong, Z. H. Rao, *Acta Crystallogr.* **D54**, 470-472 (1998).

30. S. Sakaki, Y.-i. Nishijima, H. Koga, K. Ohkubo, *Inorg. Chem.* **28**, 4061-4063 (1989).

31. S. Sakaki, Y.-i. Nishijima, K. Ohkubo, *J. Chem. Soc. Dalton Trans.* **4**, 1143-1148 (1991).

32. J. R. Pladziewicz, M. A. Accola, P. Osvath, A. M. Sargeson, *Inorg. Chem.* **32**, 2525-2533 (1993).

33. P. A. Boriak, D. W. Christianson, J. Kingerywood, G. M. Whitesides, *J. Med. Chem.* **38**, 2286-2291 (1995).

34. R. Raag, H. Li, B. C. Jones, T. L. Poulos, *Biochemistry* **32**, 4571-4578 (1993).

Chapter 4

Substrate Turnover in an Open Conformation of Cytochrome $P450_{cam}$

Acknowledgement:

Michael Green helped collect the Raman spectra reported in this chapter. Many thanks go to Peter Green for help with GC-MS and members of the Beauchamp group for their expertise with ESI.

INTRODUCTION

Among cytochromes P450 whose structures have been solved by X-ray crystallography, cytochrome $P450_{cam}$ (P450) shields its active site from bulk solvent particularly well. The conformational dynamics of P450 during substrate binding, and the paths taken by substrates and water molecules to reach the active center have been subjects of considerable research. A recent crystal structure of P450 complexed with $[Ru\text{-}C_9\text{-}Ad]Cl_2$ (Figure 4.1; adamantane is covalently attached via an alkyl linker to the photosensitizer ruthenium tris-2,2'-bipyridine) defines a clear path from solution to the heme, and confirms that large structural changes can accompany substrate binding (1). The adamantyl moiety sits above the heme in close proximity to the position normally occupied by adamantane (Figure 4.2), and the amide functionality forms a hydrogen bond to Tyr 96, mimicking the natural substrate camphor.

Interestingly, the Ru-photosensitizer displaces the loop connecting the F and G helices by more than 5 Å to reveal a large substrate channel above the heme. $P450_{cam}$ contains two exceptionally strong salt bridges (ΔG_{tot} ~ -3 kcal/mol) between Asp 251 and two residues at the periphery of the loop, Lys 178 and Arg 186. Studies in WT and D251N of camphor binding with varying ionic strength and solution dielectric have implicated these noncovalent bonds as playing an important role in substrate binding

Figure 4.1. Ru-compounds (1) and (3) for the study of P450 catalysis in an open conformation. While (1) competes with camphor for the P450 active site, (2) is able to share the pocket with camphor. 2-adamantylacetamide (2) is analagous to compound (1), without the Ru-tether; (2) induces a full low to high spin conversion at the heme.

(**1**) $[Ru\text{-}C_9\text{-}Ad]^{2+}$

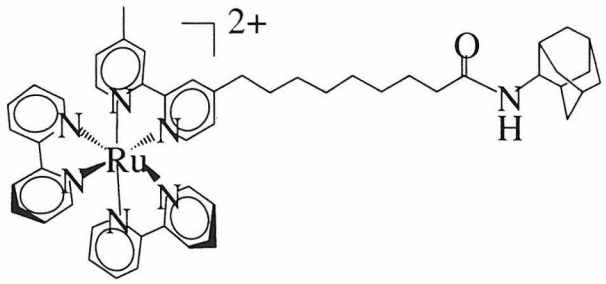

(**2**) 2-Adamantylacetamide

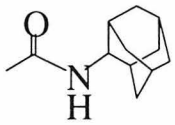

(**3**) $[Ru\text{-}C_{10}]^{2+}$

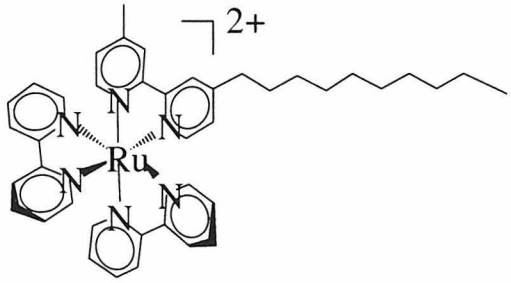

Figure 4.2. Top: X-ray crystal structure of the P450:Ru-C_9-Ad complex (both Λ and Δ isomers shown) at 1.55 Å resolution. The $\{Ru(bpy)_3\}^{2+}$ moiety sits at the mouth of the P450 channel, and displaces the loop connecting the F and G helices by over 5 Å. The helix above the heme (I helix) appears tightly coiled. Bottom: X-ray crystal structure of the P450:adamantane complex at 2.1 Å resolution. The substrate occupies the same position in this structure, but the I helix appears less alpha helical.

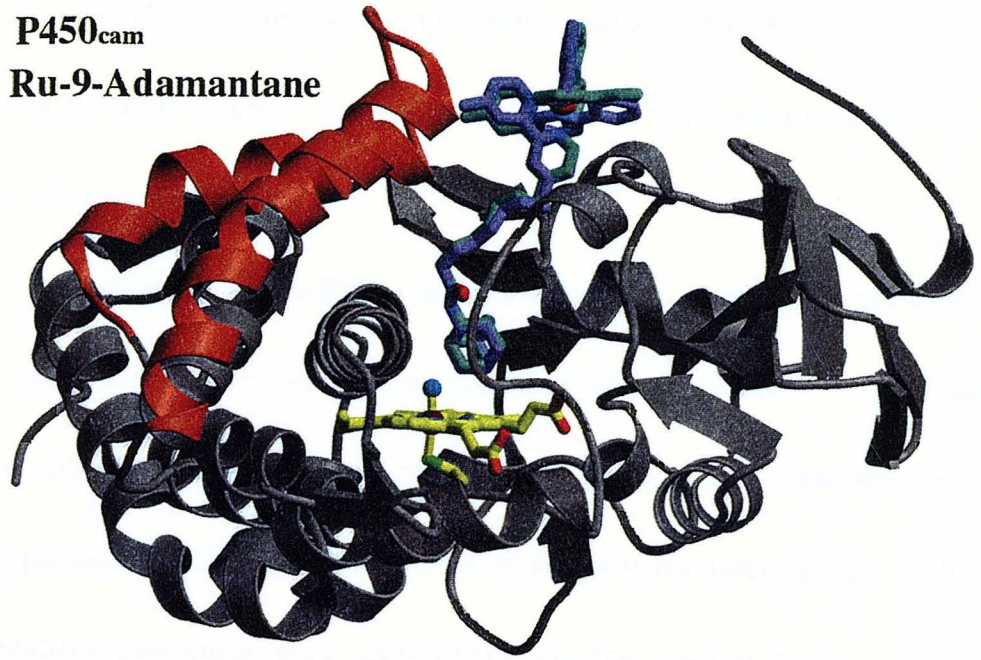
P450cam
Ru-9-Adamantane

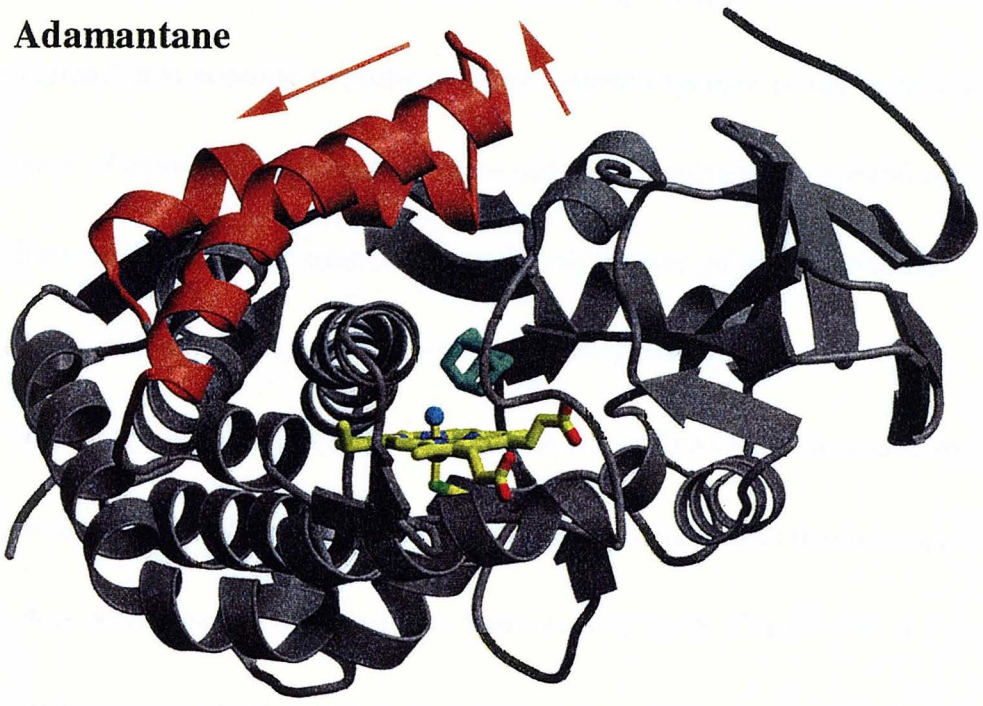
Adamantane

(2). A similar F-G loop was also identified at the mouth of the substrate channel in cytochrome P450BM-3 and P450terp, although it appears to be much more flexible in these enzymes (3). Experimental and theoretical work (4) has shown that P450s use the F-G loop to cap the channel and control the entrance and egress of substrate, product, and/or water from the pocket.

P450 binds [Ru-C_9-Ad]Cl_2 with high affinity (K_D = 0.3 μM), and as evidenced from the crystal structure, in the bound state allows the diffusion of water molecules directly into the active site. In this form, $P450_{cam}$ more closely resembles P450BM-3 which possesses a broad, open channel of roughly the same length (~ 20 Å) and hydroxylates long-chain fatty acids (5,6). Having trapped $P450_{cam}$ in this "open conformation," it is possible to probe whether solvent exposure of the heme inactivates the enzyme. Fundamental questions remain about the malleability of P450 active sites, and efforts to harness the tremendous catalytic power of these enzymes for new applications in bioremediation and catalysis are widespread (7,8).

The study of P450 dioxygen activation has identified critical proton transfer steps leading to dioxygen scission, but the source of the water molecules that drive protonation at the active center has not been explored until recently (8,9). The control of proton flux during hydroxylation of substrates such as adamantane, which do not exclude water from the active site, is particularly unresolved. Substrate-free P450 usually holds 5 or 6 water

molecules in the active site (10), including distal water ligation to the heme iron, but camphor binding appears to completely desolvate the interior of P450 (11). In proton inventory experiments, 28 water molecules were implicated as playing a role during camphor hydroxylation (12). This finding suggests that the P450 hydrophobic cavity is "leaky" on the time scale of proton transfer to dioxygen, and that water molecules play roles on the periphery of the enzyme. Mutagenesis studies (13), biochemical experiments (14), and theoretical work (9) have suggested that Asp 251 and the heme propionates supply protons to the catalytic site through important hydrogen-bonding interactions at the protein-solvent interface. The possibility that water molecules may enter and leave by the substrate channel is rarely considered.

Recent time-resolved X-ray crystal structures (PDB code 1d28) by Schlichting et al. show that dioxygen binding to the ferrous $P450_{cam}$:camphor complex induces rearrangement of the catalytically important I helix (15). These conformational changes – in which the carbonyl oxygen of the highly conserved Asp 251 flips 90^0 out towards Asn 255 (and the protein surface) and the amide nitrogen of Thr 252 rotates toward the heme pocket – are strikingly similar to those observed in the P450:Ru-C_9-Ad structure (Figure 4.3) (1). In both structures, these processes tightly coil the I-helix and allow the binding of two additional water molecules in the active site pocket.

Figure 4.3. Close up of the P450 active site complexed with [Ru-C_9-Ad]Cl_2. The water bound to the heme is stabilized by a chain of hydrogen bonds. New alternate conformations of D251 and T252 are shown which strongly resemble their positions in the recently solved P450 Fe^{2+}-O_2 structure. The amide of T252 twists away from the substrate to point towards the heme and stabilize the heme aquo ligand, as well as several other water molecules in the active site.

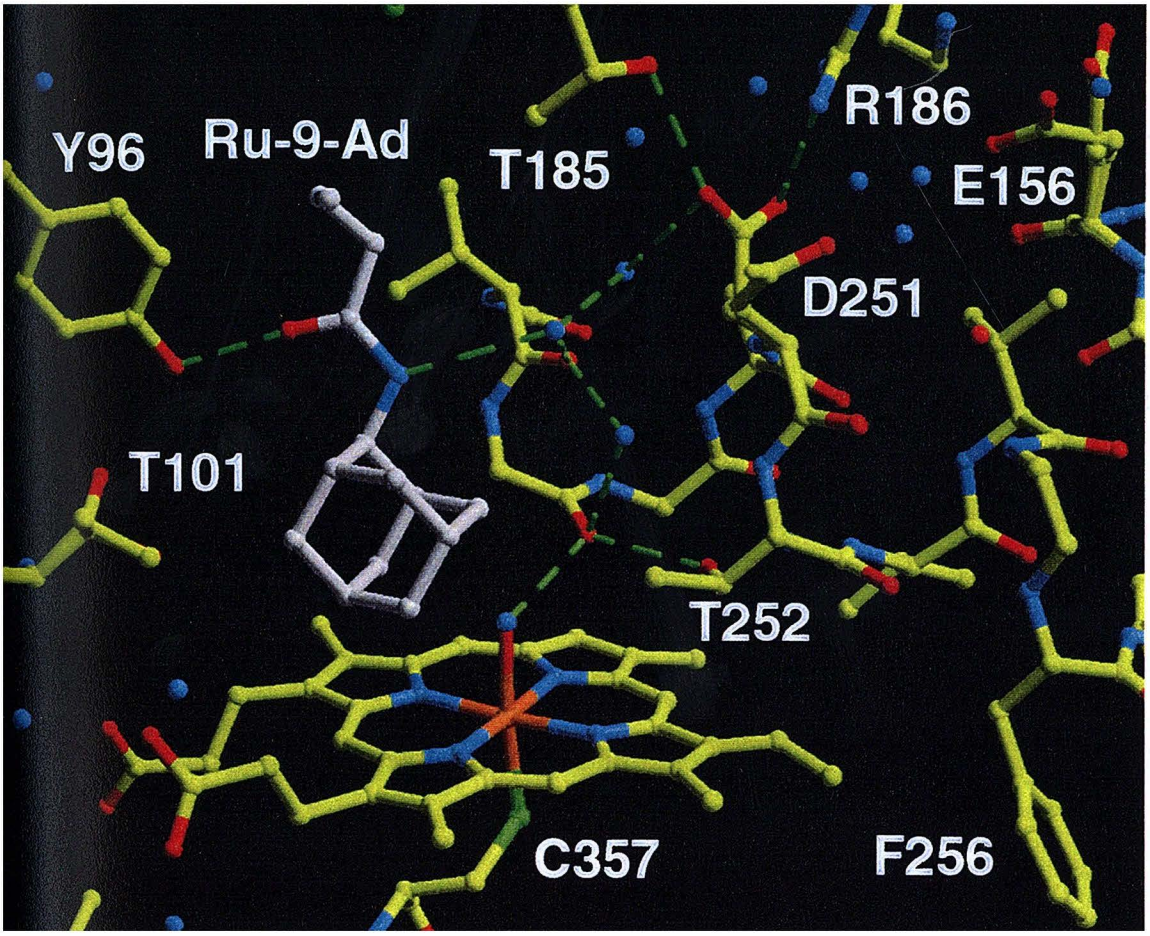
Y96
Ru-9-Ad
T185
R186
E156
D251
T101
T252
C357
F256

We report here that [Ru-C_9-Ad]Cl_2, despite opening the P450 cavity, is a viable substrate, as shown by a new electrospray mass spectroscopy assay. The rate and efficiency of [Ru-C_9-Ad]Cl_2 hydroxylation is compared to the untethered analog, 2-adamantantyl acetamide (Figure 4.1). Resonance Raman spectroscopy of Fe^{2+}-CO substrate complexes has been shown previously to be a sensitive reporter of the heme environment (16-19), and solution measurements comparing the binding of Ru-C_9-Ad to adamantane agree with the crystal structure and substrate turnover results. Experiments attempting P450-mediated Ru-C_9-Ad hydroxylation with steady-state photolysis suggest that turnover may be occurring in very low yields. In addition, a ternary complex involving P450, camphor, and Ru-C_{10} (Figure 4.1) has been characterized by time-resolved emission measurements. We have probed the enzymatic activity of this previously uncharacterized, but potentially biologically relevant open conformation of the enzyme, by comparing camphor hydroxylation rates in the ternary complex to natural camphor catalysis.

MATERIALS AND METHODS

General

[Ru-C_9-Ad]Cl_2 (**1**), 2-adamantylacetamide (**2**), and [Ru-C_{10}]Cl_2 (**3**) were synthesized as described in Appendix B. P450, PdR, and Pd were expressed and purified with minor modifications to literature procedures (20-23), see Appendix A. NADH and adamantane were purchased from Sigma and used without further purification. A miniature oxygen electrode was purchased from Microelectrodes, Inc. and the voltage output calibrated with solutions containing 0%, 21% (ambient), and 100% dioxygen.

UV-vis titrations were performed using a Hewlett Packard 8452A spectrophotometer and a Hewlett Packard 89090A stirrer/temperature controller, at 20 °C with stirring (500 rpm). Time-resolved emission experiments and data analysis with *Kinfit, Decon*, and *MATLAB* were performed as described previously, with the exception that the P450:Ru-C_{10}:camphor ternary complexes were not degassed during the titration or subsequent laser experiments.

Resonance Raman Spectroscopy on P450 Fe^{2+}-CO Substrate Complexes. Samples (200 μL, 100 μM P450 in standard KPi/ KCl buffer, substrate concentration = 1 mM) were prepared in glass NMR tubes fitted with a rubber septum. The solutions were gently bubbled with CO for several minutes before adding a spatula tip of dithionite. Formation of the Fe^{2+}-CO complex was verified by UV-vis (λ_{max} = 446 nm). Samples were excited at 441 nm with a HeCd laser (Liconix model 424ONB, 40 mW), and the

Raman scatter was focused using longitudinal and transverse collection optics onto a double spectrometer (SPEX 1403, 0.85 m) interfaced to a PC via the SPEX MSD2 module. The signal was collected using a PMT (Hamamatsu R955) powered by Pacific Precision Instruments (1100 V). The sample control unit, photon counter, amplifier/discriminator, and buffered interface were all from EG&G Instruments.

Hydroxylation of [Ru-C_9-Ad]Cl_2 with NADH/PdR/Pd/P450. A 4 mL solution (20 mM potassium phosphate buffer, 100 mM KCl, pH = 7.4) was prepared containing 1 μM P450, 1 μM PdR, 10 μM Pd, 20 μM [Ru-C_9-Ad]Cl_2, and 200 μM NADH (ε = 6.22 $M^{-1}cm^{-1}$ @ 340 nm). The consumption of NADH was monitored at 340 nm by UV-vis spectroscopy. Once >95% of the NADH was consumed, the reaction was quenched by the addition of 40 μL of a 1 M ethanolic camphor solution (ratio camphor/[Ru-C_9-Ad]Cl_2 ~ 500) to displace [Ru-C_9-Ad]Cl_2 from P450 and rapidly consume any remaining NADH. This solution was concentrated by centrifugation (Centricon, YM-10) to a minimum volume, and an additional milliliter of camphor-saturated phosphate buffer was added to the protein and centrifuged to remove any remaining Ru. The flow-through, containing hydroxylated [Ru-C_9-Ad]Cl_2, camphor, and buffer was rotary evaporated to dryness. Two cycles of acetonitrile (5 mL) addition, decanting, and rotary evaporation were performed to separate the buffer salts from the ruthenated species. The ruthenium concentration was

quantified by UV-vis (ε_{456} = 14,500 $M^{-1}cm^{-1}$). [Ru-C_9-Ad-OH]Cl_2 was diluted to 10 μM in acetonitrile, and its purity confirmed by electrospray mass spectroscopy (Figure 4.4).

Attempted Light-activated Hydroxylation of [Ru-C_9-Ad]. Steady-state visible irradiation of a 4 mL solution (20 mM potassium phosphate buffer, 100 mM KCl, pH = 7.4) containing 10 μM P450, 10 μM [Ru-C_9-Ad]Cl_2, and 100 μM catalase was performed for two hours. The Ru-complex was extracted as described above and analyzed by ESI.

Electrospray Mass Spectroscopy. Samples (~ 10 μM) contained in a 500 μL Hamilton syringe were injected at a rate of 5 μL/min into the LcQ (Finnigan Mat); typical runs required less than 100 μL per sample, and data sets were averages of 50 scans.

Calibration of ESI. A 10 μM stock solution of [Ru-C_9-Ad]Cl_2 in acetonitrile was combined with 10 μM [Ru-C_9-Ad-OH]Cl_2 in varying proportions (4:1 to 1:4). Each solution was injected three different times, with intermediary blank runs of pure acetonitrile. Relative peak intensities were determined using analysis software, which deconvolved the spectra to assign one singly charged peak to each compound. A calibration graph (Figure 4.5) was generated from this data which showed that the ionization efficiency of Ru-C_9-Ad and Ru-C_9-Ad-OH were identical (slope = 0.96) within

Figure 4.4. ESI mass spectra showing the doubly charged starting material, $[Ru\text{-}C_9\text{-}Ad]^{2+}$ barely visible on the left, and the conversion to products, $[Ru\text{-}C_9\text{-}Ad\text{-}OH]^{2+}$, on the right.

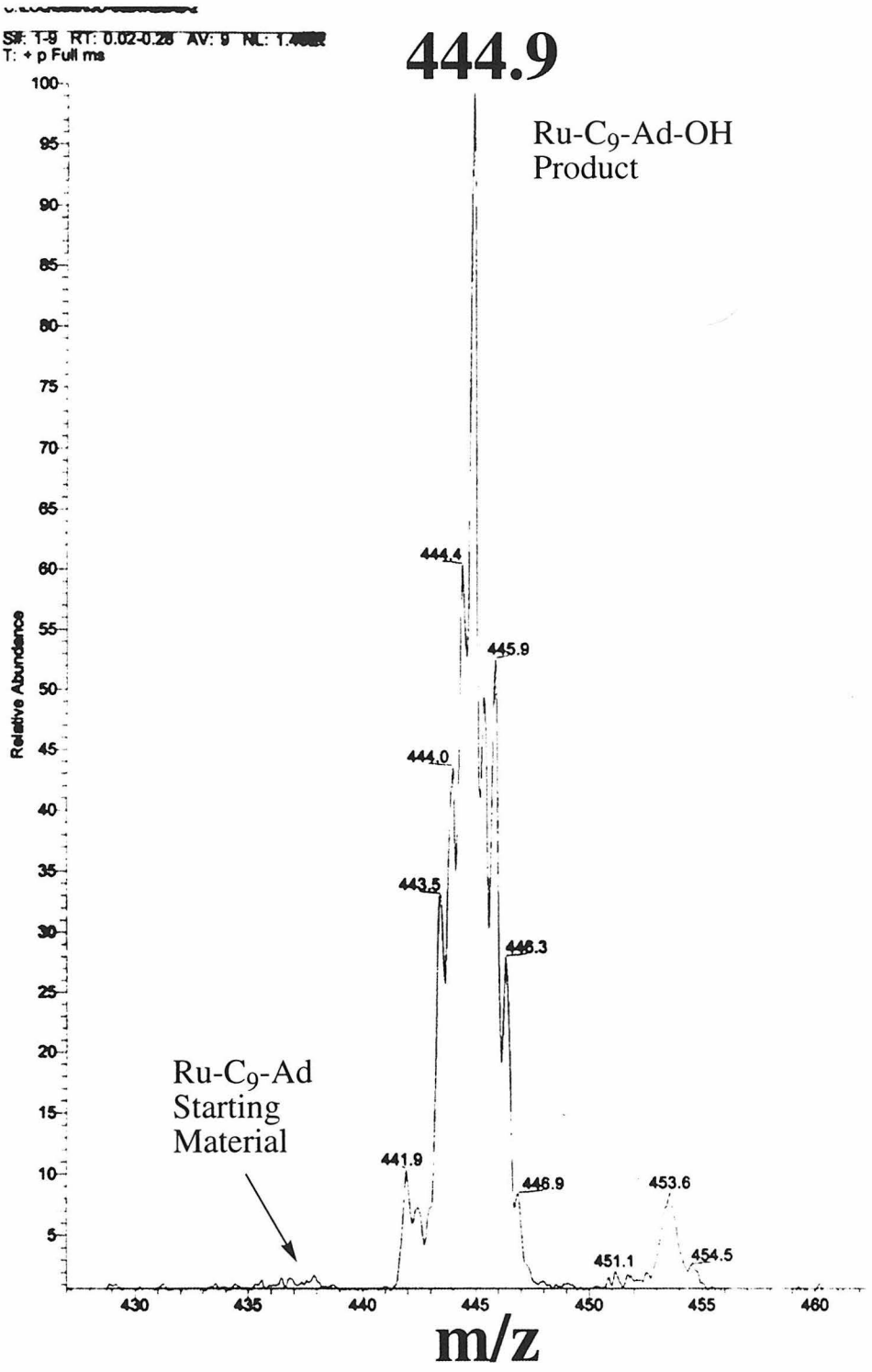
444.9
Ru-C9-Ad-OH
Product
Ru-C9-Ad
Starting
Material
Relative Abundance
m/z
444.4
445.9
444.0
443.5
446.3
441.9
446.9
453.6
451.1
454.5

Figure 4.5. Calibration line showing the relationship between the ratio of $[Ru\text{-}C_9\text{-}Ad]^{2+}$ / $[Ru\text{-}C_9\text{-}Ad\text{-}OH]^{2+}$ in solution to the relative ionization intensity of both cations in the ESI.

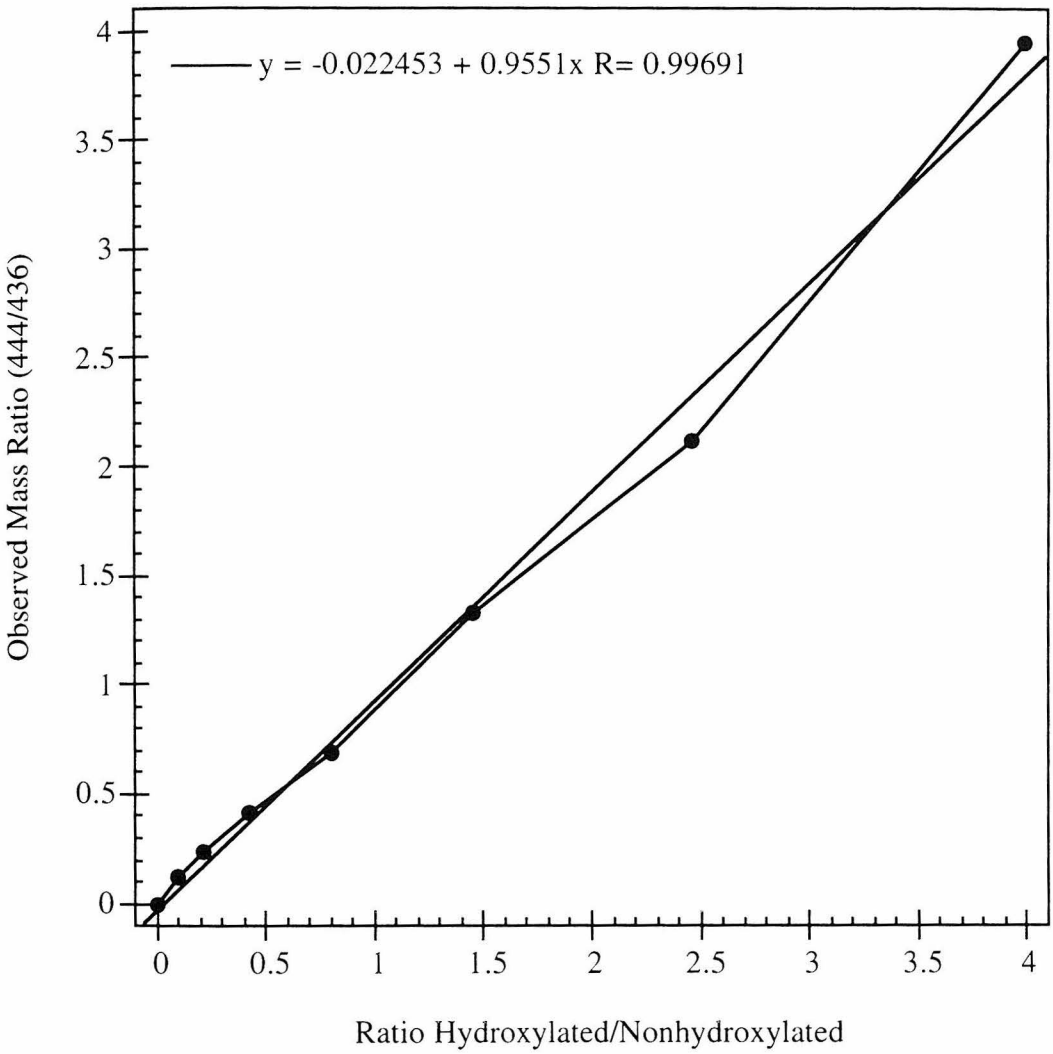
y = -0.022453 + 0.9551x R= 0.99691
Observed Mass Ratio (444/436)
Ratio Hydroxylated/Nonhydroxylated
0
0.5
1
1.5
2
2.5
3
3.5
4

experimental error. This information was crucial in quantifying hydroxylated product yields relative to starting material in the analysis of subsequent turnover experiments.

Monitoring O_2/NADH Consumption. The oxygen electrode was calibrated at 20 °C (linear response with $[O_2]$, 0-100% O_2), and connected to a LeCroy oscilloscope interfaced to a PC using freely available LeCroy software. The O_2 electrode (3 mm diameter with Teflon casing) was pushed through a septum, which formed an airtight seal with the mouth of a standard 1 cm pathlength cuvette. The quality of the seal was tested by filling the cuvette with deoxygenated buffer and monitoring oxygen concentration; insignificant leakage was observed during 1 hour. All UV-vis experiments were conducted with stirred samples at 20 °C. Kinetics experiments were run in kinetics mode (Biosym) with 1 mL samples containing 1 μM PdR, 10 μM Pd, 1 μM P450, and either 50 μM $[Ru\text{-}C_9\text{-}Ad]Cl_2$ or 1 mM adamantane. Experiments were initiated upon addition of 200 μM NADH, and absorbance at 340 nm was measured simultaneously with O_2 consumption.

Enzyme Turnover of Camphor. A 4 mL solution (20 mM potassium phosphate buffer, 100 mM KCl, pH = 7.4) was prepared containing 1 μM P450, 1 μM PdR, 10 μM Pd, 400 μM camphor, and 200 μM NADH (ε = 6.22 $M^{-1}cm^{-1}$ @ 340 nm). The consumption of

NADH was monitored at 340 nm by UV-vis spectroscopy and O_2 consumption monitored with the microelectrode. Once all of the NADH was consumed, a known amount of 3-*endo*-bromocamphor was added, and the mixture was extract three times with an equal volume of methylene chloride. The organic extract was concentrated by evaporation and analyzed by GC.

GC-MS. Samples were analyzed by a VG 7070E mass spectrometer in line with an HP 5700 gas chromatograph equipped with a 30-m HP-1 capillary column (0.25 mm inner diameter, film thickness 0.25 μm) and interfaced with a PC. The organic extract was loaded onto the column at 40 °C, and eluted with a standard program (40 °C – 150 °C, 40 °C/min; 150 °C – 250 °C, 15 °C/min).

RESULTS

Resonance Raman Studies of P450 Fe^{2+}-CO:Substrate Complexes

As shown in Figure 4.6 and as was reported previously (17), the CO-stretching mode in the P450-carbon monoxide complex is quite sensitive to the nature of the substrate. This indicates a direct interaction between the bound CO and the substrate

Figure 4.6. Variation of the resonance Raman Fe^{2+}-(CO) stretching mode with substrate. Spectra for Ru-C_{11}-Ad, Ru-C_9-Ad, and adamantane differ little, varying by only a few cm^{-1} in their peak maximum.

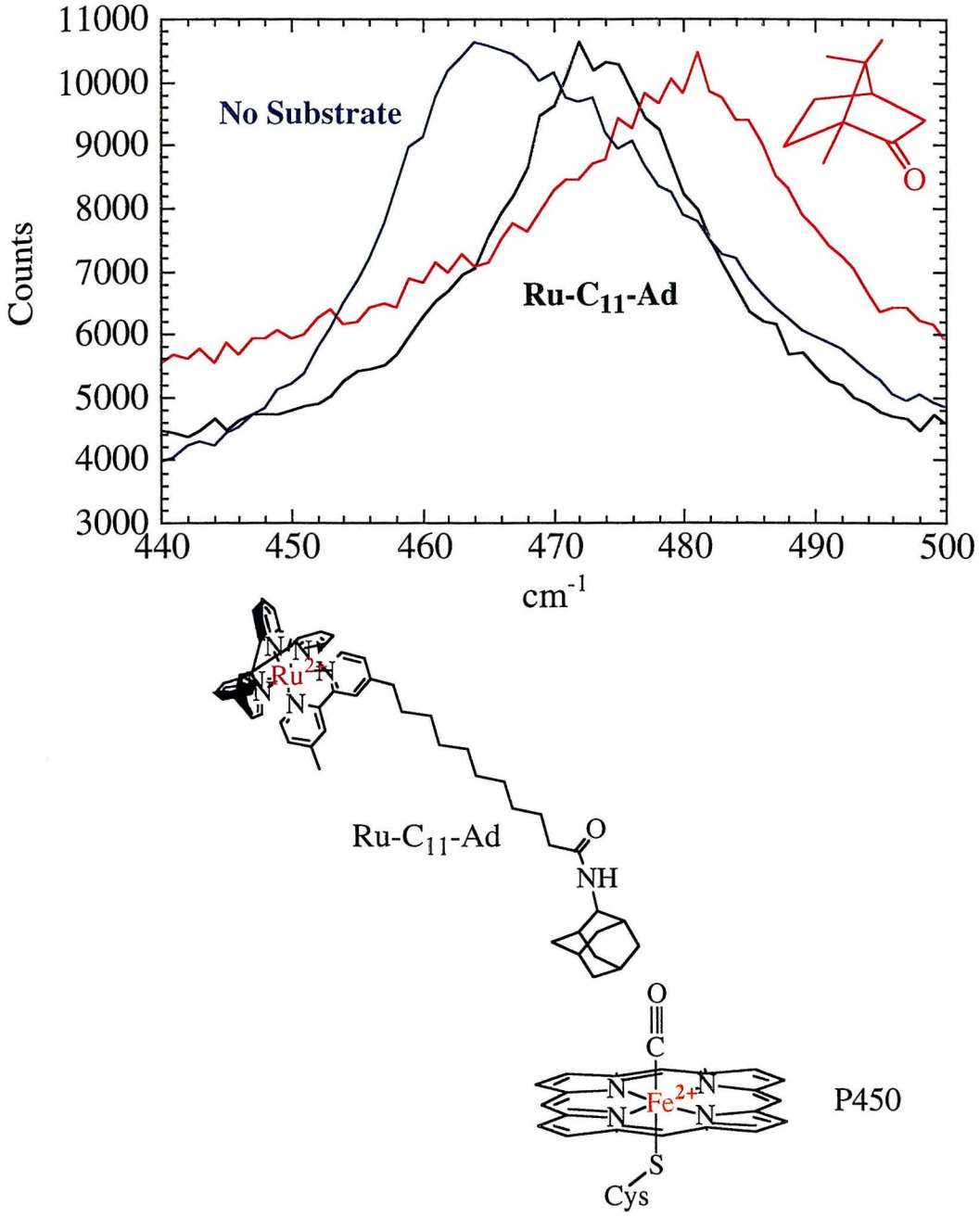
11000
10000
9000
8000
7000
6000
5000
4000
3000
Counts
No Substrate
Ru-C11-Ad
O
440
450
460
470
480
490
500
cm-1
Ru2+
Ru-C11-Ad
O
NH
O
C
Fe2+
S
Cys
P450

Table 4.1. Substrate Analog Induced Changes of the CO-Stretching Mode in P450

Substrate	ν Fe-(CO)[a]
None	463[b]
Ru-C_{11}-Ad	472
Ru-C_9-Ad	474
Adamantane	476
Camphor	482[b]

[a]All units are in cm^{-1}.

[b]These values are in good agreement with published values for substrate-free (465 cm^{-1}) and camphor-bound P450 (484 cm^{-1}) (19).

molecule which agrees with IR absorption work of O'Keefe et al. (24). Camphor-bound Fe^{2+}-CO P450 has ν_{CO} ~ 1940 cm^{-1} and camphor-free has two bands at ~1942 cm^{-1} and 1963 cm^{-1} which have been assigned to a bent and upright geometry, respectively. The Fe-(CO) stretching frequency differs by 4 cm^{-1} between Ru-C_{11}-Ad, Ru-C_9-Ad, and adamantane, suggesting that these substrates bind with slightly increasing proximity to the heme (Table 1). The fact that these stretching frequencies (472-476 cm^{-1}) are approximately midway between those found for substrate-free and camphor-bound suggests that CO is bound mostly upright in solution. The similarity between the binding modes of Ru-Ad compounds and adamantane in solution agrees with the X-ray structure determination.

Kinetics and Efficiency of Ru-C_9-Ad and 2-Adamantylacetamide Hydroxylation

By supplying electrons to P450 via the natural route (NADH-->PdR-->Rd-->P450), the rate of Ru-C_9-Ad hydroxylation was found to be 10 $\pm$ 2 μmol NADH/min/μmol P450 (Figure 4.7). The error in the rate measurement stemmed mostly from the choice of data points--the rate appeared fastest at the earliest time points, as is generally observed for enzyme-mediated catalysis. This rate is remarkably slower than the consumption of NADH in the absence of any substrate (30 μmol NADH/min/μmol P450, Figure 4.7). These data suggest that P450 oxidase chemistry (conversion of O_2 into

Figure 4.7. Top: Rate of NADH consumption in turnover studies of Ru-C_9-Ad. The slope indicates a rate of 8 μmol NADH/min/μmol P450. Bottom: Control experiment showing the rate of NADH consumption (~ 30 μmol NADH/min/μmol P450) in the absence of any substrate.

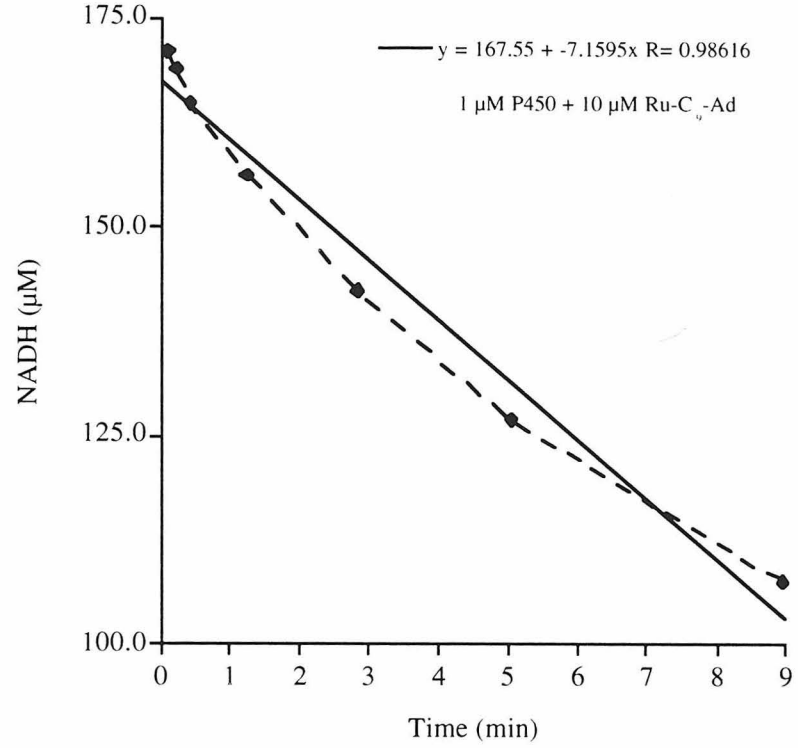
y = 167.55 + -7.1595x R= 0.98616
1 µM P450 + 10 µM Ru-C -Ad
NADH (µM)
175.0
150.0
125.0
100.0
0
1
2
3
4
5
6
7
8
9
Time (min)

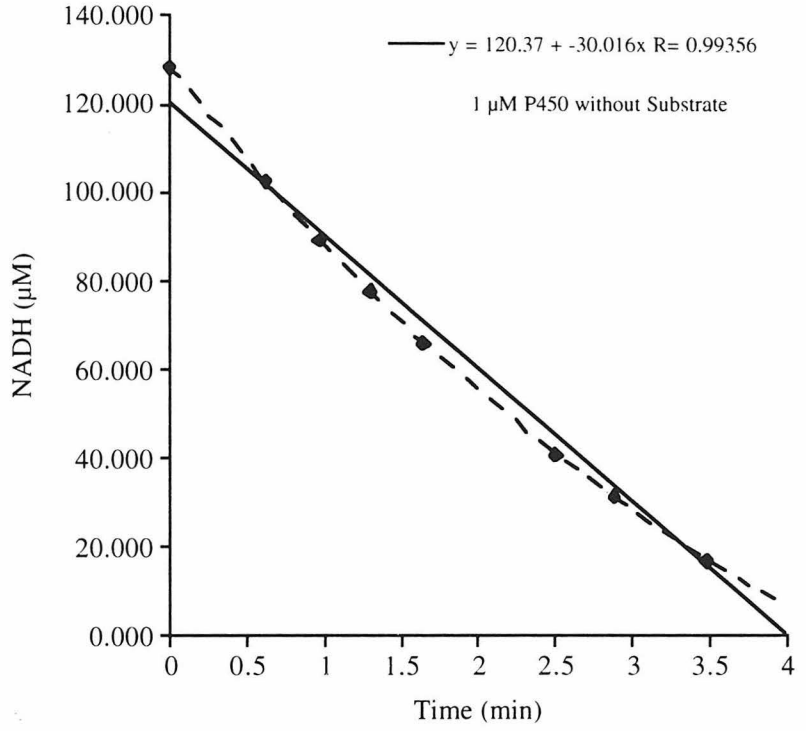
y = 120.37 + -30.016x R= 0.99356
1 µM P450 without Substrate
NADH (µM)
140.000
120.000
100.000
80.000
60.000
40.000
20.000
0.000
0
0.5
1
1.5
2
2.5
3
3.5
4
Time (min)

water) outcompetes the slow hydroxylation of Ru-C_9-Ad threefold, which should greatly limit the yield of product formation. In a control experiment with NADH/PdR/Pd and no P450, the rate was found to be roughly 1 μmol NADH/min, thus most of the observed NADH decay may be attributed to P450-mediated catalysis. Product assays indeed show that the yield of hydroxylated product, Ru-C_9-Ad-OH, is only 10% based on the starting NADH concentration. Just based on the competing oxidase activity, the maximum predicted yield of hydroxylated product would be ~ 25%. Thus, a 10% product yield is effectively a 40% yield based on the background oxidase activity.

The rate of 2-adamantylacetamide (**2**) hydroxylation was found to be 90 ± 20 μmol NADH/min/μmol P450, in good agreement with the literature value for 1-adamantylacetamide (~ 110 μmol NADH/min/μmol P450) (25). This hydroxylation rate is roughly ten times faster than that of Ru-C_9-Ad, which is not surprising in light of the fact (**2**) produces a 95% spin conversion of the heme, compared to only 25% for Ru-C_9-Ad. The hydroxylation of Ru-C_9-Ad may also be slowed by the conformational changes observed in Asp 251 and Thr 252, which could affect the delivery of protons leading to dioxygen scission.

The ratio of product formation/NADH consumption with 2-adamantylacetamide is only 47 ± 3%, however, which is half that reported for 1-adamantylacetamide (25). Thus, these results show that hydroxylation of the model compound, 2-

adamantylacetamide, while much faster than Ru-C_9-Ad, occurs with roughly the same efficiency when the background oxidase activity has been subtracted.

Light-activated Ru-C_9-Ad Hydroxylation

Having established that Ru-C_9-Ad turnover is possible via the biological ET route, numerous attempts were made to effect enzyme turnover through steady-state visible irradiation of P450:Ru-C_9-Ad in the presence of *para*-methoxydimethylaniline and dioxygen. Precautions were taken to minimize photodegradation: a 450 nm cutoff filter was used to shield the sample from UV light, and most experiments were conducted at 4 °C to minimize sample heating and to decelerate P420 formation. In addition, experiments were conducted in the presence of catalase to eliminate H_2O_2 which would both damage the enzyme and hydroxylate adamantane, giving a false positive result. Preliminary results suggest that oxidized products are formed in this reaction (Figure 4.8).

Energy-Transfer Measurements Identifying a P450:Camphor:Ru-C_{10} Ternary Complex

Titration of camphor into a stoichiometric (5 μM) solution of P450 and Ru-C_{10} was monitored by UV-vis and energy-transfer measurements, as described in

Figure 4.8. Electrospray mass spectrum showing a possible oxidized Ru-C_9-Ad product isolated after photolysis of the P450:Ru-C_9-Ad complex. Zooming in on this species shows it is doubly charged and has a similar profile to the spectrum of hydroxylated Ru-C_9-Ad, shown in Figure 4.4.

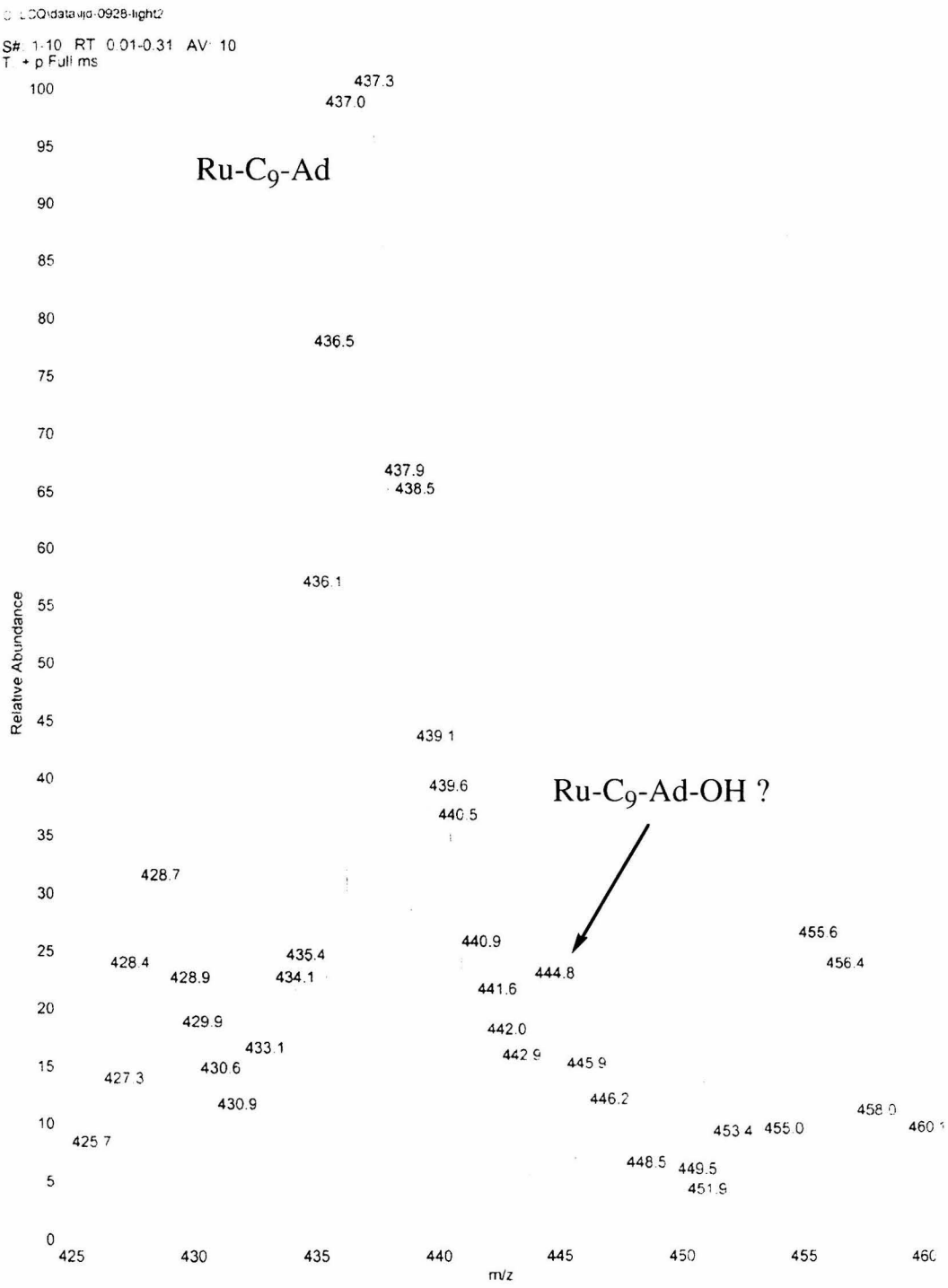
S# 1-10 RT 0.01-0.31 AV 10
T + p Full ms
Ru-C9-Ad
Ru-C9-Ad-OH ?
Relative Abundance
m/z
437.3
437.0
436.5
437.9
438.5
436.1
439.1
439.6
440.5
428.7
428.4
428.9
435.4
434.1
429.9
433.1
430.6
427.3
430.9
425.7
440.9
444.8
441.6
442.0
442.9
445.9
446.2
455.6
456.4
453.4
455.0
458.0
448.5
449.5
451.9

Figure 4.9. A two substrate, ternary binding model for the P450 (E):camphor (C): Ru-C_{10} (R) system.

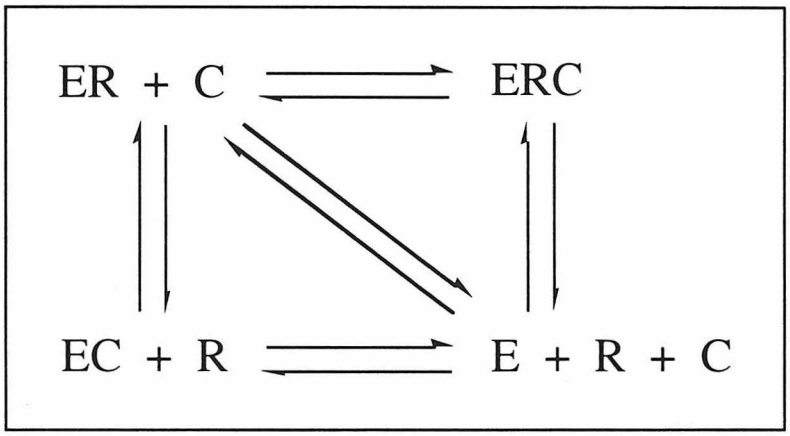
ER + C
ERC
EC + R
E + R + C

Chapters 2-3. The binding of camphor to this P450:Ru complex (K_D = 3.6 ± 0.2 μM) is virtually the same as that observed for P450 alone (K_D = 3.1 ± 0.2 μM, Chapter 3) (26). Additionally, a full low-to-high spin conversion of the heme is observed upon camphor titration. These results indicate that Ru-C_{10} does not perturb camphor binding at the active site. Confirmation of ternary complex formation came from Ru^{2+*} decay profiles at varying camphor concentrations which showed only modest changes in the fraction of quenched Ru^{2+*} emission. The "two-substrate ternary binding model" is shown in Figure 4.9.

The persistence of roughly 25% bound (quenched) $[Ru\text{-}C_{10}]^{2+*}$ at high camphor concentrations represents half of the originally bound Ru (~ 50%, K_D ~ 2 μM), and indicates that the affinity of Ru-C_{10} for the P450:camphor complex (K_D ~ 10 μM) is not greatly different than for P450 alone. The presence of three distinct quenching processes became evident upon fitting the emission profile to a tri-exponential decay; constraining the fit to three distinct rate constants improved the fitting considerably and gave the consistently best chi^2 values. Weighting the relative coefficients gave the percentage of Ru-C_{10} in each phase (Figure 4.10).

Kinetics and Efficiency of Camphor Hydroxylation in the Ternary Complex

Figure 4.10. The coefficients corresponding to the three different states of Ru (free, bound to P450 alone, or bound in the ternary complex) as a function of camphor concentration. The rate of decay, k_d, of unbound Ru^{2+*} in aerated solution was determined: $k_d = 2.5 \times 10^6\ s^{-1}$. The rate of Ru^{2+*} decay when bound to P450 was found to be $k_{P450} = 9.8$ x 106 s^{-1}. Finally, the Ru^{2+*} emission is considerably longer-lived in the ternary complex, decaying with the rate constant $k_{tern} = 7.8 \times 10^6\ s^{-1}$. The relative percentage of each component can be calculated by dividing one coefficient by the sum of all of the coefficients.

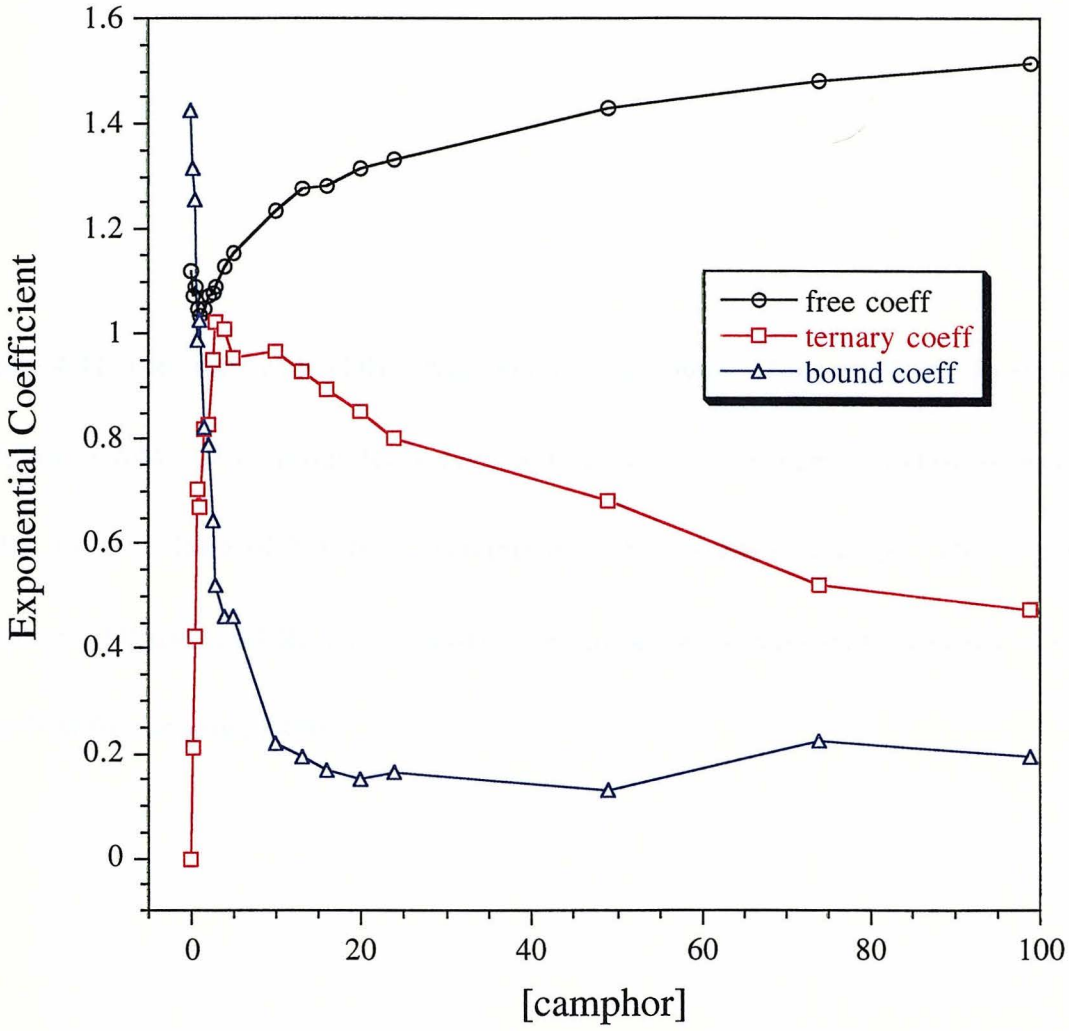
Exponential Coefficient
[camphor]
free coeff
ternary coeff
bound coeff
0
0.2
0.4
0.6
0.8
1
1.2
1.4
1.6
0
20
40
60
80
100

Figure 4.11. Top: Rate of NADH consumption in the complex between P450 (1 μM) and camphor (1 mM). The initial decay rates were typically ~ 600 μmol NADH/min/μmol P450. Bottom: Rate of NADH consumption in the complex between P450 (1 μM), camphor (100 μM) and Ru-C_{10} (10 μM). The initial decay rates were typically ~ 300 μmol NADH/min/μmol P450.

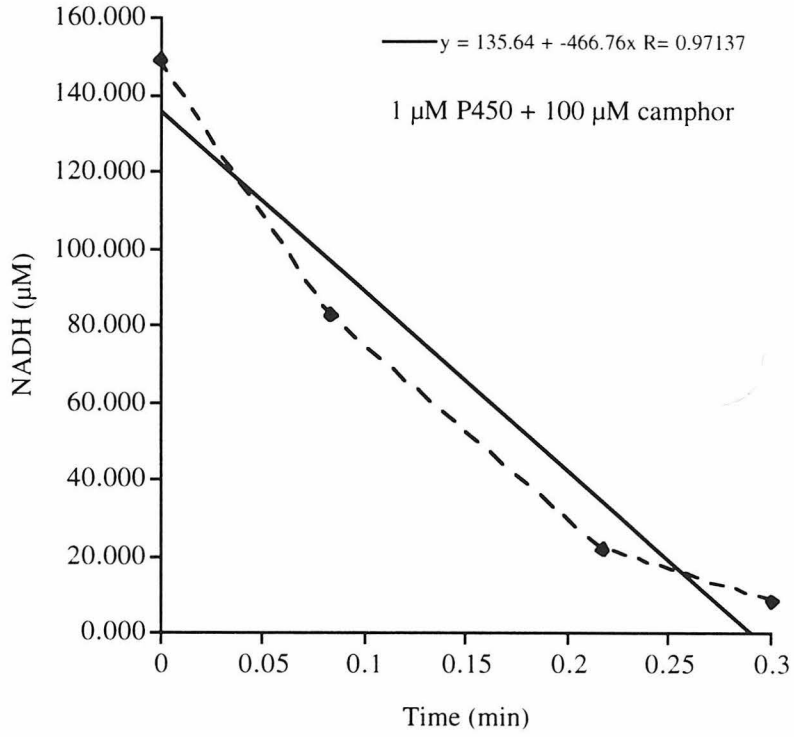
y = 135.64 + -466.76x R= 0.97137
1 μM P450 + 100 μM camphor
NADH (μM)
160.000
140.000
120.000
100.000
80.000
60.000
40.000
20.000
0.000
0
0.05
0.1
0.15
0.2
0.25
0.3
Time (min)

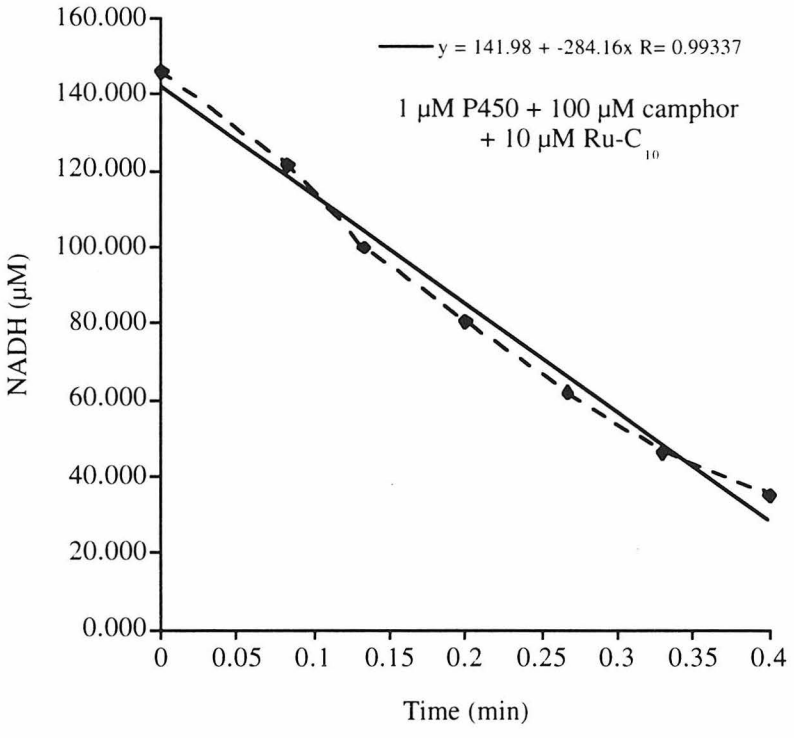
y = 141.98 + -284.16x R= 0.99337
1 μM P450 + 100 μM camphor
+ 10 μM Ru-C10
NADH (μM)
160.000
140.000
120.000
100.000
80.000
60.000
40.000
20.000
0.000
0
0.05
0.1
0.15
0.2
0.25
0.3
0.35
0.4
Time (min)

The rate of NADH consumption was found to be ~ 600 μmol NADH/min/μmol P450, in good agreement with literature values (27,28). The addition of Ru-C_{10} (10 equivalents relative to enzyme) was found to decrease the rate of hydroxylation to approximately 300 μmol NADH/min/μmol P450 (Figure 4.11). Further experiments with varying concentrations of Ru-C_{10} will determine the extent to which the Ru-substrate inhibits camphor turnover.

DISCUSSION

The result that the yield of hydroxylated 2-adamantylacetamide is only half that observed with 1-adamantylacetamide may shed insight on the positioning of critical residues at the active site. While only a small perturbation of the substrate, moving the amide may greatly affect its ability to hydrogen bond with Asp 251 and Thr 252. The movement of these amino acids has been shown to stabilize water molecules at the active site (1,15) and may affect the delivery of protons necessary for efficient coupling. Repositioning the amide of Ru-C_9-Ad would be predicted to double the yield of hydroxylation. The design of bulkier Ru-substrates which displace water from the pocket in the open conformation should also promote hydroxylation chemistry.

P450 hydroxylates most substrates, including adamantane, much more slowly than camphor, most likely because solvation of the heme lowers the reduction potential for the first electron transfer. In most cases, ET is rate limiting in the substrate hydroxylation reaction. The fact that camphor displaces water and converts the heme to high spin in the presence of Ru-C_{10} indicates that the reduction potential should be unchanged in the ternary complex. The factors controlling the overall efficiency of the hydroxylation reaction are not completely understood. Almost 100% coupling and high stereoselectivity in the reaction with camphor has been attributed to the substrate's tight binding (K_D ~ 1 μM), a hydrogen bond with Tyr 96 and hydrophobic contacts with the protein that orient the molecule correctly.

The finding that the rate of NADH consumption during camphor hydroxylation was roughly halved in the ternary complex invites several different explanations. Changes in the reduction potential of the heme, greater solvent access leading to uncoupling, or inactivation of the enzyme in the ternary complex are all possible explanations. Monitoring NADH consumption as a function of the concentration of ternary complex (which is a function of Ru-C_{10} concentration), as well as quantification of the uncoupling yields will elucidate this rate discrepancy.

It is interesting to note that the conditions for achieving crystallization of the open enzyme - high ionic strength (100 mM NaOAc, 200 mM NH_4OAc), and low solvent

dielectric (~ 10% PEG 8000) – have been shown in other work to destabilize the salt bridges holding the F-G loop (2,29). "Loosening" the channel in this way has been shown to be similar to changing Asp 251 to asparagine (30). Normally, P450 is crystallized in the presence of 0.25 M KCl, with potassium stabilizing the substrate bound in the closed conformation (11). Therefore, replacement of K^+ with Na^+, should disfavor the closed conformation. Furthermore, the finding that the crystals nucleated best at 4 °C mirrors the thermodynamics of camphor binding to the Asp251Asn (31); the association constant for camphor (ln K_{eq} ~ 14.2) decreases above 15 °C for this mutant. This behavior is in marked contrast to WT P450, in which the association constant for camphor (ln K_{eq} ~ 14.2) decreases *below* 15 °C (32). The perturbation of the bifurcated salt bridge upon Ru-C_9-Ad binding changes the thermodynamics of substrate binding and appears to dictate the conditions under which the complex crystallizes.

CONCLUSION

Open P450 structures have been shown to hydroxylate both natural and unnatural substrates with appreciable rates and yields. This work represents the first study of P450 in this solvent exposed conformation, and will potentially shed light on important

mechanistic questions regarding amino acid conformational changes and the delivery of protons associated with dioxygen activation. Although the enzyme is optimized for the substrate camphor, P450 exhibits considerable flexibility in the range of molecules it binds and oxidizes.

In addition, these energy-transfer studies have identified one of the first examples of a ternary complex in cytochrome P450. Energy transfer provides a sensitive tool for studying complex P450:substrate interactions in solution. This technique can yield significant structural information about P450 active sites in the absence of a crystal structure. The large size and hydrophobic nature of P450 substrate channels makes multiple substrate binding a likely event during catalysis.

Finally, optimizing Ru-substrates for binding affinity and turnover efficiency are two very different problems, and efforts have only just begun to address the issues raised in this chapter concerning the accommodation of important catalytic residues at the active site. The goal of designing Ru-substrates for enzyme photoactivation will require a synergy of both important aspects of P450 catalysis.

REFERENCES AND NOTES

1. I. J. Dmochowski, B. R. Crane, J. J. Wilker, J. R. Winkler, H. B. Gray, *Proc. Natl. Acad. Sci. USA* **96**, 12987-12990 (1999).

2. E. Deprez, et al., *Biochemistry* **33**, 14464-14468 (1994).

3. S. S. Boddupalli, et al., *Proc. Natl. Acad. Sci. USA* **89**, 5567-5571 (1992).

4. G. E. Arnold, R. L. Ornstein, *Biophys. J.* **73**, 1147-1159 (1997).

5. H. Y. Li, T. L. Poulos, *Nat. Struct. Biol.* **4**, 140-146 (1997).

6. I. F. Sevrioukova, H. Y. Li, H. Zhang, J. A. Peterson, T. L. Poulos, *Proc. Natl. Acad. Sci. USA* **96**, 1863-1868 (1999).

7. H. Joo, L. Zhanglin, F. H. Arnold, *Nature* **399**, 670-673 (1999).

8. J.-A. Stevenson, A. C. G. Westlake, C. Whittock, L.-L. Wong, *J. Am. Chem. Soc.* **118**, 12846-12847 (1996).

9. T. I. Oprea, G. Hummer, A. F. Garcia, *Proc. Natl. Acad. Sci. USA* **94**, 2133-2138 (1997).

10. T. L. Poulos, B. C. Finzel, A. J. Howard, *Biochemistry* **25**, 5314-5322 (1986).

11. T. L. Poulos, B. C. Finzel, A. J. Howard, *J. Mol. Biol.* **195**, 687-700 (1987).

12. C. DiPrimo, S. G. Sligar, G. H. B. Hoa, P. Douzou, *FEBS Letters* **312**, 252-254 (1992).

13. M. Vidakovic, S. G. Sligar, H. Y. Li, T. L. Poulos, *Biochemistry* **37**, 9211-9219 (1998).

14. C. DiPrimo, E. Deprez, G. H.-B. Hoa, P. Douzou, *Biophys. J.* **68**, 2056-2061 (1995).

15. I. Schlichting, et al., *Science* **287**, 1615-1622 (2000).

16. O. Bangcharoenpaurpong, P. M. Champion, S. A. Martinis, S. G. Sligar, *J. Chem. Phys.* **87**, 4273-4284 (1987).

17. C. Jung, G. H. B. Hoa, K.-L. Schroeder, M. Simon, J. P. Doucet, *Biochemistry* **31**, 12855-12862 (1992).

18. T. Uno, Y. Nishimura, R. Makino, T. Iizuka, Y. I. Tsuboi, *J. Biol. Chem.* **260**, 2023-2026 (1985).

19. A. V. Wells, P. Li, P. M. Champion, *Biochemistry* **31**, 4384-4393 (1992).

20. J. A. Peterson, M. C. Lorence, B. Amarneh, *J. Biol. Chem.* **265**, 6066-6073 (1989).

21. P. W. Roome, J. C. Philley, J. A. Peterson, *J. Biol. Chem.* **258**, 2593-2598 (1983).

22. C. A. Tyson, J. D. Lipscomb, I. C. Gunsalus, *J. Biol. Chem.* **247**, 5777-5784 (1972).

23. M. J. Hintz, D. M. Mock, L. L. Peterson, K. Tuttle, J. A. Peterson, *J. Biol. Chem.* **257**, 14324-14332 (1982).

24. D. H. O'Keefe, R. E. Ebel, J. A. Peterson, J. C. Maxwell, W. S. Caughey, *Biochemistry* **17**, 5845-5852 (1978).

25. J. J. D. Voss, P. R. Ortiz de Montellano, *J. Am. Chem. Soc.* **117**, 4185-4186 (1995).

26. E. J. Mueller, P. J. Loida, S. G. Sligar, in *Cytochrome P450: Structure, Mechanism, and Biochemistry, 2nd edn* P. R. Ortiz de Montellano, Ed. (Plenum Press, New York, 1995) pp. 83-124.

27. W. A. Atkins, S. G. Sligar, *J. Am. Chem. Soc.* **109**, 3754-3760 (1987).

28. P. J. Loida, S. G. Sligar, *Biochemistry* **32**, 11530-11538 (1993).

29. V. Lounnas, R. C. Wade, *Biochemistry* **36**, 5402-5417 (1997).

30. C. DiPrimo, E. Deprez, S. G. Sligar, G. H. B. Hoa, *Biochemistry* **36**, 112-118 (1997).

31. N. C. Gerber, University of Illinois (1993).

32. B. W. Griffin, J. A. Peterson, *Biochemistry* **11**, 4740-4746 (1972).

Chapter 5

Submillisecond Photooxidation and Reduction of Cytochrome P450 via Sensitizer-linked Substrates[‡]

[‡]Adapted from J. J. Wilker, I. J. Dmochowski, J. H. Dawson, J. R. Winkler, H. B. Gray, *Angew. Chem. Int. Ed.* **38**, 90-92 (1999).

Acknowledgement:

Jon Wilker synthesized many of the ruthenium compounds and helped with most of the experiments described in this chapter. Also, many thanks go to John Dawson for discussions relating to P450-substrate interactions and to Mary Lamczyk in his lab for providing P450 for initial studies.

INTRODUCTION

Rigorous characterization of metalloenzyme oxidation states is essential to understanding metabolic processes at a molecular level. Reactive intermediates in enzymatic catalysis are of special interest, but they are frequently too short-lived to be examined directly. A case in point is the high-valent heme that is believed to be a catalytic intermediate in the oxygenation reactions of cytochrome $P450_{cam}$ (P450) (1, 2). This oxidant has eluded detection thus far, raising questions concerning its role in the catalytic cycle (1, 3).

We have shown previously that reactive high-valent hemes of peroxidases can be prepared in solutions containing photogenerated ruthenium-diimine oxidizing agents (4, 5). Formation of $[Ru(bpy)_3]^{3+}$ via the flash-quench approach oxidizes the heme of both horseradish peroxidase (HRP) and microperoxidase-8 (MP-8) in less than a microsecond (Eq. 1abc). In both heme systems, electron transfer is observed to occur from the iron to

$$Ru(bpy)_3^{2+} \xrightarrow{h\nu} Ru(bpy)_3^{2+*} \quad \textbf{(a)}$$

$$Ru(bpy)_3^{2+*} + Ru(NH_3)_6^{3+} \longrightarrow Ru(bpy)_3^{3+} + Ru(NH_3)_6^{2+} \quad \textbf{(b)}$$

$$Ru(bpy)_3^{3+} + (P)Fe^{III}\text{-}OH_2 \longrightarrow (P^{\bullet+})Fe^{III}\text{-}OH_2 / (P)Fe^{IV}{=}O + 2\,H^+ + Ru(bpy)_3^{2+} \quad \textbf{(c)}$$

the oxidized porphyrin (Eq. 1c). HRP, however, achieves a twice oxidized state after reaction with a second equivalent of $Ru(bpy)_3^{3+}$. This compound I, $(P^{\bullet+})Fe^{IV}=O$, species can be observed either under steady-state conditions, or be generated in a time resolved fashion by starting with the ferryl, compound II species (Figure 5.1).

From examining the P450 catalytic cycle (Chapter 1), it would seem possible to generate reactive intermediates from both the forward (reductive) and reverse (oxidative) directions. Analagous to the peroxidase photooxidation described above, Ru^{3+} could first oxidize either the P450 iron or porphyrin (these relative oxidation potentials may be different for thiolate-ligated hemes), and by subsequent one-electron, two-proton (water-splitting) reactions achieve the compound I state. Our attempts to use the same bimolecular approach with P450 failed, however, owing in part to the inefficiency of electron transfer (ET) between external redox agents and a deeply buried heme.

Presented in this chapter is a new photochemical method for the delivery of both electrons and holes to buried redox sites. By tethering a Ru-photosensitizer to a protein substrate, we have succeeded in reducing the P450 heme much more rapidly than has been possible previously, and we have also generated a hitherto unobserved oxidized state of the enzyme. The strategy of linking sensitizers to substrates opens the door to exploration of reactive redox states in enzyme interiors.

Figure 5.1. Oxidative flash-quench scheme by which HRP is oxidized to the compound I state. These chemistries, and the oxidation states shown, serve as a model for possible high-valent intermediates in oxygenases, such as P450.

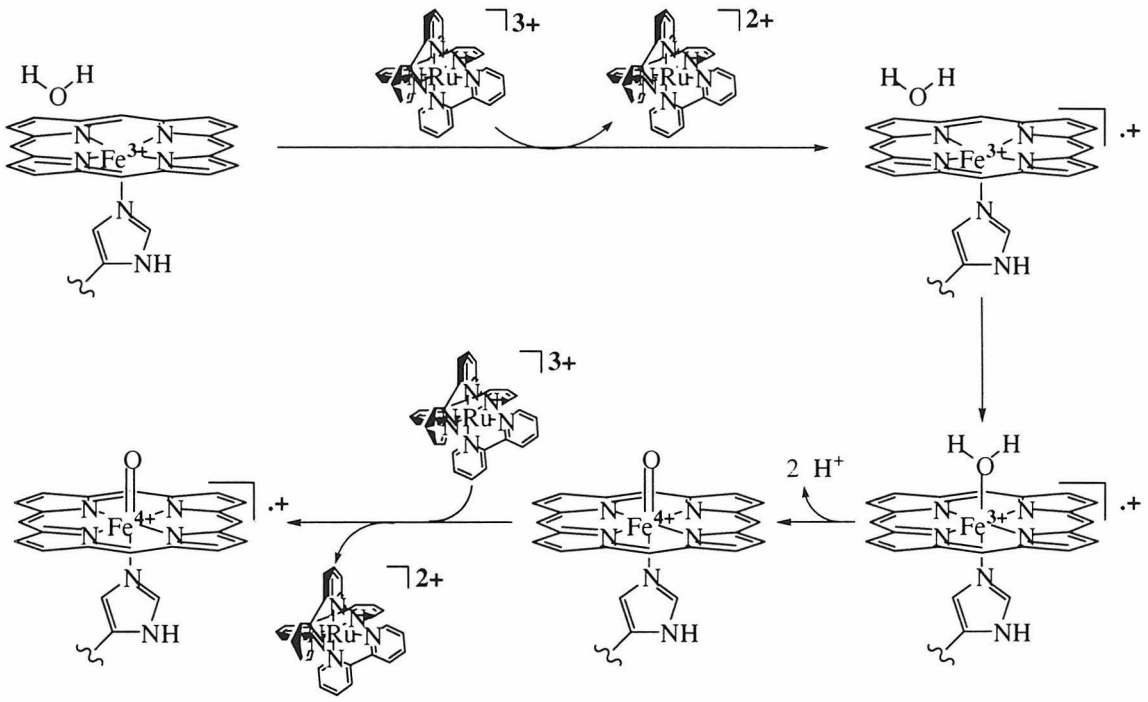

Compound I *Compound II*

We described previously (Chapters 1-4) how the photosensitizer $[Ru(bpy)_3]^{2+}$ is linked by a hydrocarbon chain to a species with high affinity for the P450 heme pocket: imidazole (Im), adamantane (Ad) or ethyl benzene (EB) (6) (Figure 5.2). Imidazole may ligate the heme iron directly (7), whereas the substrates adamantane (8) and ethyl benzene (9) bind strongly to the hydrophobic active site cavity. Adamantanone displaces ligated water from the enzyme active site, $[P_{cys}Fe^{3+}\text{-}OH_2]$ (P_{cys} is the cysteine thiolate-ligated protoporphyrin IX of P450), to yield five-coordinate $[P_{cys}Fe^{3+}]$ (10). Ethyl benzene binding, in contrast, leaves the six-coordinate resting state relatively unperturbed.

Addition of stoichiometric Ru-Ad to ferric P450 shifts the Soret absorption maximum from 417 to 415 nm and creates a shoulder at 391 nm, indicating binding of the adamantyl moiety in the heme region (11). This peak shift is attributed to lengthening of the $Fe^{III}\text{-}OH_2$ bond or partial water displacement from the $[P_{cys}Fe^{3+}\text{-}OH_2]$ resting state, both of which accompany the binding of adamantyl compounds in the heme cavity (12). In addition to this absorbance change, there is a decrease in the excited state (Ru^{2+*}-Ad) lifetime (13) that has been attributed to quenching by a Förster energy-transfer process. The normally monophasic luminescence decay profile of Ru^{2+*}-Ad (k_{1decay} = 2.2 x 10^6 s^{-1}) becomes biphasic (k_{1decay} = 2.2 x 10^6 s^{-1}, k_{2decay} = 7.7 x 10^6 s^{-1}) in the presence of P450, with the faster phase accounting for 77% of Ru^{2+*} quenching.

Figure 5.2. Sensitizer-linked substrates (Ru-Ad, Ru-EB) and ligands (Ru-Im) for photooxidation and reduction of P450.

Ru-Im

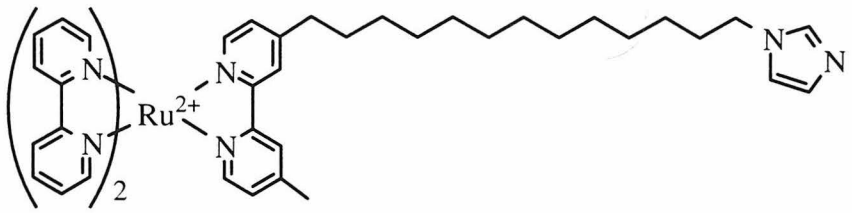

Ru-Ad

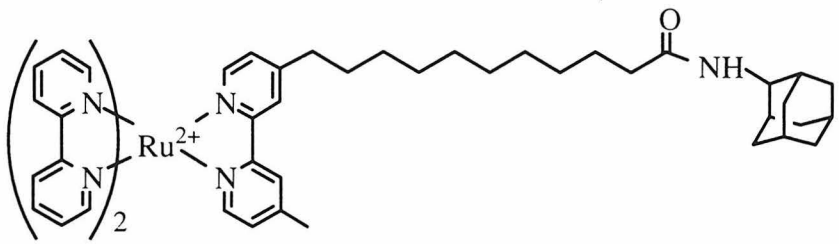

Ru-EB

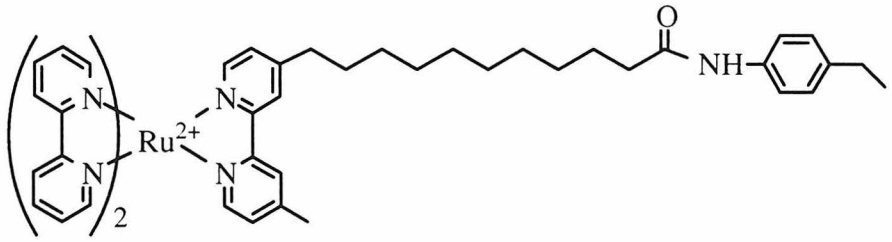

We attribute the rapid luminescence decay (k_{2decay}) to Ru-Ad-P450 interaction; the dissociation constant (K_D) is 0.69 μM for the complex between Ru-Ad and P450 (14).

The Soret absorption maximum of ferric P450 in the presence of equimolar Ru-Im shifts from 417 to 420 nm, indicating ligation of the imidazole by the heme iron (7). Luminescence decay of the Ru^{2+*}-Im:P450 complex is also biphasic (k_{1decay} = 2.2 x 10^6 s^{-1}, k_{2decay} = 7.0 x 10^6 s^{-1}). Approximately 68% of Ru^{2+*} quenching occurs via the faster, energy-transfer, phase (k_{2decay}); K_D = 1.5 μM for Ru-Im:P450.

A 1:1 mixture of Ru-EB and P450 does not display an altered Soret absorption maximum; however, Ru^{2+*}-EB is quenched in the presence of P450. The faster of two decay processes (k_{1decay} = 2.2 x 10^6 s^{-1}, k_{2decay} = 1.2 x 10^7 s^{-1}) accounts for 70% of Ru^{2+*}-EB decay, indicating K_D = 1.0 μM for the Ru-EB:P450 complex. Addition of excess camphor ($K_D \approx 1$ μM) (2) to Ru-EB:P450 displaces the Ru-linked substrate completely, as judged by an increased contribution of the slower luminescence decay process (k_{1decay}). We conclude that all three sensitizer-linked substrates bind tightly to the active site of P450.

METHODS AND MATERIALS

Cytochrome $P450_{cam}$ and the Ru-substrates and reductive quenchers were prepared as described in the Appendices. Highly purified (R_z > 1.4), decamphored P450 was stored at –70 °C and thawed just before use. Distilled water was further purified by a Barnstead Nano-Pure system. Tris(2,2'-bipyridine)ruthenium(II) chloride and cobalt (III) pentammine chloride (Strem) were used as received. Hexaammineruthenium(III) chloride (Strem) was recrystallized from a minimum of warm hydrochloric acid. The reductive quencher, *para*-methoxy-*N,N*-dimethylaniline (*p*-MDMA), was sublimed (at 30 °C) and stored sealed under argon in a refrigerator. Precautions were taken to avoid exposing the quencher to light, oxygen, and heat. Periodically, either sublimation or recrystallization of *p*-MDMA from warm water was performed to restore the purity of the white solid. Static absorption spectra were recorded on an HP-8452A spectrophotometer. Steady-state photolysis experiments were conducted with an Oriel 75 watt halogen lamp.

Transient Absorbance Spectroscopy

Solution experiments were performed in sealed cuvettes with P450 and Ru-substrate in 100 mM KCl and 20 mM KPhos buffer, pH 7.4. Samples were fitted with a magnetic stir bar and deoxygenated by repeated evacuations on a vacuum line followed by backfilling with purified argon (3 x 10 cycles). The quenchers, cobalt (III)

pentammine chloride and *p*-MDMA are poorly soluble in aqueous buffer at 5 mM and 10 mM, respectively, and required considerable stirring to dissolve.

All samples were excited with either a XeCl excimer (Lambda-Physik LPX 210i, 308 nm)-pumped dye laser (Lambda-Physik FL 3002, 25-ns FWHM) with coumarin 480 dye (Exciton, 480 nm) or a tunable (220-2000 nm, excitation at 480 nm) optical parametric oscillator (Spectra Physics, MOPO) pumped by a frequency-tripled Q-switched Nd:YAG laser (Spectra Physics, 355 nm, 350 mJ/pulse, 8-ns FWHM). The YAG fired continuously at 10 Hz; thus, for longer time base experiments (> 50 ms) software was written to control the opening and closing of a shutter to select desired pulses.

The laser output was attenuated with a polarizer as needed to give 1-2 mJ/pulse at the sample. Laser shots with energies differing by more than 10% from the mean value (laser pulses detected by a photodiode and selected by a discriminator, Phillips Scientific Model 6930) were rejected. The probe light for single-wavelength transient absorption measurements was provided by a 75 watt continuous-wave arc lamp (PTI model A 1010) and focused on the entrance slit of an ISA double 0.1 meter monochromator. For time bases $\leq$ 100 μs, increased light intensity and, correspondingly, higher signal to noise was achieved by pulsing the lamp synchronously with the laser excitation (generally 10 Hz). Counter-propagating pump and probe beams were aligned on the sample cuvette. Signal

was detected by a Hamamatsu photomultiplier tube (R928); the output signal amplified, digitized (Sony/Tektronix digitizer, Model RTD710A), and recorded on a PC. For time bases 5 μs-1 ms (1024 points/data array), a high-speed (200 MHz) current to voltage amplifier built at Brookhaven National Laboratory was used. For time bases ≥ 1 ms, a slow amplifier (PSD Corp.) was used. Kinetics data are averages of at least 250 laser shots. Transient absorption traces were typically fit to mono- or biexponential functions ($y = c_0 + c_1e^{-(ken + k0)t} + c_2e^{-k0t}$) using the least-squares fitting program *Kinfit*.

For multiwavelength transient absorption experiments (Figure 5.3), probe light was provided by either a microsecond or nanosecond flash lamp powered by the discharge of a variable number of capacitors. The probe beam was delivered by a short fiber optic cable to a beam splitter; roughly 10% of the light was reflected and focused on a fiber optic leading to the reference channel of the diode array detector. The remaining probe light was focused onto a fiber optic directed towards the sample, and made coincident with the pump beam. The probe light was collected by f/2.5 mirrors (bored at the center with small holes for passage of the laser beam) and focused on a fiber optic cable. The fibers containing the reference and probe channels were vertically aligned (3.5 mm apart) and the beams focused onto the entrance slit of the monochromator (SPEX 270M).

Figure 5.3. Schematic of the BILRC nanosecond experiment table used to collect full spectrum transient absorption data with a diode array detector. Probe light from the flash lamp is sent via a fiber optic through a beam splitter and focused onto separate reference and sample fiber optics.

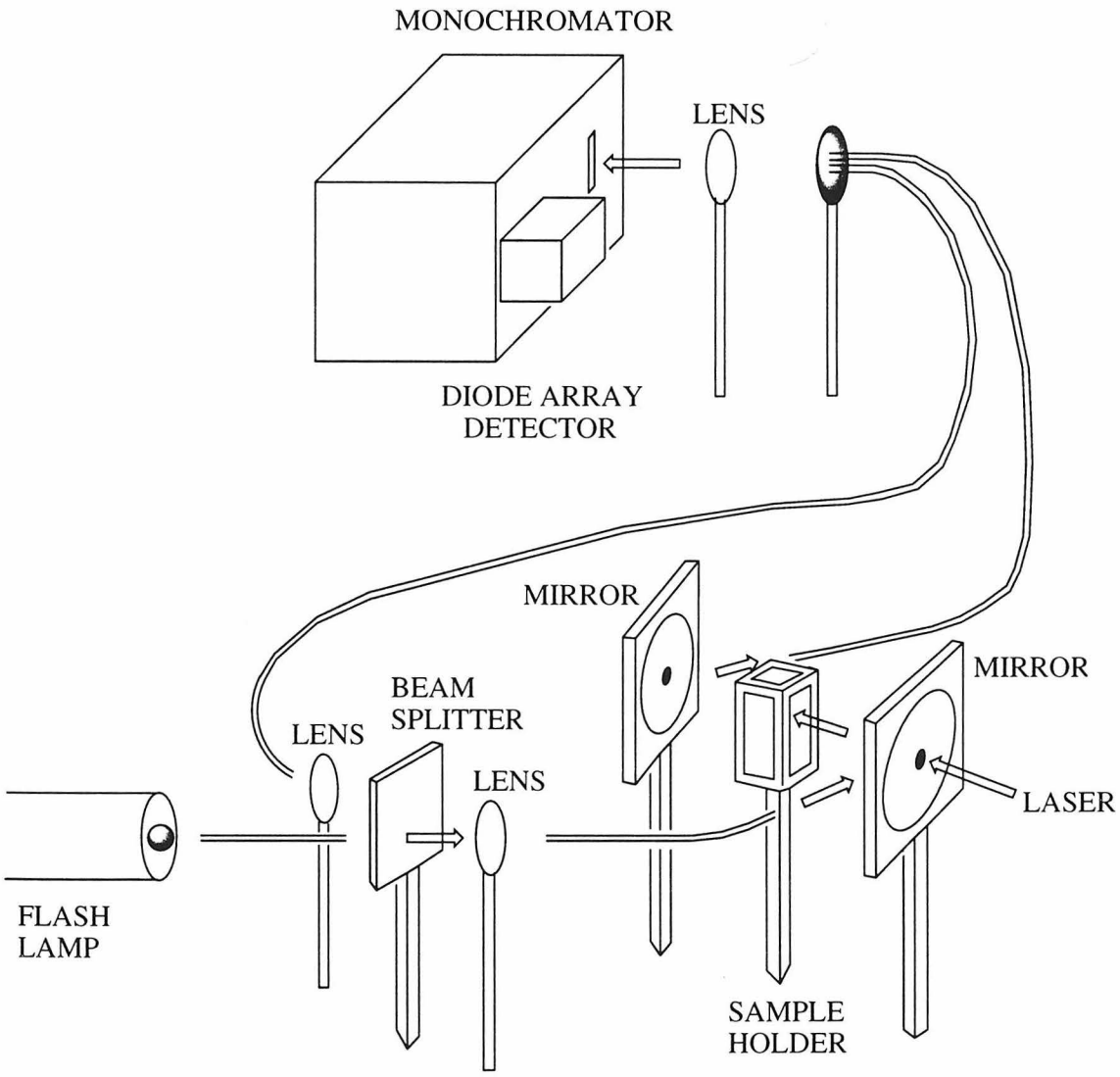
MONOCHROMATOR
LENS
DIODE ARRAY
DETECTOR
MIRROR
MIRROR
BEAM
SPLITTER
LENS
LENS
LASER
FLASH
LAMP
SAMPLE
HOLDER

Efficient light collection at the sample necessitated minimization of laser scatter by focusing and collimating the pump beam. Particularly in instances where it was important to measure absorbance changes at wavelengths near the laser line, extra probe light was directed at the sample and then filtered (with any scattered laser light) before the monochromator. $[Ru(bpy)_3]^{2+}$ (MLCT centered at 456 nm) was generally excited between 480 and 490 nm to minimize spectral overlap (and therefore, collected scatter) during observations in the Soret (380-450 nm). Intensities of probe and reference beams were determined by a diode array detector that was controlled by a Princeton Instruments (model ST-116) instrument and interfaced to a PC using commercial data collection software (*Winspec*). The time resolution was set by delaying the probe pulse (after the laser fire) using a signal delay generator (EG&G). Without a programmed delay, the microsecond flash lamp fired 14 ± 14 μs after the laser, as determined by an oscilloscope. For all but the longest time bases (> 1 s), the 10 Hz laser pulses emitted from the YAG were intercepted from the MOPO at 1 Hz (with the variable-delay shutter described above).

Data were collected and arithmetically manipulated by running a homemade *WinSpec* macro to control the position of a shutter and the timing sequence of blank, excitation, and intermittent stirring cycles. The position of the monochomator and the grating (either 300 or 1200 grooves/mm) was set with a *LabView* routine. Due to the

changing dispersion of light with wavelength, it was necessary to calibrate the x (wavelength) axis by sticking at least three different interference filters in front of the probe light and measuring their peak intensities as recorded by the diode array detector. A calibration function for the diode array was generated by fitting these peaks to the known interference wavelengths. Likewise, offset problems on the y axis (most problematic for data sets with small OD changes) were normalized from the intensities collected during single-wavelength experiments.

RESULTS

Laser excitation of Ru^{2+}-Im followed by reductive quenching with *p*-MDMA (15) yields a powerful reductant, $[Ru\text{-}Im]^+$ (E^0 = - 1.24 V vs. NHE) (16, 17). In the presence of P450, $[Ru\text{-}Im]^+$ is converted rapidly to Ru^{2+}-Im. Concomitant with this $[Ru\text{-}Im]^+$ oxidation is heme reduction, as evidenced by a Soret shift from 420 to 445 nm (7, 18). The rate constant (k_{ET}) for $[Ru\text{-}Im]^+ \rightarrow Fe^{3+}$ electron transfer is 2 x 10^4 s^{-1} (Figure 5.4). Similar kinetics (k_{ET} = 2 x 10^4 s^{-1}) are observed upon reductive quenching of the Ru^{2+*}-EB:P450 complex; a 417 to 390 nm Soret shift results from the $[Ru\text{-}EB]^+ \rightarrow Fe^{3+}$ reaction (Figure 5.5). Reductive quenching of the Ru^{2+*}-Ad:P450 complex yields spectroscopic

Figure 5.4. Single-wavelength transient absorption: Δ-absorbance versus time plots for the reaction of $[Ru\text{-}Im]^+$ with P450. Changes in the Soret region (bleach of Fe^{3+}-Im at 420 nm and increase of Fe^{2+}-Im at 445 nm) were observed after laser excitation of a 10 μM P450, 10 μM Ru-C_{13}-Im, 10 mM *p*-MDMA sample.

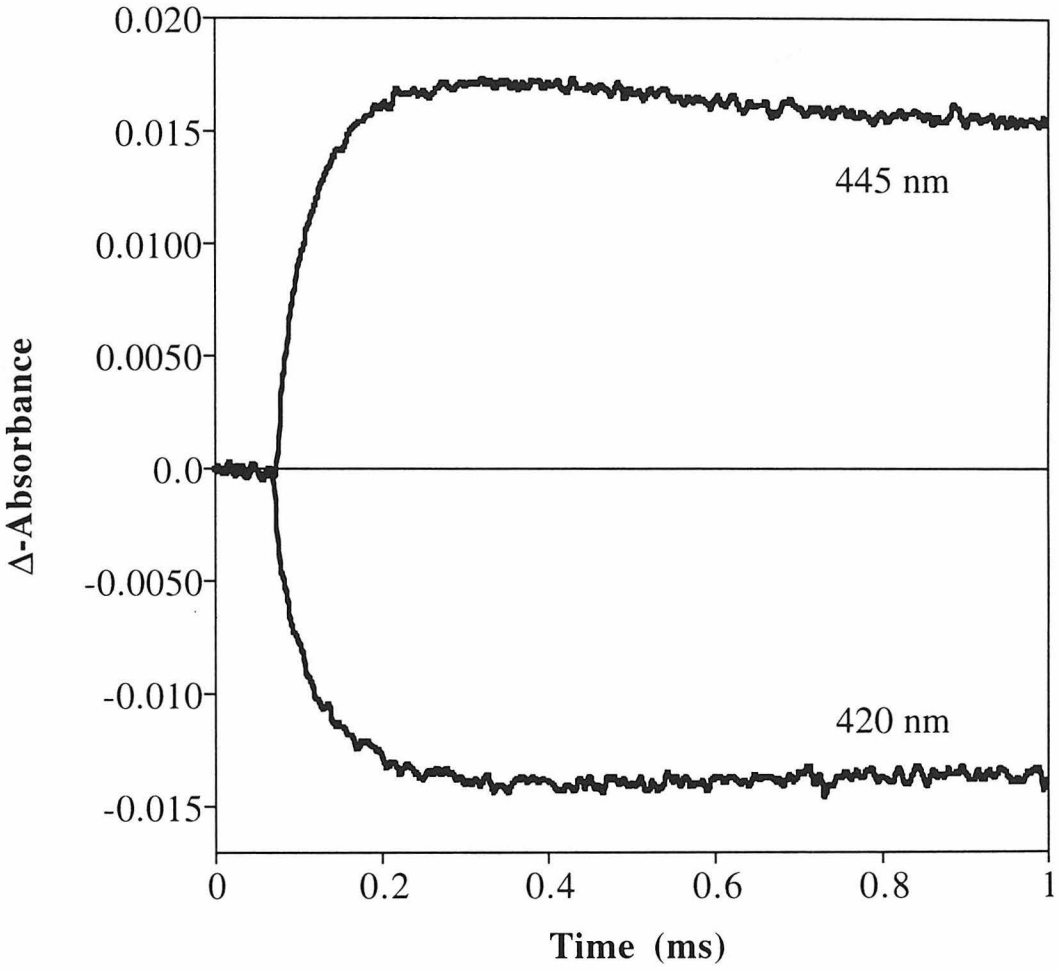
0.020
0.015
0.0100
0.0050
0.0
-0.0050
-0.010
-0.015
Δ-Absorbance
445 nm
420 nm
0
0.2
0.4
0.6
0.8
1
Time (ms)

Figure 5.5. Diode array spectra of P450 at various time delays during and after photoreduction by $[Ru\text{-}EB]^+$. The broad, sloping intensity at 350 nm at 14 μs can be assigned to spectral contributions from $[Ru\text{-}EB]^+$ and *p*-MDMA.

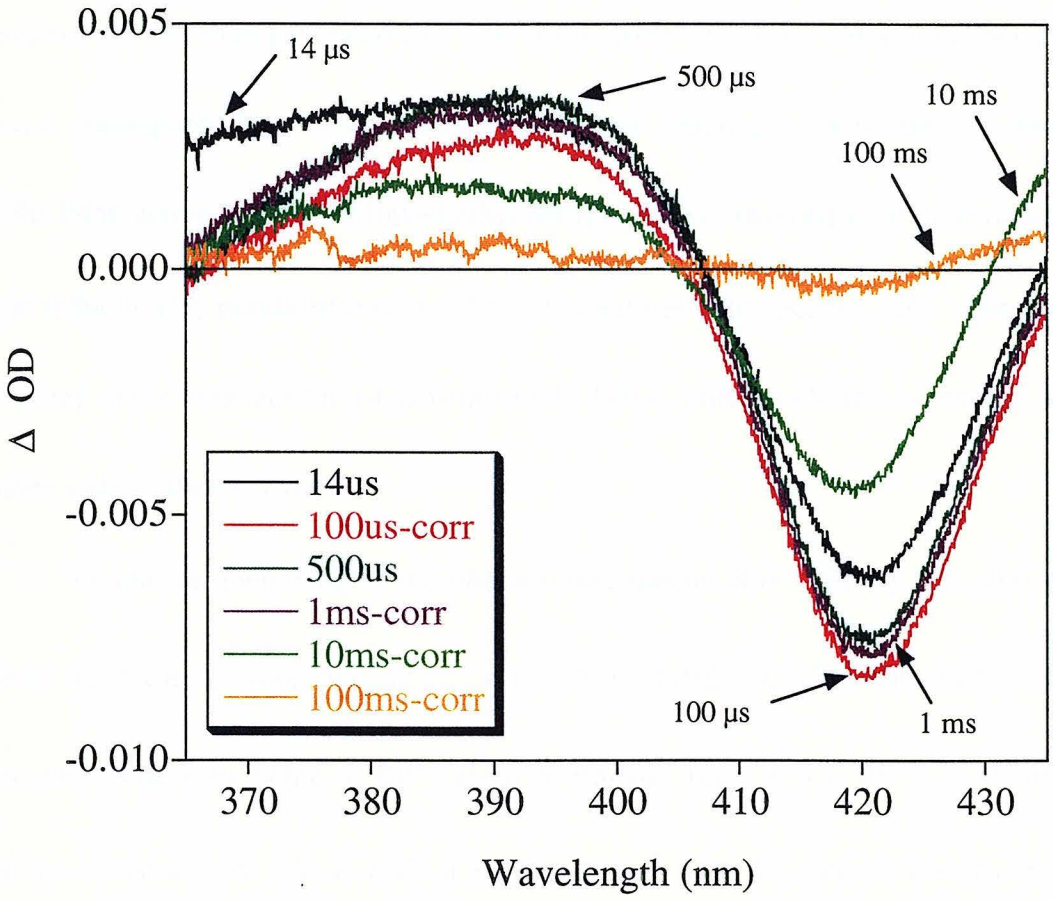
0.005
0.000
-0.005
-0.010
Δ OD
370
380
390
400
410
420
430
Wavelength (nm)
14 µs
500 µs
10 ms
100 ms
100 µs
1 ms
14us
100us-corr
500us
1ms-corr
10ms-corr
100ms-corr

changes comparable to those seen for Ru^{2+*}-EB:P450. This blue-shifted Soret indicates that the reduction product is the previously unobserved $[P_{cys}Fe^{2+}\text{-}OH_2]^-$ form of P450 (Figure 5.5) (19). Further confirmation of heme reduction is the production of $[P_{cys}Fe^{2+}\text{-}CO]^-$ (λ_{max} = 446 nm) upon steady-state visible irradiation of Ru^{2+}-EB:P450 in the presence of *p*-MDMA and carbon monoxide. The relatively high rate of heme reduction in the photogenerated $[Ru\text{-}EB]^+$:P450 complex shows that a direct bond to the iron is not required for efficient Ru-heme electronic coupling. Indeed, electron tunneling to the P450 active site via Ru-linked ethyl benzene is over two orders of magnitude faster than reduction by putidaredoxin ($k \approx 50\ s^{-1}$), a natural redox partner (20). The efficient coupling of the sensitzer-linked substrate to the heme can be exploited to generate a high-valent state of the enzyme.

Oxidative quenching of the photoexcited species Ru^{2+*}-EB by $[Co(NH_3)_5Cl]^{2+}$ yields Ru^{3+}-EB, a strong oxidant (E° = 1.26 V vs. NHE) (*4, 17*). The Ru^{3+}-EB:P450 complex undergoes heme to Ru^{3+} electron transfer (k_{ET} = 6 x 10^3 s^{-1}), yielding an oxidized product with a Soret peak at 390 nm (Figure 5.6). This absorption change is not observed upon laser photolysis of the Ru^{2+}-EB:P450 complex in the absence of $[Co(NH_3)_5Cl]^{2+}$. A comparison of diode array spectra (Figure 5.7) showing WT and Y96F photooxidation (1 ms after laser excitation) suggests that Tyr 96 scavenges $[Ru\text{-}EB]^{3+}$, resulting in smaller yields of oxidized WT P450. The oxidized species could be a

Figure 5.6. Single-wavelength transient absorption spectra: Δ-absorbance versus time plots for the reaction between Fe^{3+}-aquo P450 (λ_{max} = 417 nm) and $[Ru\text{-}EB]^{3+}$. The photoxidation product, centered at 390 nm, was observed with the same kinetics as the disappearance of the starting species at 417 nm. Samples were 10 μM P450, 10 μM Ru-EB, and 5 mM $[Co(NH_3)Cl]^{2+}$.

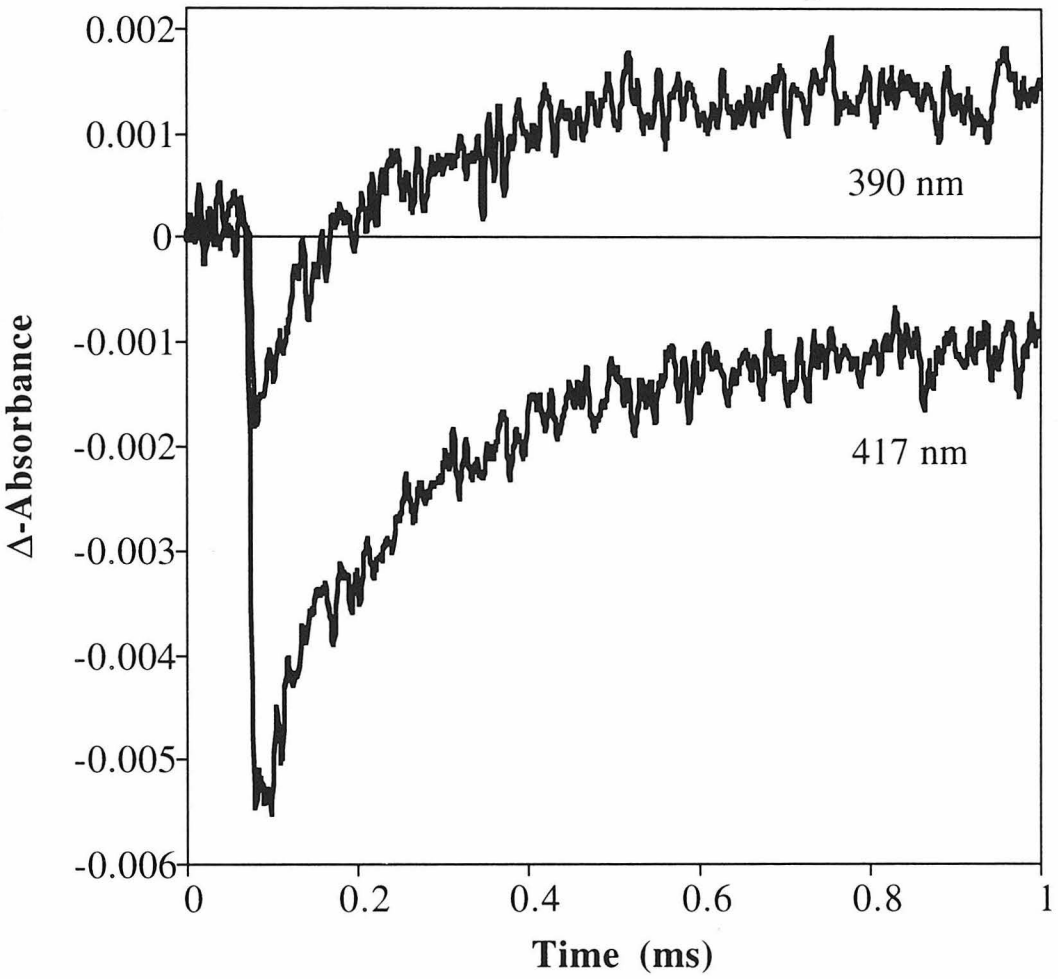
0.002
0.001
0
-0.001
-0.002
-0.003
-0.004
-0.005
-0.006
Δ-Absorbance
390 nm
417 nm
0
0.2
0.4
0.6
0.8
1
Time (ms)

Figure 5.7. Diode array spectra of P450 showing photooxidation by $[Ru\text{-}EB]^{3+}$ 1 ms after laser excitation. The absorbance changes are due mostly to oxidation of P450. Oxidized spectra of WT P450 and Y96F are fairly similar in profile, but differ in intensity; higher yields in the mutant enzyme suggest that tyrosine intercepts some of the Ru^{3+} before it oxidizes the heme.

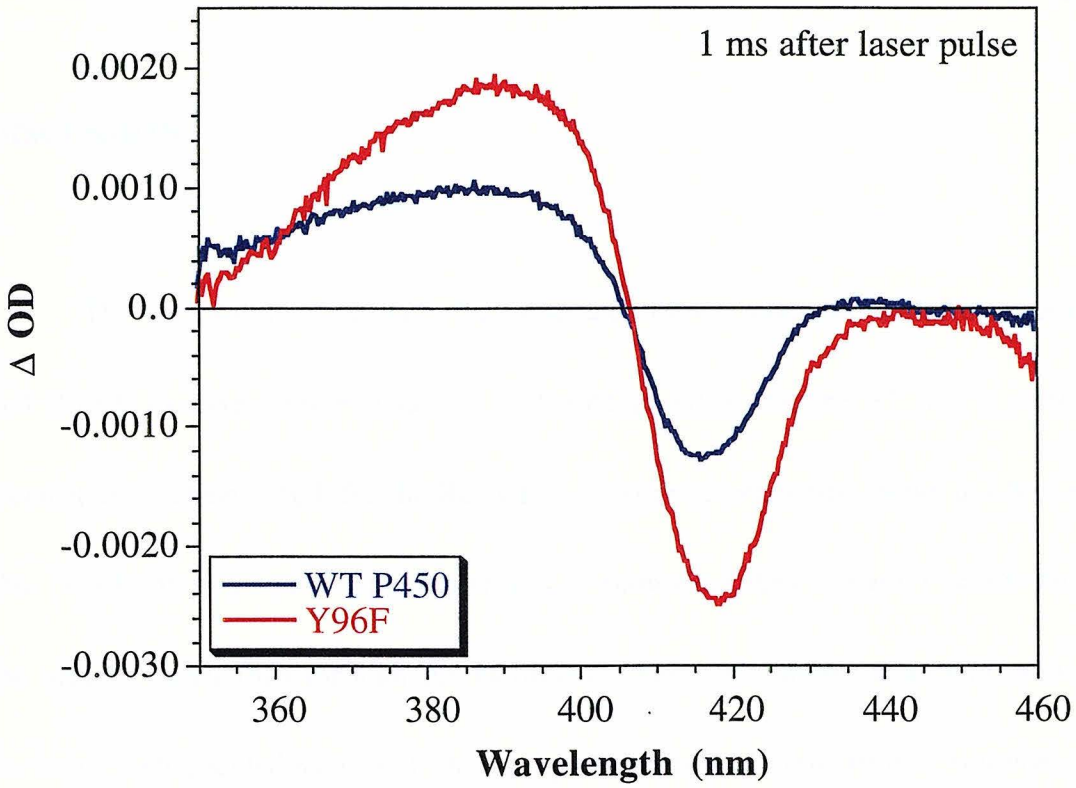
1 ms after laser pulse
0.0020
0.0010
0.0
-0.0010
-0.0020
-0.0030
Δ OD
WT P450
Y96F
360
380
400
420
440
460
Wavelength (nm)

porphyrin π-cation radical, $[P^{+\cdot}{}_{cys}Fe^{3+}\text{-}OH_2]^+$, or an iron^{IV} species, $[P_{cys}Fe^{4+}\text{-}OH_2]^+$. The blue-shifted Soret band in the spectrum of the oxidized heme accords with the radical formulation (21); indeed, porphyrin π-cation radicals often display Soret bands that are blue-shifted from those of resting hemes (22-24).

DISCUSSION

The observation of virtually the same rate of P450 reduction with Ru-Im, Ru-Ad, and Ru-EB deserves further analysis. Also observed is that the ET rate is relatively insensitive to chain length for the Ru-$(CH_2)_{9\text{-}13}$ series (compounds shown in Chapter 2). One possibility that would explain both sets of anomalous data is that ET occurs through the protein rather than through the methylene chain. Computer modeling, however, shows no well-coupled pathway from the top of the channel to the heme. Additionally, it is observed that the yield of electron injection from the shorter $[Ru\text{-}C_7\text{-}EB]^+$ to the heme is markedly smaller (and the rate is an order of magnitude slower), suggesting that electrons, in fact, tunnel through the methylene chain (and through space) to the heme.

A more compelling hypothesis, then, is that the observed reduction rate is dominated by the back electron transfer between $[Ru(bpy)_3]^+$ and *p*-MDMA$^{\bullet+}$ ($k_q \sim 4 \times 10^9$

$M^{-1}s^{-1}$). The observed rate and yield of the forward reaction (Ru^{+}-EB Fe^{3+} --> Ru^{2+}-EB Fe^{2+}) correlates with the yield of Ru^{+} generated (ε = 12,000 $M^{-1}cm^{-1}$ for $Ru(bpy)^{+}$ and ε = 8000 $M^{-1}cm^{-1}$ for *p*-$MDMA^{\bullet+}$ at 510 nm). Because the yield of Ru^{+}-EB Fe^{3+} varies with laser power, the quencher concentration, and the accessibility of $\{Ru(bpy)_3\}^{2+*}$ to the quencher (each Ru-substrate binds slightly differently), it is extremely difficult to draw comparisons between compounds. However, qualitatively, the yields of ET products appear to be highest with Ru-C_9-EB and Ru-C_{10}-EB and decrease by roughly a factor of 10 as the chain length is shortened (-$(CH_2)_7$) or lengthened (-$(CH_2)_{13}$).

Low yields, and possibilities for P450 photodegradation by the oxidative flash/quench chemistry make it unlikely that high-valent intermediates will be accessible to study by this route (Figure 5.8). Additionally, P450 has many tyrosines and tryptophans that compete with the heme for the highly oxidizing Ru^{3+}. Prospects for generating reactive intermediates via the reductive route (Figure 5.8) appear much more promising. Improvements in the design of Ru-substrates (conjugated linkers, optimized driving forces and chain lengths) will permit electron transfer to P450 in the sub-microsecond regime. Such advances are necessary to observe short-lived intermediates, but also to study P450 in the presence of dioxygen, since O_2 reacts rapidly with photoinduced reducing agents to form superoxide. Rapid electron injection into oxy P450 should allow the observation of reactive intermediates on the catalytic pathway.

Figure 5.8. Proposed flash-quench scheme for generating P450 high-valent intermediates by both oxidative and reductive chemistries.

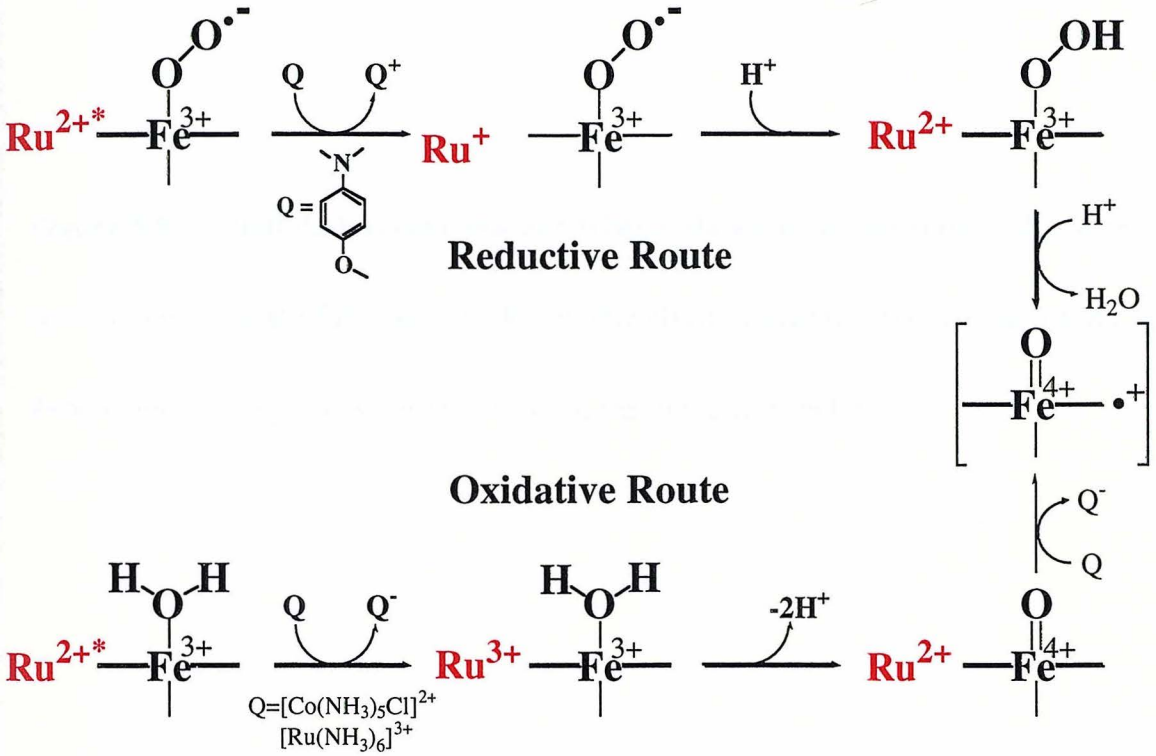
Ru2+*
Fe3+
Q
Q+
Ru+
Q =
N
O
H+
OH
Ru2+
Reductive Route
H+
H2O
Fe4+
•+
Oxidative Route
Q-
Q
H
O
Ru3+
-2H+
Q=[Co(NH3)5Cl]2+
[Ru(NH3)6]3+

Figure 5.9. Overall flash/quench reaction scheme showing the preparation of new redox states in the P450:Ru-EB complex. Reversible electron-transfer processes return Ru and P450 to their resting states within 100 ms of the initial laser pulse.

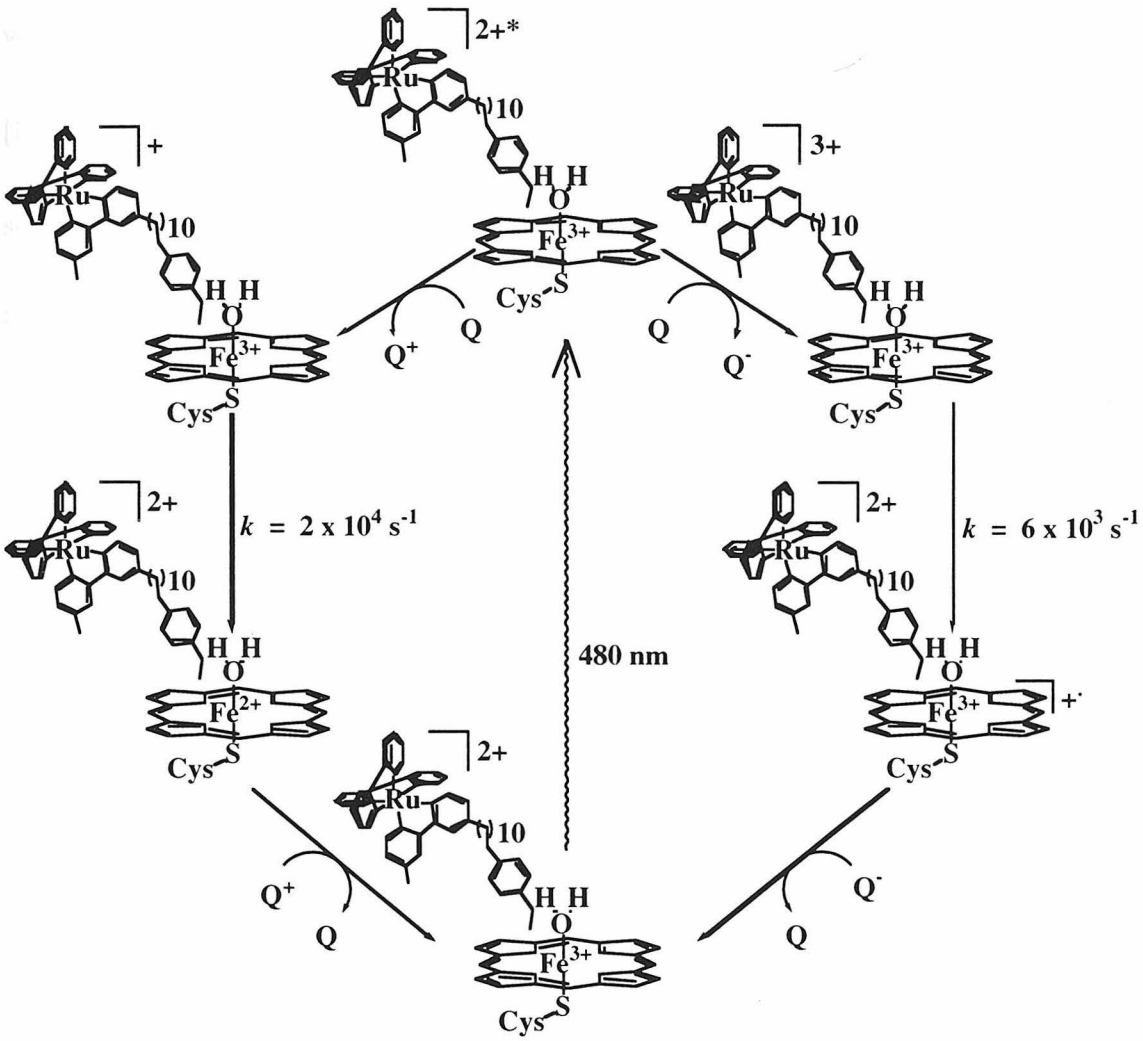
2+*
+
3+
2+
2+
2+
+·
Ru
10
H H
O
Fe3+
Fe2+
Cys
S
Q+
Q
Q-
k = 2 x 10^4 s^-1
k = 6 x 10^3 s^-1
480 nm

CONCLUSION

By employing sensitizer-linked substrates, we have prepared new oxidized and reduced states of P450 (Figure 5.9). These flash/quench methods provide a wide time window to study highly reactive forms of the enzyme. Both $[P_{cys}Fe^{II}\text{-}OH_2]^-$ and $[P^{+\cdot}{}_{cys}Fe^{III}\text{-}OH_2]^+$ are formed in ~0.1 ms and persist for ~100 ms. Improved design of sensitizers, quenchers, linkers, and substrates will lead to even faster electron and hole injection into P450 and other redox-active enzymes.

REFERENCES AND NOTES

1. M. Sono, M. P. Roach, E. D. Coulter, J. H. Dawson, *Chem. Rev.* **96**, 2841-2887 (1996).

2. E. J. Mueller, P. J. Loida, S. G. Sligar, in *Cytochrome P450. Structure, Mechanism, and Biochemistry* P. R. Ortiz de Montellano, Ed. (Plenum Press, New York, 1995), pp. 83-124.

3. L.-L. Wong, *Curr. Op. Chem. Biol.* **2**, 263-268 (1998).

4. J. Berglund, T. Pascher, J. R. Winkler, H. B. Gray, *J. Am. Chem. Soc.* **119**, 2464-2469 (1997).

5. D. W. Low, J. R. Winkler, H. B. Gray, *J. Am. Chem. Soc.* **118**, 117-120 (1996).

6. The synthesis of Ru-EB is typical: reaction of thionyl chloride with 10-bromodecanoic acid, followed by addition of 4-ethylaniline, gives the corresponding amide. Addition of the amide to a solution of 4,4'-dimethyl-2,2'-bipyridine and lithium diisopropylamide yields the derivatized bpy, which was reacted with $[Ru(bpy)_2Cl_2]$ to give Ru-EB.

7. J. H. Dawson, L. A. Anderson, M. Sono, *J. Biol. Chem.* **257**, 3606-3617 (1982).

8. R. E. White, M. B. McCarthy, K. D. Egeberg, S. G. Sligar, *Arch. Bioch. Biophys.* **228**, 493-502 (1984).

9. D. Filipovic, M. D. Paulsen, P. J. Loida, S. G. Sligar, R. L. Ornstein, *Biochem. Biophys. Res. Comm.* **189**, 488-495 (1992).

10. R. Raag, T. L. Poulos, *Biochemistry* **30**, 2674-2684 (1991).

11. All studies were performed under an argon atmosphere with 10 μM ruthenium complex, 10 μM enzyme in 100 mM potassium chloride, 20 mM potassium phosphate buffer at pH 7.4 and room temperature.

12. T. L. Poulos, J. Cupp-Vickery, H. Li, in *Cytochrome P450. Structure, Mechanism, and Biochemistry* P. R. Ortiz de Montellano, Ed. (Plenum Press, New York, 1995), pp. 125-150.

13. Excitation at 480 nm (20-ns pulse width); the experimental setup has been described.[5]

14. Soret shifts from addition of the ruthenium complexes to P450 are small. Competitive binding assays of camphor and Ru-Ad with P450 by Soret absorption shifts yielded a K_D value of 0.68 μM.

15. G. A. Mines, M. J. Bjerrum, M. G. Hill, D. R. Casimiro, I.-J. Chang, J. R. Winkler, H. B. Gray, *J. Am. Chem. Soc.* **118**, 1961-1965 (1996).

16 Reductive quenching of $[Ru^{II}(bpy)_3]^{2+}$ yields a ruthenium complex containing a coordinated bpy anion radical, $[Ru^{II}(bpy)_2(bpy^{-\cdot})]^{+}$ (K. Kalyanasundaram, *Photochemistry of Polypyridyl and Porphyrin Complexes* (Academic Press Ltd., London, 1992), p. 108).

17. Reduction potentials are for $[Ru(bpy)_3]^{2+}$ (K. Kalyanasundaram, *Photochemistry of Polypyridyl and Porphyrin Complexes* (Academic Press Ltd., London, 1992), p. 144). The E° values of derivatives with substrate-terminated hydrocarbon chains should be similar.

18. J. H. Dawson, L. A. Andersson, M. Sono, *J. Biol. Chem.* **258**, 13637-13645 (1983).

19. The [$P_{his}Fe^{2+}$-OH_2] form of myoglobin exhibits a Soret band 15-nm blue-shifted from [$P_{his}Fe^{2+}$] (D. C. Lamb, V. Prusakov, N. Engler, A. Ostermann, P. Schellenberg, F. G. Parak, G. U. Nienhaus, *J. Am. Chem. Soc.* **120**, 2981-2982 (1998)). Typical bulk reduction of P450 results in five-coordinate $[P_{cys}Fe^{2+}]^-$ with a Soret peak at 408 nm. The product of [$P_{cys}Fe^{3+}$-OH_2] reduction by $[Ru\text{-}EB]^{1+}$ displays a Soret peak at 390 nm.

20. M. J. Hintz, D. M. Mock, L. L. Peterson, K. Tuttle, J. A. Peterson, *J. Biol. Chem.* **257**, 14324-14332 (1982).

21. The cysteine thiolate ligand could stabilize an Fe^{IV} state of P450. Hydrogen bonding to this thiolate (T. L. Poulos, B. C. Finzel, A. J. Howard, *J. Mol. Biol.* **195**, 687-700 (1987)), however, decreases the donor strength. Although the reaction product of iodosobenzene and P450 exhibits a 393 nm Soret band (R. C. Blake II, M. J. Coon *J. Biol. Chem.* **264**, 3694-3701 (1989)), the Soret of chloroperoxidase red-shifts upon ferryl formation (R. Nakajima, I. Yamazaki, B. W. Griffin *Biochem. Biophys. Res. Comm.* **128**, 1-6 (1985)). The blue-shifted Soret band exhibited by the heme in the oxidized Ru-EB:P450 complex is not unlike that of P420, a common P450 decomposition product (S. A. Martinis, S. R. Blank, L. P. Hager, S. G. Sligar, G. H. B. Hoa, J. J. Rux, J. H. Dawson *Biochemistry* **35**, 14530-14536 (1996)). Formation of P420, however, is largely irreversible, whereas oxidized Ru-EB:P450 returns to the resting state without appreciable decomposition.

22. P. Gans, G. Buisson, E. Duee, J.-C. Marchon, B. S. Erler, W. F. Scholz, C. A. Reed, *J. Am. Chem. Soc.* **108**, 1223-1234 (1986).

23. R. H. Felton, G. S. Owen, D. Dolphin, J. Fajer, *J. Am. Chem. Soc.* **93**, 6332-6334 (1971).

24. A. Wolberg, J. Manassen, *J. Am. Chem. Soc.* **92**, 2982-2991 (1970).

CHAPTER 6

Submicrosecond Electron Injection into Cytochrome $P450_{cam}$

Acknowledgement:

This work was done in collaboration with Alex Dunn.

INTRODUCTION

The development of ruthenium photosensitizers with high affinity for the cytochrome $P450_{cam}$ (P450) active site has established a new method for rapidly modulating enzyme oxidation states. Photoexcitation of P450:Ru-(alkyl linker)-substrate conjugates in the presence of an oxidative or reductive quencher has been shown to effect heme redox chemistry on submillisecond time scales (1). Recently, our efforts have focused on accelerating the rate-limiting electron-transfer (ET) step in P450 catalysis on route to generating reactive catalytic species (2). With this goal, three new *conjugated* sensitizer-linked probes were synthesized (Figure 6.1abc). Laser excitation of (c) allows direct photoreduction of P450 on *submicrosecond* time scales. These rate enhancements, in the absence of a reductive quencher, greatly extend the utility of this approach for biophysical studies of short-lived enzyme intermediates.

In previous work with *saturated*, alkyl-tethered, sensitizer-linked substrates (3), it was shown that P450 complexation significantly quenches $\{Ru(bpy)_3\}^{2+*}$ by Förster energy transfer, not ET. Due to the shortened Ru excited-state lifetime, even an efficient reductive quencher such as *para*-methoxy-*N,N*-dimethylaniline (*p*-MDMA) (4,5), generates little of the long-lived, highly reducing (E^0 = - 1.24 V vs. the normal hydrogen electrode, NHE) (6) $[Ru\text{-substrate}]^+$ necessary for P450 reduction. Myriad problems

Figure 6.1a-e. Top: Three conjugated sensitizer-linked probes in their presumed orientation relative to cytochrome $P450_{cam}$ (thiolate-ligated heme). Compound (a) cannot form a covalent bond to the heme; the perfluorobiphenyl moiety most likely occupies the substrate pocket. Luminescence quenching of the excited state of (a) by P450 has been assigned to a purely Förster energy-transfer process. Compounds (b) and (c) may bind the heme iron directly, as judged from a blue shift (417 → 420 nm) in the Soret. Luminescence quenching of the excited states of (b) and (c) by P450 has been assigned to both Förster energy-transfer and electron-transfer processes. Bottom: Model compounds (d) and (e) for electrochemical studies and control experiments involving transient absorption spectroscopy.

(a) Ru-biphenF_9

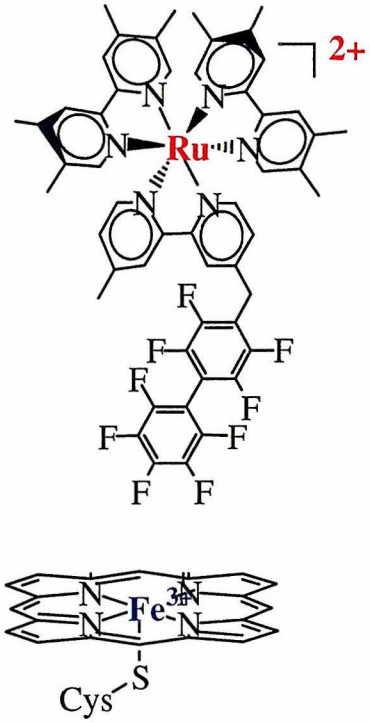

(b) Ru-biphen-im

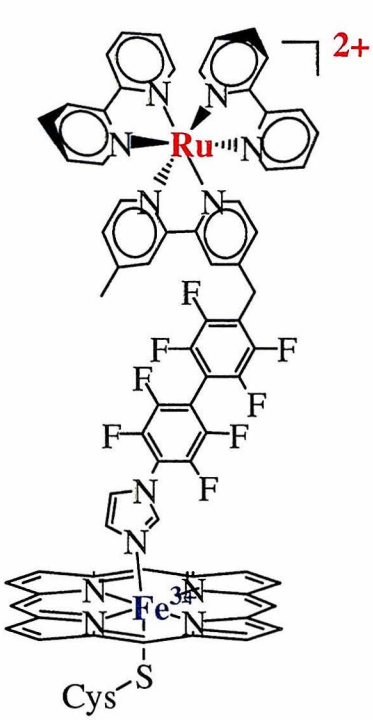

(c) tmRu-biphen-im

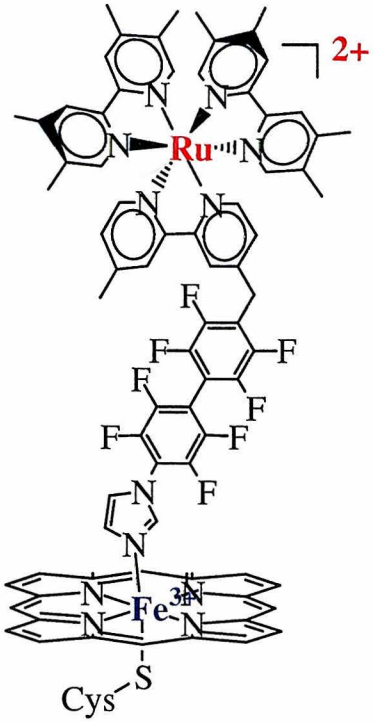

(d) biphenF_9-im

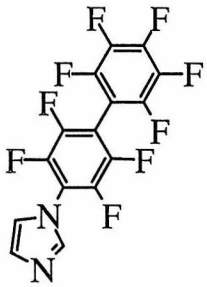

(e) tmRu

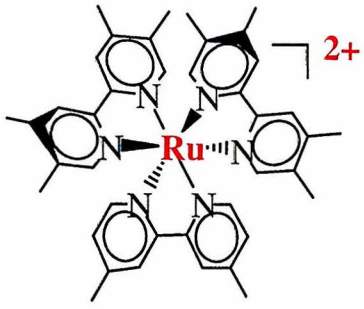

with *p*-MDMA include poor water solubility, dioxygen sensitivity, ability to displace Ru-substrates from the active site, and intense spectral features in the oxidized state, *p*-$MDMA^{\bullet+}$. Ongoing efforts to photogenerate reactive metalloenzyme intermediates in both solution and protein crystals motivated the design of sensitizer-linked probes capable of injecting electrons more rapidly and without ancillary quenchers.

In this chapter the emission lifetimes and transient absorption of three similar conjugated compounds (a-c) bound to P450 are examined; these data highlight the importance of two parameters – driving force and pathway - in excited-state electron injection. Substantial differences in binding and rates of reduction accompany subtle steric and electronic changes in the Ru-probes (a-c). The optimized compound, tmRu-biphenF_8-im (c), reduces $P450_{cam}$ with a rate constant almost one million times that of the natural Fe_2S_2 redox partner, putidaredoxin (k = 50 s^{-1})! Importantly, the hydrophobicity and histidine-mimicking imidazole functionality of Ru-probes such as (b) and (c) should permit studies of many other natural and unnatural enzyme active sites.

MATERIALS AND METHODS

General

Absorption spectra were recorded on an HP-8452A spectrophotometer. Steady-state emission measurements were made on an ISS K2 fluorometer exciting at 470 nm and scanning from 500-800 nm. All electrochemical measurements were made using a CH Instruments Electrochemical Workstation interfaced to a PC using CH Instruments software. Time-resolved luminescence, steady-state emission, single-wavelength and diode array transient absorption measurements, and all standard procedures involving sample preparation were performed as described in previous chapters. Unless stated otherwise, all experiments were performed in 50 mM KPi, 100 mM KCl, pH 7.4 buffer.

Syntheses

Compounds (a-c) were synthesized by procedures similar to those described for Ru-substrates and Ru-Im probes (Appendix B). Addition of excess perfluorobiphenyl to a solution of 4,4'-dimethyl-2,2'-bipyridine (GFS) and lithium diisopropylamide yields the derivatized bpy. Reacting this compound directly with $[Ru(bpy)_2Cl_2]$ yields (a). Otherwise, addition of stoichiometric imidazole and K_2CO_3 in freshly distilled DMSO yields bpy-biphenyl(F_8)-im, which was reacted with either $[Ru(bpy)_2Cl_2]$ or $[Ru(tmbpy)_2Cl_2]$ to yield (b) and (c), respectively. The syntheses of (d) and (e) are described in full detail in Appendix B.

Electrochemistry

Cyclic voltammetry (CV) was performed at ambient temperature with a normal three-electrode configuration consisting of a highly polished glassy carbon working electrode, a platinum auxiliary electrode, and a standard calomel electrode reference. The working electrode was separated from the reference compartment by a fritted disk. Acetonitrile solutions contained 0.1 M tetrabutylammonium hexafluorophosphate (freshly recrystallized) as the supporting electrolyte. Samples were rigorously bubbled with argon for several minutes prior to data collection. All compounds were studied as their PF_6^- salts. All potentials are reported vs. NHE, using the relationship $E^0(NHE) = E^0(SCE) + 242$ mV.

$Ru^{3+/2+}$ and $Ru(bpy_2)(bpy')^{0/\bullet-}]^{2+}$ couples for compounds (a), (b), (c), and (e) were recorded and corrected for the junction potential using ferrocenium/ferrocene as an internal standard. In our cell, CV of 0.05 mM ferrocene solution in 0.1 M tetrabutylammonium hexafluorophosphate gave $E^0(Fc^+/Fc) = 498$ mV vs. SCE. Junction potentials in acetonitrile were found to be 191 mV.

RESULTS

Binding of Ru compounds to P450 was determined by UV-vis and luminescence lifetime measurements, as described previously (1,3). Addition of equimolar tmRu-biphenF_9 (a) to substrate-free P450 perturbed the absorption spectrum very little (λ_{max} remained at 417 nm). Time-resolved emission experiments, however, showed that P450 binds (a) tightly (K_D = 0.9 μM). The normally monophasic Ru^{2+*} luminescence profile became biphasic in the presence of P450 ([enzyme] = 4.8 μM, [Ru] = 4.5 μM, 65% k_{bound} = 1.0 x 10^7 s^{-1}, 35% k_{free} = 2.0 x 10^6 s^{-1}). The observed decay is attributed to quenching of the bound Ru^{2+*} by a Förster energy-transfer process (7), similar to that observed with other Ru-probes (3). No transient absorption signals other than those associated with the decay of Ru^{2+*} were observed for this complex, indicating the absence of an ET process. Based on Förster analysis (see Appendix C) of the overlap between Ru^{2+*} emission and P450 absorption spectra (Figure 6.2), R_0 is calculated to be 18.8 Å (Table 6.1). The rate of Ru^{2+*} energy transfer ($k_{en} = k_{bound} - k_{free}$ = 8.0 x 10^6 s^{-1}) predicts a Ru-Fe distance of 19.7 Å, which agrees well with modeling studies of Ru-biphenF_9 bound to the open P450 structure (Chapter 2).

Addition of equimolar Ru-biphenF_8-im (b) to substrate-free P450 red shifted the absorption spectrum (λ_{max} = 417 → 420 nm), similarly to known Fe^{3+}-imidazole P450 complexes (8). The Q-bands were also red shifted from ferric-aquo P450 (Figure 6.2), although less than most ferric-imidazole complexes. The observed biphasic Ru^{2+*}

Figure 6.2. Top: Q-bands of P450 bound to (a) (substrate-free spectrum), (b), and (c). The spectral overlap of the Ru^{2+*} emission with the Q-band absorption gives the Förster distance, as described in Appendix C. Below: Emission spectra of $[Ru(bpy)_3]^{2+*}$, Ru-Im (b), and tmRu-Im (a, c). Integration of the area under each spectrum and comparison to a standard $[Ru(bpy)_3]^{2+}$ solution gave the quantum yields as described in Appendix D. Q.Y. ($Ru(bpy)_3^{2+}$) = 0.042, Q.Y. (Ru-Im, (b)) = 0.025, Q.Y. (tmRu-Im, (a, c)) = 0.0094.

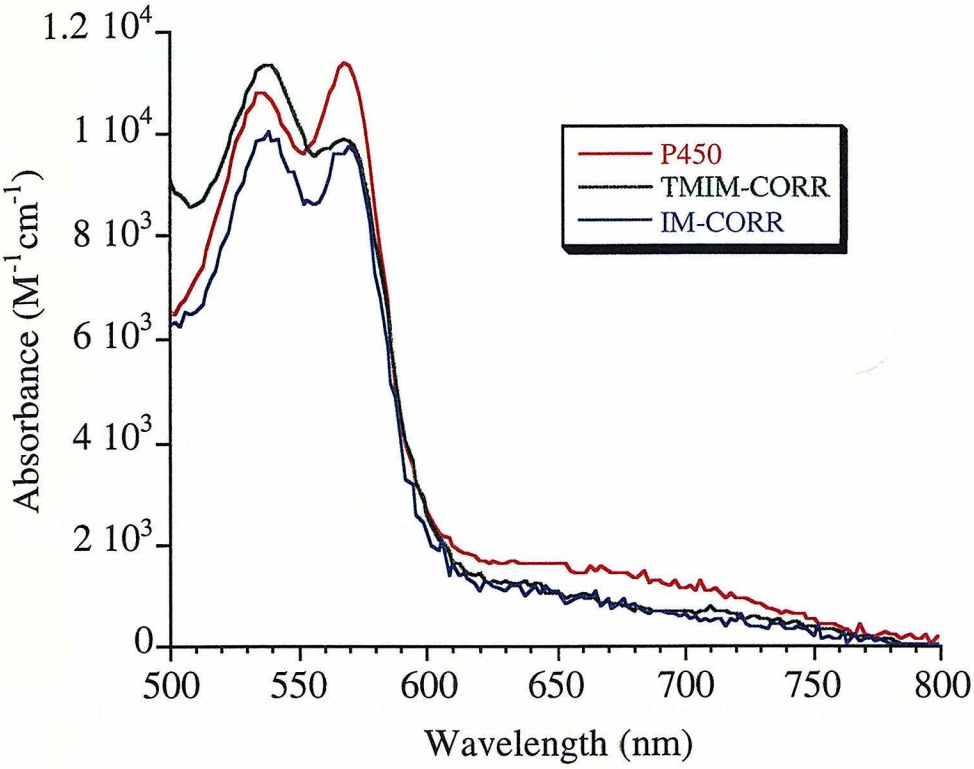
1.2 10^4
1 10^4
8 10^3
6 10^3
4 10^3
2 10^3
0
Absorbance (M^-1cm^-1)
500
550
600
650
700
750
800
Wavelength (nm)
P450
TMIM-CORR
IM-CORR

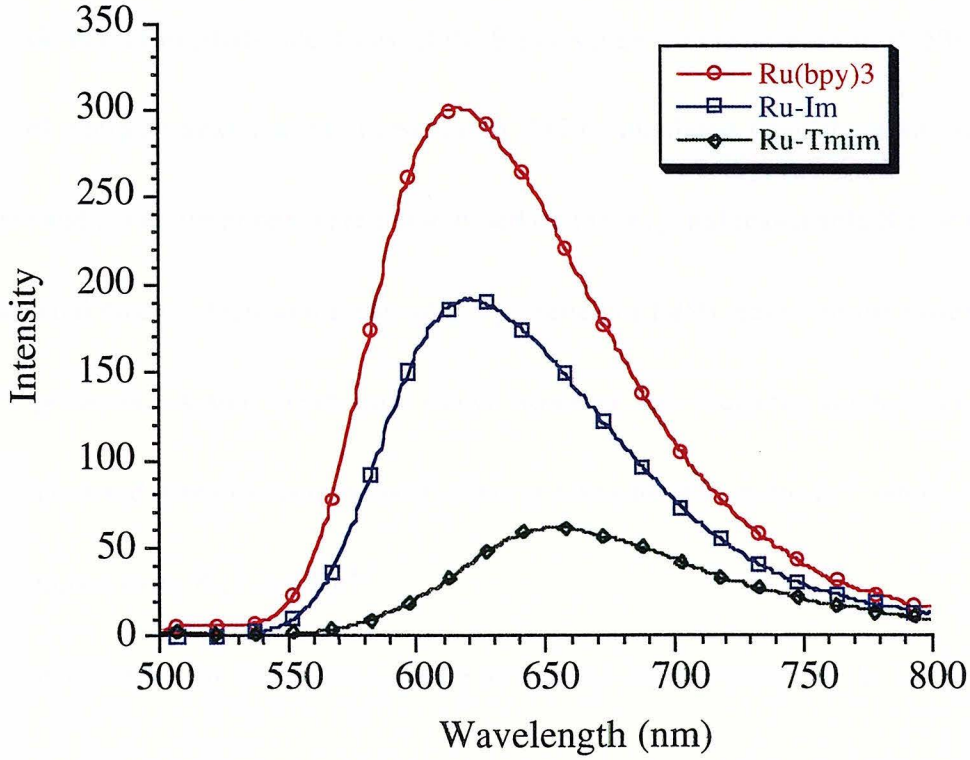
350
300
250
200
150
100
50
0
Intensity
500
550
600
650
700
750
800
Wavelength (nm)
Ru(bpy)3
Ru-Im
Ru-Tmim

Table 6.1. K_D, k_{ET}, k_{en}, R_0, and Ru-Fe distances of Ru-probes (a-c)*

Ru	K_D(μM)	$k_d(s^{-1})$[a]	$k_{en}(s^{-1})$[b]	$k_{ET}(s^{-1})$[c]	R_0(Å)	Ru-Fe(Å)[d]
(a)	0.9	4.6 E6	8.0 E6	N/A	18.8	19.7
(b)	3.7 (0.4)	2.0 (0.1) E6	8.5 E6	1 E6	22.1	17.7
(c)	0.5 (0.1)	4.6 (0.1) E6	9.5 E6	8 E6	18.0	17.7

*Uncertainties are given in parentheses, and constitute the standard deviation of four different measurements.

[a]Intrinsic rate of excited-state decay of the Ru complex (in the absence of P450).

[b]Rate of energy transfer in the presence of P450, calculated from the emission profile. For (b) and (c) assumptions were made based on (a), k_{obs}, and reasonable Ru-Fe distances.

[c]Calculated rate of electron transfer in the presence of P450, based on the observed yield of ET products. Actual yields (and rates), however, are probably much higher. Yields were calculated using extinction coefficients at 420 and 445 nm for Fe^{2+} while subtracting contributions from Ru^{3+} and Ru^{2+*}.

[d]The metal-metal (Ru-Fe) distance serves as a useful representation of the D-A pair.

Figure 6.3. Single-wavelength transient absorption: Δ-absorbance versus time plots for the reaction of [Ru-biphenF_8-Im]$^+$ with P450. Changes in the Soret region (bleach of Fe^{3+}-Im at 420 nm and increase of Fe^{2+}-Im at 445 nm) were observed after laser excitation of a 5.3 μM P450, 5.3 μM Ru sample.

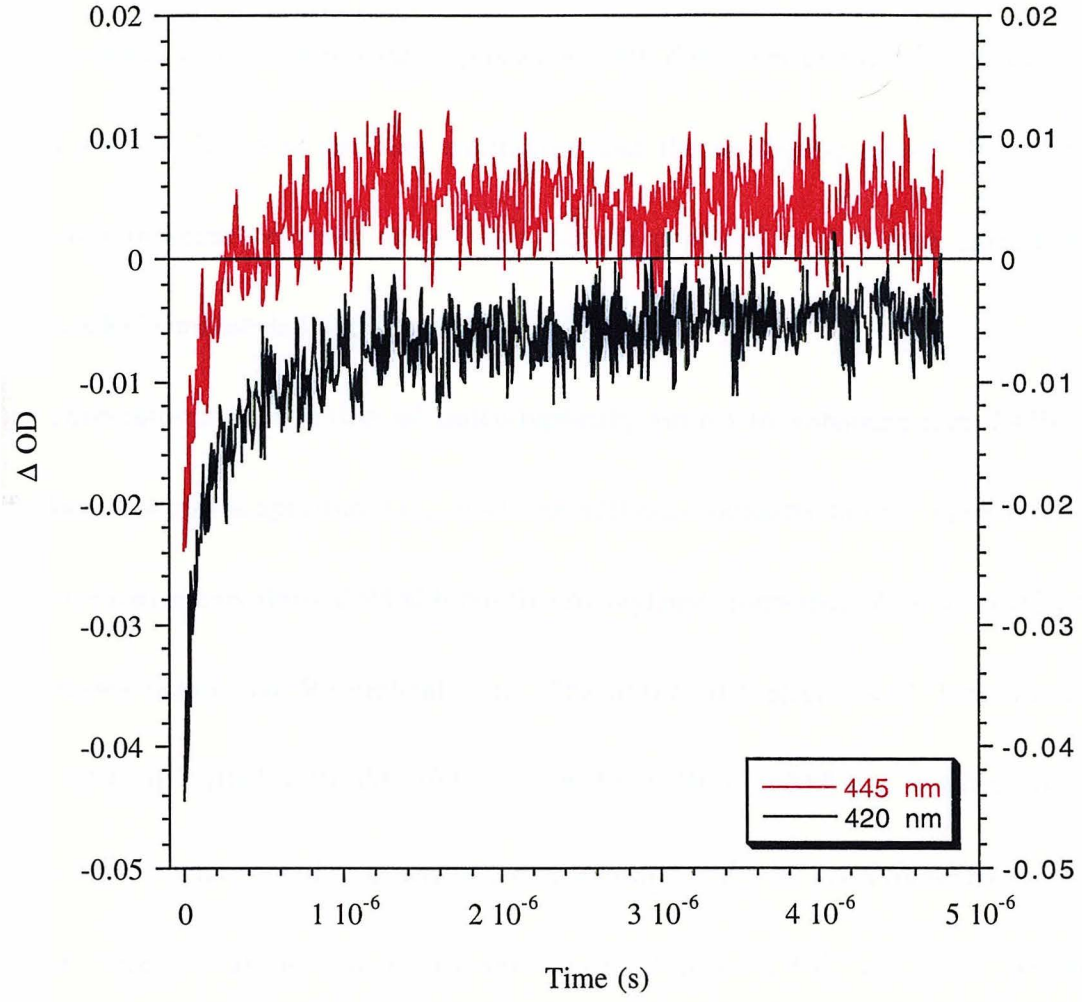
0.02
0.01
0
-0.01
-0.02
-0.03
-0.04
-0.05
Δ OD
0
1 10-6
2 10-6
3 10-6
4 10-6
5 10-6
Time (s)
445 nm
420 nm

luminescence profile ([P450] = [Ru] = 10 μM, 55% k_{bound} = 1.2 x 10^7 s^{-1}, 45% k_{free} = 2.0 x 10^6 s^{-1}) confirmed P450 binding (K_D = 3.7 ± 0.2 μM). At early times (τ ~ 300 ns) transient absorption signals were observed for not only decaying Ru^{2+*} but also increasing Ru^{3+}-Im-Fe^{2+} (Figure 6.3), permitting assignment of Ru^{2+*} quenching to *both Förster energy-transfer and electron-transfer* processes. All of the unbound Ru^{2+*} returned to the ground state within 5 μs of laser excitation, and the remaining signal (Figure 6.4, absorption increase centered at 445 nm, bleach centered at 420 nm) agreed with numerous Fe^{2+}-imidazole P450 species (9).

Stoichiometric addition of tmRu-biphenF_8-im (c) to substrate-free P450 red shifted the absorption spectrum (λ_{max} = 417 → 420 nm), similarly to (b). Time-resolved emission experiments showed P450 binds this methylated compound (K_D = 0.5 ± 0.2 μM) considerably better than Ru-biphenF_8-im. The observed biphasic Ru^{2+*} luminescence profile ([P450] = [Ru] = 10 μM, 80% k_{bound} = 4.0 x 10^7 s^{-1}, 20% k_{free} = 4.5 x 10^6 s^{-1}) (Figure 6.5) was attributed to quenching of the bound Ru^{2+*} by *predominantly electron transfer*. Transient absorption signals were observed for both Ru^{2+*} and tmRu^{3+}-Im-Fe^{2+} at the earliest times (τ ~ 10 ns) accessible to the BILRC nanosecond laser system (Figure 6.6), and achieved a maximum Δ absorbance 30 ns after the laser pulse (Figure 6.7). The product of this direct photoinduced ET appears virtually the same as that observed upon reduction of the P450:(c) complex with dithionite and laser photolysis (Figure 6.8). This

Figure 6.4. Transient absorption of the P450:Ru-biphenF_8-im complex, collected 5 μs after laser excitation. Δ Absorption intensities were obtained by fitting transient absorption kinetics for several different wavelengths in the Soret region. At 5 μs, all of the Ru^{2+*} has been consumed, and the observed difference spectrum is a sum of the absorption changes caused by (P450) Fe^{2+}-Im and Ru^{3+}.

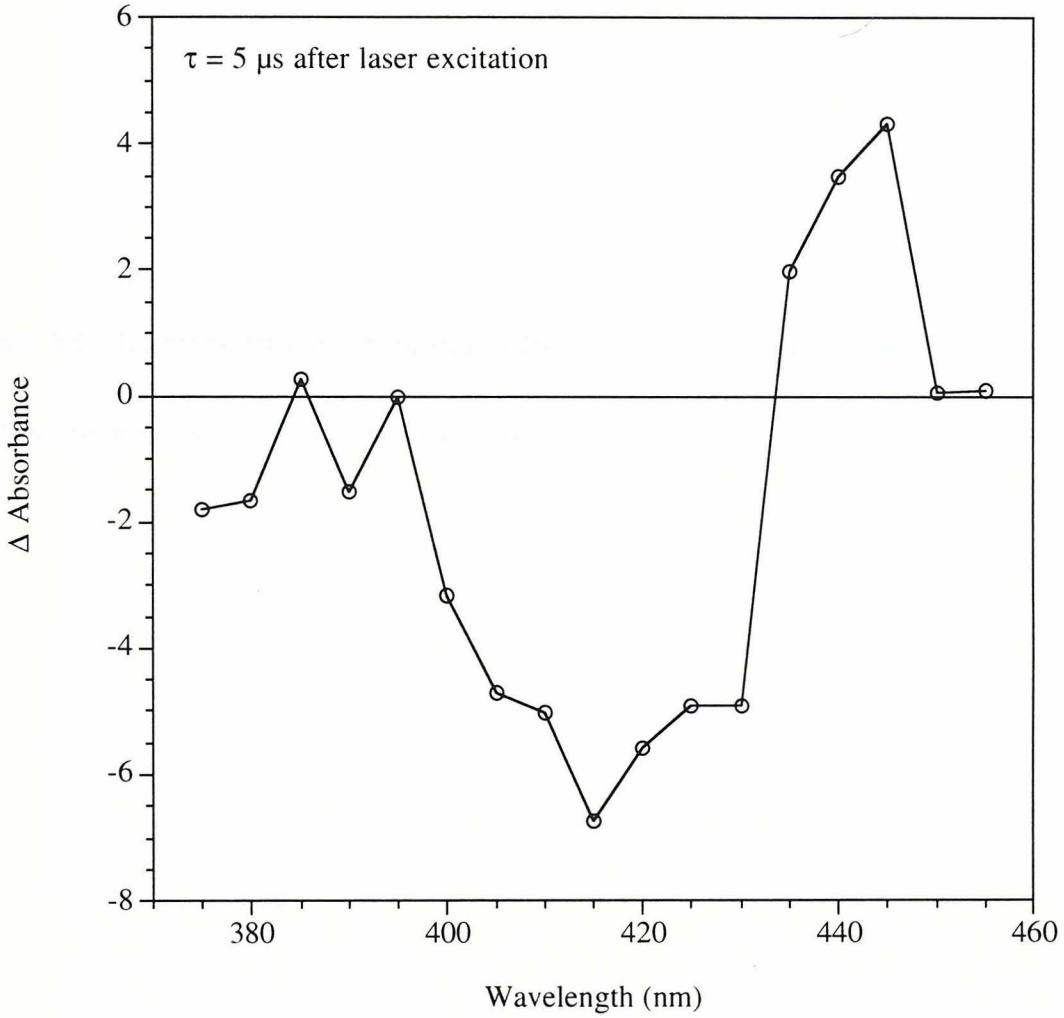
τ = 5 μs after laser excitation
Δ Absorbance
Wavelength (nm)
6
4
2
0
-2
-4
-6
-8
380
400
420
440
460

Figure 6.5. Luminescence decay profile (620 nm) for tmRu-biphenF_8-im^{2+*} both free in solution (monophasic) and bound to P450 (biphasic).

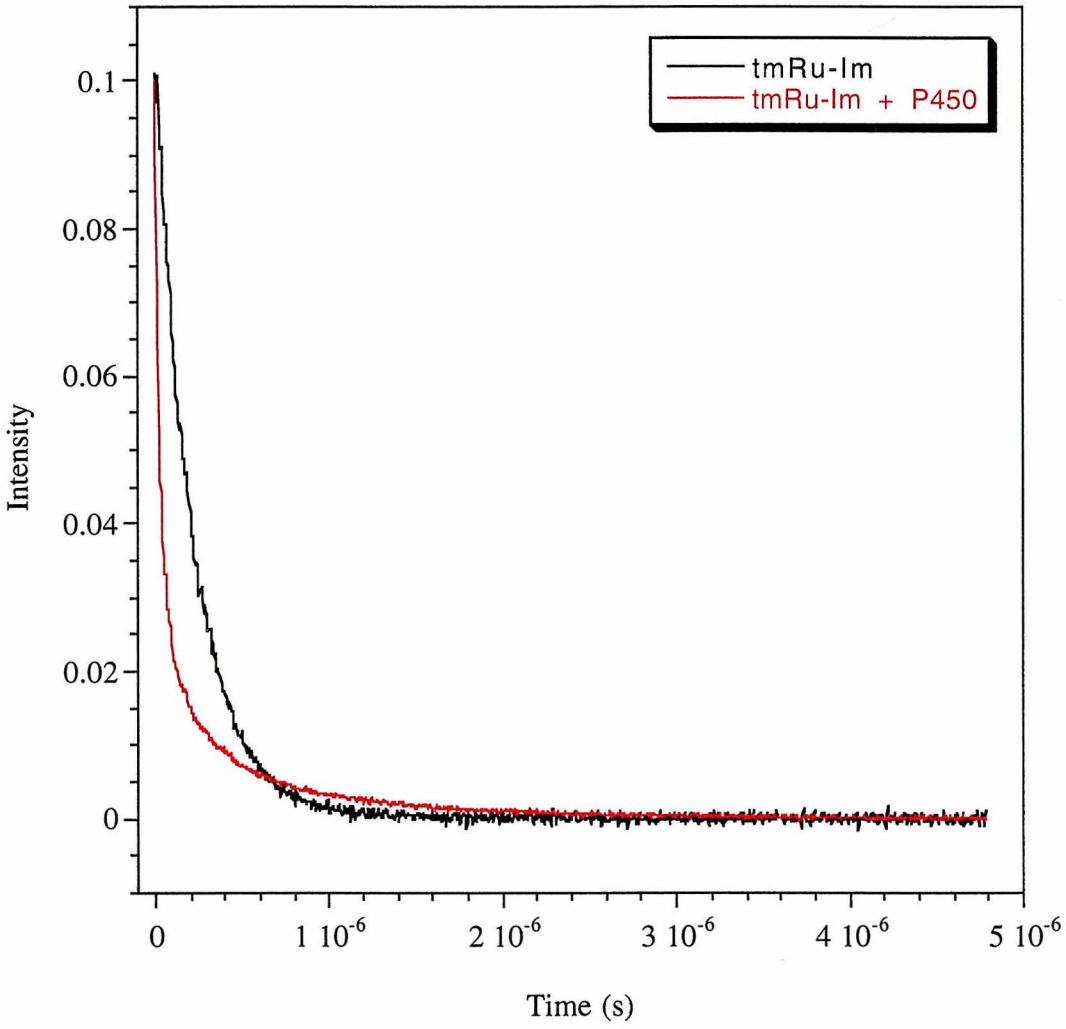
tmRu-Im
tmRu-Im + P450
Intensity
0.1
0.08
0.06
0.04
0.02
0
0
1 10-6
2 10-6
3 10-6
4 10-6
5 10-6
Time (s)

Figure 6.6. Transient absorption kinetics profile of P450 bound to (c), collected at 445 nm (top) and 420 nm (bottom). P450] = [Ru] = 11 μM, laser power = 3.3 mJ/pulse.

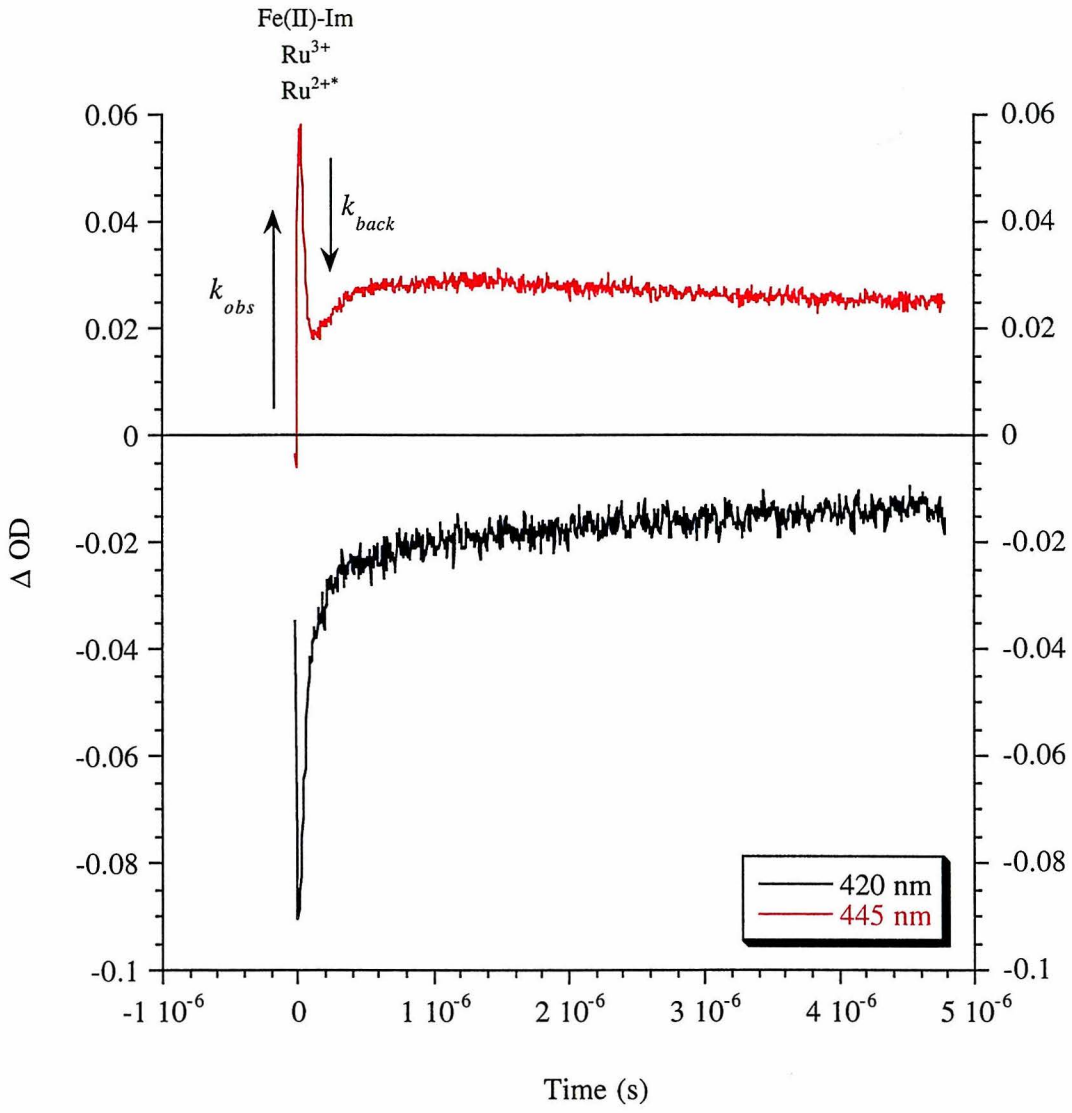
Fe(II)-Im
Ru3+
Ru2+*
k back
k obs
0.06
0.04
0.02
0
-0.02
-0.04
-0.06
-0.08
-0.1
Δ OD
-1 10-6
0
1 10-6
2 10-6
3 10-6
4 10-6
5 10-6
Time (s)
420 nm
445 nm

Figure 6.7. Top: Transient absorption of the excited state of Ru-biphenF_8-im, collected 10 ns after laser excitation ([Ru] = 8.9 μM, laser power = 3.3 mJ/pulse). Bottom: Transient absorption of the P450:Ru-biphenF_8-im complex, collected 30 ns after laser excitation ([P450] = [Ru] = 8.9 μM, laser power = 3.3 mJ/pulse). Δ Absorption intensities were obtained by fitting transient absorption kinetics for several different wavelengths in the Soret region. At 30 ns, the observed difference spectrum is a sum of the absorption changes caused by Ru^{2+*} (shown above, $\Delta\varepsilon$ Ru^{2+*} - Ru^{2+} = - 2400 $M^{-1}cm^{-1}$ at 445 nm, -1500 $M^{-1}cm^{-1}$ at 420 nm), Ru^{3+} ($\Delta\varepsilon$ Ru^{3+} - Ru^{2+} = -9000 $M^{-1}cm^{-1}$ at 445 nm, −6000 $M^{-1}cm^{-1}$ at 420 nm), and P450 Fe^{2+}-Im ($\Delta\varepsilon$ Fe^{2+} - Fe^{3+} = 81,000 $M^{-1}cm^{-1}$ at 445 nm, −82,000 $M^{-1}cm^{-1}$ at 420 nm, calculated from the spectra shown in Figure 6.5).

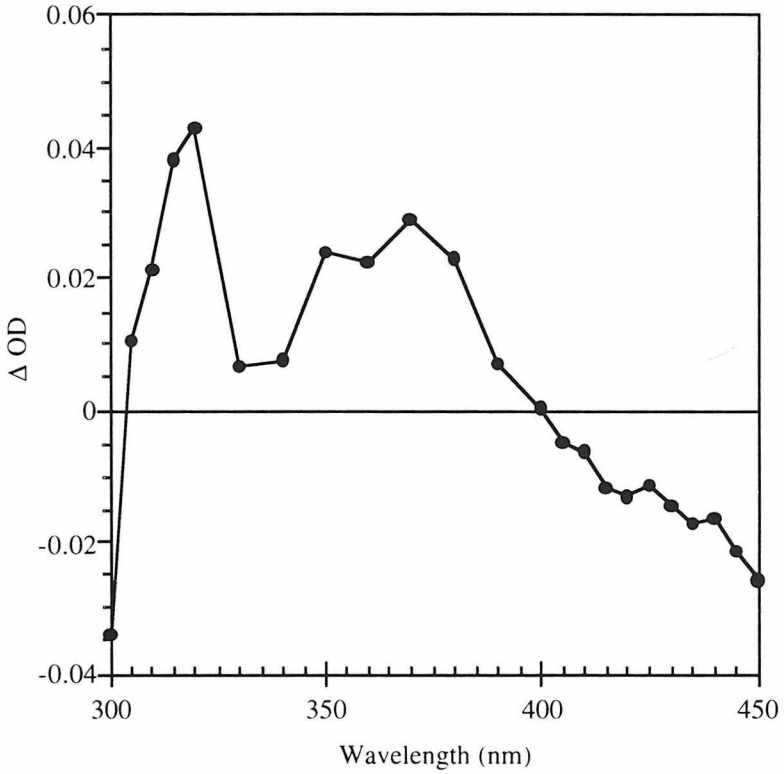
0.06
0.04
0.02
0
-0.02
-0.04
Δ OD
300
350
400
450
Wavelength (nm)

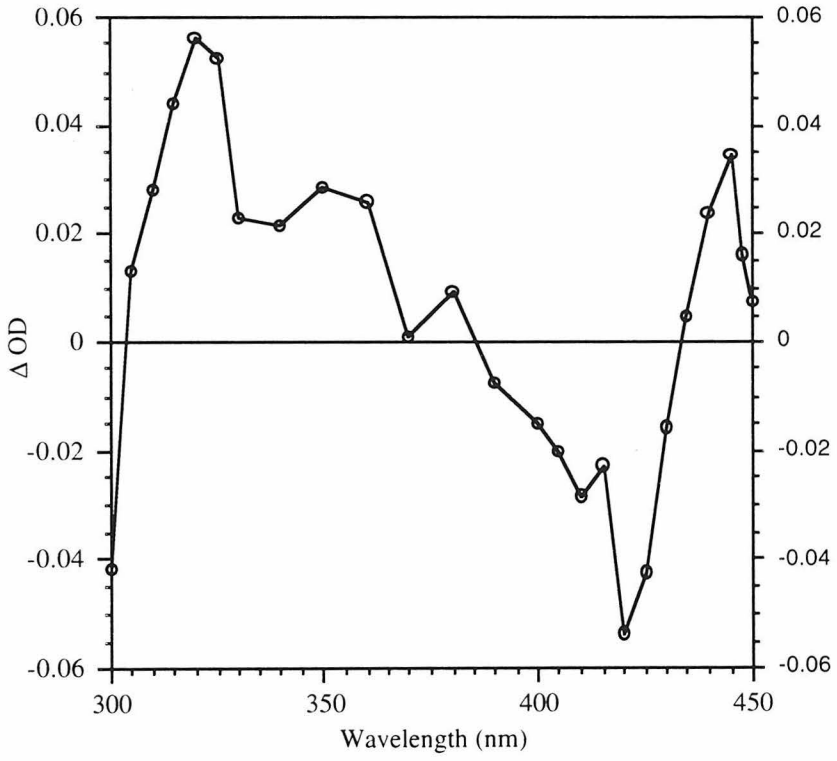
0.06
0.04
0.02
0
-0.02
-0.04
-0.06
Δ OD
300
350
400
450
Wavelength (nm)

Figure 6.8. UV-vis absorption spectra of tmRu-biphenF_8-Im (c) alone and complexed with both ferric and ferrous P450; all species are 5.2 μM. The Fe^{2+}-Im spectrum is not shown below 400 nm, because dithionite dominates the absorbance in this region. Extinction coefficients at the absorbance maxima of ferric (ε_{420} = 100,000 $M^{-1}cm^{-1}$) and ferrous (ε_{445} = 103,000 $M^{-1}cm^{-1}$) are quite similar. tmRu-biphenF_8-Im has an absorbance maximum at 444 nm (ε_{444} = 14,500 $M^{-1}cm^{-1}$). In the ferrous state, the P450 Q-bands coalesce and gain intensity (ferric, ε_{540} = 11,000 $M^{-1}cm^{-1}$, ε_{568} = 10,000 $M^{-1}cm^{-1}$; ferrous, ε_{546} = 12,700 $M^{-1}cm^{-1}$), as is typical for P450:imidazole complexes.

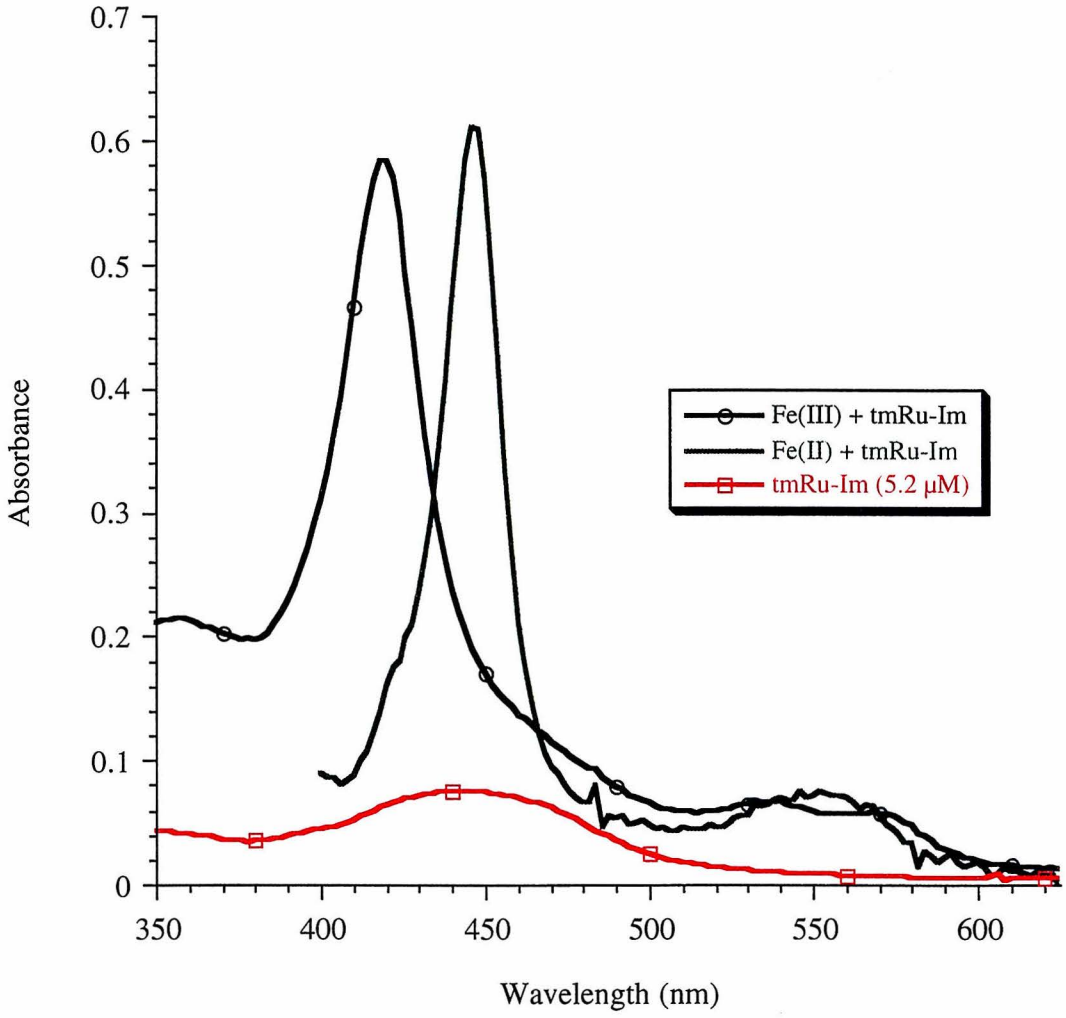
0.7
0.6
0.5
0.4
0.3
0.2
0.1
0
Absorbance
350
400
450
500
550
600
Wavelength (nm)
Fe(III) + tmRu-Im
Fe(II) + tmRu-Im
tmRu-Im (5.2 μM)

Fe^{2+}:imidazole-Ru complex persists for several hours at room temperature without degradation.

Direct Photoinduced Reduction

Having established that excited-state ET, Ru^{2+*}-->Fe^{3+}, occurs with conjugated Ru-Im probes (b) and (c), it remains to determine the rates of both the forward and back, Fe^{2+}-->Ru^{3+}, ET processes. The observed rate (k_{obs}) at which the ruthenium excited state decays is the sum of three competing first-order processes: ET (k_{ET}), energy transfer (k_{en}), and the intrinsic (radiative + nonradiative) decay to ground state (k_d) (Eq. 6.1).

$$k_{obs} = k_{ET} + k_{en} + k_d \qquad (6.1)$$

k_d may be determined by time-resolved emission experiments of the Ru-probes themselves, alone in solution. Since all of the Ru^{2+*} emission profiles are biphasic exponential decays in the presence of P450, it is best to subtract the unquenched rate (k_d) from the quenched rate (k_{obs}) in order to get $k_{obs} - k_q = k_{ET} + k_{en}$. Solving for k_{ET} requires finding the yield of reduction based on the concentration of *bound* excited state generated each laser pulse. Based on the dissociation constant for calculated for (b) and (c):

$$\%Ru^{2+*}(bound) = \%Ru(bound) \times [Ru^{2+*}] \qquad (Eq.\ 6.2)$$

Figure 6.9. Power dependence of the ΔOD at 445 nm ([P450] = [tmRu-biphenF_8-Im] = 10 μM). Saturation occurs ~ 3.3 mJ/pulse, showing that nearly 100% of the Ru has been excited.

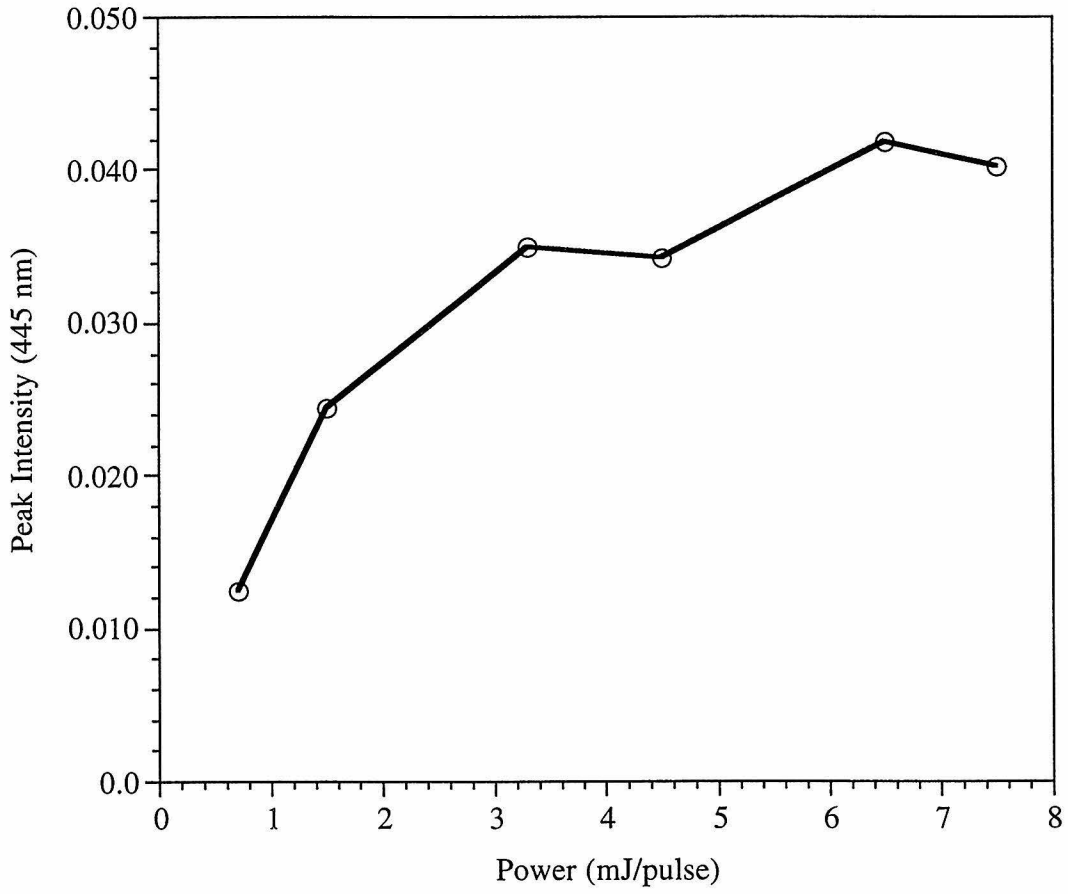
0.050
0.040
0.030
0.020
0.010
0.0
Peak Intensity (445 nm)
0
1
2
3
4
5
6
7
8
Power (mJ/pulse)

The dependence of the ET rate on excited-state yield makes such calculations extremely sensitive to the laser power. Power dependence studies gave a good indication of the fraction of the ruthenium excited with each laser shot (Figure 6.9). It was found empirically that exciting the sample with more than ~ 3.3 mJ/pulse (beam diameter ~2 mm) was sufficient to achieve nearly quantitative Ru^{2+*}. Additionally, the ΔOD amplitudes (from fits of kinetics traces) make it is possible to calculate the concentration of Ru^{2+*} at 370 nm (Ru^{2+*} - Ru^{3+}, $\Delta\varepsilon = 8050\ M^{-1}cm^{-1}$, work by I.J. Chang). Calculations of the Fe^{2+} yield can be made at 420 nm (Fe^{2+}-Fe^{3+}, $\Delta\varepsilon = -82{,}000\ M^{-1}cm^{-1}$), and at 445 nm ($Fe^{2+}$-$Fe^{3+}$, $\Delta\varepsilon = 81{,}000\ M^{-1}cm^{-1}$, once the back reaction is taken into account (Eq 6.3):

$$\frac{\partial(Fe^{II})}{\partial t} = k_{ET}[Ru^{2+*}] - k_{back}[Fe^{2+}] \qquad \text{(Eq. 6.3)}$$

From Eq. 6.1 and the definition of a first-order rate expression, we get:

$$\frac{\partial(Ru^{2+*})}{\partial t} = k_{obs}[Ru^{2+*}] \qquad \text{(Eq. 6.4)}$$

which integrates to:

$$[Ru^{2+*}] = [Ru^{2+*}]_0\ e\text{^}(-k_{obs}t) \qquad \text{(Eq. 6.5)}$$

where $[Ru^{2+*}]_0$ is the initial concentration of *bound* excited-state Ru. Plugging this back into Eq. 6.3, we get:

$$\frac{\partial(Fe^{II})}{\partial t} = k_{ET}[Ru^{2+*}]_0\ e\text{^}(-k_{obs}t) - k_{back}[Fe^{2+}] \qquad \text{(Eq. 6.6)}$$

Solving the differential equation for Fe^{II} as a function of time gives:

$$Fe^{II}(t) = \frac{k_{ET}\,[Ru^{2+*}]_0}{k_{back} - k_{obs}} \left(e\,\wedge(-k_{obs}t) + e\,\wedge(-k_{back}t)\right) \qquad \text{(Eq. 6.7)}$$

Thus, plugging in the concentration of Fe^{II} and the time (t) yields k_{ET}, since all of the other variables are experimentally measurable quantities. For the P450:(c) complex ([P450] = [Ru] = 8.9 μM; [unbound Ru] = 1.85 μM, $\Delta\varepsilon$ = -2400 $M^{-1}cm^{-1}$ at 445 nm), the maximum ΔOD at 445 nm (observed at 30 ns) was 40 ± 2 mOD (Figure 6.8). Adjusting for the bleach from the unbound Ru^{2+*} at 445, the ΔOD at 445 nm increases to 44.5 mOD. Since $[Ru^{3+}] = [Fe^{2+}]$, and $\Delta\varepsilon(Ru) / \Delta\varepsilon(Fe) = 1/9$ at 445 nm, the total absorbance change due to the reduction of iron is adjusted upward to 49.5 mOD, which corresponds to 0.61 μM Fe^{2+}-Im (8.7% yield based on bound Ru). Plugging this concentration (at t = 30 ns) into Eq. 6.7 with a measured back electron transfer rate, k_{back}, of 3 x 10^7 s^{-1}, and a k_{obs} of 3.9 x 10^7 s^{-1}, yields an ET rate, k_{ET} = 8.1 x 10^6 s^{-1}. Evaluating Eq. 6.1 gives k_{en} ~ 2.6 x 10^7 s^{-1}, which is a factor of 3 faster than predictions for a Förster energy-transfer process. Judging from the energy-transfer rate and distance found in the P450:(a) complex, k_{en} should be roughly 9.5 x 10^6 s^{-1}. Using this value, Förster analysis of the overlap between $tmRu^{2+*}$ emission and P450 absorption spectra predicts R_0 = 22.1 Å and a Ru-Fe distance of 17.7 Å, in good agreement with the crystal structure (Table 1).

The reason for the discrepancy between calculated and predicted rates stems from one of three reasons: 1) the calculated yield of reduced P450 is only 25% of the true value, 2) the back ET rate is considerably faster (~ 1 x 10^8 s^{-1}) than measured and is poorly resolved in the response time of the instrument, or 3) the majority of Ru^{2+*} decays by a different and unassigned pathway (i.e., Dexter energy transfer). Without further experiments, particularly picosecond transient absorption, and better spectral deconvolution, it will be difficult to discriminate between these alternate explanations.

Yields of reduction in the P450:Ru-biphenF_8-im complex, observed 5 μs after laser excitation, are 1 ± 0.5% (based on the fraction of bound Ru) using the procedure described for tmRu-biphenF_8-Im. This yield predicts that the rate of electron transfer is approximately 1 x 10^6 s^{-1}, and by Förster analysis, R_0 = 22.1 Å, and Ru-Fe = 17.7 Å. The transient absorption kinetics (Figure 6.3) fail to exhibit the submicrosecond reduction phase observed with (c), but otherwise yield similar spectral features.

Interestingly, in P450 complexes of both (b) and (c), the ground state back electron transfer (Ru^{3+}-Im-Fe^{2+} → Ru^{2+}-Im-Fe^{3+}) does not return all of the enzyme to its resting ferric state. In fact, three observably different back ET processes whose rates span 6-7 orders of magnitude are observed. Since the OD changes are much larger with (c), and the back ET rates are similar for both compounds, our analysis shall focus on the latter.

Figure 6.10. Diode array spectra of direct photoinduced reduction of the (P450) Fe^{3+}-im-biphenF_8-Rutm complex at various time intervals after laser excitation. The reduced enzyme returns to the ferric resting state by three different channels, with some of the ET products persisting for up to a second.

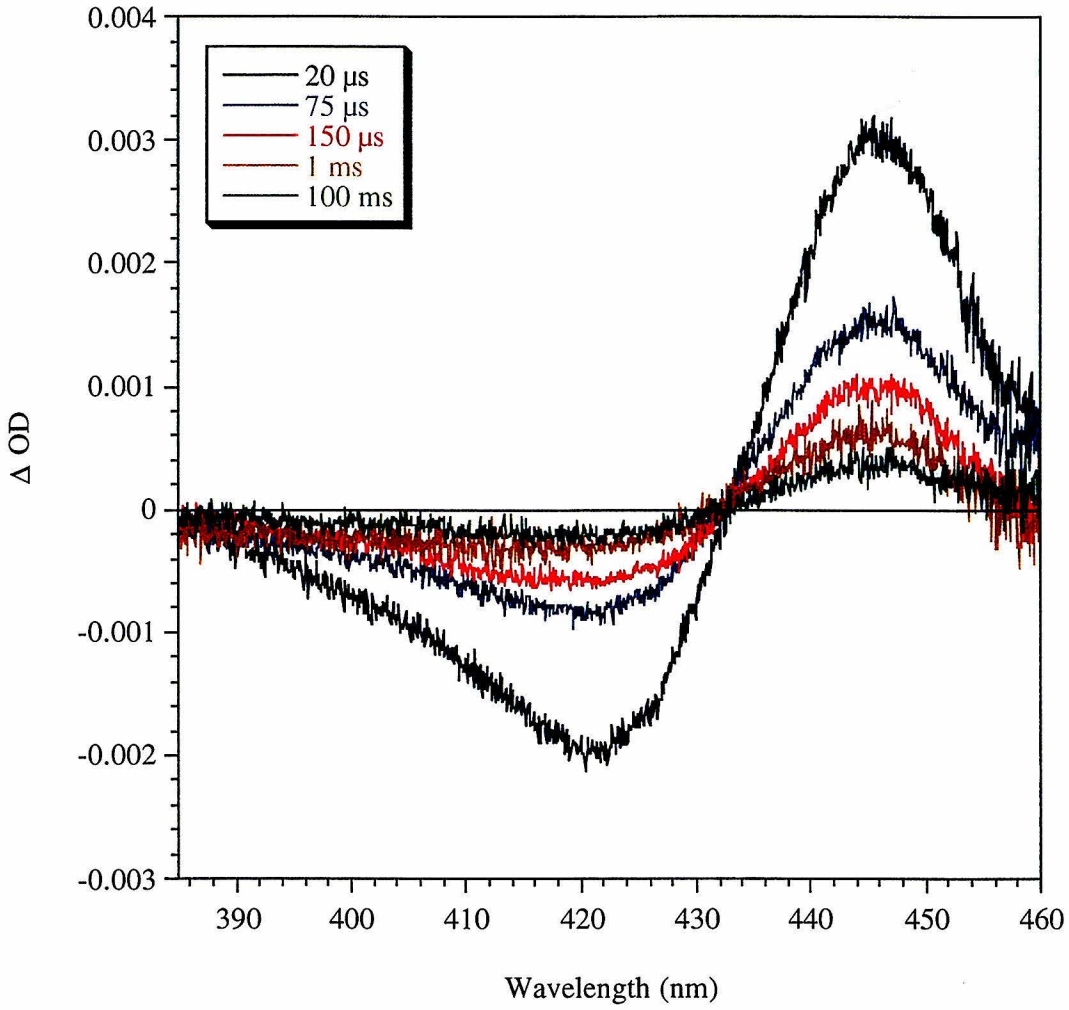
0.004
0.003
0.002
0.001
0
-0.001
-0.002
-0.003
Δ OD
20 µs
75 µs
150 µs
1 ms
100 ms
390
400
410
420
430
440
450
460
Wavelength (nm)

Any explanation for the three observed back ET rates must be consistent with the observation that the initially formed Fe^{2+}-Im P450 species bleaches but does not change its spectral profile (i.e., imidazole remains bound) during the entire back reaction (microseconds to seconds). The diode array spectrum of (c) shows a consistently red-shifted Soret on all time scales (Figure 6.10). Having excluded, therefore, the possibility of ligand exchange, and considering that bimolecular ET reactions should not compete with the rapid intramolecular (Ru^{3+}-im-Fe^{2+} → Ru^{2+}-im-Fe^{3+}) ET, it is most likely that the protein scavenges some of the Ru^{3+}. Indeed, Tyr 29 has recently been implicated in the chiral discrimination of Ru-substrates binding to the P450 channel (10). Based on the yield of reduced P450 at 5 μs (~ 2%) relative to 30 ns (~ 9%), and the predicted back ET rate (k_{back} = 3 x 10^7 s^{-1}), we infer that the Tyr → Ru^{3+} ET reaction must be occurring with a rate constant of k ~ 6.0 x 10^6 s^{-1}. The low yields of this reaction make observations of a tyrosine radical ($Tyr^{\bullet+}$) difficult by transient absorption spectroscopy (λ_{max} = 420 nm) (11). Consistent with this explanation, however, is the apparent disappearance of most Ru^{3+} absorbance (observed at 320 nm) by 250 ns. The slower back ET rate (k = 2 x 10^4 s^{-1}) is proposed to occur from Fe^{2+}-Im → $Tyr^{\bullet+}$. The forward and back ET processes are summarized in Figure 6.11.

Most (~ 80%) of the remaining Fe^{2+}-Im appears, in fact, to decay by this second back ET process, but a small fraction of the reduced P450 persists for ~ 1 second after the

Figure 6.11. Overall electron-transfer scheme for photoreduction of the P450:[$Ru(tmbpy)_2(bpy\text{-}biphenF_9\text{-}im)]Cl_2$ complex. Rates of energy transfer and electron transfer are based on the calculated yields of the reduced (Fe^{2+}-im) enzyme (see text for details). For this complex, the dominant decay channel for Ru^{2+*} is ET, presumably due to the fully conjugated path to the heme, and the extra driving force for reduction provided by the tetramethylated bipyridyl ligands. Highly exergonic back electron transfer occurs rapidly from Fe^{2+}-im to Ru^{3+}. Competing with this process is believed to be oxidation of Tyr 29 which sits in close proximity (~ 3 Å) to the Ru moiety, and allows the reduced protein to persist for tens of microseconds. A third back ET pathway (not shown) must involve scavenging of the tyrosyl radical, either by oxidation of exogenous Ru^{2+} or other reductants in solution. This bimolecular process allows a small fraction (~ 5%) of the reduced, imidazole-bound protein to persist for 1 second in solution.

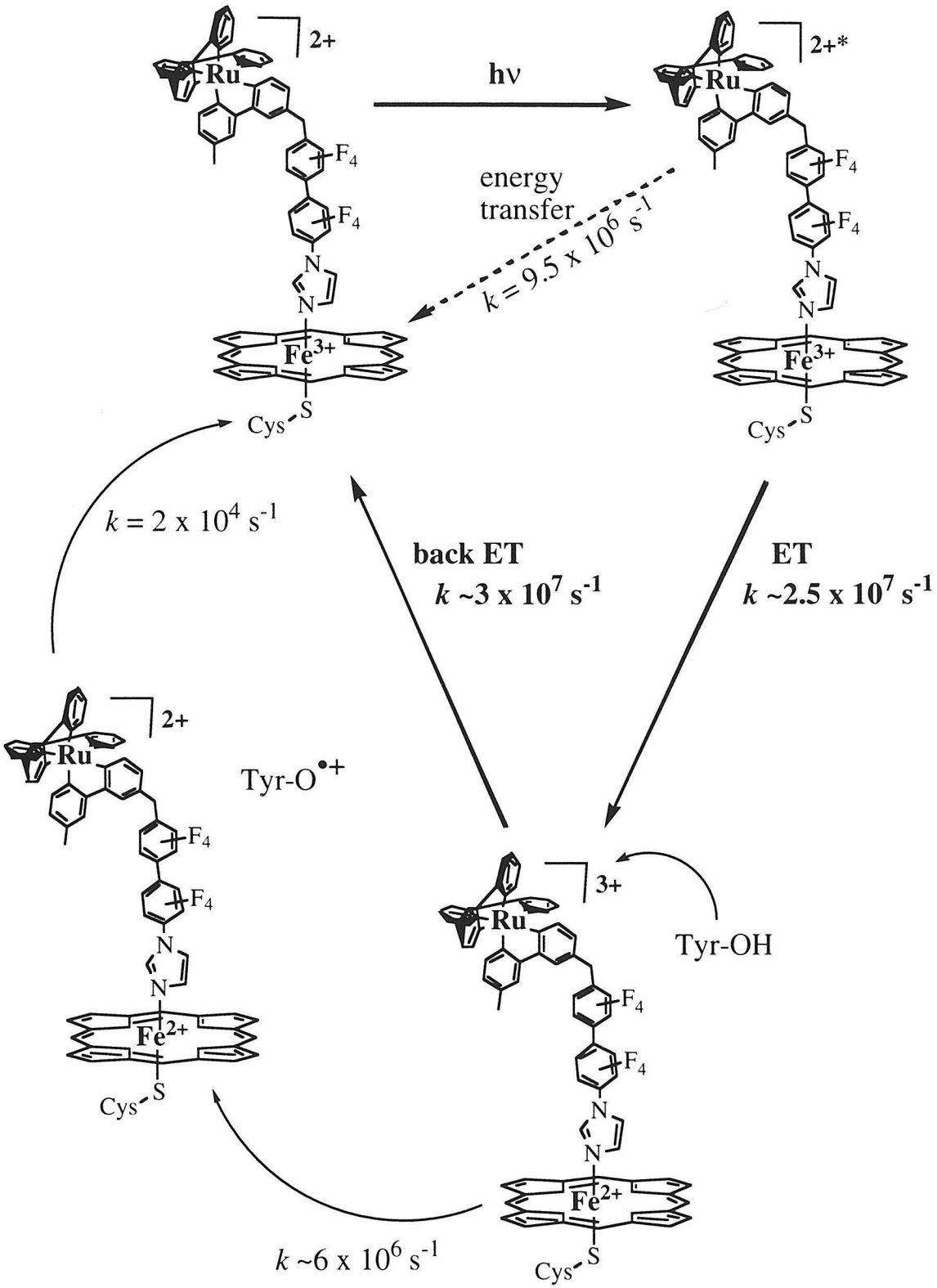
2+
Ru
hν
2+*
F4
F4
energy
transfer
k = 9.5 x 10^6 s^-1
N
N
Fe3+
Cys
S
k = 2 x 10^4 s^-1
back ET
k ~3 x 10^7 s^-1
ET
k ~2.5 x 10^7 s^-1
Tyr-O•+
Fe2+
3+
Tyr-OH
k ~6 x 10^6 s^-1

laser pulse. Presumably, one of several bimolecular processes is at play – bound and free $Ru^{2+/3+}$ exchange reactions, as well as protein-protein ET reactions. In support of this hypothesis is the finding that the addition of micromolar tmRu (e) to a 1:1 P450:(c) complex changed the back electron transfer step from a primarily first-order process to a second-order process dependent on the concentration of (e).

No changes in the Soret were observed upon laser excitation of P450 complexed with perfluorobiphyenyl imidazole (d). Thus, photodissociation appears to be an unlikely process with any of these compounds. Compound (e) and $[Ru(bpy)_3]^{2+}$ were not quenched upon addition of P450, indicating that a tether is essential for binding as well as energy/electron transfer. In all cases, sample integrity was monitored by UV-vis before and after each experiment, and no photo-mediated degradation was observed. Binding of the Ru-probes was shown to be fully reversible by displacing the compounds with camphor and returning the enzyme to its 5-coordinate ferric resting state.

To determine whether rapid electron injection from the Ru excited state of (c) to the heme operates by hopping (bipyridyl → perfluorobiphenyl → heme) rather than tunneling, electrochemistry was performed on both the model compound (e) (Figure 6.12) and on (c) (Figure 6.13). The bridging model compound (d) exhibited quasi-reversible waves by CV as observed previously for perfluorobiphenyl (12). The reduction potential of the bridge lies several hundred millivolts below that of the excited

Figure 6.12. Cyclic voltammogram on an edge-plane graphite electrode of tmRu (e) in acetonitrile at a scan rate of 100 mV s^{-1} at 298 K.

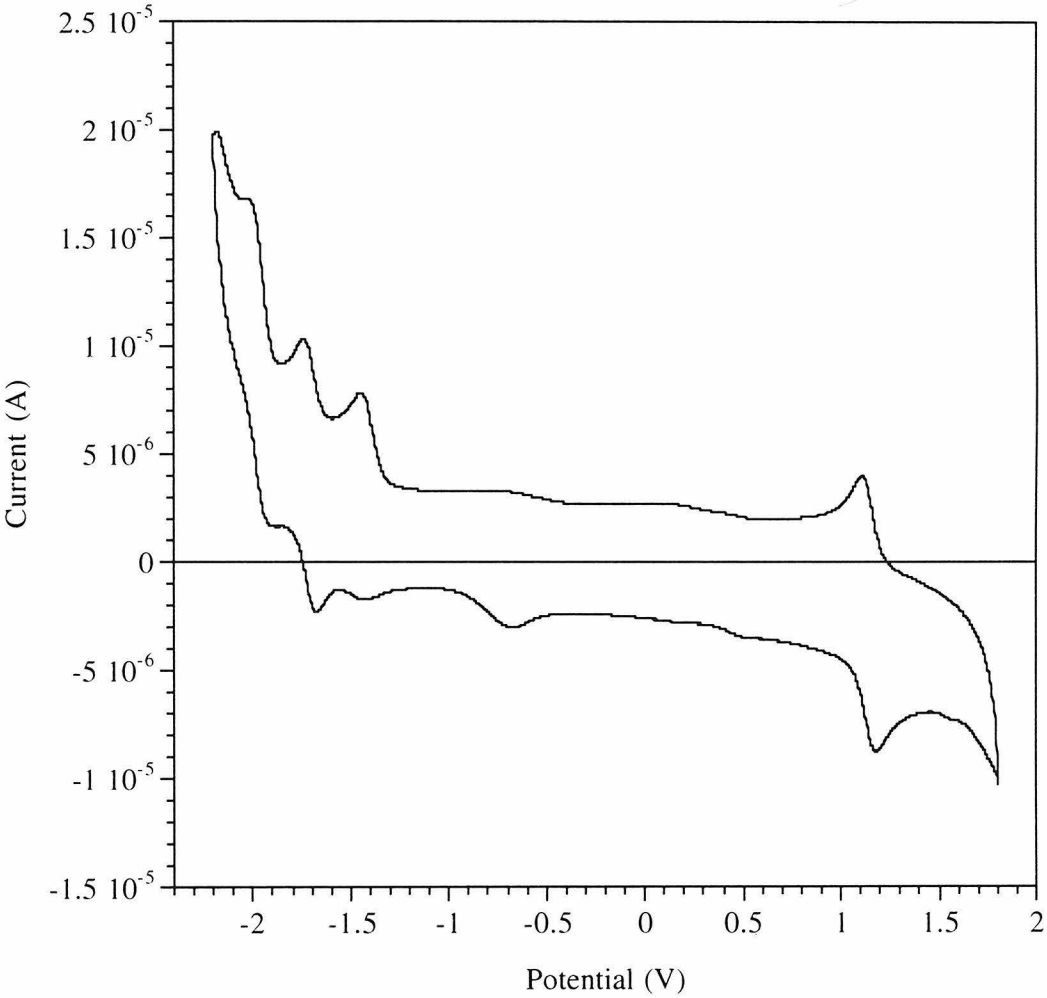
2.5 10-5
2 10-5
1.5 10-5
1 10-5
5 10-6
0
-5 10-6
-1 10-5
-1.5 10-5
Current (A)
-2
-1.5
-1
-0.5
0
0.5
1
1.5
2
Potential (V)

Figure 6.13. Cyclic voltammogram on an edge-plane graphite electrode of tmRu-biphenF_8-im in acetonitrile at a scan rate of 100 mV s^{-1} at 298 K.

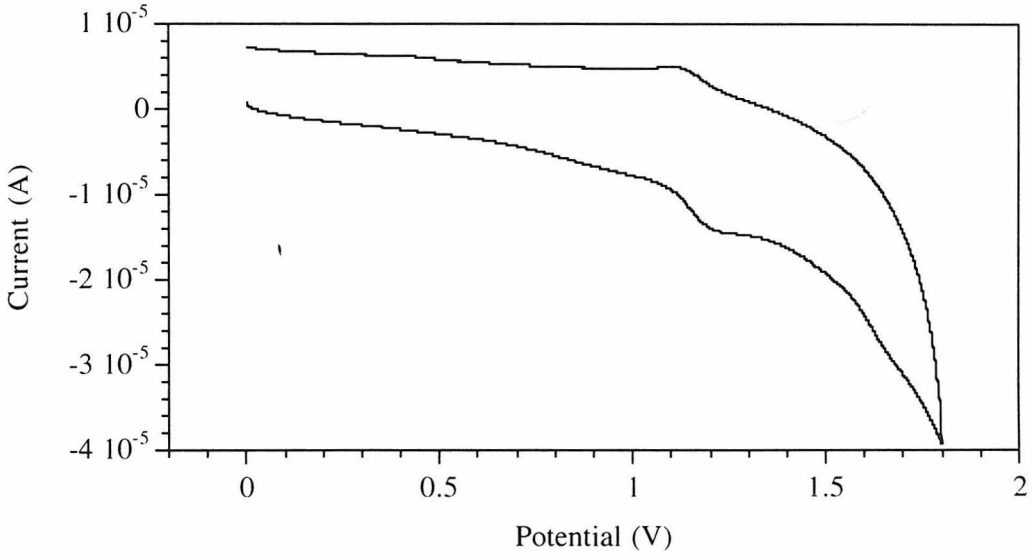
1 10-5
0
-1 10-5
-2 10-5
-3 10-5
-4 10-5
Current (A)
0
0.5
1
1.5
2
Potential (V)

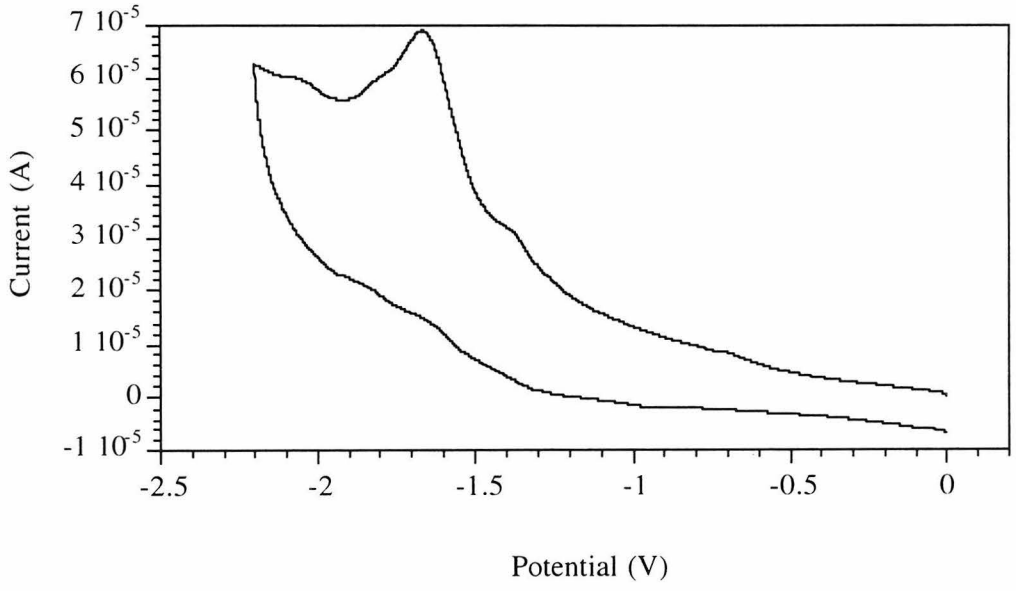
7 10-5
6 10-5
5 10-5
4 10-5
3 10-5
2 10-5
1 10-5
0
-1 10-5
Current (A)
-2.5
-2
-1.5
-1
-0.5
0
Potential (V)

state of (a-c), and electron hopping may be discounted as a viable mechanism for electron transfer.

DISCUSSION

The bulkier, conjugated Ru-probes described in this chapter bind extremely well; (c) binds, in fact, better than the saturated Ru-Im probes synthesized previously (Chapter 2). It is likely that the enhanced affinity is driven by hydrophobic interactions, particularly involving the perfluorinated bridge and the addition of 8 methyl groups on the terminal Ru moiety. Evidently, the greater steric bulk does not preclude binding, and raises the question of how close to the heme a slightly smaller photosensitizer (i.e., $[Ru(CN)_4(bpy)]^{2-}$) might bind the active site. Energy-transfer calculations predict that (b) and (c) bind 2-3 Å closer to the heme than the Ru-probes described in Chapter 2. The rigidity of the conjugated bridge, and also, perhaps, the angle at which the bridge is canted from the bipyridyl ligand (Figure 6.1), appears to promote a smaller Ru-Fe distances.

It is quite possible that the heme iron does not covalently bond (perfluorobiphenyl)imidazole in the ferric state. The Soret and Q-bands are only

modestly red-shifted, with the relative intensities of the α and β bands changing slightly relative to the Fe^{3+}-OH_2 resting state (Figure 6.2). This behavior contrasts the binding of imidazole and Ru-C_{13}-Im which red shift the Q-bands by several nanometers. In principle, the imidazole could act as a Lewis base and deprotonate Fe^{3+}-aquo; the modestly red-shifted Soret would then correspond to a Fe^{3+}-hydroxy species.

Interestingly, the imidazole-perfluorobiphenyl model compound (d) shows a similar absorption spectrum (λ_{max} = 420 nm) upon binding P450 in the ferric state. This suggests that the lack of significant absorbance changes may be due to the electron-withdrawing nature of the perfluorobiphenyl bridge rather than the size of these conjugated molecules. The predicted π-acidity and weakened σ-donating ability of this interesting new imidazole ligand would greatly stabilize lower oxidation states, and, in fact, the standard Fe^{2+}-Im spectrum (λ_{max} = 446 nm) is observed upon reduction (Figure 6.8). Further support for this hypothesis comes from emission lifetime binding studies of the 1:1 P450:(b) complex; the Ru^{2+*} profile is highly quenched by ET and predominantly monophasic, suggesting that the Ru-Im probe is much more tightly bound to Fe^{2+} P450. A strong preference for imidazole in the ferrous oxidation state is quite unusual for heme enzymes, and points to a complex equilibrium in the ferric state. Such ligand exchange processes should be pH sensitive and will be explored in the future with UV-vis and

electrochemical measurements, as well in experiments with ruthenium model compounds to determine the π-acidity of this ligand.

The yield of reduced P450 ($Ru^{2+*}/Fe^{3+} \rightarrow Ru^{3+}/Fe^{2+}$) appears to depend heavily on the excited-state driving force as well as the availability of a through-bond covalent pathway to the heme. The addition of eight methyl groups on the bipyridyl ligands lowers the reduction potential by approximately 160 mV which increases both the rate of reduction and yield of ET products by an order of magnitude. With both Ru-Im compounds, the reduction potential of the heme is roughly -300 mV vs. NHE (~50 mV higher than that expected for an imidazole-ligated P450 heme, due to the electrophilicity of perfluorobiphenyl). The excited-state reduction potential of (c) is approximately -1.0 V, providing substantial driving force for reduction ($-\Delta G \sim 0.7$ V) in a nearly activationless reaction. The thermodynamics of this reaction await electrochemical measurements and temperature dependence studies.

The advantage of a directly covalent pathway for excited-state electron transfer is evident from the lack of ET products with (a). This Ru moiety is calculated to bind an additional 2 Å from the heme (Table 1), which would require a substantial through-space jump from the biphenyl to the iron. One exciting finding with (a) was that it forms a stable ternary complex with either imidazole or carbon monoxide, as shown by energy-transfer measurements. Photoexcitation of the P450:Ru-biphen:imidazole complex

yielded reduced (Fe^{2+}-Im) protein, due presumably to either a shorter through-space jump or a lower reorganization energy for Fe $^{3+/2+}$-Im than for reduction of the ferric aquo heme. Successful photoinduced ET in this ternary complex bodes well for future studies of dioxygen activation and light-activated substrate turnover.

CONCLUSION

Conjugated sensitizer-linked probes bind with high affinity and promote rapid electron transfer to the buried P450 heme. Submicrosecond rates of electron injection from Ru^{2+*} to the iron agree with experiment and theoretical predictions for well-coupled ET reactions that are nearly driving force optimized (13-16). Large enhancements of the rate and yield of ET were achieved with the use of tetramethylated bipyridyl ligands attached to the Ru photosensitizer. Quantification of the rate of electron injection was complicated by the difficulty of determining the yield of Fe^{2+}-Im formed in this reaction. Conjugated Ru-probes which target the P450 ferrous oxy complex hold great promise for studies of oxygen activation.

REFERENCES AND NOTES

1. J. J. Wilker, I. J. Dmochowski, J. H. Dawson, J. R. Winkler, H. B. Gray, *Angew. Chem. Int. Ed.* **38**, 90-92 (1999).

2. E. J. Mueller, P. J. Loida, S. G. Sligar, in *Cytochrome P450: Structure, Mechanism, and Biochemistry, 2nd edn* P. R. Ortiz de Montellano, Ed. (Plenum Press, New York, 1995) pp. 83-124.

3. I. J. Dmochowski, B. R. Crane, J. J. Wilker, J. R. Winkler, H. B. Gray, *Proc. Natl. Acad. Sci. USA* **96**, 12987-12990 (1999).

4. S. Gould, T. R. O'Toole, T. J. Meyer, *J. Am. Chem. Soc.* **112**, 9490-9496 (1990).

5. K. Miedlar, P. K. Das, *J. Am. Chem. Soc.* **104**, 7462-7469 (1982).

6. K. Kalyanasundaram, *Photochemistry of Polypyridine and Porphyrin Complexes* (Academic Press, Lmtd., London, 1992).

7. T. Förster, in *Modern Quantum Chemistry* O. Sinanoglu, Ed. (Academic Press, New York, 1965), vol. III, pp. 93-137.

8. J. H. Dawson, L. A. Andersson, M. Sono, *J. Biol. Chem.* **257**, 3606-3617 (1982).

9. J. H. Dawson, L. A. Andersson, M. Sono, *J. Biol. Chem.* **258**, 13637-13645 (1983).

10. I. J. Dmochowski, J. R. Winkler, H. B. Gray, *J. Inorg. Biochem. (in press)* (2000).

11. Y. Chen-Barrett, et al., *Biochemistry* **34**, 7847-7853 (1995).

12. B. H. Campbell, *Anal. Chem.* **44**, 1659-1663 (1972).

13. R. A. Marcus, N. Sutin, *Biochim. Biophys. Acta* **811**, 265-322 (1985).

14. H. B. Gray, J. R. Winkler, *Annu. Rev. Biochem.* **65**, 537-561 (1996).

15. A. Helms, D. Heiler, G. McLendon, *J. Am. Chem. Soc.* **114**, 6227-6238 (1992).

16. W. B. Davis, W. A. Svec, M. A. Ratner, M. R. Wasielewski, *Nature* **396**, 60-63 (1998).

APPENDIX A

P450, Pd, and PdR Growth, Purification, and Handling

Acknowledgements:

The molecular biology and protein purification expertise of Alex Bilwes and Brian Crane contributed immeasurably to the development of efficient P450 growth and purification strategies.

MATERIALS AND METHODS

General

Absorption spectra were recorded on an HP-8452A spectrophotometer. All reagents were of the highest available quality. Distilled water was further purified by a Barnstead Nano-Pure system and filtered through a 0.2 μM membrane before use in FPLC purifications. The pH of buffer solutions was typically checked with a Beckman pHI-32 pH meter standardized against pH 7 and 10 buffer solutions (VWR). All FPLC columns and equipment were obtained from Pharmacia.

Transforming cells to make P450, Pd, or PdR

The following procedure works best with fresh plasmid; if the P450 plasmid is of suspect purity, fresh plasmid should be grown. The procedure for growing fresh plasmid requires transforming the P450 cDNA (pUS 200 is wild type), isolating colonies, growing 10 mL of cells in terrific broth (TB), and isolating the pellet. Isolation of the plasmid from the pellet was performed by following directions on p. 18 of the QIAPrep Handbook. Cell transformation, in any case, is a necessary step for cell growth. Any P450 prep should begin with freshly transformed cells.

The P450 plasmid was dissolved in buffer to make a 25 ng/μL solution (check by UV absorbance, A_{max} = 0.5). The plasmid (2 μL) and 50 μL of either super competent Nova Blue cells or TB-1 competent cells were put in an eppendorf tube, and left on ice for 30 minutes. Then, the tube was placed in a 42 °C bath for 45 seconds, and returned to the ice for 2 minutes. SOC media (300 μL) was added, and the tube was shaken at 37 °C for 1 hour. This step allows the cell walls to rebuild before exposure to ampicillin.

An aliquot (20 μL) was poured onto one room temperature agar plate (with ampicillin), and the remaining solution poured onto a second plate. The liquid was spread on the plates with either sterilized glass beads or a glass rod. The plates were left at 37 °C for roughly 16 hours, after which large single colonies were evident. The identical cell transformation procedure was followed for Pd (with pDS 200 plasmid) and PdR (with pDS 301 plasmid).

P450 Growth

A single colony was picked with a sterile toothpick, then dropped into a 1 L flask containing 200 mL of sterilized terrific broth (TB) and freshly added ampicillin (~ 50 mg/200 mL). The flask was shaken vigorously for 12 hours at 37 °C, during which time the solution became very cloudy. Then, the cells were spun down by ultracentrifugation (50,000 rpm, 30 minutes) and the supernatant discarded. The cell pellet was transferred

to a 6 L flask containing 2 L of sterilized TB and fresh ampicillin. The flask was shaken at 37 °C for approximately 14 hours, or until the reddish color of the cells appeared to be saturated. After 12 hours of growth, the color was monitored every 2 hours by centrifuging small aliquots from the flask. Again, the cells were isolated by ultracentrifugation with yields of generally 5 g of reddish cell paste/L of TB. The cells were either frozen and stored indefinitely or taken on directly to the purification steps.

A 3-Day P450 Purification

After cell lysis, it is important to perform the first anion exchange column as quickly as possible since it removes all proteases and nucleic acids. After this stage, if the protein is kept refrigerated, and in the presence of camphor, KCl, and DTT, it degrades only very slowly to its inactive form, the catch-all "P420" state. Elevated temperatures and organic solvents (i.e. acetone) particularly accelerate this process, especially in the absence of camphor. Separation of P450 and P420 by chromatography, while possible, is somewhat difficult. Thus, it is advised to handle the protein quickly but carefully. The simple purification procedure listed below can be performed in less than three days.

Five buffers were used for the following purification steps. Buffer A is 40 mM potassium phosphate (KPi), pH 7.5, containing 1 mM camphor (dissolve in 1 mL ethanol,

add to 1 L water), and 2 mM DTT. Buffer B is the same as buffer A, with the addition of 1 M KCl. Buffer C is the same as buffer A, except at pH 6.5. Likewise, buffer D is the same as buffer B, at pH 6.5. Buffer P is buffer A with 100 mM KCl—the protein is quite stable in this buffer, even at room temperature. It is worth noting, however, that DTT binds P450, and both DTT and camphor were removed before substrate binding assays with a PD-10 (gel filtration) column.

Cell lysis was most efficiently accomplished by sonication. First, the cells were dissolved in a tall glass beaker with roughly 5 mL of buffer A per gram of cell paste. A spatula tip of lysozyme was added to further promote cell lysis. While magnetic stirring, and with the cells on ice, the sample was sonicated on full power (using the large probe). One-minute intervals, spaced 5 minutes apart to minimize foaming, were performed at least 5 times until the solution appeared homogeneous and dark red. Next, the P450 solution was transferred to 25-mL ultracentrifuge tubes, whose weight was balanced by pairs. Spinning down the solutions (50,000 rpm, 1 hour, 4 °C) gave brownish pellets. The *top half* of the supernatant was carefully pipetted and filtered using a 0.2 μm Nalgene filter. Care was taken to avoid pipetting the precipitate, since this clogs the filter. Gradually, the remaining supernatant was filtered; more than one filter was often necessary. For slightly higher yields, the pellets were redissolved in buffer A,

ultracentrifuged for 30 minutes, and the supernatant filtered. This filtering step removes all of the (many) insoluble impurities and readies the protein for purification by FPLC.

The general, tried-and-true, purification strategy for P450 is to alternate anion exchange with size exclusion columns until the protein is electrophoretically pure (R_z, OD 392 nm/OD 280 nm, should exceed 1.5). P450 purification is most efficiently achieved by FPLC, although gravity columns are also effective (albeit slower and less precise). All chromatography should be performed at 4 °C. By FPLC, a total of four chromatography steps is generally necessary.

First, a HiPrep 16/10 QXL (fast-flow anion exchange) column was equilibrated with buffer A. Using a superloop, maximum 40 mL of the protein was loaded and injected onto the column. A gradient of buffer B (flow rate = 6 mL/min; 0-80 mL, 0%; 80-140 mL, ramp to 30%, 140-160 mL, 100%, 160-220 mL, 0%) separated the solution into three distinct bands (see Figure A.1). By pooling the red fractions (the middle band), R_z approached 0.6. The protein was highly concentrated (< 3 mL) with an amicon (YM-10 filter), and carefully loaded (minimizing air bubbles) onto a Sephadex 75 (10/60 prep grade) gel filtration column equilibrated with 85% buffer A/15% buffer B. Maintaining the flow rate at 1.0 mL/min (< 0.5 mPa back pressure), the first band appeared at ~ 40 mL, the second (most pure fraction) at 60 mL, and final impurity at 80 mL (see Figure A.2). The most pure fractions (R_z ~ 0.8) were pooled, concentrated to ~ 10 mL, and

Figure A.1. FPLC trace of the first P450 purification step, using a fast flow anion exchange column. The center fraction contained intact P450.

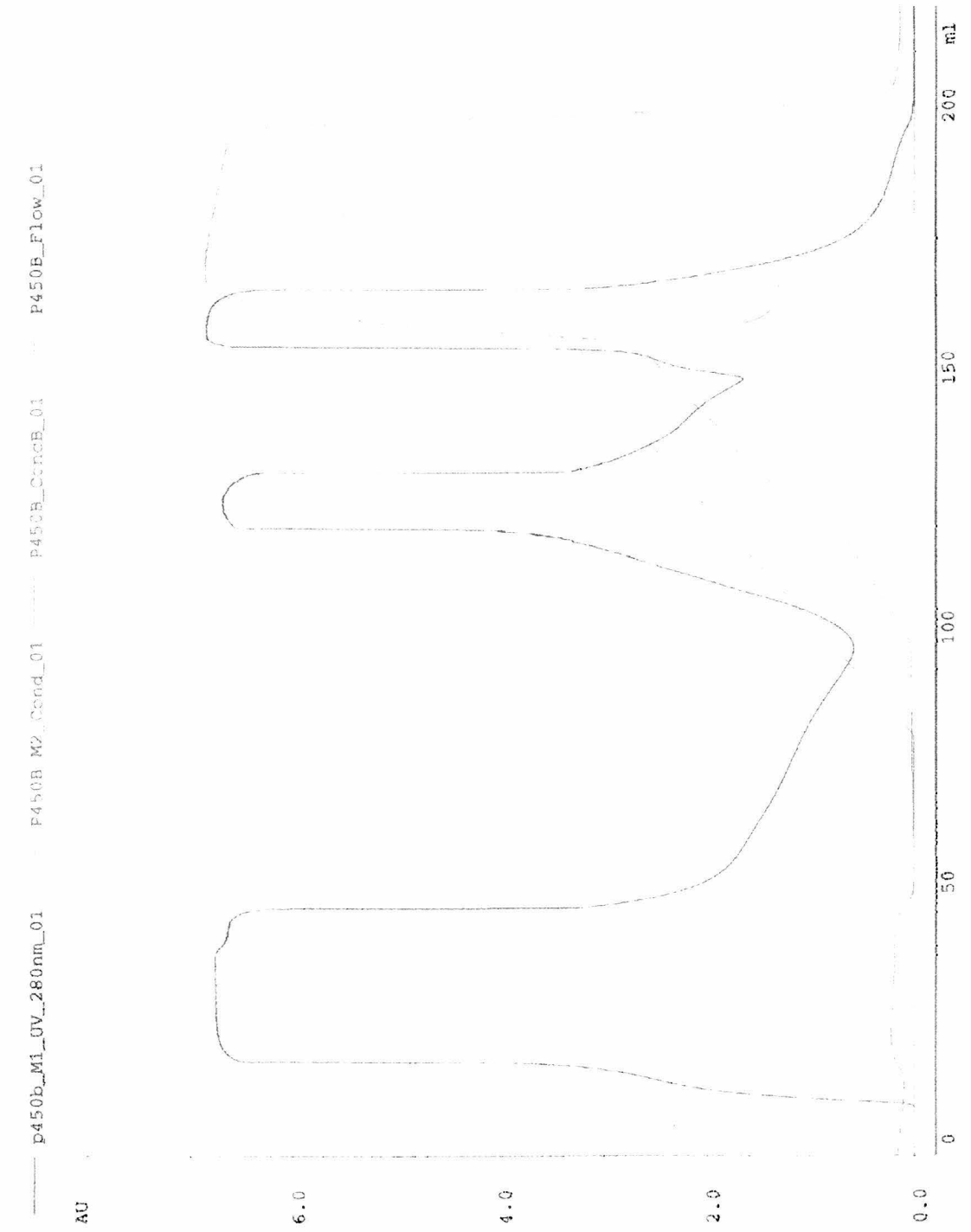
p450b_M1_UV_280nm_01
P450B M2 Cond_01
P450B_ConcB_01
P450B_Flow_01
AU
6.0
4.0
2.0
0.0
0
50
100
150
200
ml

Figure A.2. FPLC trace of the second P450 purification step, using a gel filtration column. The center fraction contained intact P450.

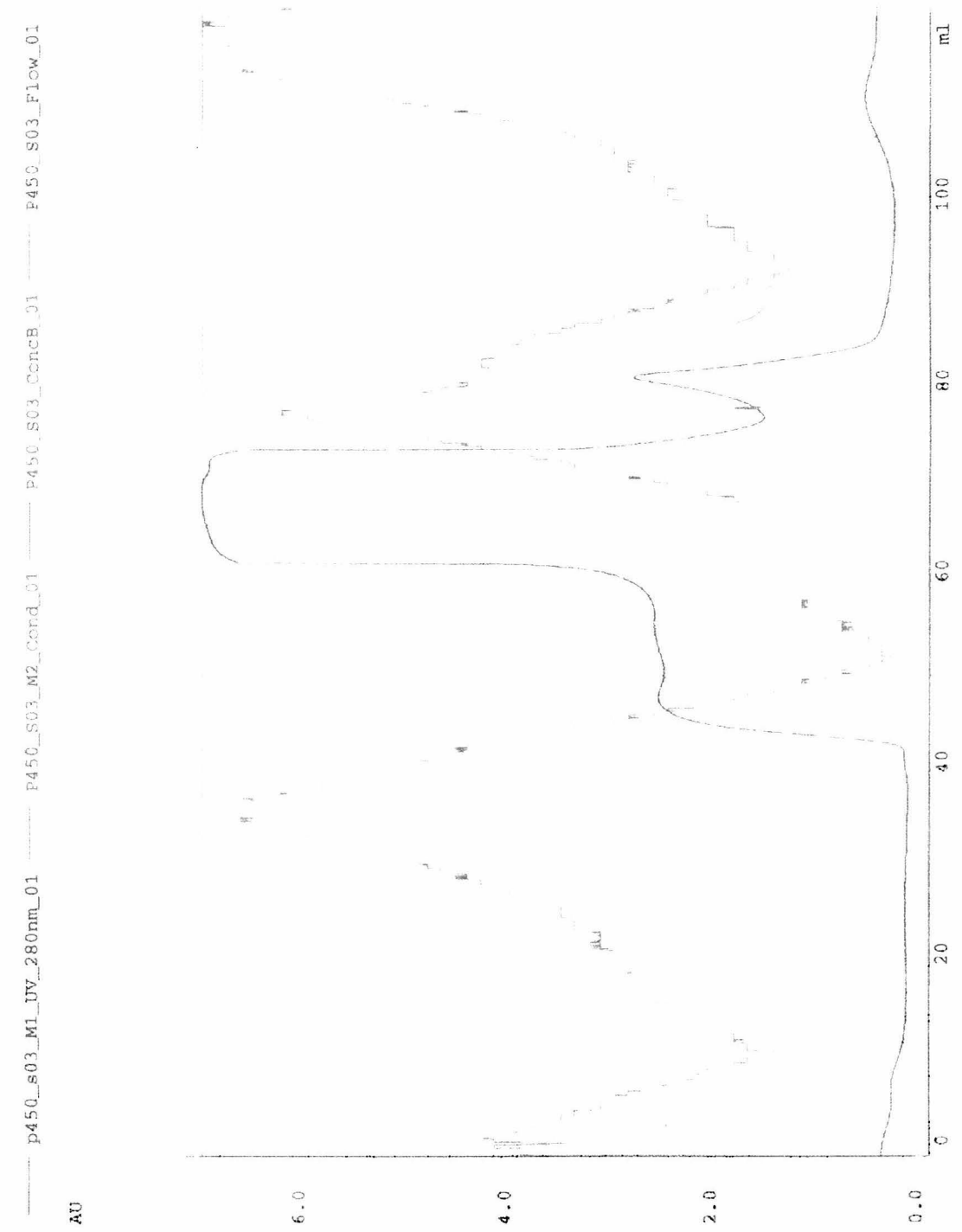
p450_s03_M1_UV_280nm_01
P450_S03_M2_Cond_01
P450_S03_ConcB_01
P450_S03_Flow_01
AU
6.0
4.0
2.0
0.0
0
20
40
60
80
100
ml

Figure A.3. FPLC trace of the third P450 purification step, using a desalting column. The protein elutes first followed by the salt.

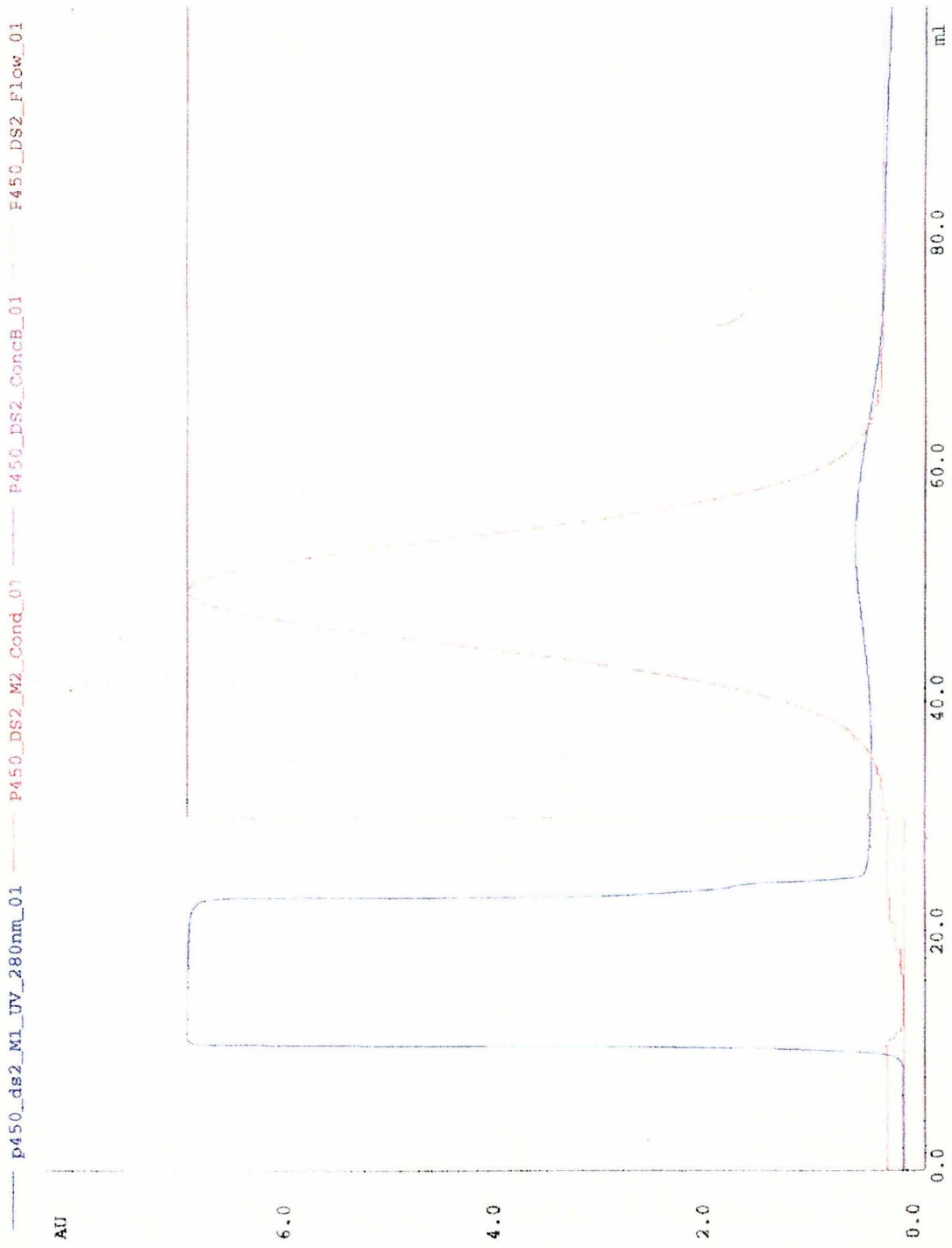
p450_ds2_M1_UV_280nm_01
P450_DS2_M2_Cond_01
P450_DS2_ConcB_01
P450_DS2_Flow_01
AU
6.0
4.0
2.0
0.0
0.0
20.0
40.0
60.0
80.0
ml

Figure A.4. FPLC trace of the fourth P450 purification step, using an anion exchange column. The first major fraction contained nearly pure P450.

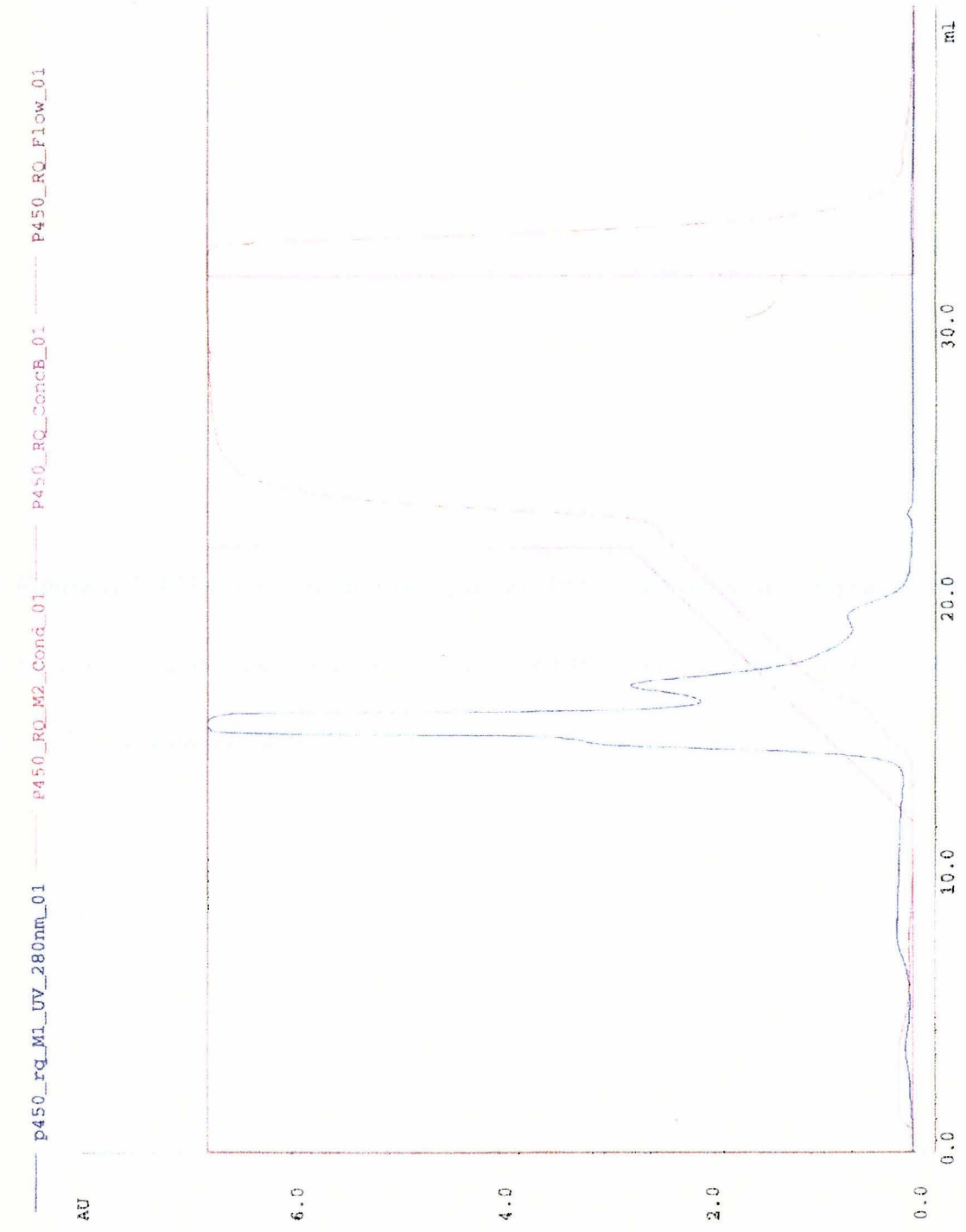
p450_rq_M1_UV_280nm_01
P450_RQ_M2_Cond_01
P450_RQ_ConcB_01
P450_RQ_Flow_01
AU
6.0
4.0
2.0
0.0
0.0
10.0
20.0
30.0
ml

Figure A.5. FPLC trace of the fifth (and last) P450 purification step, repeating the gel filtration column. Only one peak eluted, and the center fractions contained highly purified cytochrome P450.

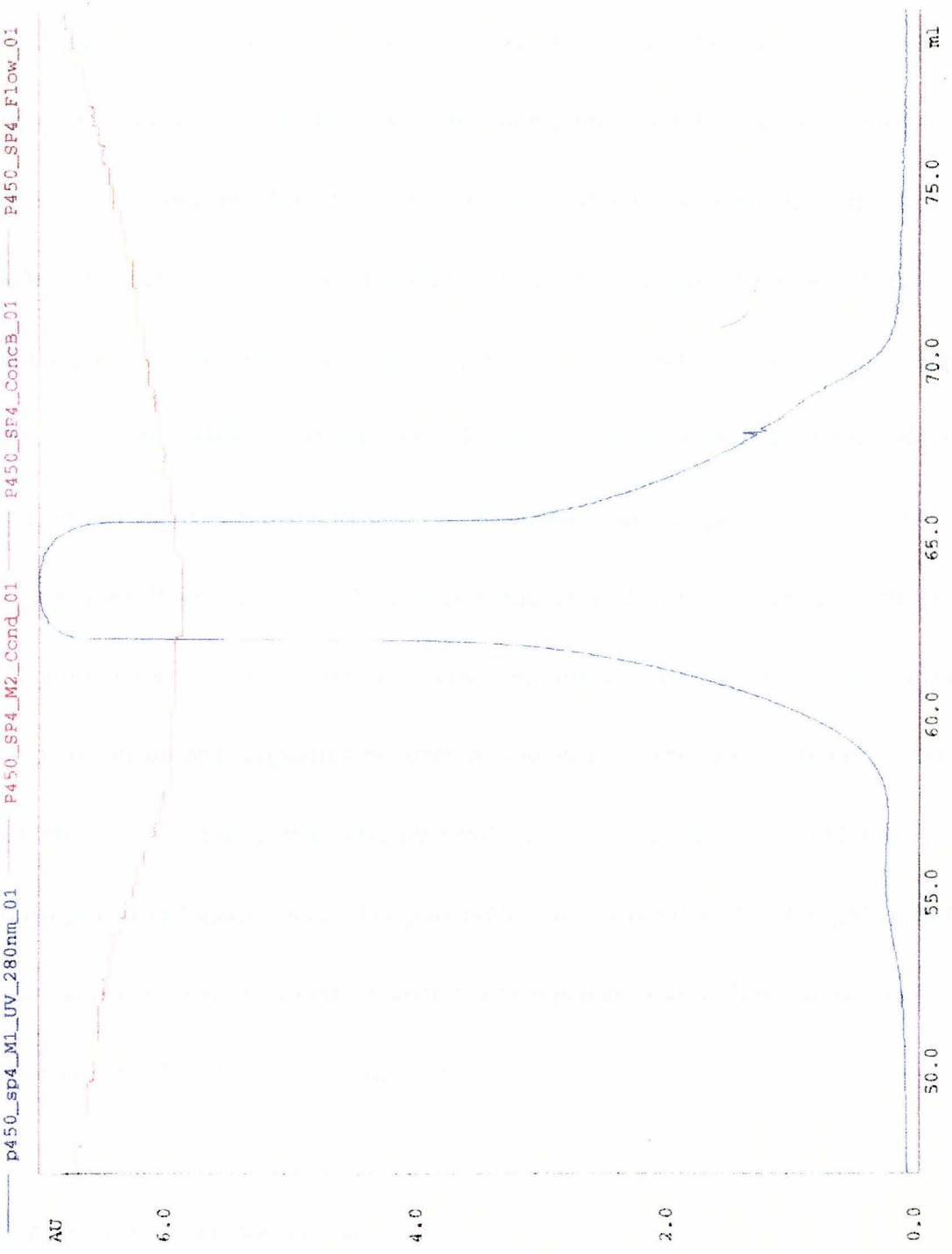
p450_sp4_M1_UV_280nm_01
P450_SP4_M2_Cond_01
P450_SP4_ConcB_01
P450_SP4_Flow_01
AU
6.0
4.0
2.0
0.0
50.0
55.0
60.0
65.0
70.0
75.0
ml

exchanged with buffer C. This was most quickly achieved by running a desalting column (HiPrep 26/10)--equilibration at 10 mL/min with buffer C, and P450 elution at 5 mL/min. The protein eluted first in buffer C, with the salt trailing 20 mL behind (see Figure A.3).

Next, a SourceQ (HR 16/10) column was equilibrated with buffer C, and the P450 loaded (maximum 10 mL). Separation into three distinct bands (Figure A.4) occurred with a gradient of buffer D (flow rate = 5 mL/min; 0-15 mL, 0%; 15-25 mL, ramp to 30%, 25-35 mL, 100%, 35-45 mL, 0%). Fractions from the first, most prominent peak, were pooled and concentrated by amicon. R_z at this stage was generally ~ 1.3. Finally, the Sephadex 75 gel filtration column was re-equilibrated with 85% buffer A/15% buffer B, and the P450 (< 3 mL) carefully loaded. Elution at 1 mL/min (Figure A.5) yielded one predominant peak appearing between 60 and 70 mL. The center fractions generally had ratios > 1.5. Failure to achieve pure P450 at this stage required an additional anion exchange chromatography step. The pure protein was concentrated (> 100 μM) in buffer P containing fresh DTT (2 mM), transferred to eppendorf tubes, flash frozen (liquid N_2) and stored at –70 °C for future experiments.

Pd, PdR Growth and Purification

Growth and purification of Pd and PdR were similar to the procedure for $P450_{cam}$. Neither protein exhibited the same time dependent loss of expression, however, as was

exhibited by P450 plasmids. Published purification procedures for Pd (1,2) and PdR (3) served as useful guidelines. Two buffers were used: buffer F was 50 mM Tris-HCl, pH 7.4 with 2 mM DTT, and buffer G also contained 1 M KCl. After dissolving in buffer F, sonication, ultracentrifugation, and microfiltration, chromatography was performed on both proteins at 4 °C using gravity columns. DEAE (Sephacel) anion exchange chromatography (0 to 300 mM KCl gradient) preceeded G-100 Sephadex gel filtration (100 mM KCl). The accepted R_z (A_{455}/A_{280}) for pure Pd is > 0.40, while for PdR R_z (A_{425}/A_{280}) should be greater than 0.14 (4). The concentration of oxidized Pd was determined at either 414 nm (ε = 10.0 $mM^{-1}cm^{-1}$) or 455 nm (ε = 10.4 $mM^{-1}cm^{-1}$) (2,5). The molar absorptivity of the flavoprotein was 10.8 $mM^{-1}cm^{-1}$ at 455 nm (3). Denaturation was significant even at 4 °C, and both proteins were flash frozen and stored at –70 °C immediately after purification.

Removing camphor from P450 for laser experiments and protein crystallization

In most P450 experiments involving Ru-substrates, it was necessary to first remove the camphor. This was easily achieved by desalting the protein on a gel filtration column with camphor-free buffer at 4 °C. Due to potassium ion stabilization of the substrate bound form of $P450_{cam}$ (6,7), potassium free buffers were used to make substrate free enzyme. One PD-10 column was equilibrated with 40 mM Tris-HCl, pH 7.4, and a

second PD-10 column with buffer Q (50 mM KPi, 100 mM KCl, pH 7.4). Addition of < 1 mL P450 onto the first PD-10 preceeded elution with 40 mM Tris-HCl. The camphor free protein was collected and loaded onto the second buffer exchange column. A UV-vis spectrum of the camphor free P450 should have a sharp peak centered at 417 nm (ε = 115,000 $M^{-1}cm^{-1}$) (8). The purity was checked by measuring the ratio of the absorbance at 417 nm/280 nm. Since ε_{392} = 102,000 $M^{-1}cm^{-1}$, this ratio was converted to the more familiar R_z (392/280) value by dividing by 1.13.

On ice, the camphor free protein was stable for several hours, although extra P450 was usually flash frozen immediately. Experience has shown that flash-frozen, camphor-free P450 may be thawed once and used in subsequent experiments without degradation. The state of the protein was determined by adding camphor and observing the completeness of the shift to 392 nm. Alternatively, bubbling CO into the sample, adding dithionite, and observing the size of the peak at 446 nm (ε = 120,000 $M^{-1}cm^{-1}$) and the presence of any shoulder at 422 nm (P420 Fe^{2+}-CO) allowed quantification of the protein quality (9).

REFERENCES AND NOTES

1. I. C. Gunsalus, G. C. Wagner, *Meth. Enzymol.* **52**, 166-188 (1978).

2. M. J. Hintz, D. M. Mock, L. L. Peterson, K. Tuttle, J. A. Peterson, *J. Biol. Chem.* **257**, 14324-14332 (1982).

3. P. W. Roome, J. C. Philley, J. A. Peterson, *J. Biol. Chem.* **258**, 2593-2598 (1983).

4. J. A. Peterson, M. C. Lorence, B. Amarneh, *J. Biol. Chem.* **265**, 6066-6073 (1990).

5. M. Holden, M. Mayhew, D. Bunk, A. Roitberg, V. Vilker, *J. Biol. Chem.* **272**, 21720-21725 (1997).

6. T. L. Poulos, B. C. Finzel, A. J. Howard, *Biochemistry* **25**, 5314-5322 (1986).

7. I. C. Gunsalus, G. C. Wagner, *Bacterial $P450_{cam}$ Methylene Monooxygenase Components: Cytochrome m, Putidaredoxin, and Putidaredoxin Reductase*, Methods in Enzymology (Academic Press, New York, NY, 1978).

8. J. H. Dawson, L. A. Andersson, M. Sono, *J. Biol. Chem.* **257**, 3606-3617 (1982).

9. J. H. Dawson, L. A. Andersson, M. Sono, *J. Biol. Chem.* **258**, 13637-13645 (1983).

Appendix B

Synthesis and Characterization of Ru-Substrates, Reductive Quenchers, and Model Compounds

Acknowledgement:

This compendium was greatly facilitated by the efforts of Jon Wilker, and benefits from his work, as well as that of Alex Dunn. Thanks also go to Brian Crane and Kevin Hoke for helping with the synthesis of some of the model compounds.

INTRODUCTION

Presented in this appendix are practical syntheses of several types of $\{Ru(bpy)_3\}^{2+}$-tethered probes, two reductive quenchers, and several model compounds. Many compounds have been excluded from this collection, including several Ru-norbornyl probes that proved difficult to synthesize and bound less tightly than their ethyl benzene and adamantyl counterparts. Also excluded from this text are over a dozen bpy-substrates joined by an ether linkage. These compounds were synthesized by nucleophilic attack of a deprotonated hydroxy substrate on an alkylbromide. Unfortunately, an elimination reaction contributed to a significant side product that was almost chromatographically inseparable from the bromide starting material.

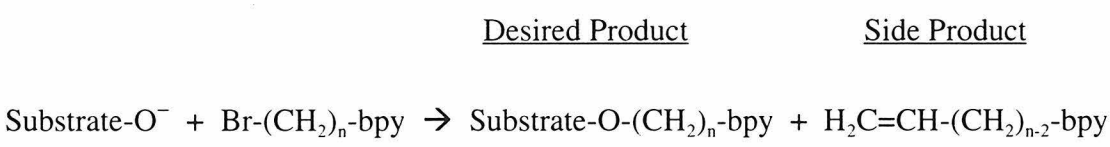

Different reaction conditions (temperature, solvent, base) varied the ratio of product/side reaction, but it was always necessary to purify the ether by column chromatography (several times). Due to this complication, few of these compounds were ruthenated, but, in binding tests with P450, Ru-ether-substrates bound as well as their Ru-amide-substrate analogs (K_D ~ 1 μM). The ease of synthesizing Ru-substrates with amide linkages, and

the versatile hydrogen bond donor-acceptor character of the amide functionality strongly recommended this approach.

The design of Ru-ligands centered on imidazole-terminated compounds, due in part to the ease of displacing a variety of electrophiles with imidazole. The Ru-ligands were more difficult to purify, in general, and gave lower yields than the corresponding Ru-substrates; in a major side reaction, both the bpy and imidazole moieties were ruthenated. It has not been determined conclusively whether Ru-Im compounds bind the ferric iron or just hydrogen bond to the Fe^{3+}-OH_2 enzyme. The small blue shift (3 nm) suggests competition between aquo and Ru-imidazole ligands for Fe^{3+} P450. Such competition is not evident with unfunctionalized imidazole (7 nm blue shift), presumably because the enzyme is able to exclude water from the pocket when binding the smaller ligand. Lipscomb previously observed the remarkable 400x enzymatic discrimination between 1-phenyl imidazole (K_D = 0.1 μM) and 4-phenyl imidazole (K_D = 40 μM) (1). Poulos et al. crystallized both P450:imidazole complexes and attributed their different affinities to differences in desolvating the two ligands upon binding to iron (2). The uncoordinated nitrogen of 4-phenyl imidazole appears to dramatically lower the affinity of this inhibitor for the hydrophobic pocket, and it is presumably on this basis that P450 prefers Ru-C_{13}-Im over Ru-C_{11}-Im. In the ferrous state, where water is a poor ligand, it is

possible to drive the enzyme all the way to Fe^{2+}-im-C_{13}-Ru (peak at 446 nm) by adding dithionite and photolysing the sample.

The reductive quenchers described in this appendix are only two of the several that were synthesized and tested. The quencher *para*-methoxy-*N,N*-dimethylaniline (*p*-MDMA) is a very efficient quencher, $k_q = 2.6 \pm 0.4 \times 10^9\ M^{-1}s^{-1}$, depending on ionic strength (μ), with large cage escape yields; $\eta = 0.73$ when $\mu = 0$ (3,4). However, as employed in Chapter 5, it is poorly soluble in water ($\leq$ 10 mM), binds P450 tightly, is very light and oxygen sensitive, and the fast recombination of $p\text{-MDMA}^{\bullet+}$ and $\{Ru(bpy)_3\}^{1+}$ ($k_{recomb} = 3 \pm 1 \times 10^9\ M^{-1}s^{-1}$) limits the yield of the forward ET reaction between [Ru-alkyl-substrates]$^{1+}$ and ferric P450 (3,4).

Efforts to find a efficient reductive quencher with greater solubility and lower P450 affinity led to the cyanometalate complexes, $K_4Mo(CN)_8$ and $K_4W(CN)_8$ (5). Although both of these compounds possess cage escape efficiencies of over 80% and generated $\{Ru(bpy)_3\}^{1+}$ in high yields, anomalous transients were observed in the presence of P450 that persisted on very long time scales. Other alternatives (europium(II), $[Fe(CN)_6]^{2+}$, Na_2SO_3, ascorbate) possess bimolecular quenching constants too small to compete with the inherent quenching of P450:[Ru-substrate]$^{2+*}$ by energy transfer (6,7). Thus, the search came full circle--modification of *p*-MDMA with the attachment of bulky water-solubilizing moieties to the aniline core. Increasing solubility,

for example with *para*-methoxy-*N,N*-diethoxyaniline, was not difficult; but, surprisingly, this quencher (like most others) still competed with camphor for the P450 pocket.

This challenge was finally resolved by synthesizing the crown ether aniline complex. This compound (which binds both sodium and potassium, and is therefore

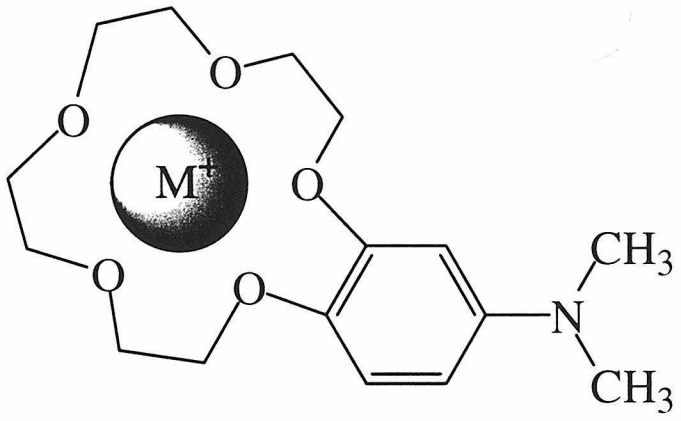

Crown aniline reductive quencher

positively charged in solution) proved to be extremely soluble and showed no affinity for the P450 active site. Problematically, however, it had a much smaller bimolecular quenching rate constant (k_{recomb} ~ 1 x 10^8 $M^{-1}s^{-1}$) than *p*-MDMA, probably due to the electron-withdrawing cation. Although working at high concentrations of quencher (> 100 mM) was a viable option, the starting materials for this quencher are expensive and under most conditions it appeared that *p*-MDMA gave higher yields of reduced P450. The best solution, in the end, was to eliminate the need for a reductive quencher altogether--a strategy that was implemented in Chapter 6.

MATERIALS AND METHODS

General

All manipulations were conducted under an argon atmosphere using standard Schlenk techniques. Solvents used for synthesis were dried, degassed and distilled according to standard procedures (8,9). Reactions were performed at room temperature unless otherwise stated. All reagents were used as received. NMR spectra were recorded on a General Electric QE300, and later a Varian *Mercury* 300, generally using dry $CDCl_3$ or $CDCl_2$ as solvent. ^1H NMR spectral assignments refer to the schematic provided in depicting a typical bpy' ligand used in this study.

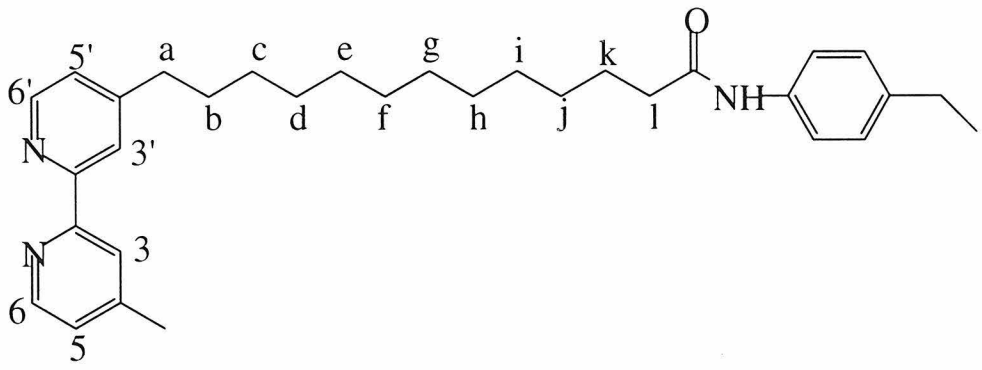

Synthesis of Ru-Substrates and Ru-Ligands

bpy-C_9-Ad. The synthesis of bpy-C_9-Ad is typical of all bpy-C_x-Ad complexes presented. Thionyl chloride (24.50 g, 206 mmol) and 8-bromooctanoic acid (5.46 g, 24.5 mmol) were combined and refluxed for 1.5 h. Excess $SOCl_2$ was removed by vacuum to yield a brown liquid that was dissolved in ether (20 mL) and transferred to an addition funnel. The acid chloride was added over 20 min to an ether (20 mL) solution of 2-adamantanamine hydrochloride (11.97 g, 63.8 mmol) and triethylamine (22.50 g, 222 mmol) chilled in an ice bath. The resulting slurry was stirred at 0 °C for 3 h and then overnight at room temperature. The reaction solution was added to water (75 mL) and extracted with ether (75 mL) in a separatory funnel. After washing the organic layer with 0.1 M HCl (3 x 75 mL), water (2 x 75 mL), and saturated brine (2 x 75 mL), the solution was dried over $MgSO_4$ and solvent removed by rotary evaporation. The off-white solid was used directly without purification for attachment to Me_2bpy.

Diisopropylamine (8.09 g, 79.9 mmol), *n*-butyl lithium (80 mmol in hexanes), and cold THF (25 mL) were combined in a 500 mL Schlenk flask at 0 °C. A cold solution of 4,4'-dimethyl-2,2'-bipyridine (6.41 g, 34.8 mmol) in THF (180 mL) was added by cannula over 15 min, and was stirred for an additional 15 min. The amide was dissolved in THF (120 mL) and cannulated dropwise into the bipyridine, turning the solution from burgundy to black. After 3 h on an ice bath, the reaction was allowed to proceed overnight at room temperature. The reaction solution was transferred to a separatory

funnel with water (250 mL) and extracted with ether (150 mL). The organic layer was washed with saturated $NaHCO_3$ (2 x 125 mL), water (3 x 300 mL), and saturated brine (2 x 200 mL). After drying with $MgSO_4$ and vacuum, a beige solid was obtained. The product was eluted as the second band by silica gel column chromatography (3:2 ethyl acetate/hexanes). Yield was 3.40 g (30.2% based on 8-bromooctanoic acid) of a pale yellow oil. ^{1}H NMR ($CDCl_3$): δ 1-2 (m's), 2.20 (t, CH_2-amide), 2.42 (s, bpy-CH_3), 2.59 (t, bpy-CH_2), 4.09 (m), 5.79 (m), 7.21 (d, bpy 5 and 5'), 8.23 (s, bpy 3 and 3'), 8.58 (d, bpy 6 and 6'). See Figure B.1.

bpy-C_{11}-Ad. The synthesis of this compound is similar to that described for bpy-C_9-Ad. The starting material 2-adamantanamine hydrochloride necessitated the addition of 3.5 equivalents of triethylamine. ^{1}H NMR ($CDCl_3$): δ 1-2 (m's), 2.21 (t, CH_2-amide), 2.42 (s, bpy-CH_3), 2.60 (t, bpy-CH_2), 4.02 (m), 5.78 (m), 7.19 (d, bpy 5 and 5'), 8.23 (s, bpy 3 and 3'), 8.59 (d, bpy 6 and 6').

bpy-C_{10}. This compound was prepared in a manner analogous to that of bpy-C_{16}. ^{1}H NMR ($CDCl_3$): δ 0.82 (t, chain -CH_3), ~1.3 (m, CH_2c-i), 1.78 (p, CH_2b), 2.55 (s, bpy-CH_3), 2.79 (t, bpy-CH_2), 7.31 (t, bpy 5 and 5'), 8.51 (s, bpy 3 or 3'), 8.59 (s, bpy 3 or 3'), 8.70 (t, bpy 6 and 6'). See Figure B.2.

Figure B.1. ^{1}H NMR spectrum of bpy-C_9-Ad in $CDCl_3$. This spectrum is representative of all bpy-C_n-Ad compounds.

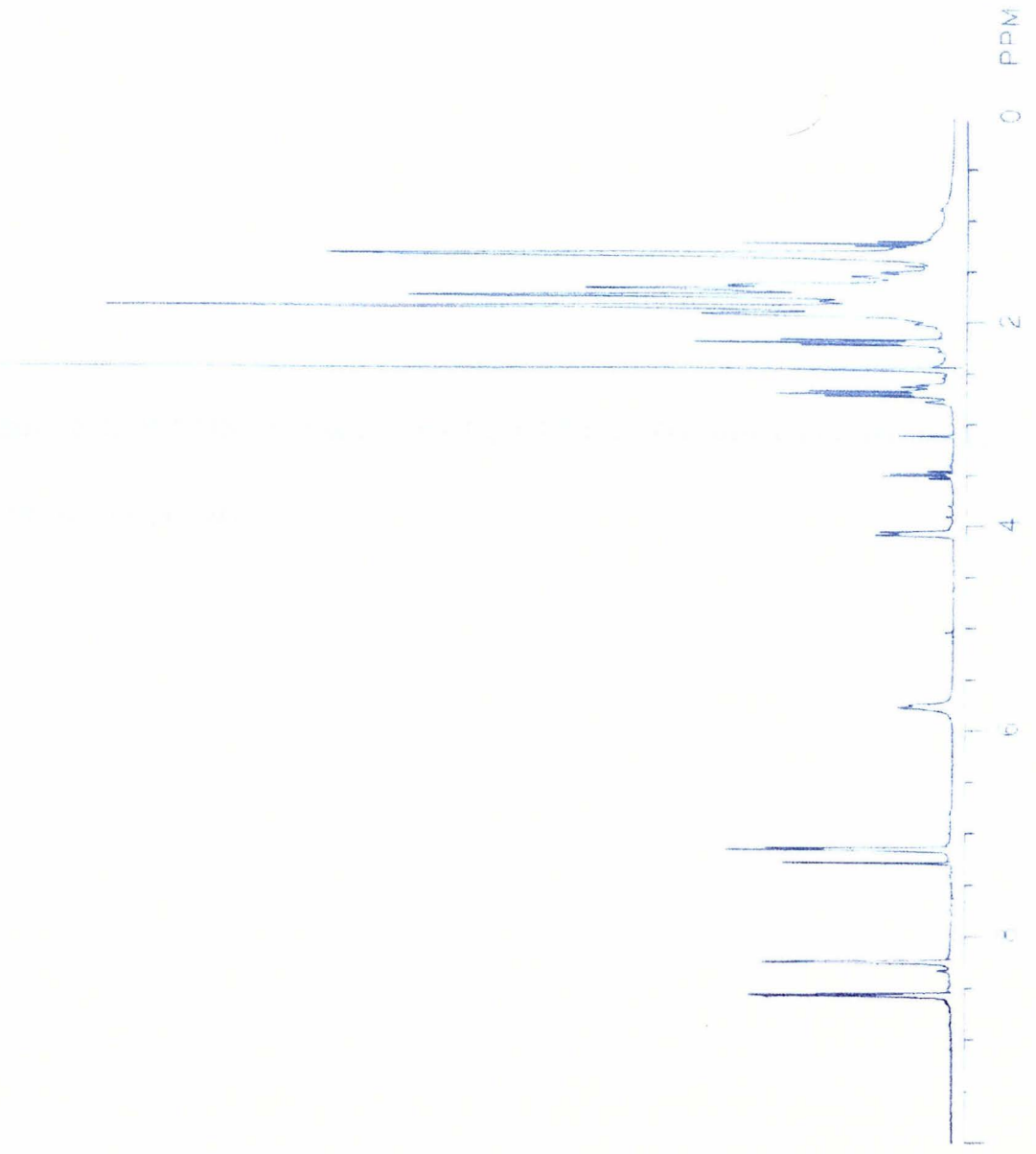
PPM
0
2
4
6
8

Figure B.2. ^{1}H NMR spectrum of bpy-C_{10} in $CDCl_3$. This spectrum is representative of all bpy-C_n compounds.

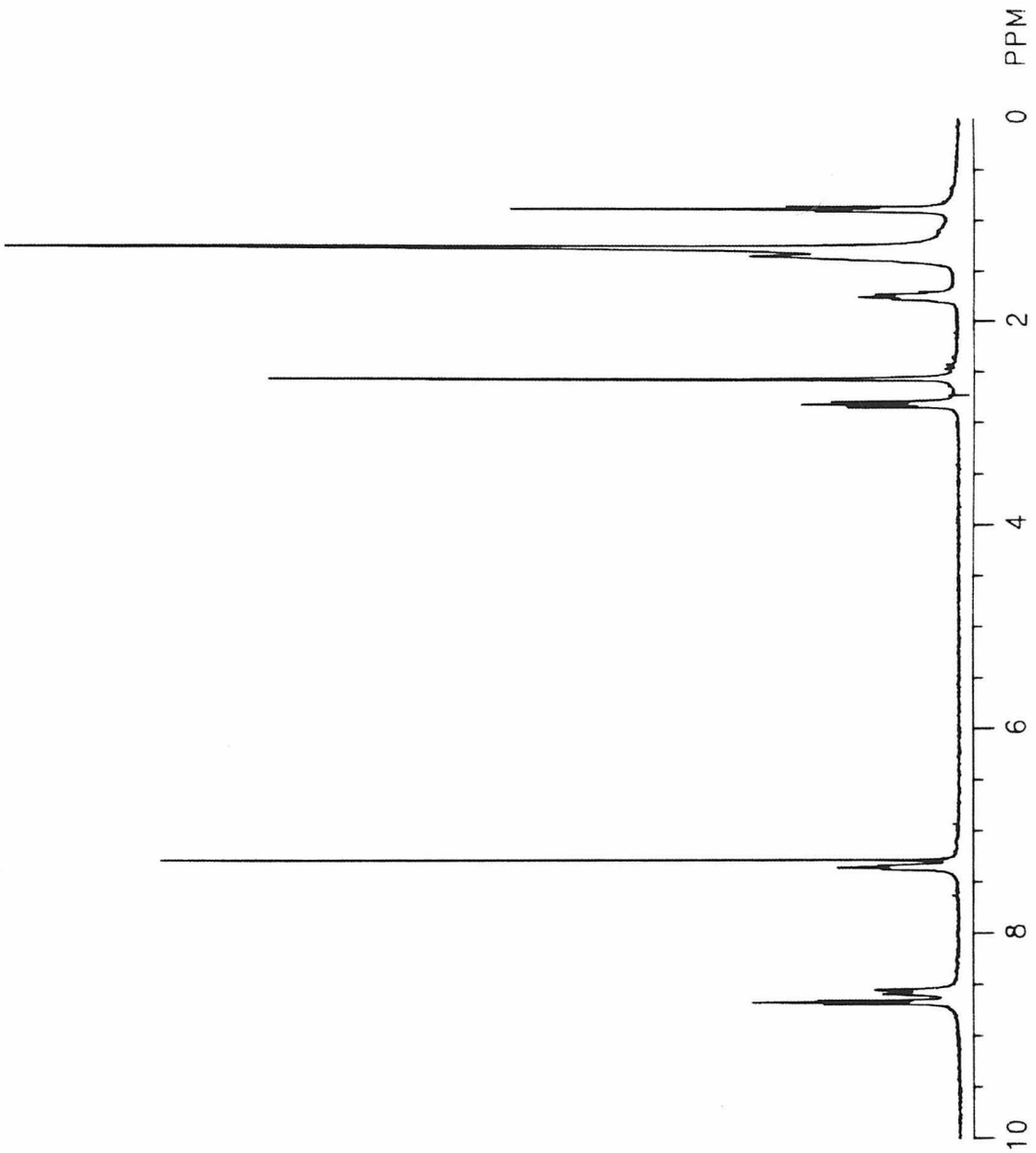
PPM
0
2
4
6
8
10

bpy-C_{16}. Diisopropylamine (5.79 g, 57.2 mmol), *n*-butyl lithium (57.3 mmol in hexanes) and cold THF (30 mL) were combined in a 500 mL Schlenk flask over an ice bath. A cold solution of 4,4'-dimethyl-2,2'-bipyridine (4.56 g, 24.7 mmol) in 180 mL of THF was added by cannula over 5 min. To this solution was added 1-bromohexadecane (6.29 g, 21.6 mmol) in THF (50 mL). The reaction was stirred on ice for ~ 3 h, then allowed to warm to room temperature for further stirring overnight. The reaction solution was transferred to a 1 L separatory funnel with water (250 mL) and ether (150 mL). The organic layer was washed with saturated $NaHCO_3$ (2 x 125 mL), water (2 x 300 mL) and saturated brine (3 x 200 mL). After drying with $MgSO_4$, solvent was removed by vacuum and the product purified by silica gel column chromatography using 4:1 hexanes:ethyl acetate as eluent. Yield was 2.40 g (34.4%) of a white solid. ^{1}H NMR ($CDCl_3$): δ 0.89 (t, chain -CH_3), ~1.3 (m, CH_2c-o), 1.75 (p, CH_2b), 2.57 (s, bpy-CH_3), 2.80 (t, bpy-CH_2), 7.33 (t, bpy 5 and 5'), 8.52 (s, bpy 3 or 3'), 8.55 (s, bpy 3 or 3'), 8.67 (t, bpy 6 and 6').

bpy-C_{11}-Br. This compound was prepared in a manner analogous to that of bpy-C_{13}-Br. ^{1}H NMR ($CDCl_3$): δ ~1.7 (m, CH_2c-i), 1.71 (p, CH_2b), 1.79 (p, CH_2j), 2.43 (s, bpy-CH_3), 2.70 (t, bpy-CH_2), 3.40 (t, CH_2-Br), 7.18 (d, bpy 5 and 5'), 8.25 (s, bpy 3 and 3'), 8.59 (t, bpy 6 and 6').

bpy-C_{13}-Br. Diisopropylamine (0.770 g, 7.61 mmol), *n*-butyl lithium (7.60 mmol in hexanes) and THF (10 mL) were combined in a Schlenk flask at -70 °C. The solution was warmed to 0 °C over 15 min. The solution was again chilled to -70 °C and 1,12-dibromododecane (25.0 g, 7.62 mmol) added as a solid. After warming to 0 °C, stirring continued for ~4 h. The solution was transferred to a separatory funnel to which water (15 mL) and ether (15 mL) were added. The organic layer was washed with saturated $NaHCO_3$, dried with $MgSO_4$ and evaporated to a solid under vacuum. Silica gel column chromatography with $CHCl_3$ as the eluent yielded 1.31 g (40.0%) of a white solid. ^{1}H NMR ($CDCl_3$): δ ~1.7 (m, CH_2c-k), 1.75 (p, CH_2b), 1.85 (p, CH_2l), 2.55 (s, bpy-CH_3), 2.76 (t, bpy-CH_2), 3.48 (t, CH_2-Br), 7.26 (d, bpy 5 and 5'), 8.40 (d, bpy 3 and 3'), 8.65 (t, bpy 6 and 6'). See Figure B.3.

bpy-C_{11}-Im. This compound was prepared by a procedure identical to that of bpy-C_{13}-Im. ^{1}H NMR ($CDCl_3$): δ ~1.3 (m, CH_2c-i), 1.72 (m, CH_2b and j), 2.45 (s, bpy-CH_3), 2.72 (t, bpy-CH_2), 3.91 (t, CH_2-imid), 6.82 (s, imid H-5), 7.09 (s, imid H-4), 7.20 (d, bpy 5 and 5'), 7.45 (s, imid H-2), 8.21 (s, bpy 3 and 3'), 8.55 (t, bpy 6 and 6').

bpy-C_{13}-Im. Imidazole (1.0 g, 15 mmol) and bpy-C_{13}-Br (0.30 g, 0.70 mmol) were combined in a flask with THF (50 mL) and refluxed for 4 days. Solvent was removed

Figure B.3. ^{1}H NMR spectrum of bpy-C_{13}-Br in $CDCl_3$. This spectrum is representative of all bpy-C_n-Br compounds.

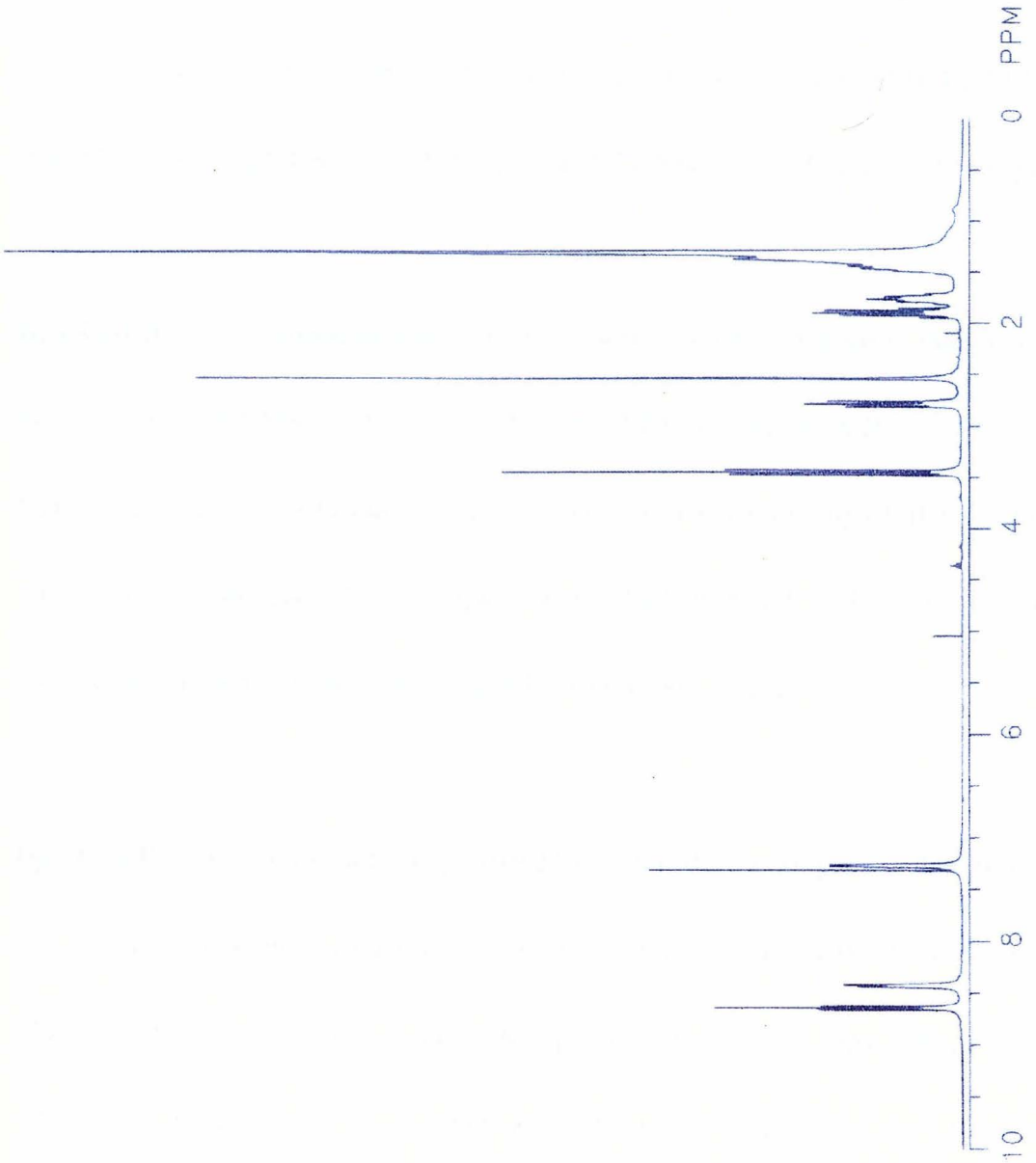
PPM
0
2
4
6
8
10

under vacuum and the resulting solid was dissolved in $CHCl_3$ for washing by saturated $NaHCO_3$, water and saturated brine. The product was purified by silica gel column chromatography using ethyl acetate as eluent to yield 0.26 g (90%) of a white solid. ^1H NMR ($CDCl_3$): δ ~1.3 (m, CH_2c-k), 1.71 (p, CH_2b), 1.76 (p, CH_2l), 2.42 (s, bpy-CH_3), 2.73 (t, bpy-CH_2), 3.95 (t, CH_2-imid), 6.90 (s, imid H-5), 7.10 (s, imid H-4), 7.19 (d, bpy 5 and 5'), 7.68 (s, imid H-2), 8.24 (s, bpy 3 and 3'), 8.60 (t, bpy 6 and 6'). See Figure B.4.

bpy-C_7-EB. This compound was prepared by a procedure analogous to that provided for bpy-C_{11}-EB. ^1H NMR ($CDCl_3$): δ 1.24 (t, ethyl-CH_3), 1.42 (m, CH_2c and d), 1.77 (m, CH_2b and e), 2.39 (t, CH_2-amide), 2.59 (q, ethyl-CH_2), 2.60 (s, bpy-CH_3), 2.77 (t, bpy-CH_2), 7.11 (d, benzene), 7.29 (d, bpy 5 or 5'), 7.42 (d, bpy 5 or 5'), 7.51 (d, benzene), 8.08 (s, br, amide-H), 8.58 (s, bpy 3 and 3'), 8.69 (t, bpy' 6 and 6').

bpy-C_9-EB. This compound was prepared by a procedure analogous to that provided for bpy-C_9-EB. ^1H NMR ($CDCl_3$): δ 1.19 (t, ethyl-CH_3), 1.40 (m, CH_2c-f), 1.77 (p, CH_2g), 1.80 (p, CH_2b), 2.42 (t, CH_2-amide), 2.60 (q, ethyl-CH_2), 2.75 (s, bpy-CH_3), 2.81 (t, bpy-CH_2), 7.11 (d, benzene), 7.50 (d, benzene), 7.59 (m, bpy 5 and 5'), 8.10 (s, br, amide-H), 8.75 (m, bpy 3 and 3'), 9.00 (m, bpy 6 and 6').

Figure B.4. ^{1}H NMR spectrum of bpy-C_{13}-Im in $CDCl_3$. This spectrum is representative of all bpy-C_n-Im compounds.

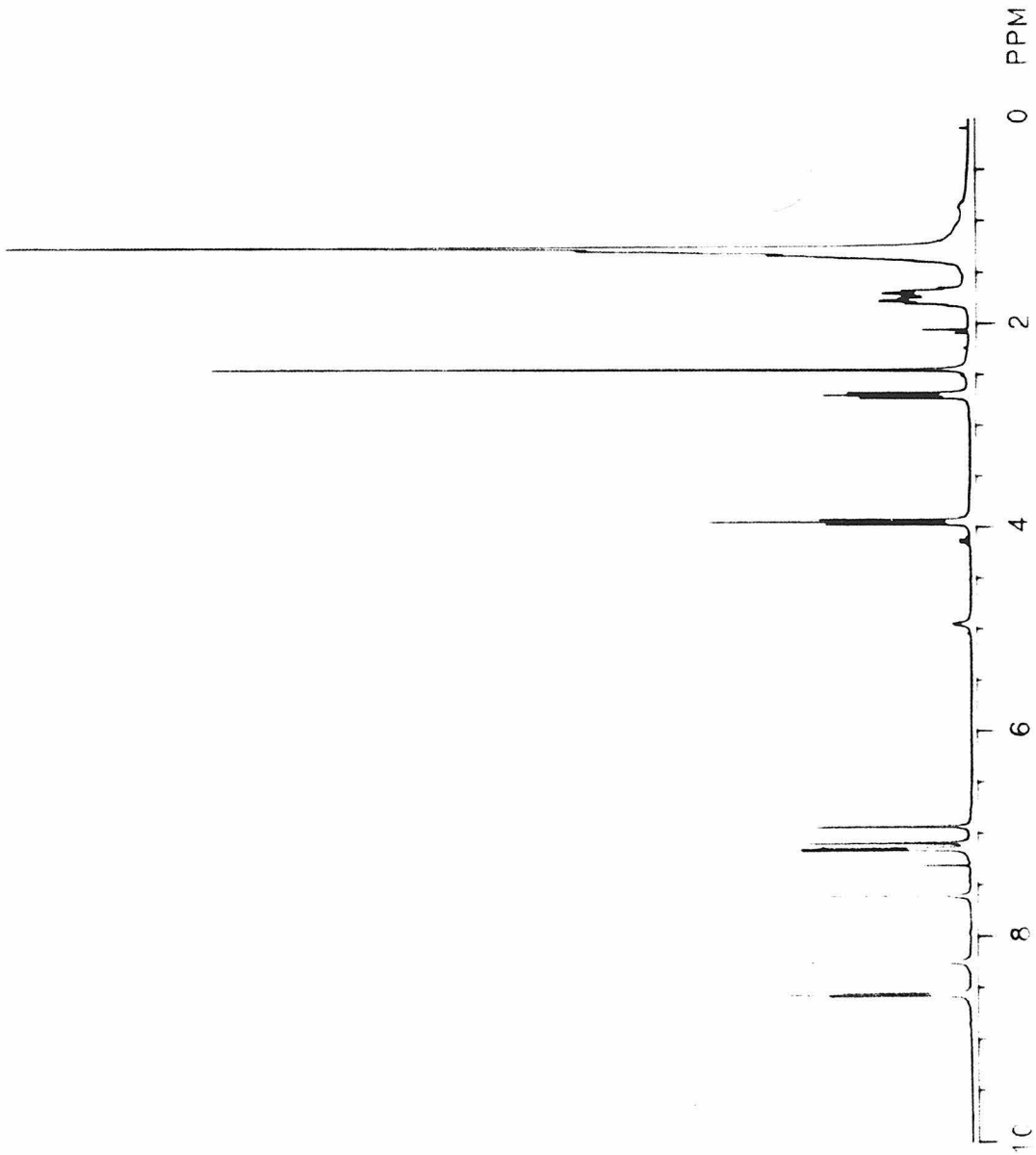
PPM
0
2
4
6
8
10

bpy-C_{10}-EB. This compound was prepared by a procedure analogous to that provided for bpy-C_{11}-EB. ^{1}H NMR ($CDCl_3$): δ 1.26 (t, ethyl-CH_3), 1.36 (m, CH_2c-g), 1.74 (m, CH_2b and h), 2.34 (t, CH_2-amide), 2.52 (s, bpy-CH_3), 2.61 (q, ethyl-CH_2), 2.75 (t, bpy-CH_2), 7.15 (d, benzene), 7.26 (m, bpy 5.5'), 7.47 (d, benzene), 8.41 (s, amide-H), 8.45 (m, bpy 3 and 3'), 8.60 (t, bpy 6 and 6').

bpy-C_{11}-EB. The synthesis of bpy-C_{11}-EB is typical for all bpy-C_x-EB compounds presented. Thionyl chloride (19.6 g, 165 mmol) and 9-bromononanoic acid (5.16 g, 20.5 mmol) were combined and refluxed for 2.5 h. Excess $SOCl_2$ was removed by vacuum to yield a brown solution that was transferred to an addition funnel. The acid chloride was added over 5 min to an ether (20 mL) solution of 4-ethylaniline (6.63 g, 54.7 mmol) chilled on an ice bath. The resulting slurry was stirred on the ice bath for ~ 3 h and then overnight at room temperature. Water (75 mL) and ether (75 mL) were added to the reaction solution in a separatory funnel. After washing of the organic layer with 0.1 M HCl (3 x 75 mL), water (2 x 75 mL) and saturated brine (2 x 75 mL), the solution was dried over $MgSO_4$ and solvent removed under vacuum. This grey/brown solid amide is used for attachment to 4,4'-dimethyl-2,2'-bipyridine without purification. Yields of the final ligand are highest when the amide is used immediately after preparation.

Diisopropylamine (2.92 g, 28.9 mmol), *n*-butyl lithium (28.8 mmol in hexanes)

and cold THF (25 mL) were combined in a 500 mL Schlenk flask chilled over an ice bath. A cold solution of 4,4'-dimethyl-2,2-bipridine (2.30 g, 12.5 mmol) in 120 mL of THF was added by cannula over 15 min. To this solution was added the amide in THF (90 mL) by cannula over 15 min. After ~3 h on the ice bath, the reaction was allowed to proceed overnight at room temperature. The reaction solution was transferred to a separatory funnel with water (250 mL) and ether (150 mL). The organic layer was washed with saturated $NaHCO_3$ (2 x 125 mL), water (3 x 300 mL) and saturated brine (2 x 200 mL). After drying with $MgSO_4$ and vacuum, a beige solid resulted. The product was purified by silica gel column chromatography using 3:1 hexanes:ethyl acetate for an eluent. Yield was 1.52 g (16.2% based on 9-bromononanoic acid) of a white solid. ^1H NMR ($CDCl_3$): δ 1.19 (t, ethyl-CH_3), 1.25 (m, CH_2c-h), 1.73 (m, CH_2b and i), 2.28 (t, CH_2-amide), 2.41 (s, bpy-CH_3), 2.60 (q, ethyl-CH_2), 2.71 (t, bpy-CH_2), 7.17 (d, benzene), 7.18 (m, bpy 5.5'), 7.22 (s, amide-H), 7.38 (d, benzene), 8.22 (s, bpy 3 and 3'), 8.56 (t, bpy 6 and 6'). See Figure B.5.

bpy-C_{12}-EB. This compound was prepared by a procedure analogous to that provided for bpy-C_{11}-EB. ^1H NMR ($CDCl_3$): δ 1.23 (t, ethyl-CH_3), 1.24 (m, CH_2c-i), 1.73 (m, CH_2b and j), 2.28 (t, CH_2-amide), 2.49 (s, bpy-CH_3), 2.68 (q, ethyl-CH_2), 2.75 (t, bpy-CH_2),

7.22 (d, benzene), 7.30 (m, bpy 5.5'), 7.43 (d, benzene), 7.41 (s, amide-H), 8.29 (s, bpy 3 and 3'), 8.60 (t, bpy 6 and 6').

bpy-C_{13}-EB. This compound was prepared by a procedure analogous to that provided for bpy-C_{11}-EB. ^{1}H NMR ($CDCl_3$): δ 1.20 (t, ethyl-CH_3), 1.26 (m, CH_2c-j), 1.74 (m, CH_2b and k), 2.29 (t, CH_2-amide), 2.43 (s, bpy-CH_3), 2.70 (q, ethyl-CH_2), 2.79 (t, bpy-CH_2), 7.18 (d, benzene), 7.21 (m, bpy 5.5'), 7.40 (s, amide-H), 7.45 (d, benzene), 8.29 (s, bpy 3 and 3'), 8.61 (t, bpy 6 and 6').

[Ru(bpy)$_2$(bpy-C_9-Ad)]Cl_2. The synthesis of [Ru(bpy)$_2$(bpy-C_9-Ad)]Cl_2 is typical of all [Ru(bpy)$_2$(bpy')]Cl_2 complexes presented here. The ligand bpy-C_9-Ad (505 mg, 1.10 mmol) and *cis*-[Ru(bpy)$_2Cl_2$] (538.6 mg, 1.04 mmol) were combined with 5:1 water/ethanol (18 mL) and refluxed for 12 h. Solvent was removed under vacuum and the dark red solid was dissolved in water (60 mL). This aqueous solution was combined with a solution of NH_4PF_6 (1.20 g, 7.36 mmol) in water (20 mL) to yield an orange precipitate. The aqueous slurry was extracted with CH_2Cl_2 (75 mL); the organic layer was washed with 1 M HCl (2 x 50 mL), 1 M NaOH (2 x 50 mL), and water (2 x 75 mL) prior to rotary evaporation. The PF_6^- salt of this ruthenium complex was purified by silica gel flash chromatography (column dimensions 30 x 4.5 cm) employing an eluent of

Figure B.5. ^{1}H NMR spectrum of bpy-C_{11}-EB in $CDCl_3$. This spectrum is representative of all bpy-C_{11}-EB compounds.

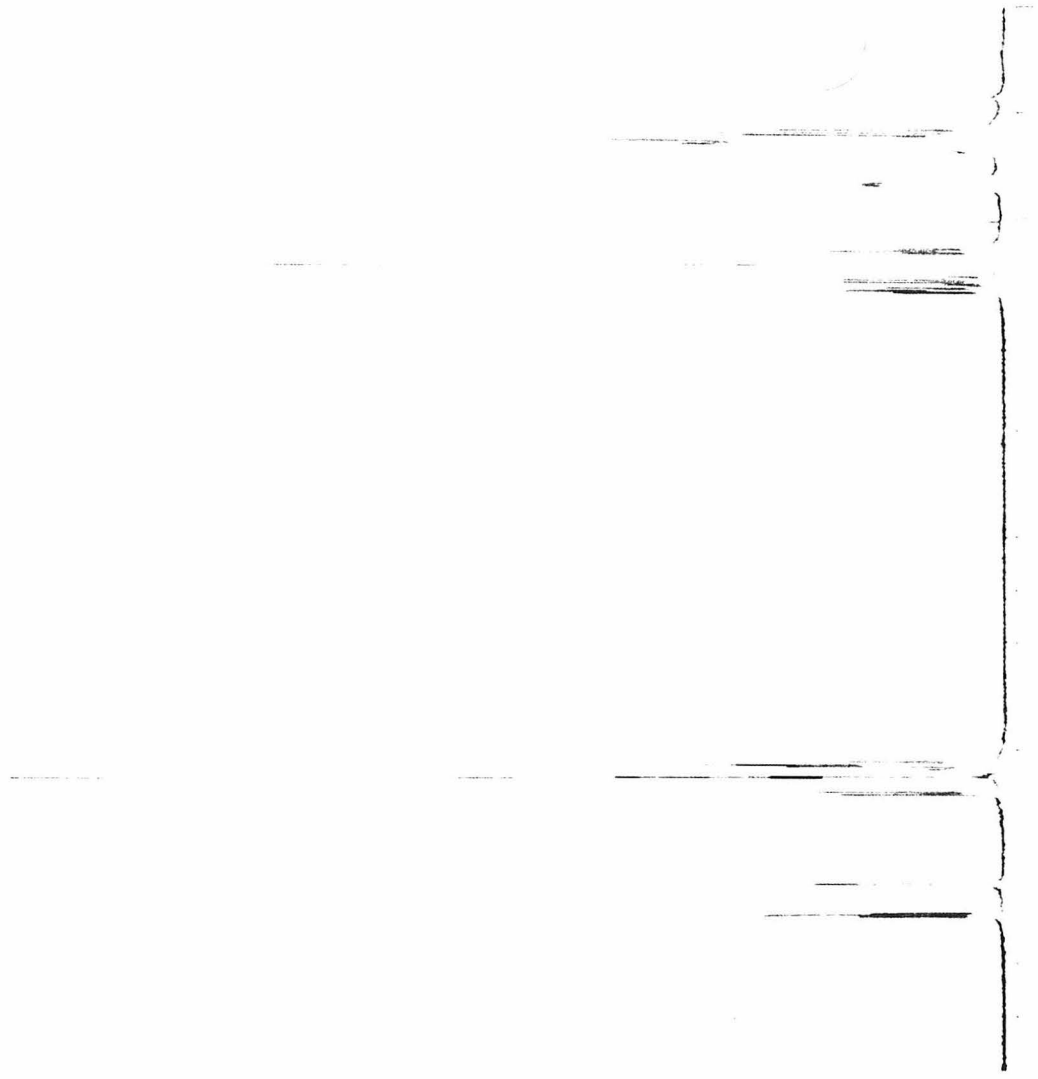

3% methanol in CH_2Cl_2. Pure product PF_6^- salt was found in elution volumes 550 – 1300 mL. Further product could be obtained by running a second column on the initial 200 – 550 mL. Volumes 550 – 1300 mL were combined and dried by rotary evaporation.

In order to metathesize the ruthenium complex to the Cl^- salt, the purified PF_6^- salt was dissolved in MeOH (10 mL) and loaded onto a CM Sepharose cation exchange column (2 x 13 cm). The column was washed with water (600 mL) and 25 mM NaCl (600 mL). The ruthenium complex was then eluted with 500 mM NaCl (300 mL) and dried by vacuum. The desired $[Ru(bpy)_2(bpy\text{-}C_9\text{-}Ad)]Cl_2$ was isolated from the NaCl-containing solid by repeated washings with CH_2Cl_2, followed by filtering and drying under vacuum. Yield of the dark red solid was 195 mg (20.0%). Yields of this procedure are generally 20–30%, and approach 60% with repeated column chromatography on the crude reaction mixture. ^1H NMR (CD_2Cl_2): δ 0.8-2 (m's), 2.21 (t, CH_2-amide), 2.65 (s, bpy'-CH_3), 2.78 (t, bpy'-CH_2), 3.62 (m), 3.95 (m), 6.32 (m), 7.23 (m), 7.45 (m), 7.70 (m), 8.18 (m), 8.77 (s), 8.80 (s), 9.20 (m).). See Figure B.6. LRMS (electrospray, positive ion) calcd for $C_{50}H_{57}N_7ORu$ ($M + H^+$) *m/z* 874, found 874. UV-vis [λ (Δε), H_2O]: 206 nm (74,200), 244 (26,000), 286 (80,100), 454 (14,500). See Figure B.7.

$[Ru(bpy)_2(bpy\text{-}C_{11}\text{-}Ad)]Cl_2$. This complex was prepared by a procedure similar to that described for $[Ru(bpy)_2(bpy\text{-}C_9\text{-}Ad)]Cl_2$. ^1H NMR (CD_2Cl_2): δ 0.8-2 (m's), 2.18 (t, CH_2-

Figure B.6. ^{1}H NMR spectrum of $[Ru(bpy)_2(bpy\text{-}C_9\text{-}Ad)]Cl_2$ in CD_2Cl_2. This spectrum is representative of all $[Ru(bpy)_2(bpy')]Cl_2$ compounds.

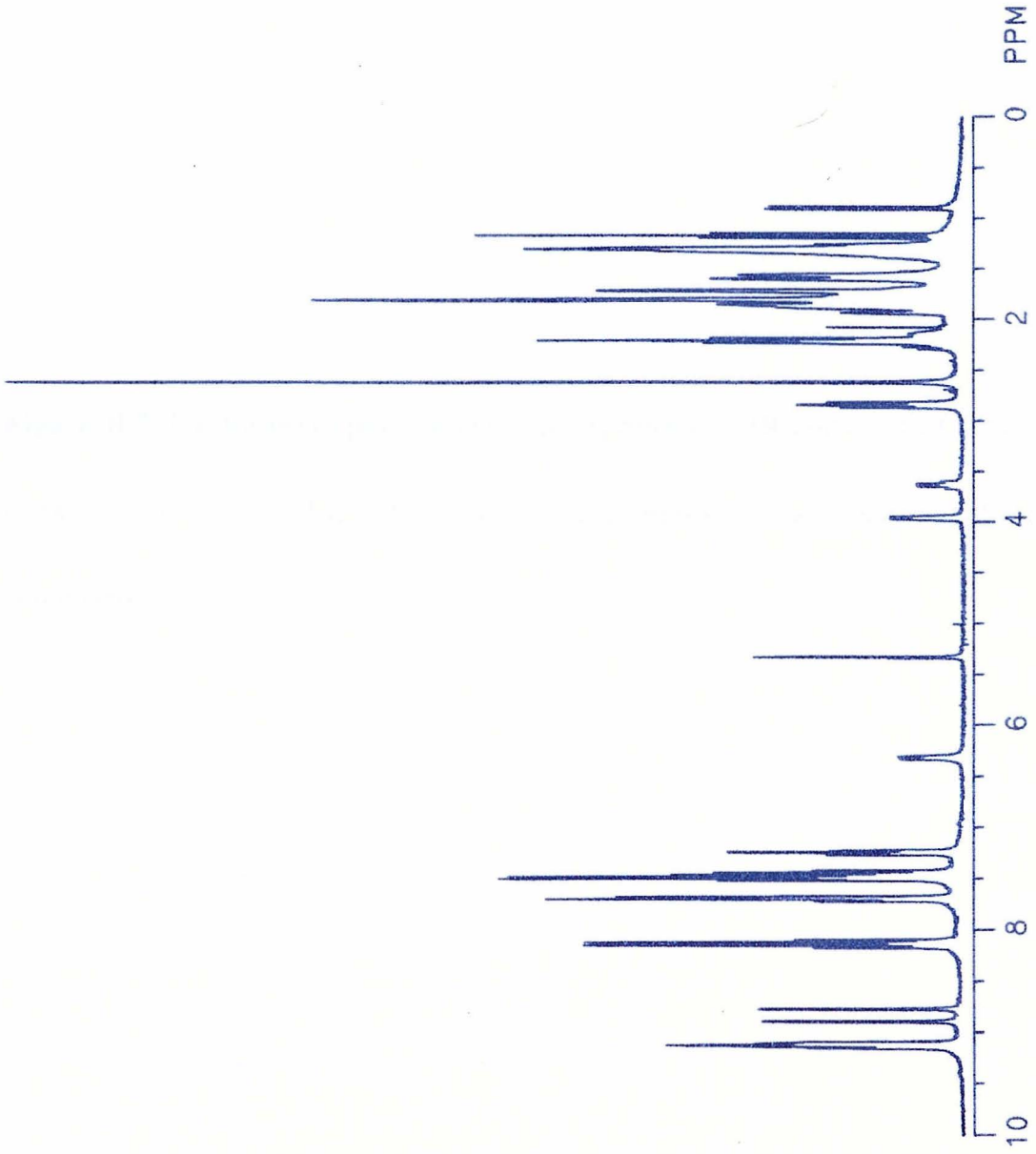
PPM
0
2
4
6
8
10

Figure B.7. Electrospray (positive ion) mass spectrum of $[Ru(bpy)_2(bpy\text{-}C_9\text{-}Ad)]Cl_2$ in CD_2Cl_2 (~ 10 μM). This spectrum is representative of all $[Ru(bpy)_2(bpy')]Cl_2$ compounds.

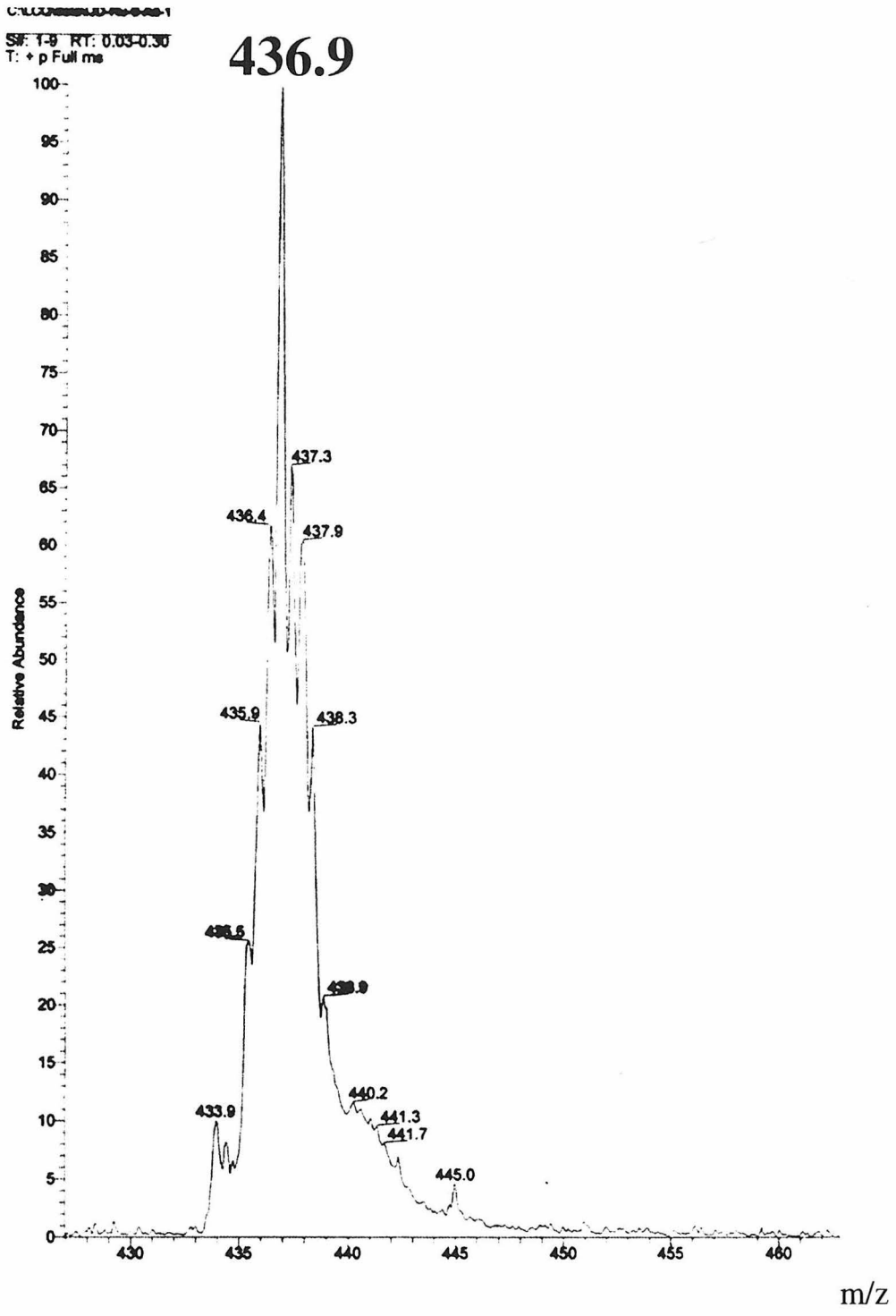
436.9
SM: 1-9 RT: 0.03-0.30
T: + p Full ms
Relative Abundance
100
95
90
85
80
75
70
65
60
55
50
45
40
35
30
25
20
15
10
5
0
437.3
436.4
437.9
435.9
438.3
433.9
440.2
441.3
441.7
445.0
430
435
440
445
450
455
460
m/z

amide), 2.64 (s, bpy'-CH_3), 2.81 (t, bpy'-CH_2), 3.96 (m), 5.90 (m), 7.25 (m), 7.49 (m), 7.72 (m), 8.19 (m), 8.59 (s), 8.69 (s), 9.95 (m). LRMS (electrospray, positive ion) calcd for $C_{52}H_{61}N_7ORu$ (M - H^+) *m/z* 900, found 900.

[Ru(bpy)$_2$(bpy-C$_{10}$)]Cl$_2$. This complex was prepared by a procedure similar to that described for [Ru(bpy)$_2$(bpy-C$_9$-Ad)]Cl$_2$. ^{1}H NMR (CD_2Cl_2): δ 0.91 (t, chain-CH_3), ~1.3 (m, CH_2c-i), 1.76 (p, CH_2b), 2.72 (s, bpy'-CH_3), 2.81 (t, CH_2a), 7.27 (m), 7.51 (m), 7.72 (m), 8.15 (m), 8.74 (s), 8.79 (s), 9.22 (m). LRMS (electrospray, positive ion) calcd for $C_{41}H_{46}N_6Ru$ (M - H^+) *m/z* 723, found 723.

[Ru(bpy)$_2$(bpy-C$_{16}$)]Cl$_2$. This complex was prepared by a procedure similar to that described for [Ru(bpy)$_2$(bpy-C$_9$-Ad)]Cl$_2$. ^{1}H NMR (CD_2Cl_2): δ 0.90 (t, chain-CH_3), ~1.3 (m, CH_2c-o), 1.77 (p, CH_2b), 2.69 (s, bpy'-CH_3), 2.80 (t, CH_2a), 7.29 (m), 7.55 (m), 7.76 (m), 8.20 (m), 8.75 (s), 8.80 (s), 9.21 (m). LRMS (electrospray, positive ion) calcd for $C_{47}H_{58}N_6Ru$ (M - H^+) *m/z* 807, found 807.

[Ru(bpy)$_2$(bpy-C$_{11}$-Im)]Cl$_2$. This complex was prepared by a procedure similar to that described for [Ru(bpy)$_2$(bpy-C$_9$-Ad)]Cl$_2$. ^{1}H NMR (CD_3OD): δ ~1.3 (m, CH_2c-i), 1.78 (CH_2b and j), 2.65 (s, bpy'-CH_3), 2.76 (t, bpy'-CH_2), 4.01 (t, CH_2-imid), 6.92 (s, imid H-

5), 7.12 (s, imid H-4), 7.33 (m), 7.49 (m), 7.68 (m), 7.75 (m), 8.19 (t), 8.62 (s), 8.68 (s), 8.74 (d).

[Ru(bpy)$_2$(bpy-C$_{13}$-Im)]Cl$_2$. This complex was prepared by a procedure similar to that described for [Ru(bpy)$_2$(bpy-C$_9$-Ad)]Cl$_2$. ^{1}H NMR (CD_2Cl_2): δ ~1.3 (m, CH_2c-k), 1.72 (CH_2b and l), 2.60 (s, bpy'-CH_3), 2.85 (t, bpy'-CH_2), 3.99 (t, CH_2-imid), 7.04 (m). 7.26 (m), 7.48 (m), 7.71 (m), 8.13 (m), 8.63 (s), 8.70 (s), 9.07 (m). LRMS (electrospray, positive ion) calcd for $C_{47}H_{54}N_8Ru$ (M + H^+) *m/z* 833, found 833.

[Ru(bpy)$_2$(bpy-C$_7$-EB)]Cl$_2$. This complex was prepared by a procedure similar to that described for [Ru(bpy)$_2$(bpy-C$_9$-Ad)]Cl$_2$. ^{1}H NMR (CD_2Cl_2): δ 1.05 (t, ethyl-CH_3), 1.25 (m, CH_2c and d), 1.51 (p, CH_2e), 1.70 (p, CH_2b), 2.35 (t, CH_2-amide), 2.40 (q, ethyl-CH_2), 2.52 (s, bpy'-CH_3), 2.80 (t, bpy'-CH_2), 6.82 (d, benzene), 7.20 (m), 7.40 (m), 7.60 (m), 7.73 (d, benzene), 8.00 (m), 9.05 (m), 9.18 (s). LRMS (electrospray, positive ion) calcd for $C_{46}H_{47}N_7ORu$ (M - H^+) *m/z* 814, found 814.

[Ru(bpy)$_2$(bpy-C$_9$-EB)]Cl$_2$. This complex was prepared by a procedure similar to that described for [Ru(bpy)$_2$(bpy-C$_9$-Ad)]Cl$_2$. ^{1}H NMR (CD_2Cl_2): δ 1.21 (t, ethyl-CH_3), 1.30 (m, CH_2c-f), 1.60 (p, CH_2g), 1.77 (p, CH_2b), 2.45 (t, CH_2-amide), 2.52 (q, ethyl-CH_2),

2.58 (s, bpy'-CH_3), 2.65 (t, bpy'-CH_2), 7.05 (d, benzene), 7.26 (t), 7.50 (m), 7.70 (m), 7.78 (d, benzene), 8.15 (m), 8.85 (s), 9.00 (t). LRMS (electrospray, positive ion) calcd for $C_{48}H_{51}N_7ORu$ (M - H^+) *m/z* 842, found 842.

[Ru(bpy)$_2$(bpy-C$_{10}$-EB)]Cl$_2$. This complex was prepared by a procedure similar to that described for [Ru(bpy)$_2$(bpy-C_9-Ad)]Cl_2. ^{1}H NMR (CD_2Cl_2): δ 1.13 (t, ethyl-CH_3), 1.21 (m, CH_2c-g), 1.52 (p, CH_2h), 1.68 (p, CH_2b), 2.41 (t, CH_2-amide), 2.52 (q, ethyl-CH_2), 2.58 (s, bpy'-CH_3), 2.83 (t, bpy'-CH_2), 7.00 (d, benzene), 7.24 (t), ~7.4 (m), 7.67 (m), 7.73 (d, benzene), ~8.1 (m), 8.83 (s), 8.92 (m), 9.05 (m). LRMS (electrospray, positive ion) calcd for $C_{49}H_{53}N_7ORu$ (M - H^+) *m/z* 856, found 856.

[Ru(bpy)$_2$(bpy-C$_{11}$-EB)]Cl$_2$. This complex was prepared by a procedure similar to that described for [Ru(bpy)$_2$(bpy-C_9-Ad)]Cl_2. ^{1}H NMR (CD_2Cl_2): δ 1.17 (t, ethyl-CH_3), 1.25 (m, CH_2c-h), 1.61 (p, CH_2i), 1.77 (p, CH_2b), 2.48 (t, CH_2-amide), 2.59 (q, ethyl-CH_2), 2.63 (s, bpy'-CH_3), 2.90 (t, bpy'-CH_2), 7.06 (d, benzene), 7.29 (m), ~7.5 (m), 7.78 (d, benzene), ~8.1 (m), 8.83 (s), 8.93 (s), ~9.1 (m). LRMS (electrospray, positive ion) calcd for $C_{50}H_{55}N_7ORu$ (M - H^+) *m/z* 870, found 870.

[Ru(bpy)$_2$(bpy-C$_{12}$-EB)]Cl$_2$. This complex was prepared by a procedure similar to that described for [Ru(bpy)$_2$(bpy-C$_9$-Ad)]Cl$_2$. ^{1}H NMR (CD_2Cl_2): δ 1.22 (t, ethyl-CH_3), 1.32 (m, CH_2c-i), 1.60 (p, CH_2j), 1.72 (p, CH_2b), 2.40 (t, CH_2-amide), 2.56 (q, ethyl-CH_2), 2.60 (s, bpy'-CH_3), 2.74 (t, bpy'-CH_2), 7.08 (d), 7.25 (d), ~7.5 (m), 7.70 (m), 8.10 (m), 8.65 (s), 8.72 (s), 8.95 (m), 9.65 (s). LRMS (electrospray, positive ion) calcd for $C_{51}H_{57}N_7ORu$ (M - H^+) *m/z* 884, found 884.

[Ru(bpy)$_2$(bpy-C$_{13}$-EB)]Cl$_2$. This complex was prepared by a procedure similar to that described for [Ru(bpy)$_2$(bpy-C$_9$-Ad)]Cl$_2$. ^{1}H NMR (CD_2Cl_2): δ 1.25 (CH_2c-j), 1.28 (t, ethyl-CH_3), 1.61 (p, CH_2k), 1.74 (p, CH_2b), 2.46 (t, CH_2-amide), 2.59 (q, ethyl-CH_2), 2.62 (s, bpy'-CH_3), 2.81 (t, bpy'-CH_2), 7.10 (d), 7.26 (t), ~7.5 (m), 7.73 (m), ~8.1 (m), 8.59 (s), 8.62 (s), ~8.9 (m). LRMS (electrospray, positive ion) calcd for $C_{52}H_{59}N_7ORu$ (M - H^+) *m/z* 898, found 898.

Synthesis of Reductive Quenchers

***para*-methoxy-*N,N*-dimethylaniline.** This quencher was prepared in a similar manner to published procedures (10,11). *para*-methoxyaniline (*p*-anisidine, Aldrich, 5.0 g) was placed in a flask with neat methyl iodide (15 mL), fit with a condenser and refluxed for

12 hours under argon. The precipitated iodide salt of the quaternary amine was filtered and dried under high vacuum. Crude yield = 11.62 grams, 98% by weight. The aniline salt was put in a flask with 1.5 equivalents of NaOH (2.4 g) and amyl alcohol as solvent (50 mL). Refluxing for 6 hours (~ 152 °C) gave a yellow solution which was filtered on a coarse frit to remove the brown precipitate. The filtrate was washed in a separatory funnel with saturated NaCl solution (100 mL). The top (dark brown) organic layer was dried with $MgSO_4$, and a short path distillation removed the amyl alcohol (59-79 °C) under high vacuum (~ 1 mm Hg).

Column chromatography was performed in the dark, using 50% EtOAc/50% hexanes as eluent. Three bands emerged; the first band was a fluorescent impurity, the second and third bands were the di- (r_f ~ 0.7) and monomethyl aniline (r_f ~ 0.65), respectively. Rotary evaporation of the middle fractions gave the product in modest yield (~ 1 gram, 16% based on starting *p*-anisidine). The off-white solid was further purified by sublimation (high vacuum, heated at 30 °C, collected on a small cold finger). Product isolated at this stage was sufficiently pure for reductive quenching purposes. Due to its short shelf-life (stored at 4 °C, under argon, protected from light), the compound was frequently recrystallized from warm water before use. ^{1}H NMR ($CDCl_3$): δ 3.30 (s, N-CH_3, 6H), 3.88 (s, O-CH_3, 3H), 7.58 (d, 2H), 7.15 (d, 2H). GC-MS calcd for $C_9H_{13}NO$ ($M - H^+$) *m/z* 150, found 150.

4'-(dimethylamino)-benzo-15-crown-5. 4-aminobenzo-15-crown-5 (Aldrich, 610 mg) and MeI (5 mL) were refluxed for 3 hours under argon while stirring. The solution was filtered to remove most MeI, and the gray powder was dried on a high vacuum line. The solid was put in a 25 mL round bottom flask with Na_2CO_3 (0.00132 mol, 0.140 g) and amyl alcohol (3 mL) and refluxed under argon for five hours. The amyl alcohol was washed twice with water, and dried on a high vacuum line overnight. Column chromatography proved unable to separate the monomethyl and dimethyl products, which appeared to be stoichiometric by NMR.

Thus, the mixture was reacted with 1 equivalent of decanoyl chloride (to generate the amide from the monomethyl impurity and render it separable by column chromatography). Dropwise addition of the acid chloride was performed in chloroform at 0 °C. The reaction ran 6 hours, and was extracted with water. Most of the desired product was in the aqueous phase, and was isolated by rotary evaporation. Purification was achieved by silica gel chromatography (EtOAc, 6% MeOH, 1% NEt_3), and the first few fractions contained the pure dimethyl aniline derivative (colorless oil). Yield = 125 mg, 19% based on starting crown ether. ^{1}H NMR ($CDCl_3$): δ 2.85 (s, N-CH_3, 6 H), 3.67 (m, -CH_2CH_2-, 8H), 3.81 (m, -CH_2, 2H), 3.84 (m, -CH_2, 2H), 4.01 (m, -CH_2, 2H), 4.08 (m, -CH_2, 2H), 6.24 (pair of doublets, 1 H), 6.80 (d, 1 H), 6.36 (d, 1 H), 6.80 (d, 1 H). ESI (electrospray, positive ion) calcd for $C_{16}H_{25}NO_5$ (M - H^+) *m/z* 312, found 312. Also

found, 334 (+ Na^+) and 350 (+ K^+). The 15-crown-5 ether derivative prefers sodium, but binds both cations in the gas phase.

Synthesis of Model Compounds

2-adamantylacetamide. The hygroscopic white solid 2-adamantylamine was prepared by dissolving 2-adamantylamine•HCl (Aldrich) in H_2O/NaOH, extracting with methylene chloride, drying with $MgSO_4$, filtering, and rotary evaporating. This reagent (500 mg) was dissolved in methylene chloride (20 mL), put on ice, and acetic anhydride (~ 5 equiv.) added dropwise. The reaction was left to run overnight, and worked up by addition of sodium bicarbonate solution, and extraction with $MeCl_2$. The solution was washed twice with H_2O and dried with $MgSO_4$. The white crystalline product looked clean by TLC (50% CH_2Cl_2/EtOAc, imaged with paraanisaldehyde, r_f ~ 0.25) and NMR without further purification. ^1H NMR ($CDCl_3$): δ 1.62-1.90 (m's, 15 H), 4.05 (br's, $-CH_3$), 5.82 (br's, N-H, amide).

4-(N-imidazole)-2,2',3,3',4',5,5',6,6'-fluorobiphenyl. Perfluorobiphenyl (133.6 mg, 0.4 mmol), imidazole (27.2 mg, 0.4 mmol), and K_2CO_3 (55.3 mg, 0.4 mmol) were put in a round bottom flask with freshly distilled DMSO, and the reaction was run under argon

for 24 hours at 30 °C. Work up involved adding 25 mL H_2O and extracting three times with 25 mL $MeCl_2$. The organic layer was dried over MgSO4, filtered, and rotovapped. TLC (EtOAc) showed two spots (monoimidazole, r_f= 0.75; diimidazole, r_f = 0.5; consumed starting perfluorobiphenyl, r_f = 1). The mixture was purified on silica gel using 50% EtOAc/hexanes as the eluent. Yield = 75 mg (49%) of the desired monoimidazole product with nearly an equal amount of the bisimidazole compound. ^{1}H NMR (CD_2Cl_2): δ 7.20 (br, 1H), 7.23 (m, 1H), 7.78 (br, 1H). ^{19}F NMR (CD_2Cl_2): δ -129 (m, 2F), -130 (m, 2F), -139 (m, 2F), -141.5 (m, 2F), -151.7 (m, 1F). ESI (electrospray, positive ion) calcd for $C_{15}H_3N_2F_9$ (M - H^+) *m/z* 383, found 383.

4,4'-bis(N,N'-imidazole)-2,2',3,3',5,5',6,6'-fluorobiphenyl. Isolated in the procedure above, this compound was synthesized in nearly quantitative yields by using three equivalents of imidazole and K_2CO_3. The product was purified on silica gel using 70% EtOAc/hexanes as eluent. ^{1}H NMR (CD_2Cl_2): δ 7.32 (br, 1H), 7.37 (m, 1H), 7.87 (br, 1H). ^{19}F NMR (CD_2Cl_2): δ -136.9 (m, 4F), -148 (d, 4F). ESI (electrospray, positive ion) calcd for $C_{18}H_6N_4F_{98}$(M - H^+) *m/z* 431, found 431.

4,4',5,5'-tetramethyl-2,2'-bipyridine. This bipyridyl ligand (Me_4bpy) was synthesized following published procedures (12). The brown liquid lutidine (3,4-dimethylpyridine,

Aldrich, 477 g, 4.45 mol) and Pd/C (10% Pd on carbon, Aldrich, ~ 40 g) were combined in a 2-liter flask with a reflux condenser, refluxed and stirred for 8 days. While still hot, the black solution was filtered on celite and cooled on ice. The beige crystals were collected with a Bückner funnel, washed with ether, and recrystallized with 1:1 $CHCl_3$/toluene. The off-white crystals crashed out of solution in the freezer, and were collected by filtration. Yield = 18.9 g, 4.0%. ^{1}H NMR ($CDCl_3$): δ 2.31 (s, -CH_3, 6H), 2.37 (s, -CH_3, 6H), 8.20 (s, 2H), 8.40 (s, 2H).

[Ru(Me_4bpy)$_2Cl_2$]•2H_2O. This was synthesized by a modification of published procedures (13). $RuCl_3$•3H_2O (Aldrich, 927 mg, 3.56 mmol), Me_4bpy (1.50 g, 7.08 mmol), LiCl (2.23 g, 52.6 mmol), and hydroquinone (EM, 1.96 g, 17.8 mmol) were dissolved in anhydrous dimethoxyethane (100 mL) and distilled methanol (50 mL). The solution was purged with argon for 20 minutes and refluxed under argon for 24 hours. Water (225 mL) was added to the cooled solution, and the brownish purple solid was collected on a medium frit and washed thoroughly with H_2O. The product was dissolved in $MeCl_2$ (450 mL) and washed with water (3 x 450 mL) until the aqueous layer was colorless. The organic layer was dried with $MgSO_4$ and rotary evaporated. The dark purple powder was reprecipitated from minimal $MeCl_2$ with ether, collected by filtration, and dried under high vacuum; yield = 600 mg, 28%.

[Ru(tmbpy)$_2$(4-hydroxymethyl-4'-methylbipyridine)](PF$_6$)$_2$. Ru(tmbpy)$_2$Cl$_2$ (100 mg, 0.168 mmol) and 4-hydroxymethyl-4'-methylbipyridine (73.9 mg, 0.369 mmol, synthesized exactly according to published procedures (14)) were put in a round bottom flask with H_2O (5 mL) and EtOH (2 mL) and refluxed under argon for 3 hours. The ethanol was removed by rotary evaporation, and orange crystals were obtained by adding a concentrated solution of $(NH_4)PF_6$, filtering on a frit and drying on an aspirator. Purification was performed on an 8" alumina column eluting with 2:1 toluene/acetonitrile. A dark nonfluorescent band eluted first, followed by the major orange band (product); brown and red junk stuck to the column. Yield = 40 mg, 25%.

DISCUSSION

A general methodology was developed to synthesize Ru-probes in good yields and with minimal effort. The first chromatography step generally gave 30% yields of the pure bpy' ligand, based on the starting bromoamide. Non-fluorescing silica TLC plates were used for all bpy ligand syntheses, since bpy coordinates the metal in the fluorescing plates, causing the spot to streak. The TLC plates were stained with a ferric salt solution, which turned the bpy spots red and made imaging easy, quick, and non-toxic. The

second chromatography step was tried on ion exchange as well as alumina media before settling on silica gel as the best support.

The ruthenation step generally yielded 60% pure Ru-substrate, while for Ru-ligands this final step yielded only ~ 30%. One useful tip (credit goes to Alex Dunn) is to elute the Ru-compounds with nitrate in the solvent--this minimizes streaking and isolates the product as the water soluble nitrate salt (obviating the need for metathesis). Metathesis was not always time consuming, however; it was possible to dissolve the more hydrophobic [Ru-substrate]$(PF_6)_2$ salts in dry acetone, and metathesize directly with tetrabutylammonium chloride, avoiding ion exchange chromatography completely. Unfortunately, due to the high solubility of many Ru-substrate chloride salts in both organic and aqueous solutions (an interesting property!), this was not always possible. Cation exchange chromatography often served as a final purification, as well as metathesis step.

The synthesis of *p*-MDMA was quite straightforward; the purification, however, was not. Unfortunately, separation of the mono and di-methyl products proved difficult. One tip worth following would be to react the mixture with decanoyl chloride, as was done to synthesize 4'-(dimethylamino)-benzo-15-crown-5. The conversion of the monomethyl side product to the decyl amide should make purification much easier.

Finally, $Ru(Me_4bpy)_2(Cl)_2 \cdot 2H_2O$ is a useful precursor for many high driving force excited-state ET reactions. The redox potential generally decreases 20 mV/methyl group, making $[Ru(Me_4bpy)_2(dmbpy)]^{2+}$ ~ 200 mV more negative than $Ru(bpy)_3$! Several different variants were synthesized to tune the driving force (i.e., $Ru(dmbpy)_2Cl_2$) or to make the complex reactive with surface cysteines (i.e., $Ru(tmbpy)_2$(4-bromomethyl-4'-methylbipyridine]$(PF_6)_2$) (14), but it is left to the reader to explore these other avenues.

REFERENCES AND NOTES

1. J. D. Lipscomb, *Biochemistry* **19**, 3590-3599 (1980).

2. T. L. Poulos, A. J. Howard, *Biochemistry* **26**, 8165-8174 (1987).

3. K. Miedlar, P. K. Das, *J. Am. Chem. Soc.* **104**, 7462-7469 (1982).

4. R. E. Sassoon, S. Gershuni, J. Rabani, *J. Phys. Chem.* **96**, 4692-4698 (1992).

5. T. E. Mallouk, J. S. Krueger, J. E. Mayer, C. M. G. Dymond, *Inorg. Chem.* **28**, 3507-3510 (1989).

6. C. Creutz, *Inorg. Chem.* **17**, 1046-1051 (1978).

7. C. Creutz, N. Sutin, B. S. Brunschwig, *J. Am. Chem. Soc.* **101**, 1297-1298 (1979).

8. A. J. Gordon, R. A. Ford, *The Chemist's Companion. A Handbook of Practical Data, Techniques, and References* (John Wiley and Sons, New York, 1972).

9. D. D. Perrin, W. L. F. Armarego, *Purification of Laboratory Chemicals* (Butterworth-Heinemann Ltd., Boston, 3rd Ed., 1988).

10. G. A. Mines, California Institute of Technology (1997).

11. M. Sekiya, M. Tomie, N. J. Leonard, *J. Org. Chem.* **33**, 318-322 (1968).

12. G. A. Mines, et al., *J. Am. Chem. Soc.* **118**, 1961-1965 (1996).

13. S. Gould, T. R. O'Toole, T. J. Meyer, *J. Am. Chem. Soc.* **112**, 9490-9496 (1990).

14. L. Geren, S. Hahm, B. Durham, F. Millet, *Biochemistry* **30**, 9450-9457 (1991).

APPENDIX C

Förster Energy-Transfer Calculations with P450:Ru-Probe Complexes

Acknowledgement:

Thanks go to Mike Machczynski for sharing his *MATLAB* routine for initial Förster energy-transfer calculations.

INTRODUCTION

Resonance energy transfer is commonly used in structural and dynamical studies of biomolecules. This technique provides information on molecular dimensions of 10 to 100 Å, with spatial and temporal resolution that surpasses most other biophysical measurements. Such data provide critical insights into molecular function in complex biological systems (1-3).

The phenomenon of dipolar interactions between donor (D) and acceptor (A) chromophores was first observed by Perrin almost a century ago, and a theory was proposed by Förster in the 1940's to describe the long-range interactions (4) which was verified experimentally by Stryer in the 1960's (5). The Förster rate equation (4) describes the energy transfer associated with very weak interactions between donor and acceptor (Eq. C.1):

$$k_{obs} = \frac{1}{\tau_D}\left(1 + \left(\frac{R_0}{r}\right)^6\right), \quad R_0{}^6 = 8.785 \times 10^{-5} \frac{\kappa^2 \phi_D J}{n^4}$$

where τ_D is the donor intrinsic lifetime, r is the D-A (Ru-iron) distance, R_0 is the Förster distance (the D-A distance at which half of the emission is quenched by energy transfer),

κ^2 is the D-A orientation factor, ϕ_D is the intrinsic quantum yield of the donor (in water), n is the index of refraction, and *J* is the D-A overlap integral (Eq. C.2):

$$J = \int F_D(\lambda)\varepsilon_A(\lambda)\lambda^4 d\lambda,$$

Where F_D is the peak-normalized donor fluorescence spectrum, and ε_A is the molar absorptivity of the acceptor. Extensive analysis of the factors influencing energy-transfer rates has been the subject of many reviews (1-5).

For the purposes of the experiments described in this thesis, it was easiest to use *MATLAB* for the calculation of the overlap integral, J, from which R_0, and then D-A distances were derived. A simple *MATLAB* script with directions for manipulating the absorbance and emission spectra is included below.

MATERIALS AND METHODS

General

A Hewlett Packard 8452A spectrophotometer was used to collect absorption spectra (500-800 nm) with 2 nm resolution. Fluorescence measurements were made on an ISS K2 fluorometer. Calculations were performed using *MATLAB* on a Macintosh

PowerPC. Emission lifetime measurements were performed using a nanosecond laser system (BILRC), as described in previous chapters.

Quantum Yield Determination

The fluorometer had been previously calibrated for emission in the visible to near infrared region, and the calibration was checked against $[Ru(bpy)_3]^{2+}$. By exciting between 450-470 nm and scanning from 500-800 nm, typically with 1 nm resolution, spectra of a blank (buffer), $[Ru(bpy)_3]^{2+}$ (standard), and various Ru-substrates were collected. Luminescence intensities were normalized for their absorption at the excitation frequency (typically 470 nm); the spectra were integrated using *MATLAB* and compared to $[Ru(bpy)_3]^{2+}$ to find relative quantum yields. ϕ_D^{H2O} for $[Ru(bpy)_3]^{2+}$ was taken to be 0.042, an average of several literature values. From this, ϕ_D^{H2O} was determined to be 0.0094 for $Ru(tmbpy)_2(dmbpy)$ and 0.025 for $Ru(bpy)_2(dmbpy)$.

Absorption Spectra Manipulation

For the 1:1 P450:Ru spectra, all Ru absorbance was subtracted, and the spectra were corrected for unbound P450 based on the percentage bound determined from energy transfer experiments. The UV-vis data were interpolated in *MATLAB* to give an OD at 1 nm intervals, and divided by the P450 concentration to determine the ε ($M^{-1}cm^{-1}$) spectra.

CALCULATIONS

```
% This function calculates Förster distances given inputs of a donor emission
% spectrum and an acceptor (epsilon) absorption spectrum.
% The two spectra must be ASCII files and have the same x-axis.  The interp1
% function is typically used to linearly interpolate points for the absorption
% spectrum, since the diode array detector only has 2 nm resolution.

kappa=sqrt (2/3);
index=1.33;
qyield=0.042;
lambda=500:800

% The assumption was made that the donor fluorophore rotates freely and is
% randomly oriented relative to the heme (kappa = sqrt (2/3)).
% The quantum yield was typically < 0.042 for Ru-substrates in water.
% The spectral overlap was generally not calculated for wavelengths > 800 nm
% due to the decreased sensitivity of the PMT detector and the tiny
% Ru emission and P450 absorption in the near infrared.

load fluor
load abs

% fluor = fluorescence spectrum
% abs = absorption extinction coefficient for P450 with the HP spectrophotometer
% lambda = wavelength (nm)
% trapz integrates the spectral overlap

y=fluor.*abs.*(lambda.^4)
J=((trapz(lambda,y))/trapz(lambda,fluor))

R0=(8.785e-5*(kappa.^2)*(index.^(-4))*qyield*J).^(1/6)
```

The D-A distance, r, was calculated by rearranging Eq. C.1 to give Eq. C.3.

$$r = \frac{R_0}{\left(\frac{\tau_D}{\tau_{obs}} - 1\right)}^{1/6}$$

DISCUSSION

These energy-transfer calculations give surprisingly accurate Ru-iron distances, especially considering that $\{Ru(bpy)_3\}^{2+*}$ emission is mostly triplet in character and the heme ground state is a singlet. The insensitivity of R_0 to most of the parameters makes the agreement between theory and experiment seem fortuitous. However, the experimentally measured ratio τ_D/τ_{obs} is crucial for determining an accurate Ru-iron distance (r), and this value should be precise to within $\pm$ 5% by the methods employed. Small errors in the quantum yield or spectral overlap only propagate small errors; the success of the final prediction rests on the accuracy of the emission lifetimes and the quality of the absorption and emission spectra.

REFERENCES AND NOTES

1. P. Wu, L. Brand, *Anal. Biochem.* **218**, 1-13 (1994).

2. N. L. Vekshin, *Energy Transfer in Macromolecules* (SPIE Optical Engineering Press, Bellingham, 1997).

3. M. R. Eftink, *Principles*. J. R. Lakowicz, Ed., Topics in Fluorescence Spectroscopy (Plenum Press, New York, 1991), vol. 2.

4. T. Förster, in *Modern Quantum Chemistry* O. Sinanoglu, Ed. (Academic Press, New York, 1965), vol. III, pp. 93-137.

5. L. Stryer, *Annu. Rev. Biochem.* **47**, 819-846 (1978).

APPENDIX D

The Apparent Dissociation Constant of a Racemic Mixture: A Mathematical Analysis of the Competition between Ru Stereoisomers

Acknowledgement:

Jay Winkler recognized this problem; he called my attention to it, and he pointed the way to its solution.

INTRODUCTION

For most of the work presented in this thesis, the Ru-substrates were racemic mixtures of Λ and Δ isomers. Not much thought was given to the "impurity" of these compounds. After all, it stood to reason that the stereoisomers should bind similarly to the large cavity of the enzyme. In addition, assuming that the Ru^{1+}--Fe^{3+}/Ru^{3+}--Fe^{2+} electron-transfer reactions are mediated by the intervening bridge-substrate moiety (the high rates of electron transfer make this point strongly), then the ET path should be identical for both isomers. So what's the problem?

Pandora's Box was opened with the decision to resolve Λ and Δ Ru-C_9-Ad isomers. Electron density that is best attributed to the two $\{Ru(bpy)_3\}^{2+}$ isomers was smeared out in the P450: Ru-C_9-Ad X-ray structure, raising questions about whether one compound binds better, in a different position, etc. In addition, high thermal factors prevented clear assignments of the entire alkyl chain of either isomer. There were two assignable positions for the chain (each belonging to a different isomer?), and distinguishing the methylene chain(s) from a chain of water molecules proved difficult. Many of the active-site amino acid side chains exist in alternate conformations in this structure (Chapter 4), raising the possibility that the two isomers interact differently with the protein interior.

The chiral separation of Λ and Δ Ru-C_9-Ad (described in Chapter 3) yielded very small quantities (~ 1 mg) of the pure enantiomers. Obtaining dissociation constants for Λ and Δ isomers proved straightforward and gave consistent results by three independent methods. Problems arose, however, in drawing comparisons between the binding of each of the isomers and their racemic mixture. The syllogism K_D(racemic) = (K_D(Λ) + K_D(Δ)) / 2 was shown to be false. In fact, since there is direct competition between Λ and Δ for the same binding site, the *apparent* K_D(racemic) depends not only on K_D(Λ) and K_D(Δ), but also on the concentration of ruthenium and protein. As a general rule, when there is little enantiomeric discrimination (K_D(Λ) ~ K_D(Δ)) the apparent K_D(racemic) is weighted towards the better binding isomer. However, in the limiting case in which one isomer is "dirt" and the other an excellent substrate, competition for the binding site vanishes. With only 50% viable substrate, there is correspondingly only 50% ES complex formation (based on available Ru). Depending on the relative concentrations of protein and Ru, the apparent dissociation constant of the racemic mixture can appear very poor indeed.

The following is a derivation of the solution to this problem. It proved simplest to test the model based on the initial equilibrium conditions with *Mathematica*. Cubic equations are best done on a computer!

MATERIALS AND METHODS

General

Titrations were performed, and data were analyzed using the equipment and techniques described in Chapter 3. Calculations were performed using *Mathematica*.

Calculations

Variables

E = Enzyme concentration free in solution
E_0 = Initial enzyme concentration
S_0 = Initial Ru concentration (both isomers)
D = Δ isomer concentration free in solution
L = Λ isomer concentration free in solution
DE = Enzyme concentration bound to Δ
LE = Enzyme concentration bound to Λ
K_{DL} = Apparent dissociation constant for the racemic mixture
K_D = Dissociation constant for Δ
K_L = Dissociation constant for Λ

$$DE \overset{K_D}{\rightleftharpoons} D + E \qquad\qquad LE \overset{K_L}{\rightleftharpoons} L + E$$

By definition, $K_D = [D][E] / [DE]$ and $K_L = [L][E] / [LE]$

Since in our laser experiments we measure the quantity of free Ru,(D + L), we combine the above equilibrium expressions to give:

$$\mathbf{K_{DL} = [D + L][E] / [DE + LE]}$$

In order to solve this expression, we need to get D in terms of L

By conservation of mass, $E_0 = E + DE + LE$

$S_0 = D + L + DE + LE$

Rearranging we get, $E = E_0 - DE - LE$

And substituting, $\mathbf{E = E_0 - S_0 + D + L}$

By definition of a racemic mixture, $0.5\ S_0 = D + DE = L + LE$

Rearranging, we have $\mathbf{DE = 0.5\ S_0 - D}$ and $\mathbf{LE = 0.5\ S_0 - L}$

Plugging **E** and **LE** back into the equilibrium expression for K_L and **E** and **DE** into the equilibrium expression for K_D, we get

$$(0.5\ S_0 - L)(K_L) = (L)(E_0 - S_0 + D + L)$$
$$(0.5\ S_0 - D)(K_D) = (D)(E_0 - S_0 + D + L)$$

Rearranging the first equation, we get $\mathbf{D = S_0 - E_0 - L + (0.5\ S_0 - L)(K_L / L)}$

Putting the second equation in terms of D, we get

$$\mathbf{D^2 + (E_0 - S_0 + D + L)(D) - 0.5\ S_0(K_D) = 0}$$

Substituting **D** into this equation gives

$$[(S_0 - E_0 - L) + (0.5\ S_0 - L)(K_L / L)]^2 +$$
$$(E_0 - S_0 + K_D + L)[S_0 - E_0 - L + (0.5\ S_0 - L)(K_L / L)] - 0.5\ S_0(K_D) = 0$$

Attempts were made to solve this equation by hand, but it proved simpler to plug it directly into *Mathematica*. The variables were redefined slightly:

$S = S_0$

$p = E_0$

$K = K_L$

$L = L$

$d = K_D$

RESULTS

```
K=200

S=5000

p=5000

Solve [{S-p-L + {.5*S-L} * {K/L}}^2 +{p-S+d+L} * {S-p-L +{.5*S-L}*{K/L}}-
.5*S*d ==0,L]
```

```
200

5000

5000
```

$$\{\{L \to -\frac{0.333333\,(460000. + 2700.\,d)}{-200. + 1.\,d} + ((0.209987 - 0.363708\,i)\,(-3.316\times10^{11} - 1.584\times10^{9}\,d - 8.79\times10^{6}\,d^2))\Big/ \left((-200. + 1.\,d)\left(-9.0272\times10^{16} - 5.85792\times10^{15}\,d - 8.1504\times10^{12}\,d^2 - 5.1516\times10^{10}\,d^3 + 7.91881\times10^{9}\,\sqrt{(-2.19591\times10^{15} - 1.6465\times10^{13}\,d + 2.26516\times10^{11}\,d^2 - 3.49485\times10^{8}\,d^3 + 1.56086\times10^{6}\,d^4 - 10028.8\,d^5 - 1.\,d^6)}\right)\text{^}(1/3)\right) - \frac{1}{-200. + 1.\,d}\left((0.132283 + 0.229122\,i)\left(-9.0272\times10^{16} - 5.85792\times10^{15}\,d - 8.1504\times10^{12}\,d^2 - 5.1516\times10^{10}\,d^3 + 7.91881\times10^{9}\,\sqrt{(-2.19591\times10^{15} - 1.6465\times10^{13}\,d + 2.26516\times10^{11}\,d^2 - 3.49485\times10^{8}\,d^3 + 1.56086\times10^{6}\,d^4 - 10028.8\,d^5 - 1.\,d^6)}\right)\text{^}(1/3)\right)\},$$

$$\{L \to -\frac{0.333333\,(460000. + 2700.\,d)}{-200. + 1.\,d} + ((0.209987 + 0.363708\,i)\,(-3.316\times10^{11} - 1.584\times10^{9}\,d - 8.79\times10^{6}\,d^2))\Big/ \left((-200. + 1.\,d)\left(-9.0272\times10^{16} - 5.85792\times10^{15}\,d - 8.1504\times10^{12}\,d^2 - 5.1516\times10^{10}\,d^3 + 7.91881\times10^{9}\,\sqrt{(-2.19591\times10^{15} - 1.6465\times10^{13}\,d + 2.26516\times10^{11}\,d^2 - 3.49485\times10^{8}\,d^3 + 1.56086\times10^{6}\,d^4 - 10028.8\,d^5 - 1.\,d^6)}\right)\text{^}(1/3)\right) - \frac{1}{-200. + 1.\,d}\left((0.132283 - 0.229122\,i)\left(-9.0272\times10^{16} - 5.85792\times10^{15}\,d - 8.1504\times10^{12}\,d^2 - 5.1516\times10^{10}\,d^3 + 7.91881\times10^{9}\,\sqrt{(-2.19591\times10^{15} - 1.6465\times10^{13}\,d + 2.26516\times10^{11}\,d^2 - 3.49485\times10^{8}\,d^3 + 1.56086\times10^{6}\,d^4 - 10028.8\,d^5 - 1.\,d^6)}\right)\text{^}(1/3)\right)\},$$

$$\{L \to -\frac{0.333333\,(460000. + 2700.\,d)}{-200. + 1.\,d} - (0.419974\,(-3.316\times10^{11} - 1.584\times10^{9}\,d - 8.79\times10^{6}\,d^2))\Big/ \left((-200. + 1.\,d)\left(-9.0272\times10^{16} - 5.85792\times10^{15}\,d - 8.1504\times10^{12}\,d^2 - 5.1516\times10^{10}\,d^3 + 7.91881\times10^{9}\,\sqrt{(-2.19591\times10^{15} - 1.6465\times10^{13}\,d + 2.26516\times10^{11}\,d^2 - 3.49485\times10^{8}\,d^3 + 1.56086\times10^{6}\,d^4 - 10028.8\,d^5 - 1.\,d^6)}\right)\text{^}(1/3)\right) + \frac{1}{-200. + 1.\,d}\left(0.264567\left(-9.0272\times10^{16} - 5.85792\times10^{15}\,d - 8.1504\times10^{12}\,d^2 - 5.1516\times10^{10}\,d^3 + 7.91881\times10^{9}\,\sqrt{(-2.19591\times10^{15} - 1.6465\times10^{13}\,d + 2.26516\times10^{11}\,d^2 - 3.49485\times10^{8}\,d^3 + 1.56086\times10^{6}\,d^4 - 10028.8\,d^5 - 1.\,d^6)}\right)\text{^}(1/3)\right)\}\}$$

```
F=S-p-L+{.5*S-L}*K/L

T=p-S+F+L

A=.5*S-F

B=.5*S-L
```

$$\left\{\frac{200\,(2500.-L)}{L}-L\right\}$$

$$\left\{\frac{200\,(2500.-L)}{L}\right\}$$

$$\left\{2500.-\frac{200\,(2500.-L)}{L}+L\right\}$$

```
2500.-L
```

$$\begin{aligned}L = &-\frac{0.3333333333333333`\,(460000.`+2700.`\,d)}{-200.`+1.`\,d}-\\ &(0.419973683298291`\,(-3.316`*^11-1.584`*^9\,d-8.79`*^6\,d^2))\Big/\\ &\Big((-200.`+1.`\,d)\Big(-9.0272`*^16-5.85792`*^15\,d-8.1504`*^12\,d^2-5.1516`*^10\,d^3+\\ &7.918806728289307`*^9\,\sqrt{(-2.1959095801937568`*^15-1.6465016146393973`*^13\\ &d+2.2651625403659848`*^11\,d^2-3.4948546824542516`*^8\,d^3+\\ &1.5608611410118407`*^6\,d^4-10028.848223896663`\,d^5-1.`\,d^6)}\Big)\wedge(1/3)\Big)+\\ &\frac{1}{-200.`+1.`\,d}\Big(0.26456684199469993`\,\Big(-9.0272`*^16-5.85792`*^15\,d-\\ &8.1504`*^12\,d^2-5.1516`*^10\,d^3+7.918806728289307`*^9\\ &\sqrt{(-2.1959095801937568`*^15-1.6465016146393973`*^13\,d+\\ &2.2651625403659848`*^11\,d^2-3.4948546824542516`*^8\,d^3+\\ &1.5608611410118407`*^6\,d^4-10028.848223896663`\,d^5-1.`\,d^6)}\Big)\wedge(1/3)\Big)\end{aligned}$$

$$\begin{aligned}&-\frac{0.333333\,(460000.+2700.\,d)}{-200.+1.\,d}-(0.419974\,(-3.316\times10^{11}-1.584\times10^{9}\,d-8.79\times10^{6}\,d^2))\Big/\\ &\Big((-200.+1.\,d)\Big(-9.0272\times10^{16}-5.85792\times10^{15}\,d-8.1504\times10^{12}\,d^2-5.1516\times10^{10}\,d^3+\\ &7.91881\times10^{9}\,\sqrt{(-2.19591\times10^{15}-1.6465\times10^{13}\,d+2.26516\times10^{11}\,d^2-\\ &3.49485\times10^{8}\,d^3+1.56086\times10^{6}\,d^4-10028.8\,d^5-1.\,d^6)}\Big)\wedge(1/3)\Big)+\\ &\frac{1}{-200.+1.\,d}\Big(0.264567\,\Big(-9.0272\times10^{16}-5.85792\times10^{15}\,d-8.1504\times10^{12}\,d^2-5.1516\times10^{10}\,d^3+\\ &7.91881\times10^{9}\,\sqrt{(-2.19591\times10^{15}-1.6465\times10^{13}\,d+2.26516\times10^{11}\,d^2-\\ &3.49485\times10^{8}\,d^3+1.56086\times10^{6}\,d^4-10028.8\,d^5-1.\,d^6)}\Big)\wedge(1/3)\Big)\end{aligned}$$

```
J={{F+L}*T}/{A+B}
```

$$\begin{aligned}&\Big\{\Big\{\Big(200\Big(2500.+\frac{0.333333\,(460000.+2700.\,d)}{-200.+1.\,d}+\\ &(0.419974\,(-3.316\times10^{11}-1.584\times10^{9}\,d-8.79\times10^{6}\,d^2))\Big/\\ &\Big((-200.+1.\,d)\Big(-9.0272\times10^{16}-5.85792\times10^{15}\,d-8.1504\times10^{12}\,d^2-5.1516\times10^{10}\,d^3+\\ &7.91881\times10^{9}\,\sqrt{(-2.19591\times10^{15}-1.6465\times10^{13}\,d+2.26516\times10^{11}\,d^2-\\ &3.49485\times10^{8}\,d^3+1.56086\times10^{6}\,d^4-10028.8\,d^5-1.\,d^6)}\Big)\wedge(1/3)\Big)-\\ &\frac{1}{-200.+1.\,d}\Big(0.264567\,\Big(-9.0272\times10^{16}-5.85792\times10^{15}\,d-8.1504\times10^{12}\,d^2-\\ &5.1516\times10^{10}\,d^3+7.91881\times10^{9}\\ &\sqrt{(-2.19591\times10^{15}-1.6465\times10^{13}\,d+2.26516\times10^{11}\,d^2-\\ &3.49485\times10^{8}\,d^3+1.56086\times10^{6}\,d^4-10028.8\,d^5-1.\,d^6)}\Big)\wedge(1/3)\Big)\Big)\end{aligned}$$

$$\left(\frac{0.\,(460000.+2700.\,d)}{-200.+1.\,d}+(0.\,(-3.316\times10^{11}-1.584\times10^{9}\,d-8.79\times10^{6}\,d^2))\Big/\right.$$
$$((-200.+1.\,d)\,(-9.0272\times10^{16}-5.85792\times10^{15}\,d-8.1504\times10^{12}\,d^2-5.1516\times10^{10}\,d^3+$$
$$7.91881\times10^{9}\,\sqrt{(-2.19591\times10^{15}-1.6465\times10^{13}\,d+2.26516\times10^{11}\,d^2-$$
$$3.49485\times10^{8}\,d^3+1.56086\times10^{6}\,d^4-10028.8\,d^5-1.\,d^6)}\,)\hat{}\,(1/3))+$$
$$\frac{1}{-200.+1.\,d}(0.\,(-9.0272\times10^{16}-5.85792\times10^{15}\,d-8.1504\times10^{12}\,d^2-5.1516\times10^{10}\,d^3+$$
$$7.91881\times10^{9}\,\sqrt{(-2.19591\times10^{15}-1.6465\times10^{13}\,d+2.26516\times10^{11}\,d^2-$$
$$3.49485\times10^{8}\,d^3+1.56086\times10^{6}\,d^4-10028.8\,d^5-1.\,d^6)}\,)\hat{}\,(1/3))+$$
$$\left(200\left(2500.+\frac{0.333333\,(460000.+2700.\,d)}{-200.+1.\,d}+(0.419974\,(-3.316\times10^{11}-\right.\right.$$
$$1.584\times10^{9}\,d-8.79\times10^{6}\,d^2))\Big/$$
$$((-200.+1.\,d)\,(-9.0272\times10^{16}-5.85792\times10^{15}\,d-8.1504\times10^{12}\,d^2-$$
$$5.1516\times10^{10}\,d^3+7.91881\times10^{9}\,\sqrt{(-2.19591\times10^{15}-$$
$$1.6465\times10^{13}\,d+2.26516\times10^{11}\,d^2-3.49485\times10^{8}\,d^3+$$
$$1.56086\times10^{6}\,d^4-10028.8\,d^5-1.\,d^6)}\,)\hat{}\,(1/3))-$$
$$\frac{1}{-200.+1.\,d}(0.264567\,(-9.0272\times10^{16}-5.85792\times10^{15}\,d-8.1504\times10^{12}$$
$$d^2-5.1516\times10^{10}\,d^3+7.91881\times10^{9}\,\sqrt{(-2.19591\times10^{15}-$$
$$1.6465\times10^{13}\,d+2.26516\times10^{11}\,d^2-3.49485\times10^{8}\,d^3+$$
$$\left.\left.1.56086\times10^{6}\,d^4-10028.8\,d^5-1.\,d^6)}\,)\hat{}\,(1/3))\right)\Big/$$
$$\left(-\frac{0.333333\,(460000.+2700.\,d)}{-200.+1.\,d}-(0.419974\,(-3.316\times10^{11}-1.584\times10^{9}\,d-\right.$$
$$8.79\times10^{6}\,d^2))\Big/((-200.+1.\,d)\,(-9.0272\times10^{16}-5.85792\times10^{15}\,d-$$
$$8.1504\times10^{12}\,d^2-5.1516\times10^{10}\,d^3+7.91881\times10^{9}\,\sqrt{(-2.19591\times10^{15}-$$
$$1.6465\times10^{13}\,d+2.26516\times10^{11}\,d^2-3.49485\times10^{8}\,d^3+$$
$$1.56086\times10^{6}\,d^4-10028.8\,d^5-1.\,d^6)}\,)\hat{}\,(1/3))+$$
$$\frac{1}{-200.+1.\,d}(0.264567\,(-9.0272\times10^{16}-5.85792\times10^{15}\,d-8.1504\times10^{12}$$
$$d^2-5.1516\times10^{10}\,d^3+7.91881\times10^{9}\,\sqrt{(-2.19591\times10^{15}-$$
$$1.6465\times10^{13}\,d+2.26516\times10^{11}\,d^2-3.49485\times10^{8}\,d^3+$$
$$\left.\left.1.56086\times10^{6}\,d^4-10028.8\,d^5-1.\,d^6)}\,)\hat{}\,(1/3))\right)\right)\Big/$$
$$\left(\left(-\frac{0.333333\,(460000.+2700.\,d)}{-200.+1.\,d}-(0.419974\,(-3.316\times10^{11}-1.584\times10^{9}\,d-8.79\times10^{6}\,d^2))\Big/\right.\right.$$
$$((-200.+1.\,d)\,(-9.0272\times10^{16}-5.85792\times10^{15}\,d-8.1504\times10^{12}\,d^2-5.1516\times10^{10}\,d^3+$$
$$7.91881\times10^{9}\,\sqrt{(-2.19591\times10^{15}-1.6465\times10^{13}\,d+2.26516\times10^{11}\,d^2-$$
$$3.49485\times10^{8}\,d^3+1.56086\times10^{6}\,d^4-10028.8\,d^5-1.\,d^6)}\,)\hat{}\,(1/3))+$$
$$\frac{1}{-200.+1.\,d}(0.264567\,(-9.0272\times10^{16}-5.85792\times10^{15}\,d-8.1504\times10^{12}\,d^2-$$
$$5.1516\times10^{10}\,d^3+7.91881\times10^{9}$$
$$\sqrt{(-2.19591\times10^{15}-1.6465\times10^{13}\,d+2.26516\times10^{11}\,d^2-$$
$$\left.\left.3.49485\times10^{8}\,d^3+1.56086\times10^{6}\,d^4-10028.8\,d^5-1.\,d^6)}\,)\hat{}\,(1/3))\right)$$
$$\left(5000.+\frac{0.\,(460000.+2700.\,d)}{-200.+1.\,d}+(0.\,(-3.316\times10^{11}-1.584\times10^{9}\,d-8.79\times10^{6}\,d^2))\Big/\right.$$
$$((-200.+1.\,d)\,(-9.0272\times10^{16}-5.85792\times10^{15}\,d-8.1504\times10^{12}\,d^2-5.1516\times10^{10}\,d^3+$$
$$7.91881\times10^{9}\,\sqrt{(-2.19591\times10^{15}-1.6465\times10^{13}\,d+2.26516\times10^{11}\,d^2-$$
$$3.49485\times10^{8}\,d^3+1.56086\times10^{6}\,d^4-10028.8\,d^5-1.\,d^6)}\,)\hat{}\,(1/3))+$$
$$\frac{1}{-200.+1.\,d}(0.\,(-9.0272\times10^{16}-5.85792\times10^{15}\,d-8.1504\times10^{12}\,d^2-5.1516\times10^{10}\,d^3+$$
$$7.91881\times10^{9}\,\sqrt{(-2.19591\times10^{15}-1.6465\times10^{13}\,d+2.26516\times10^{11}\,d^2-$$
$$3.49485\times10^{8}\,d^3+1.56086\times10^{6}\,d^4-10028.8\,d^5-1.\,d^6)}\,)\hat{}\,(1/3))-$$
$$\left(200\left(2500.+\frac{0.333333\,(460000.+2700.\,d)}{-200.+1.\,d}+(0.419974\,(-3.316\times10^{11}-\right.\right.$$
$$1.584\times10^{9}\,d-8.79\times10^{6}\,d^2))\Big/$$
$$((-200.+1.\,d)\,(-9.0272\times10^{16}-5.85792\times10^{15}\,d-8.1504\times10^{12}\,d^2-$$

$$5.1516\times10^{10}\,d^3+7.91881\times10^9\,\sqrt{(-2.19591\times10^{15}-1.6465\times10^{13}\,d+2.26516\times10^{11}\,d^2-3.49485\times10^8\,d^3+1.56086\times10^6\,d^4-10028.8\,d^5-1.\,d^6)}\,\hat{}\,(1/3)\Big)-\frac{1}{-200.+1.\,d}\Big(0.264567\Big(-9.0272\times10^{16}-5.85792\times10^{15}\,d-8.1504\times10^{12}\,d^2-5.1516\times10^{10}\,d^3+7.91881\times10^9\,\sqrt{(-2.19591\times10^{15}-1.6465\times10^{13}\,d+2.26516\times10^{11}\,d^2-3.49485\times10^8\,d^3+1.56086\times10^6\,d^4-10028.8\,d^5-1.\,d^6)}\,\hat{}\,(1/3)\Big)\Big)\Big/\Big(-\frac{0.333333\,(460000.+2700.\,d)}{-200.+1.\,d}-(0.419974\,(-3.316\times10^{11}-1.584\times10^9\,d-8.79\times10^6\,d^2))\Big/\big((-200.+1.\,d)\big(-9.0272\times10^{16}-5.85792\times10^{15}\,d-8.1504\times10^{12}\,d^2-5.1516\times10^{10}\,d^3+7.91881\times10^9\,\sqrt{(-2.19591\times10^{15}-1.6465\times10^{13}\,d+2.26516\times10^{11}\,d^2-3.49485\times10^8\,d^3+1.56086\times10^6\,d^4-10028.8\,d^5-1.\,d^6)}\,\hat{}\,(1/3)\big)+\frac{1}{-200.+1.\,d}\Big(0.264567\Big(-9.0272\times10^{16}-5.85792\times10^{15}\,d-8.1504\times10^{12}\,d^2-5.1516\times10^{10}\,d^3+7.91881\times10^9\,\sqrt{(-2.19591\times10^{15}-1.6465\times10^{13}\,d+2.26516\times10^{11}\,d^2-3.49485\times10^8\,d^3+1.56086\times10^6\,d^4-10028.8\,d^5-1.\,d^6)}\,\hat{}\,(1/3)\Big)\Big)\Big)\Big\}\Big\}\Big\}$$

Fnc=%

$$\Big\{\Big\{\Big\{\Big(200\Big(2500.+\frac{0.333333\,(460000.+2700.\,d)}{-200.+1.\,d}+(0.419974\,(-3.316\times10^{11}-1.584\times10^9\,d-8.79\times10^6\,d^2))\Big/\big((-200.+1.\,d)\big(-9.0272\times10^{16}-5.85792\times10^{15}\,d-8.1504\times10^{12}\,d^2-5.1516\times10^{10}\,d^3+7.91881\times10^9\,\sqrt{(-2.19591\times10^{15}-1.6465\times10^{13}\,d+2.26516\times10^{11}\,d^2-3.49485\times10^8\,d^3+1.56086\times10^6\,d^4-10028.8\,d^5-1.\,d^6)}\,\hat{}\,(1/3)\big)-\frac{1}{-200.+1.\,d}\Big(0.264567\Big(-9.0272\times10^{16}-5.85792\times10^{15}\,d-8.1504\times10^{12}\,d^2-5.1516\times10^{10}\,d^3+7.91881\times10^9\,\sqrt{(-2.19591\times10^{15}-1.6465\times10^{13}\,d+2.26516\times10^{11}\,d^2-3.49485\times10^8\,d^3+1.56086\times10^6\,d^4-10028.8\,d^5-1.\,d^6)}\,\hat{}\,(1/3)\Big)\Big)\Big)\Big(\frac{0.\,(460000.+2700.\,d)}{-200.+1.\,d}+(0.\,(-3.316\times10^{11}-1.584\times10^9\,d-8.79\times10^6\,d^2))\Big/\big((-200.+1.\,d)\big(-9.0272\times10^{16}-5.85792\times10^{15}\,d-8.1504\times10^{12}\,d^2-5.1516\times10^{10}\,d^3+7.91881\times10^9\,\sqrt{(-2.19591\times10^{15}-1.6465\times10^{13}\,d+2.26516\times10^{11}\,d^2-3.49485\times10^8\,d^3+1.56086\times10^6\,d^4-10028.8\,d^5-1.\,d^6)}\,\hat{}\,(1/3)\big)+\frac{1}{-200.+1.\,d}\Big(0.\,\big(-9.0272\times10^{16}-5.85792\times10^{15}\,d-8.1504\times10^{12}\,d^2-5.1516\times10^{10}\,d^3+7.91881\times10^9\,\sqrt{(-2.19591\times10^{15}-1.6465\times10^{13}\,d+2.26516\times10^{11}\,d^2-3.49485\times10^8\,d^3+1.56086\times10^6\,d^4-10028.8\,d^5-1.\,d^6)}\,\hat{}\,(1/3)\big)+\Big(200\Big(2500.+\frac{0.333333\,(460000.+2700.\,d)}{-200.+1.\,d}+(0.419974\,(-3.316\times10^{11}-1.584\times10^9\,d-8.79\times10^6\,d^2))\Big/\big((-200.+1.\,d)\big(-9.0272\times10^{16}-5.85792\times10^{15}\,d-8.1504\times10^{12}\,d^2-5.1516\times10^{10}\,d^3+7.91881\times10^9\,\sqrt{(-2.19591\times10^{15}-1.6465\times10^{13}\,d+2.26516\times10^{11}\,d^2-3.49485\times10^8\,d^3+1.56086\times10^6\,d^4-10028.8\,d^5-1.\,d^6)}\,\hat{}\,(1/3)\big)-\frac{1}{-200.+1.\,d}\Big(0.264567\Big(-9.0272\times10^{16}-5.85792\times10^{15}\,d-8.1504\times10^{12}\,d^2-5.1516\times10^{10}\,d^3+7.91881\times10^9\,\sqrt{(-2.19591\times10^{15}-1.6465\times10^{13}\,d+2.26516\times10^{11}\,d^2-3.49485\times10^8\,d^3+1.56086\times10^6\,d^4-10028.8\,d^5-1.\,d^6)}\,\hat{}\,(1/3)\Big)\Big)\Big/$$

$$\Bigl(-\frac{0.333333\,(460000. + 2700.\,\mathrm{d})}{-200. + 1.\,\mathrm{d}} - (0.419974\,(-3.316\times10^{11} - 1.584\times10^{9}\,\mathrm{d} -$$

$$8.79\times10^{6}\,\mathrm{d}^{2}))\Big/\bigl((-200. + 1.\,\mathrm{d})\bigl(-9.0272\times10^{16} - 5.85792\times10^{15}\,\mathrm{d} -$$

$$8.1504\times10^{12}\,\mathrm{d}^{2} - 5.1516\times10^{10}\,\mathrm{d}^{3} + 7.91881\times10^{9}\,\surd(-2.19591\times10^{15} -$$

$$1.6465\times10^{13}\,\mathrm{d} + 2.26516\times10^{11}\,\mathrm{d}^{2} - 3.49485\times10^{8}\,\mathrm{d}^{3} +$$

$$1.56086\times10^{6}\,\mathrm{d}^{4} - 10028.8\,\mathrm{d}^{5} - 1.\,\mathrm{d}^{6}))\wedge(1/3)\bigr) +$$

$$\frac{1}{-200. + 1.\,\mathrm{d}}\bigl(0.264567\bigl(-9.0272\times10^{16} - 5.85792\times10^{15}\,\mathrm{d} - 8.1504\times10^{12}$$

$$\mathrm{d}^{2} - 5.1516\times10^{10}\,\mathrm{d}^{3} + 7.91881\times10^{9}\,\surd(-2.19591\times10^{15} -$$

$$1.6465\times10^{13}\,\mathrm{d} + 2.26516\times10^{11}\,\mathrm{d}^{2} - 3.49485\times10^{8}\,\mathrm{d}^{3} +$$

$$1.56086\times10^{6}\,\mathrm{d}^{4} - 10028.8\,\mathrm{d}^{5} - 1.\,\mathrm{d}^{6}))\wedge(1/3))\Bigr)\Bigr)\Bigr)\Big/$$

$$\Bigl(\Bigl(-\frac{0.333333\,(460000. + 2700.\,\mathrm{d})}{-200. + 1.\,\mathrm{d}} - (0.419974\,(-3.316\times10^{11} - 1.584\times10^{9}\,\mathrm{d} - 8.79\times10^{6}\,\mathrm{d}^{2}))\big/$$

$$((-200. + 1.\,\mathrm{d})\bigl(-9.0272\times10^{16} - 5.85792\times10^{15}\,\mathrm{d} - 8.1504\times10^{12}\,\mathrm{d}^{2} - 5.1516\times10^{10}\,\mathrm{d}^{3} +$$

$$7.91881\times10^{9}\,\surd(-2.19591\times10^{15} - 1.6465\times10^{13}\,\mathrm{d} + 2.26516\times10^{11}\,\mathrm{d}^{2} -$$

$$3.49485\times10^{8}\,\mathrm{d}^{3} + 1.56086\times10^{6}\,\mathrm{d}^{4} - 10028.8\,\mathrm{d}^{5} - 1.\,\mathrm{d}^{6}))\wedge(1/3)\bigr) +$$

$$\frac{1}{-200. + 1.\,\mathrm{d}}\bigl(0.264567\bigl(-9.0272\times10^{16} - 5.85792\times10^{15}\,\mathrm{d} - 8.1504\times10^{12}\,\mathrm{d}^{2} -$$

$$5.1516\times10^{10}\,\mathrm{d}^{3} + 7.91881\times10^{9}$$

$$\surd(-2.19591\times10^{15} - 1.6465\times10^{13}\,\mathrm{d} + 2.26516\times10^{11}\,\mathrm{d}^{2} -$$

$$3.49485\times10^{8}\,\mathrm{d}^{3} + 1.56086\times10^{6}\,\mathrm{d}^{4} - 10028.8\,\mathrm{d}^{5} - 1.\,\mathrm{d}^{6}))\wedge(1/3))\Bigr)$$

$$\Bigl(5000. + \frac{0.\,(460000. + 2700.\,\mathrm{d})}{-200. + 1.\,\mathrm{d}} + (0.\,(-3.316\times10^{11} - 1.584\times10^{9}\,\mathrm{d} - 8.79\times10^{6}\,\mathrm{d}^{2}))\big/$$

$$((-200. + 1.\,\mathrm{d})\bigl(-9.0272\times10^{16} - 5.85792\times10^{15}\,\mathrm{d} - 8.1504\times10^{12}\,\mathrm{d}^{2} - 5.1516\times10^{10}\,\mathrm{d}^{3} +$$

$$7.91881\times10^{9}\,\surd(-2.19591\times10^{15} - 1.6465\times10^{13}\,\mathrm{d} + 2.26516\times10^{11}\,\mathrm{d}^{2} -$$

$$3.49485\times10^{8}\,\mathrm{d}^{3} + 1.56086\times10^{6}\,\mathrm{d}^{4} - 10028.8\,\mathrm{d}^{5} - 1.\,\mathrm{d}^{6}))\wedge(1/3)\bigr) +$$

$$\frac{1}{-200. + 1.\,\mathrm{d}}\bigl(0.\,\bigl(-9.0272\times10^{16} - 5.85792\times10^{15}\,\mathrm{d} - 8.1504\times10^{12}\,\mathrm{d}^{2} - 5.1516\times10^{10}\,\mathrm{d}^{3} +$$

$$7.91881\times10^{9}\,\surd(-2.19591\times10^{15} - 1.6465\times10^{13}\,\mathrm{d} + 2.26516\times10^{11}\,\mathrm{d}^{2} -$$

$$3.49485\times10^{8}\,\mathrm{d}^{3} + 1.56086\times10^{6}\,\mathrm{d}^{4} - 10028.8\,\mathrm{d}^{5} - 1.\,\mathrm{d}^{6}))\wedge(1/3)\bigr) -$$

$$\Bigl(200\Bigl(2500. + \frac{0.333333\,(460000. + 2700.\,\mathrm{d})}{-200. + 1.\,\mathrm{d}} + (0.419974\,(-3.316\times10^{11} -$$

$$1.584\times10^{9}\,\mathrm{d} - 8.79\times10^{6}\,\mathrm{d}^{2}))\big/$$

$$((-200. + 1.\,\mathrm{d})\bigl(-9.0272\times10^{16} - 5.85792\times10^{15}\,\mathrm{d} - 8.1504\times10^{12}\,\mathrm{d}^{2} -$$

$$5.1516\times10^{10}\,\mathrm{d}^{3} + 7.91881\times10^{9}\,\surd(-2.19591\times10^{15} -$$

$$1.6465\times10^{13}\,\mathrm{d} + 2.26516\times10^{11}\,\mathrm{d}^{2} - 3.49485\times10^{8}\,\mathrm{d}^{3} +$$

$$1.56086\times10^{6}\,\mathrm{d}^{4} - 10028.8\,\mathrm{d}^{5} - 1.\,\mathrm{d}^{6}))\wedge(1/3)\bigr) -$$

$$\frac{1}{-200. + 1.\,\mathrm{d}}\bigl(0.264567\bigl(-9.0272\times10^{16} - 5.85792\times10^{15}\,\mathrm{d} - 8.1504\times10^{12}$$

$$\mathrm{d}^{2} - 5.1516\times10^{10}\,\mathrm{d}^{3} + 7.91881\times10^{9}\,\surd(-2.19591\times10^{15} -$$

$$1.6465\times10^{13}\,\mathrm{d} + 2.26516\times10^{11}\,\mathrm{d}^{2} - 3.49485\times10^{8}\,\mathrm{d}^{3} +$$

$$1.56086\times10^{6}\,\mathrm{d}^{4} - 10028.8\,\mathrm{d}^{5} - 1.\,\mathrm{d}^{6}))\wedge(1/3))\Bigr)\Bigr)\Big/$$

$$\Bigl(-\frac{0.333333\,(460000. + 2700.\,\mathrm{d})}{-200. + 1.\,\mathrm{d}} - (0.419974\,(-3.316\times10^{11} - 1.584\times10^{9}\,\mathrm{d} -$$

$$8.79\times10^{6}\,\mathrm{d}^{2}))\Big/\bigl((-200. + 1.\,\mathrm{d})\bigl(-9.0272\times10^{16} - 5.85792\times10^{15}\,\mathrm{d} -$$

$$8.1504\times10^{12}\,\mathrm{d}^{2} - 5.1516\times10^{10}\,\mathrm{d}^{3} + 7.91881\times10^{9}\,\surd(-2.19591\times10^{15} -$$

$$1.6465\times10^{13}\,\mathrm{d} + 2.26516\times10^{11}\,\mathrm{d}^{2} - 3.49485\times10^{8}\,\mathrm{d}^{3} +$$

$$1.56086\times10^{6}\,\mathrm{d}^{4} - 10028.8\,\mathrm{d}^{5} - 1.\,\mathrm{d}^{6}))\wedge(1/3)\bigr) +$$

$$\frac{1}{-200. + 1.\,\mathrm{d}}\bigl(0.264567\bigl(-9.0272\times10^{16} - 5.85792\times10^{15}\,\mathrm{d} - 8.1504\times10^{12}$$

$$\mathrm{d}^{2} - 5.1516\times10^{10}\,\mathrm{d}^{3} + 7.91881\times10^{9}\,\surd(-2.19591\times10^{15} -$$

$$1.6465\times10^{13}\,\mathrm{d} + 2.26516\times10^{11}\,\mathrm{d}^{2} - 3.49485\times10^{8}\,\mathrm{d}^{3} +$$

$$1.56086\times10^{6}\,\mathrm{d}^{4} - 10028.8\,\mathrm{d}^{5} - 1.\,\mathrm{d}^{6}))\wedge(1/3))\Bigr)\Bigr)\Bigr)\Bigr)\}\}\}$$

```
Plot[Fnc,{d,100,300}]
```

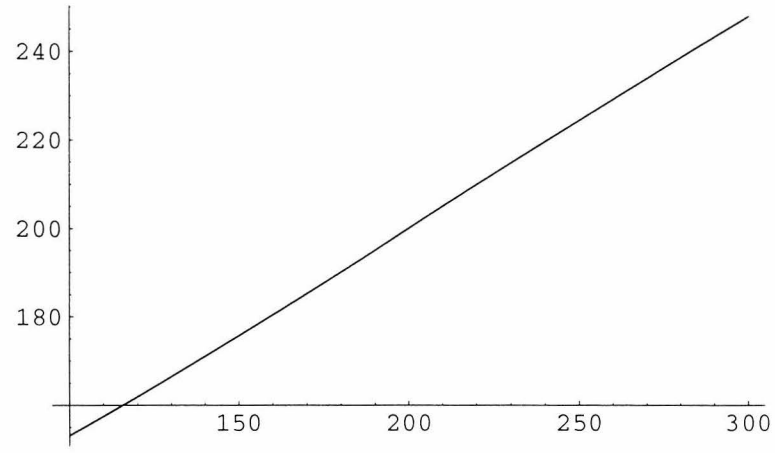


```
Plot[Fnc,{d,1,200000}]
```

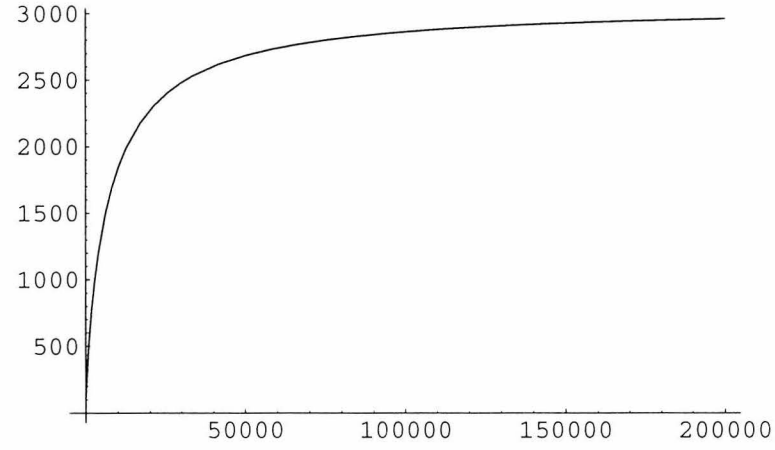

DISCUSSION

With initial inputs for S, p, and K, the equation was first solved for L in terms of K_D (d). Three solutions were found by *Mathematica*; the first two solutions contained imaginary numbers, and so the third real solution was carried on. Focusing on the boldface equations above, having found L, it was possible to solve for **D** (F), **E** (T), **DE** (A), and **LE** (B) and calculate $\mathbf{K_{DL}}$ (J) using the boldface equations above. Plots of K_{DL} vs. K_D (with constant K_L) show that when $K_D \approx K_L$, as in the first graph, K_{DL} appears linear over this narrow range and is roughly the average of both binding constants. In the case of Ru-C_9-Ad where K_L = 200 nM and K_D = 300 nM, K_{DL} works out to be 248 nM. The higher affinity Δ isomer slightly outcompetes Λ for the pocket, and lowers the apparent dissociation constant from the expected value for two 250 nM racemates. In the extreme case that K_L ~ nanomolar and K_D ~ molar ("dirt"), then the apparent dissociation constant, K_{DL}, is assymptotic, and quickly approaches the limit for the apparent dissociation constant when only half of the enzyme is bound (with L).

These simulations give predictions that are consistent with a two-state binding model (Chapter 3), and verify that the complex equilibrium expression for **D** did not violate any of the initial equilibrium conditions. Indeed, simple tests showed that the expression was mathematically correct and properly evaluated on the computer. In

addition, although the two-state model oversimplifies the myriad binding processes, all computational predictions from such a model are in good agreement with the observed experimental data. In short, the model suffices for studies of P450 with Ru-substrates in the regime where [Ru-substrate] $\leq$ [P450]. When [Ru] > [P450], multiple Ru-substrate binding events are observed, and more complex models are required.

CONCLUSION

The competition between stereoisomers proves to have a very small effect on the binding studies of Ru-C_9-Ad, and probably, by analogy, all Ru-substrates. These calculations show that the similarity between Λ and Δ K_D's reduces the need for chiral resolution. This analysis does raise some important points, however. All previously reported dissociation constants for racemic Ru-compounds are *apparent* values which vary with P450 and Ru-substrate concentration, as well as with the dissociation constants of the Λ and Δ enantiomers. At the typical micromolar concentrations, with equimolar P450:Ru, and with K_D (Δ) / K_D (Λ) ~ 2, the apparent K_D's should change very little between experiments.

Although this probably closes the story on the enatiomeric discrimination of P450 towards ruthenated compounds, this analysis may be relevant to the pharmaceutical

industry. Traditionally, generic medicines are composed of racemic mixtures. Often times, the efficacy of a drug relies on the potency of only one of the enantiomers, and relates to differences in binding affinity. Thus, for some drugs, a full mathematical analysis of racemate binding may shed light on whether large-scale chiral separations are warranted. The chiral resolution of drugs is becoming increasingly common and promises to be a growing area of pharmaceutical research.

AFTERWORD

Farewell to you and the youth I have spent with you.

It was but yesterday we met in a dream.

You have sung to me in my aloneness, and I of your longings have built a tower in the sky.

But now our sleep has fled and our dream is over, and it is no longer dawn.

The noontide is upon us and our half waking has turned to a fuller day, and we must part.

If in the twilight of memory we should meet once more, we shall speak again together and you shall sing to me a deeper song.

And if our hands should meet in another dream we shall build another tower in the sky.

THE FAREWELL

in *The Prophet*

by Kahlil Gibran